Das Puls-Echo Verfahren für Präzisionsmessungen der Schallgeschwindigkeit in Fluiden

dem Fachbereich Maschinenbau
der Helmut-Schmidt-Universität –
Universität der Bundeswehr Hamburg
vorgelegte
Habilitationsschrift

von

Dr.-Ing. Karsten Meier

aus Rehren

Hamburg, April 2006

The Pulse-Echo Method for High Precision Measurements of the Speed of Sound in Fluids

Postdoctoral Thesis

Presented
to the Department of Mechanical Engineering
of the Helmut-Schmidt-University –
University of the Federal Armed Forces Hamburg
by

Dr.-Ing. Karsten Meier

born in Rehren

Hamburg, April 2006

Contents

Nomenclature

Latin Letters

Symbol	Unit	Quantity
A	-	constant
A	m^2	area
A_0	m	constant
A_1	m	constant
A_i	Pa	amplitude of the acoustic pressure of the incident wave
A_p	m^2	piston area
A_r	Pa	amplitude of the acoustic pressure of the reflected wave
a	$\mathrm{J\,kg^{-1}}$	specific Helmholtz free energy
a	m	sender radius
$\boldsymbol{a}$	-	arbitrary vector
B	-	constant
B	$\mathrm{m^3\,kg^{-1}}$	second thermal virial coefficient
B_a	$\mathrm{s\,m^2\,kg^{-1}}$	acoustic susceptance
$\boldsymbol{b}$	-	arbitrary vector
b	-	parameter of a Gaussian source velocity distribution
b_i	$\mathrm{K^{-1}}$	coefficients of the polynomial representation of the differential thermal expansion coefficient of the sensor material
C	-	constant
C_0	F	static capacitance of a piezoelectric transducer
C_1	F	capacitive parameter in the equivalent circuit model of a piezoelectric transducer
$\boldsymbol{c}$	$\mathrm{N\,m^2}$	fourth order tensor of elastic constants
$\boldsymbol{c}^E$	$\mathrm{N\,m^2}$	fourth order tensor of elastic constants at constant electric field
$\boldsymbol{c}^D$	$\mathrm{N\,m^2}$	fourth order tensor of elastic constants at constant electric flux density
c_i	$\mathrm{K^{-1}}$	coefficients of the polynomial representation of the differential thermal expansion coefficient of the crystal
c_i	$\mathrm{J\,kg^{-1}K^{-1}}$	contribution of the ith internal degree of freedom to the specific heat capacity

c_{int}	$\mathrm{J\,kg^{-1}K^{-1}}$	contribution of the an internal degree of freedom the specific heat capacity
c_p	$\mathrm{J\,kg^{-1}K^{-1}}$	specific isobaric heat capacity
c_p^{∞}	$\mathrm{J\,kg^{-1}K^{-1}}$	specific isobaric heat capacity at infinite frequency
c_p^{iG}	$\mathrm{J\,kg^{-1}K^{-1}}$	specific isobaric heat capacity of the ideal gas
c_p^{Re}	$\mathrm{J\,kg^{-1}K^{-1}}$	residual contribution to the specific isobaric heat capacity
c^{vib}	$\mathrm{J\,kg^{-1}K^{-1}}$	vibrational contribution to the specific heat capacity
c_v	$\mathrm{J\,kg^{-1}K^{-1}}$	specific isochoric heat capacity
c_v^{∞}	$\mathrm{J\,kg^{-1}K^{-1}}$	specific isochoric heat capacity at infinite frequency
c_v^{iG}	$\mathrm{J\,kg^{-1}K^{-1}}$	specific isochoric heat capacity of the ideal gas
c_v^{Re}	$\mathrm{J\,kg^{-1}K^{-1}}$	residual contribution to the specific isochoric heat capacity
$\boldsymbol{D}$	$\mathrm{C\,m^{-2}}$	electric flux density vector
D	-	abbreviation
D_{h}	$\mathrm{m^2\,s^{-1}}$	thermal diffusivity
D_{s}	$\mathrm{m^2\,s^{-1}}$	longitudinal viscous diffusivity
D_{v}	$\mathrm{m^2\,s^{-1}}$	viscous diffusivity
$\boldsymbol{d}$	$\mathrm{C\,N^{-1}}$	third order tensor of piezoelectric constants
d	m	diameter
$\boldsymbol{E}$	$\mathrm{V\,m^{-1}}$	electric field strength vector
E	$\mathrm{N\,mm^{-2}}$	elastic modulus
$\boldsymbol{e}$	$\mathrm{C\,m^{-2}}$	third order tensor of piezoelectric constants
e_i	$\mathrm{N\,mm^{-2}}$	coefficients of the polynomial representation of the elastic modulus of the sensor material
$\boldsymbol{e}_x$	-	unit base vector pointing in positive x direction
$\boldsymbol{e}_y$	-	unit base vector pointing in positive y direction
$\boldsymbol{F}$	-	deformation gradient tensor
F	N	force
F_i	-	function that describes the temperature dependence of the contribution of the ith internal degree of freedom to the isochoric heat capacity
f	-	arbitrary function
f	Hz	frequency
f_{a}	Hz	anti-resonance frequency
f_{max}	Hz	frequency of maximum admittance
f_{min}	Hz	frequency of minimum admittance

f_r	Hz	resonance frequency with zero susceptance
f_rep	Hz	repetition frequency
$f_\mathrm{res}^\mathrm{p}$	Hz	parallel resonance frequency
$f_\mathrm{res}^\mathrm{s}$	Hz	series resonance frequency
G_a	$\mathrm{s\,m^2\,kg^{-1}}$	acoustic conductance
$\boldsymbol{g}$	$\mathrm{N\,C^{-1}}$	third order tensor of piezoelectric constants
g	$\mathrm{J\,kg^{-1}}$	Gibbs free energy
g_loc	$\mathrm{m\,s^{-2}}$	local gravitational acceleration
g	$\mathrm{J\,kg^{-1}}$	specific Gibbs free energy
$\boldsymbol{h}$	$\mathrm{m^2\,C^{-1}}$	third order tensor of piezoelectric constants
h	$\mathrm{J\,kg^{-1}}$	specific enthalpy
$\boldsymbol{I}$	-	identity tensor
I	A	electric current
i	-	imaginary unit
K_t	-	electromechanical coupling factor
k	$\mathrm{m^{-1}}$	wave number
k_h	$\mathrm{m^{-1}}$	propagation constant of the thermal sound mode
k_p	$\mathrm{m^{-1}}$	propagation constant of the propagational sound mode
k_s	$\mathrm{m^{-1}}$	propagation constant of the shear sound mode
L	$\mathrm{Pa^{-1}}$	pressure coefficient
L	m	length
L_0	m	length in the reference state (T_0, p_0)
L_1	m	distance between piezoelectric crystal and reflector
L_1	H	inductive parameter in the equivalent circuit model of a piezoelectric transducer
L_2	m	distance between piezoelectric crystal and reflector
L_c	m	crystal thickness
l	m	half thickness of a piezoelectric plate
M	$\mathrm{kg\,mol^{-1}}$	molar mass
m	-	parameter
m	kg	mass
m_i	kg	mass i of the pressure balance mass set
N	-	number of atoms in a molecule
n	-	integer constant
n	-	number of masses
$\boldsymbol{P}$	Pa	pressure tensor

P	$\mathrm{Pa\,m}$	transformed variable
p	Pa	pressure
p_0	Pa	reference pressure
p_a	Pa	acoustic pressure
p_amb	Pa	ambient pressure
p_eq	Pa	thermodynamic equilibrium pressure
p_h	Pa	contribution of thermal sound mode to the acoustic pressure
p_PB	Pa	pressure measured by a pressure balance
p_p	Pa	contribution of propagational sound mode to the acoustic pressure
$\boldsymbol{q}$	$\mathrm{W\,m^{-2}}$	heat flux vector
$\boldsymbol{q}_\mathrm{a}$	$\mathrm{W\,m^{-2}}$	acoustic contribution to the heat flux vector
$\boldsymbol{q}_\mathrm{w}$	$\mathrm{W\,m^{-2}}$	acoustic contribution to the heat flux vector in the wall
R	m	distance between a point in front of a sound source and a point on the surface of the source
R_0	Ω	resistive parameter in the equivalent circuit model of a piezoelectric transducer representing dielectric losses
R_1	Ω	resistive parameter in the equivalent circuit model of a piezoelectric transducer
R_1	m	distance of the point on the surface of a sound source to a point in front of the source, from which a sound signal reaches the point in front of the source first
R_2	m	distance of the point on the surface of a sound source to a point in front of the source, from which a sound signal reaches the point in front of the source last
R_a	$\mathrm{kg\,s^{-1}\,m^{-1}}$	acoustic resistance
$\boldsymbol{r}$	m	position vector
$\tilde{\boldsymbol{r}}$	m	position vector of a point in front of a sound source with respect to the origin
r	m	radial coordinate
$\boldsymbol{r}_0$	m	position vector of a point on the surface of a sound source with respect to the origin
r_0	m	distance of a point on the surface of a sound source from the origin
$\boldsymbol{S}$	-	strain tensor

S	-	one-dimensional strain
$\boldsymbol{s}$	$\mathrm{m^2\,N^{-1}}$	fourth order tensor of elastic compliances
$\boldsymbol{s}^D$	$\mathrm{m^2\,N^{-1}}$	fourth order tensor of elastic compliances at constant electric flux density
$\boldsymbol{s}^E$	$\mathrm{m^2\,N^{-1}}$	fourth order tensor of elastic compliances at constant electric field
s	$\mathrm{J\,kg^{-1}K^{-1}}$	specific entropy
s_a	$\mathrm{J\,kg^{-1}K^{-1}}$	acoustic specific entropy
$\boldsymbol{T}$	Pa	stress tensor
T	K	thermodynamic temperature
T_0	K	reference temperature
T_a	K	acoustic temperature
T_a^le	K	acoustic temperature under the assumption that local equilibrium is attained instantaneously
T_a^w	K	acoustic temperature in the wall
T_amb	K	ambient temperature
T_h	K	contribution of the thermal sound mode to the acoustic temperature
T_p	K	contribution of the propagational sound mode to the acoustic temperature
T_eq	K	thermodynamic equilibrium temperature
T_H	K	temperature in the heated part of the tubing system
T_T	K	temperature in the thermostat
T^vib	K	vibrational characteristic temperature
t	s	time
$\boldsymbol{u}$	m	displacement vector
u	$\mathrm{J\,kg^{-1}}$	specific internal energy
u^iG	$\mathrm{J\,kg^{-1}}$	specific internal energy of the ideal gas
u_a	$\mathrm{J\,kg^{-1}}$	acoustic specific internal energy
u_DPI	Pa	absolute uncertainty of the differential pressure indicator
u_g	$\mathrm{m\,s^{-2}}$	absolute uncertainty of the local gravitational acceleration
u_i	$\mathrm{J\,kg^{-1}}$	non-equilibrium contribution of the ith internal degree of freedom to the specific internal energy
u_i^eq	$\mathrm{J\,kg^{-1}}$	thermodynamic equilibrium contribution of the ith internal degree of freedom to the specific internal energy

u_i^{le}	$\mathrm{J\,kg^{-1}}$	local equilibrium contribution of the ith internal degree of freedom to the specific internal energy
u_p	Pa	absolute uncertainty of the pressure measurement
$u_{p_{\mathrm{amb}}}$	Pa	absolute uncertainty of the ambient pressure measurement
$u_{p_{\mathrm{PB}}}$	Pa	absolute uncertainty of a pressure balance
u_T	K	absolute uncertainty of the temperature measurement
u_w	$\mathrm{m\,s^{-1}}$	absolute uncertainty of the speed of sound measurement
$u_{\Delta h_i}$	m	absolute uncertainty of difference between geodesic heads
$u_{\Delta p_{\mathrm{hydro}}}$	Pa	absolute uncertainty of the hydrostatic pressure correction
$u_{\rho_{\mathrm{f}}}$	$\mathrm{kg\,m^{-3}}$	absolute uncertainty of the fluid density
V	V	voltage
$\dot{V}$	$\mathrm{m^3\,s^{-1}}$	volume flow
$\boldsymbol{v}$	$\mathrm{m\,s^{-1}}$	fluid velocity
$\boldsymbol{v}_{\mathrm{a}}$	$\mathrm{m\,s^{-1}}$	acoustic contribution to the fluid velocity
$\boldsymbol{v}_{\mathrm{l}}$	$\mathrm{m\,s^{-1}}$	longitudinal velocity component
$\boldsymbol{v}_{\mathrm{l,h}}$	$\mathrm{m\,s^{-1}}$	contribution of the thermal sound mode to the longitudinal velocity component
$\boldsymbol{v}_{\mathrm{l,p}}$	$\mathrm{m\,s^{-1}}$	contribution of the propagational sound mode to the longitudinal velocity component
v_0	$\mathrm{m\,s^{-1}}$	velocity of a sound source normal to its surface in source-centered coordinates
v_{r}	$\mathrm{m\,s^{-1}}$	radial velocity component
v_σ	$\mathrm{m\,s^{-1}}$	velocity of a sound source normal to its surface in observer-based coordinates
$\boldsymbol{v}_t$	$\mathrm{m\,s^{-1}}$	transverse velocity component
w	$\mathrm{m\,s^{-1}}$	speed of sound
w_0	$\mathrm{m\,s^{-1}}$	thermodynamic speed of sound
w_∞	$\mathrm{m\,s^{-1}}$	speed of sound at infinite frequency
w_{c}	$\mathrm{m\,s^{-1}}$	speed of sound at constant electric flux density in quartz normal to the Z axis
w^{f}	$\mathrm{m\,s^{-1}}$	speed of sound in a fluid
w^{iG}	$\mathrm{m\,s^{-1}}$	speed of sound in the ideal gas limit
$\boldsymbol{x}$	m	position vector in the deformed configuration
x	m	Cartesian coordinate

X_a	$\mathrm{kg\,s^{-1}\,m^{-1}}$	acoustic reactance
Y_a	$\mathrm{s\,m^2\,kg^{-1}}$	acoustic admittance
Y_m	$\mathrm{s\,kg^{-1}}$	mechanical admittance
Y_e	S	electrical admittance
y	m	Cartesian coordinate
y_a^w	-	dimensionless specific acoustic admittance of the wall
y_a^h	-	dimensionless specific acoustic admittance of the thermal boundary layer
y_a^s	-	dimensionless specific acoustic admittance of the viscous boundary layer
Z_a	$\mathrm{kg\,s^{-1}\,m^{-1}}$	acoustic impedance
Z_a^b	$\mathrm{kg\,s^{-1}\,m^{-1}}$	acoustic impedance of the material at the back of a piezoelectric transducer
Z_a^f	$\mathrm{kg\,s^{-1}\,m^{-1}}$	acoustic impedance of the material at the front of a piezoelectric transducer
Z_a^w	$\mathrm{kg\,s^{-1}\,m^{-1}}$	acoustic impedance of a solid wall
Z_m	$\mathrm{kg\,s^{-1}}$	mechanical impedance
Z_e	Ω	electric impedance
Z_e^L	Ω	electric imdepance of a mechanical load
z	-	arbitrary complex number
z	m	Cartesian coordinate
z	m	cylindrical coordinate

Greek Letters

Symbol	Unit	Quantity
α	$\mathrm{m^{-1}}$	sound absorption coefficient
α^int	$\mathrm{m^{-1}}$	dispersive contribution of an internal degree of freedom to the sound absorption coefficient
α_t	$\mathrm{N\,V^{-1}}$	transformation factor
α_th	$\mathrm{K^{-1}}$	average thermal expansion coefficient
$\alpha_\mathrm{th}^\mathrm{AS}$	$\mathrm{K^{-1}}$	thermal expansion coefficient of the acoustic sensor
$\alpha_\mathrm{th}^\mathrm{c}$	$\mathrm{K^{-1}}$	thermal expansion coefficient of the piezoelectric crystal
$\alpha_\mathrm{th}^\mathrm{cyl}$	$\mathrm{K^{-1}}$	thermal expansion coefficient of the cylinder
$\alpha_\mathrm{th}^\mathrm{p}$	$\mathrm{K^{-1}}$	thermal expansion coefficient of the piston
$\boldsymbol{\beta}$	$\mathrm{m\,F^{-1}}$	dielectric impermeability tensor

$\boldsymbol{\beta}^S$	$\mathrm{m\,F^{-1}}$	dielectric impermeability tensor at constant strain
$\boldsymbol{\beta}^T$	$\mathrm{m\,F^{-1}}$	dielectric impermeability tensor at constant stress
β	$\mathrm{Pa\,K^{-1}}$	thermal pressure coefficient
β_a	$\mathrm{m^3}$	second acoustic virial coefficient
β_th	$\mathrm{K^{-1}}$	differential thermal expansion coefficient
$\beta_\mathrm{th}^\perp$	$\mathrm{K^{-1}}$	differential thermal expansion coefficient of α-quartz perpendicular to the Z axis
$\beta_\mathrm{th}^\parallel$	$\mathrm{K^{-1}}$	differential thermal expansion coefficient of α-quartz parallel to the Z axis
Γ	-	dimensionless propagation constant
Γ_h	-	dimensionless propagation constant of the thermal sound mode
Γ_p	-	dimensionless propagation constant of the propagational sound mode
Γ_s	-	dimensionless propagation constant of the shear sound mode
γ	$\mathrm{m^2}$	abbreviation
γ_a	$\mathrm{m^6}$	third acoustic virial coefficient
Δh	m	difference between geodesic heads
Δh_i	m	difference between geodesic heads in part i of the tubing system
Δp_hydro	Pa	hydrostatic pressure correction
Δt	s	time difference
Δt_pw	s	time difference for plane wave propagation
Δt_d	s	diffraction correction for the time difference
Δt_m	s	measurement value of the time difference
Δt_R1	s	transit time of the first reflection at the sender rod
Δt_R2	s	transit time of the first reflection at the receiver rod
Δt_s	s	transit time through the sample liquid
Δt_tr	s	transit time through the sender rod, sample liquid, and receiver rod
ΔL	m	acoustic path length
δ_h	m	thermal penetration length
δ_{ij}	-	Kronecker delta
δ_s	m	shear penetration length
δ_w	m	thermal penetration length of the wall

δL	-	change of length due to mechanical deformation
$\boldsymbol{\varepsilon}$	$\mathrm{F\,m^{-1}}$	tensor of dielectric constants
$\boldsymbol{\varepsilon}^S$	$\mathrm{F\,m^{-1}}$	tensor of dielectric constants at constant strain
$\boldsymbol{\varepsilon}^T$	$\mathrm{F\,m^{-1}}$	tensor of dielectric constants at constant stress
ε	-	relative measurement uncertainty
$\varepsilon_{\mathrm{DPI}}$	-	relative uncertainty of the differential pressure indicator
ε_i	$\mathrm{J\,kg^{-1}}$	non-equilibirum amplitude of the periodic variation of the specific internal energy of the ith internal degree
$\varepsilon_i^{\mathrm{le}}$	$\mathrm{J\,kg^{-1}}$	amplitude of the periodic variation of the specific internal energy of the ith internal degree under the assumption that local equilibrium is instantaneously attained
ε_{ijk}	-	permutation symbol
ε_p	-	relative uncertainty of the pressure measurement
$\varepsilon_{p_{\mathrm{amb}}}$	-	relative uncertainty of the ambient pressure
$\varepsilon_{p_{\mathrm{PB}}}$	-	relative uncertainty of a pressure balance
ε_w	-	relative uncertainty of the speed of sound measurement
$\varepsilon_{\Delta p_{\mathrm{hydro}}}$	-	relative uncertainty of the hydrostatic pressure correction
η	$\mathrm{Pa\,s}$	viscosity
η	$\mathrm{m^2}$	abbreviation
η_{b}	$\mathrm{Pa\,s}$	bulk viscosity
φ_{i}	rad	angle of incidence
φ_{r}	rad	angle of reflection
Ψ	$\mathrm{m^2\,s^{-1}}$	velocity potential
χ_{Re}	-	reflection coefficient
κ	-	isentropic exponent, ratio of the isobaric and isochoric heat capacities
κ^{iG}	-	isentropic exponent of the ideal gas
λ	m	wave length
λ_{c}	$\mathrm{W\,m^{-1}K^{-1}}$	thermal conductivity
$\lambda_{\mathrm{c}}^{\mathrm{f}}$	$\mathrm{W\,m^{-1}K^{-1}}$	thermal conductivity of the fluid
$\lambda_{\mathrm{c}}^{\mathrm{w}}$	$\mathrm{W\,m^{-1}K^{-1}}$	thermal conductivity of the wall
λ_{p}	$\mathrm{Pa^{-1}}$	pressure coefficient
ν	-	Poisson number
Ω	-	half apex angle of a circle segment on the source surface
ω	Hz	angular frequency
$\omega_{\mathrm{res}}^{\mathrm{p}}$	Hz	angular parallel resonance frequency

$\omega_{\mathrm{res}}^{\mathrm{s}}$	Hz	angular series resonance frequency
$\mathbf{\Pi}$	Pa	viscous pressure tensor
ρ	$\mathrm{kg\,m^{-3}}$	mass density
ρ	m	radial coordinate with respect to the projection of a point in front of a sound source on the source plane
ρ_1	m	radius of the circle with center at the projection of a point in front of a sound source on the source plane, which touches the source boundary first
ρ_2	m	radius of the circle with center at the projection of a point in front of a sound source on the source plane, which touches the source boundary last
ρ_{a}	$\mathrm{kg\,m^{-3}}$	acoustic mass density contribution
ρ_{air}	$\mathrm{kg\,m^{-3}}$	mass density of air
ρ_{c}	$\mathrm{kg\,m^{-3}}$	mass density of quartz
ρ_{eq}	$\mathrm{kg\,m^{-3}}$	thermodynamic equilibrium mass density
ρ_{f}	$\mathrm{kg\,m^{-3}}$	mass density of a fluid
ρ_{m}	$\mathrm{kg\,m^{-3}}$	mass density of stainless steel masses (pressure balance)
τ_i	s	relaxation time of ith internal degree of freedom
τ_{int}	s	relaxation time of an internal degree of freedom
τ_{h}	s	thermal relaxation time
τ_{s}	s	shear relaxation time
τ_{v}	s	viscous relaxation time
Θ	-	apex angle of a circle segment on the source surface
Θ_1	-	angular coordinate on a circle segment on the source surface
ϑ	°C	temperature of the Celcius temperature scale
ϑ_0	°C	reference temperature
$\boldsymbol{\xi}$	m	position vector in the reference configuration

Indices and Abbreviations

Symbol	Quantity
0	zero frequency
AS	acoustic sensor
a	acoustic
amb	ambient

b	bulk
b	back
C	crystal
c	cylinder
DPI	differential pressure indicator
eq	equilibrium
f	front
h	thermal sound mode
i	running index
i	index in Cartesian tensor notation
i	incidence
int	internal degree of freedom
j	index in Cartesian tensor notation
iG	ideal gas
k	index in Cartesian tensor notation
l	longitudinal
l	index in Cartesian tensor notation
n	normal
PB	pressure balance
p	propagational sound mode
p	piston
p	index in condensed matrix notation
q	index in condensed matrix notation
r	reflection
s	shear sound mode
t	transverse
vib	vibrational degree of freedom
w	wall

Fundamental Physical Constants

Quantity	Symbol	CODATA Numerical Value [129]
Speed of light in vacuum	c	$299792458\ \mathrm{m\,s^{-1}}$
Boltzmann constant	k_B	$1.3806503 \cdot 10^{-23}\ \mathrm{J\,K^{-1}}$
Planck constant	h	$6.62606876 \cdot 10^{-34}\ \mathrm{J\,s}$
Molar gas constant	R_m	$8.314472\ \mathrm{J\,mol^{-1}\,K^{-1}}$

Tensor Notation

The index and symbolic tensor notations are used in parallel in this work. In index notation, the Einstein summation convention is used, which means that, if an index occurs twice in a term, then this term is to be summed with respect to this index over the range of its admissible values, for example $a_i b_i = a_1 b_1 + a_2 b_2 + a_3 b_3$ with i=1,2,3.

Symbolic Notation	Index Notation	Meaning
$\boldsymbol{a}$	a_i	vector
$\boldsymbol{b}$	b_i	vector
$\boldsymbol{A}$	A_{ij}	second order tensor
$\boldsymbol{I}$	δ_{ij}	identity tensor
∇	$\partial/\partial x_i$	Nabla operator
$\boldsymbol{a} \cdot \boldsymbol{b}$	$a_i b_i$	scalar product of two vectors
$\boldsymbol{A} \cdot \boldsymbol{b}$	$A_{ij} b_j$	product of a tensor and a vector
$\boldsymbol{a} \cdot \boldsymbol{B}$	$a_i B_{ij}$	product of a vector and a tensor
$\boldsymbol{A} \cdot \boldsymbol{B}$	$A_{ij} B_{jk}$	product of two second-order tensors
$\boldsymbol{A} : \boldsymbol{B}$	$A_{ij} B_{ji}$	scalar product of two second-order tensors
$\boldsymbol{a} \times \boldsymbol{b}$	$(\boldsymbol{a} \times \boldsymbol{b})_k = \varepsilon_{ijk} a_i b_j$	vector product
$\boldsymbol{a} \otimes \boldsymbol{b}$	$a_i b_j$	dyadic product
$\boldsymbol{A}^t$	$(A_{ij})^t = A_{ji}$	transpose of the tensor $\boldsymbol{A}$
D/Dt	$\partial/\partial t + v_i \, \partial/\partial x_i$	material derivative

Products of higher-order tensor are formed accordingly. The quantity ε_{ijk} is the permutation symbol, which is defined by

$$\varepsilon_{ijk} = \begin{cases} 1, & \text{if } ijk \text{ are an even permutation of 123} \\ -1, & \text{if } ijk \text{ are an even permutation of 123} \\ 0, & \text{otherwise} \end{cases} .$$

1 Introduction

This work summarizes the theoretical basis of the pulse-echo method for measurements of the speed of sound in fluids and describes the development and operation of an instrument for high-precision measurements over a wide temperature range and under high pressures as an example. Knowledge of the speed of sound in fluids is important because it is a basic physical quantity for understanding and describing acoustic phenomena and, furthermore, because precise speed of sound data are very useful in thermophysical properties research, for example in equation of state modelling. While some of the results of this work may be of general interest, the emphasis lies in the applications of the speed of sound in thermophysical properties research.

Acoustic phenomena occur in nature, many areas of every day life, and diverse technical applications. Examples are speech and hearing, music, noise, architectural acoustics, medical diagnostics, ultrasonic cleaning, ultrasonic manufacturing processes, or position locating systems of some animals such as bats or dolphins [92, 100]. Widely known are SONAR[1)] techniques, which are employed in military and civil navy or submarine research for position finding or locating objects. Ultrasonic mass flow and fill level sensors utilize pulse-echo measurement techniques, which were originally developed to measure the speed of sound in liquids and solids.

Further areas of application are transonic and supersonic flows [149]. They are characterized by the Mach number, which is defined as the ratio of the fluid velocity and the speed of sound in the fluid. Supersonic flows occur for example around spacecrafts upon entry into planetary atmospheres, around projectiles moving in air, in supersonic thermal jet engines, or in nozzles. In isentropic flows through convergent nozzles, the streaming velocity of the fluid at the orifice is limited to the speed of sound [10]. The acceleration of the fluid to velocities larger than the speed of sound requires convergent-divergent nozzles (Laval nozzles), in which the cross section increases behind the smallest cross section. The streaming velocity in the smallest cross section equals the speed of sound. In this application, the speed of sound is required as a basic design quantity.

In thermophysical properties research, the speed of sound is an important quantity not so much for its own sake, but mainly because valuable information about

[1)] Sound Navigation and Ranging

other properties can be derived from it. As will be shown in the following chapter, the square of the speed of sound w is given by

$$w^2 = \left(\frac{\partial p}{\partial \rho}\right)_s , \tag{1.1}$$

in which p denotes the pressure, ρ is the mass density, and s is the entropy. In this form, Eq. (1.1) is not yet useful because it relates the speed of sound to the entropy equation of state $p = p(\rho, s)$. If one chooses the temperature T in place of the entropy as an independent variable, Eq. (1.1) becomes

$$w^2 = \left(\frac{\partial p}{\partial \rho}\right)_T + \frac{T}{\rho^2 c_v}\left[\left(\frac{\partial p}{\partial T}\right)_\rho\right]^2 . \tag{1.2}$$

This relation emphasizes the role of the speed of sound between thermal and caloric properties. The speed of sound contains information about the thermal equation of state and the isochoric heat capacity, but it alone is not sufficient to determine one or both of these properties.

Davis and Gordon [36] devised a technique to derive the thermal equation of state of pure fluids from comprehensive speed of sound data sets. This method was later refined by ten Seldam and Biswas [156] and applied to determine the thermal equation of state of compressed nitrogen [21], methane [22], and argon [156]. In this method with density and temperature as independent variables, Eq. (1.2) is viewed as a differential equation for the pressure as a function of temperature. When supplemented by initial values for the pressure on one isotherm and for isochoric heat capacity on one isochore at low pressures, it can be integrated together with the equation

$$\left(\frac{\partial c_v}{\partial \rho}\right)_T = -\frac{T}{\rho^2}\left(\frac{\partial^2 p}{\partial T^2}\right)_\rho \tag{1.3}$$

to yield the thermal equation of state in the form $p = p(\rho, T)$ along isochors in the region of the speed of sound measurements. With an accurate speed of sound data set, the accuracy of the $p\rho T$ data derived from the speed of sound data can be comparable with that achieved with the best direct measurement techniques for the density as a function of pressure and temperature. Modified versions of this method were for example described by Daridon et al. [35], Trusler and co-workers [44, 46, 178, 183], Estrada-Alexanders and Justo [47], Petitet et al. [143], or ten Seldam and Biswas [157].

If the fundamental equation of state is formulated in terms of the Helmholtz free energy a, Eq. (1.2) becomes

$$w^2 = \rho^2 \left(\frac{2}{\rho} \left(\frac{\partial a}{\partial \rho} \right)_T + \left(\frac{\partial^2 a}{\partial \rho^2} \right)_T - \left[\left(\frac{\partial}{\partial T} \left(\frac{\partial a}{\partial \rho} \right)_T \right)_\rho \right]^2 \left[\left(\frac{\partial^2 a}{\partial T^2} \right)_\rho \right]^{-1} \right). \quad (1.4)$$

With the non-linear regression and multi-property fitting techniques described by Ahrendts and Baehr [2, 3] and the structural optimization method developed by Wagner [185], speed of sound data can be used together with data of further thermodynamic properties, for example $p\rho T$ and vapor pressure data, to establish empirical fundamental equations of state in terms of the Helmholtz free energy, from which all other thermodynamic properties can be calculated [11, 88, 160, 176]. As Eq. (1.2) shows, the speed of sound combines the derivatives $(\partial p/\partial T)_\rho$ and $(\partial p/\partial \rho)_T$ of the thermal equation of state and the isochoric heat capacity. If speed of sound data are used in the optimization process of a fundamental equation of state and the fundamental equation of state represents the speed of sound accurately over a wide range of temperature and density, it will also describe the thermal equation of state and the isochoric heat capacity accurately. Speed of sound data are therefore especially valuable for modelling the liquid region, where many properties depend strongly on density.

Speed of sound data in the gas region may be used to determine ideal gas heat capacities. Isochoric ideal gas heat capacities are for example required for establishing fundamental equations of state [160, 176]. In the ideal gas limit, the speed of sound is related to the specific isochoric heat capacity $c_v^{\mathrm{iG}}(T)$ by

$$[w^{\mathrm{iG}}(T)]^2 = \frac{R_\mathrm{m} T}{M} \frac{c_v^{\mathrm{iG}}(T) + R_\mathrm{m}/M}{c_v^{\mathrm{iG}}(T)}, \quad (1.5)$$

where R_m is the universal gas constant and M denotes the molar mass. The speed of sound in the ideal gas limit can easily be determined by extrapolating isothermal gas phase speed of sound data to zero pressure. The isochoric heat capacity can then be calculated from the ideal gas speeds of sound by Eq. (1.5) [17, 50, 80, 86].

Furthermore, thermal virial coefficients for the virial equation of state can be determined from isothermal gas phase speed of sound data [177]. In a first step, acoustic virial coefficients are derived from the speed of sound data. They are the coefficients $\beta_\mathrm{a}(T), \gamma_\mathrm{a}(T), \ldots$ in the series expansion of the speed of sound squared with respect to pressure

$$[w(p,T)]^2 = [w^{\mathrm{iG}}(T)]^2 [1 + \beta_\mathrm{a}(T) p + \gamma_\mathrm{a}(T) p^2 + \ldots]. \quad (1.6)$$

The acoustic virial coefficients are related to the thermal virial coefficients by differential equations. For example, the second acoustic virial coefficient $\beta_\mathrm{a}(T)$ is related to the second thermal virial coefficient $B(T)$ by

$$\beta_\mathrm{a}(T) = 2B(T) + 2[\kappa^\mathrm{iG}(T) - 1] \cdot T \frac{dB(T)}{dT} + \frac{[\kappa^\mathrm{iG}(T) - 1]^2}{\kappa^\mathrm{iG}(T)} \cdot T^2 \frac{d^2B(T)}{dT^2}, \quad (1.7)$$

where $\kappa^\mathrm{iG}(T) = [c_v^\mathrm{iG}(T) + R_\mathrm{m}/M]/c_v^\mathrm{iG}(T)$ is the isentropic exponent of the ideal gas. In order to determine the thermal virial coefficients, an empirical function may be chosen for $B(T)$, whose parameters are optimized by a nonlinear regression of the experimental data of $\beta_\mathrm{a}(T)$ [17]. Alternatively, the well-known relations between the thermal virial coefficients and the intermolecular potential-energy functions [77] provide a way to calculate $\beta_\mathrm{a}(T)$ from the pair potential. Thus, the parameters of model pair potentials may be optimized by a nonlinear regression of experimental data of $\beta_\mathrm{a}(T)$. Thermal virial coefficients may then be determined from the model pair potentials. Square-well, Kihara, or more refined model potentials have been used for this purpose [63, 82, 83, 84, 85, 86, 181, 182].

As ideal gas heat capacities, thermal virial coefficients are important for equation of state of state modelling because they are related to the derivatives of the isotherms of the thermal equation of state with respect to density in the zero-density limit. Therefore, they represent limiting cases, which an equation of state must describe correctly. Moreover, they are useful for verifying quantum chemical calculations of energy hypersurfaces for intermolecular interactions.

In view of these applications, speed of sound data are extremely valuable in thermophysical properties research. However, they are less frequently measured than for example $p\rho T$ data or vapor pressures. This applies even more so to measurements in liquids than to measurements in gases.

Experimental methods for the determination of the speed of sound in fluids can mainly be divided in two groups, which are applied in different parts of the fluid region. Acoustic resonators and interferometers are predominantly used for measurements in gases, while pulse-echo methods are mainly employed for measurements in liquids. Moreover, optical techniques, for example light scattering techniques [57, 58, 98, 107, 169, 188], have been developed for measurements of the speed of sound.

Resonator and interferometer methods employ an acoustic cavity with a well-defined geometry, in which standing sound waves are generated continuously. Both methods work best if the walls of the cavity reflect sound efficiently, which is the case for gases at low pressures. An acoustic cavity is called a resonator, if the operating

frequency is controlled by a normal mode of the cavity, and an interferometer, if the operating frequency is controlled by one of the resonance frequencies of the transducer, which generates the sound waves inside the cavity. In both methods, the speed of sound is obtained from measurements of resonance frequencies of the cavity.

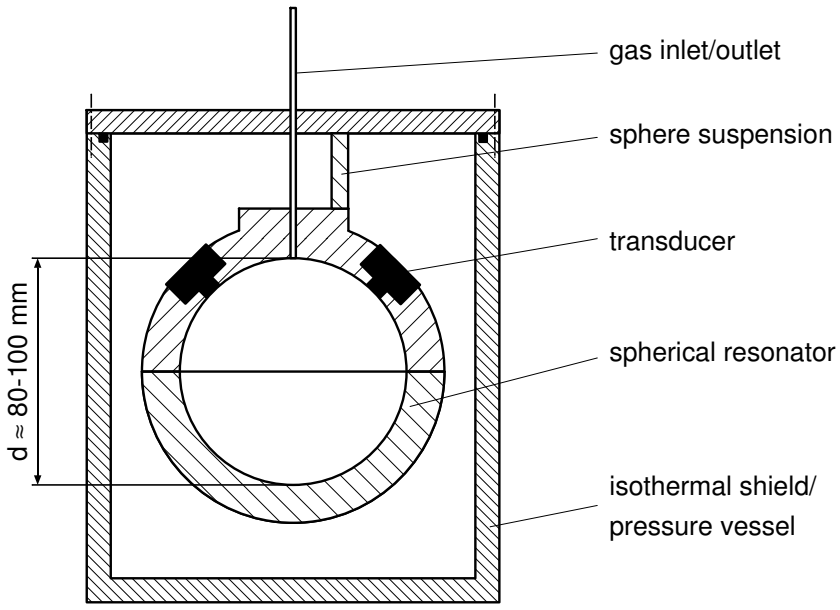

Figure 1.1. Principle design of a spherical resonator.

Today, the spherical resonator is the preferred technique for measurements in gases because it is ideally suited for highly accurate measurements. Its principle advantages lie in the existence of radial modes, in which there is no viscous boundary layer at the surface of the sphere and whose resonance frequencies are rather insensitive to geometric imperfections. A schematic drawing of a spherical resonator is depicted in Fig. 1.1. A spherical resonator consists of two hemispheres, which are either screwed together [16, 132] or are welded to each other along the equator of the sphere [53]. The sphere itself can act as a pressure vessel, or it can be placed in an external pressure vessel. Two sound transducers are employed, one to generate the resonances and one to detect them. As the radial resonances are evaluated to determine the speed of sound, it is useful to suppress the detection of non-radial modes, which are resonant close to the resonances of radial modes. For this reason, the transducers are separated by an angle of 90°, which has the advantage that, while the source transducer establishes the polar axis of the non-radial vibrational

modes of the gas, the detector resides at a node of certain non-radial vibration modes, which are then not seen by the detector. The sound generator is excited with a continuous sinusoidal signal delivered by a function generator, and a lock-in amplifier is employed to measure the amplitude and phase of the detected signal with respect to the excitation. The resonance frequencies of the radial modes are obtained from scans, in which the amplitude and phase are measured in discrete frequency steps in the vicinity of the resonances. For typical sphere diameters of about 80–100 mm, the resonance frequencies of the lowest radial modes, from which the speed of sound is usually derived, lie in the low kHz regime.

The acoustic theory of the spherical resonator was developed by Moldover, Mehl and co-workers in the 1980s [124, 121, 122, 123, 125, 130]. Based on these works, Moldover et al. [131, 132] determined the most accurate value yet of the universal gas constant R_{m} from highly precise measurements of the speed of sound in the noble gas argon at the triple point temperature of water with a spherical resonator, whose uncertainty was better than 1 ppm. Since these pioneering works by Moldover, Mehl and co-workers, many groups have copied spherical resonators, for example Beckermann [16, 17], Benedetto et al. [18], Ewing and co-workers [49, 50, 51, 52, 53], Fawcett [55], Trusler and co-workers [32, 43, 44, 45, 178, 180], or Watanabe and co-workers [80, 81]. A detailed account of the theory of the spherical resonator can also be found in the monograph of Trusler [177]. Measurement uncertainties better than 0.01 % in the speed of sound are now almost routinely achieved and can be maintained over a wide temperature range and under pressures up to about 10 MPa. In metrology, spherical resonators have been applied by several groups as primary acoustic thermometers to directly measure thermodynamic temperatures. Due to the high precision of the spherical resonator method, it was possible to detect small deviations of a few mK of the practical temperature scale ITS-90 from the true thermodynamic temperature [54, 115, 126, 133].

The basic measurement principle of pulse-echo experiments is very simple: the time of flight of an acoustic burst signal over a known distance in the sample fluid is measured, and the speed of sound is obtained as the distance divided by the measured time difference. Practical speed of sound sensors differ in the way the sound signals are guided within the sensor, and free field or guided sound propagation can be distinguished. Piezoelectric transducers operated at their resonance frequency are employed for signal generation and detection, and carrier frequencies lie between 1 and 20 MHz. Different types of acoustic sensors for pulse-echo experiments are described in the literature, see for example [38, 40, 62, 67, 93, 97,

119, 127, 135, 172, 192, 193, 194]. Besides their application for speed of sound measurements, pulse-echo experiments have also been employed to measure liquid-liquid phase boundaries in liquid mixtures [113] or to locate the melting line of pure substances [170]. Some theoretical and practical aspects of pulse-echo experiments are described in the monograph published by Thurston and Pierce [174].

Figs. 1.2 to 1.4 depict schematic drawings of three different pulse-echo speed of sound sensors described by Younglove [194], Miller [127], and Ye et al. [192, 193], respectively. In the following, these three sensors are discussed in some detail.

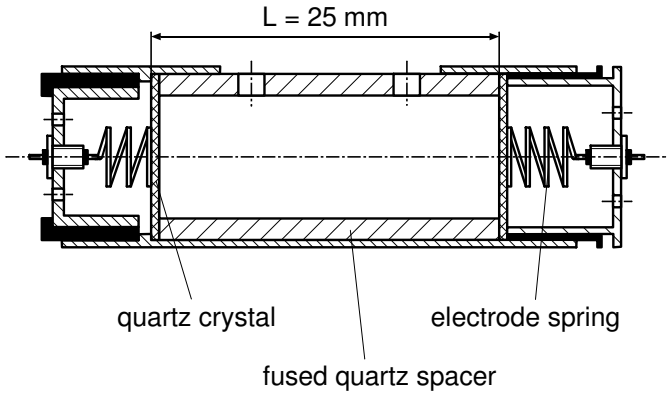

Figure 1.2. The speed of sound sensor of Younglove [194].

The design and measurement principle of the sensor described by Younglove [194] shown in Fig. 1.2 is based on a sensor, which was developed earlier by Greenspan and Tschiegg [67]. It consists of a fused quartz spacer tube, which serves as the acoustic wave guide, with piezoelectric quartz transducers with resonance frequencies of 10 MHz at both ends. One transducer serves a sender, and the other one is operated as a receiver. The quartz spacer has a length of about $L = 25$ mm, and both end surfaces are flat within a few wavelengths of visible light and parallel to each other within 1 part in 30000. The length of the spacer was determined by a length measuring device. The piezoelectric transducers were completely covered by gold electrodes on both faces so that the whole surface is acoustically active and the propagating acoustic waves are guided by the inner wall of the spacer tube. The sender is excited with rectangular pulses of 40 V amplitude and 0.1 μs duration and generates sound signals with about 30–50 sinus periods, which are reflected back and forth several times between the sender and receiver in the waveguide. The pulse repetition frequency f_{rep} is adjusted so that the echo sequences belonging

to different pulses interfere. This interference is monitored on an oscilloscope. If the time between successive input pulses equals the time an acoustic signal needs to travel back and forth between sender and receiver, constructive interference of the received echo sequences occurs. The speed of sound is then determined by $w = 2Lf_{\mathrm{rep}}$. The sensor is housed in a pressure vessel, which itself is placed in a thermostat. This instrument was operated from cryogenic temperatures to ambient temperature and under pressures up to 35 MPa, and measurement uncertainties of 0.05 % for the speed of sound were achieved [184, 194, 195].

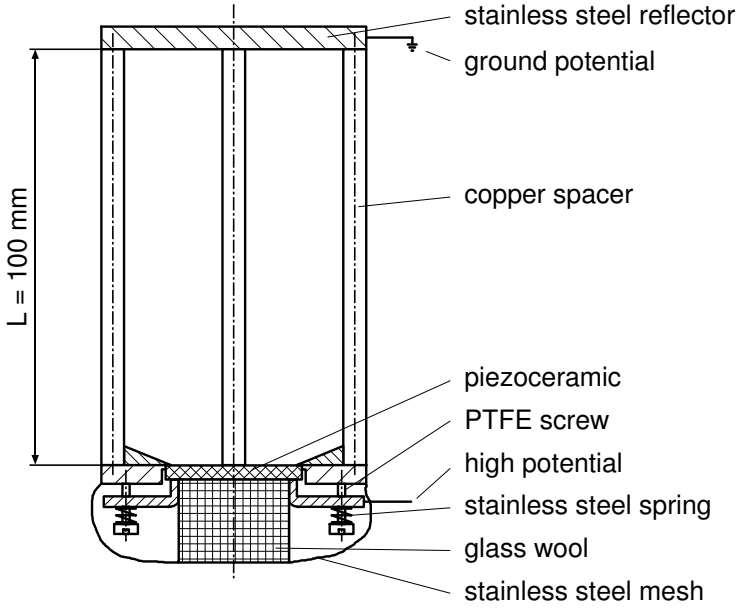

Figure 1.3. The speed of sound sensor of Miller [127].

Fig. 1.3 shows the speed of sound sensor of Miller [127]. In this sensor, a single piezoceramic transducer with a resonance frequency of 3 MHz is employed, which serves as sender and receiver. A stainless steel reflector is mounted at a distance of about $L = 100$ mm from the transducer. Parallelism between the transducer and reflector is guaranteed by three copper spacers. Copper was chosen as spacer material because its thermal expansion coefficient is well known. Since the spacers and the transducer are so far apart from each other that there are no interactions between the acoustic signals and the spacers, free field propagation can be assumed in this design. The distance between transducer and reflector is determined by a calibration measurement with a fluid, in which the speed of sound is accurately known. In order to eliminate unwanted echoes at the back of the transducer, glass wool is

placed in the space at the back as a sound absorber. The glass wool is held in place by a stainless steel mesh. As in the instrument of Younglove, the sensor is housed in a pressure vessel, which in this case is thermostatted in a circulating liquid bath thermostat. The transducer is excited by a sinusoidal burst signal and generates an acoustic signal, which is reflected several times back and forth between the transducer and reflector. The speed of sound is determined from the time difference Δt between the first two echoes of the received echo sequence as $w = 2L/\Delta t$. In the work of Miller, the time between the first two echoes was measured by the pulse-echo-overlap technique introduced by Papadakis [142]. The instrument covered the temperature range between 280 K and 450 K under pressures up to 125 MPa. Several liquids were studied with this instrument [71, 104, 105], and the measurement uncertainty of the speed of sound was estimated to be 0.05 %. An automatization of the pulse-echo overlap method suitable for computer controlled data acquisition was described by Horváth-Szabó et al. [79]. With modern digital storage oscilloscopes, the time difference between the echoes could simply be determined as the time between corresponding characteristic points of the two echoes, for example the first maxima, from the stored signal.

The speed of sound sensor developed by Ye et al. [192, 193], which is depicted in Fig. 1.4, differs in several respects from the ones of Younglove and Miller. It also involves two piezoelectric quartz transducers with resonance frequencies of 5 MHz, one of which acts as a sender and the other one acts as a receiver. However, they are not placed in direct contact with the fluid, but are coupled to it via stainless steel buffer rods. The buffer rods are screwed into a hollow cylinder, which forms the pressure vessel and contains the sample fluid. The piezoelectric transducers are adhered to the buffer rods by thin layers of viscous oil. The sender is excited at its resonance frequency and generates an acoustic signal which propagates through the sensor. The received echo pattern is more complex than for the sensors of Younglove and Miller because at each interface some part part of the signal is transmitted and some part is reflected backwards. For the determination of the speed of sound, the generated signal, the first signal reflected at the sender rod, the first received signal, which directly passed through the sender rod, fluid, and receiver rod, and the first signal reflected at the receiver rod are evaluated as shown in Fig. 1.5. With the nomenclature introduced in Fig. 1.5, the time the signal needs to pass through the sample fluid is given by $\Delta t_\mathrm{s} = \Delta t_\mathrm{tr} - (\Delta t_\mathrm{R1} - \Delta t_\mathrm{R1})/2$. If the generated and received signals are measured by a two-channel digital storage oscilloscope, the time differences can be extracted from the stored signals as above for the sensor of Miller

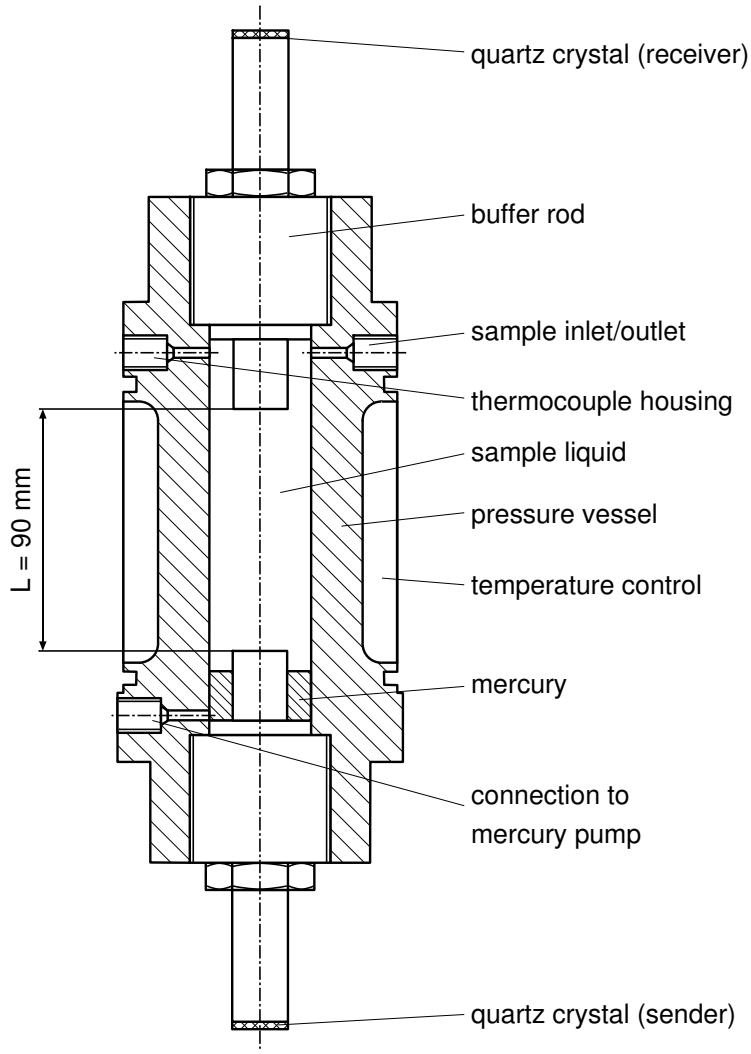

Figure 1.4. The speed of sound sensor of Ye et al. [192, 193].

as the time differences between corresponding characteristic points of the signals, for example first maxima. The distance L between the two buffer rods is determined by a calibration measurement, and the speed of sound is then given by $w = L/\Delta t_s$. As the sensor itself forms the pressure vessel, the correction for variation of the distance L due to expansion under pressure is rather large in this arrangement. The apparatus covered the temperature range between 290 and 420 K under pressures up to 70 MPa, and the measurement uncertainty of the speed of sound was about 0.1 %. Later, the sensor was modified by Daridon [34], and the apparatus was automatized by Ding et al. [38].

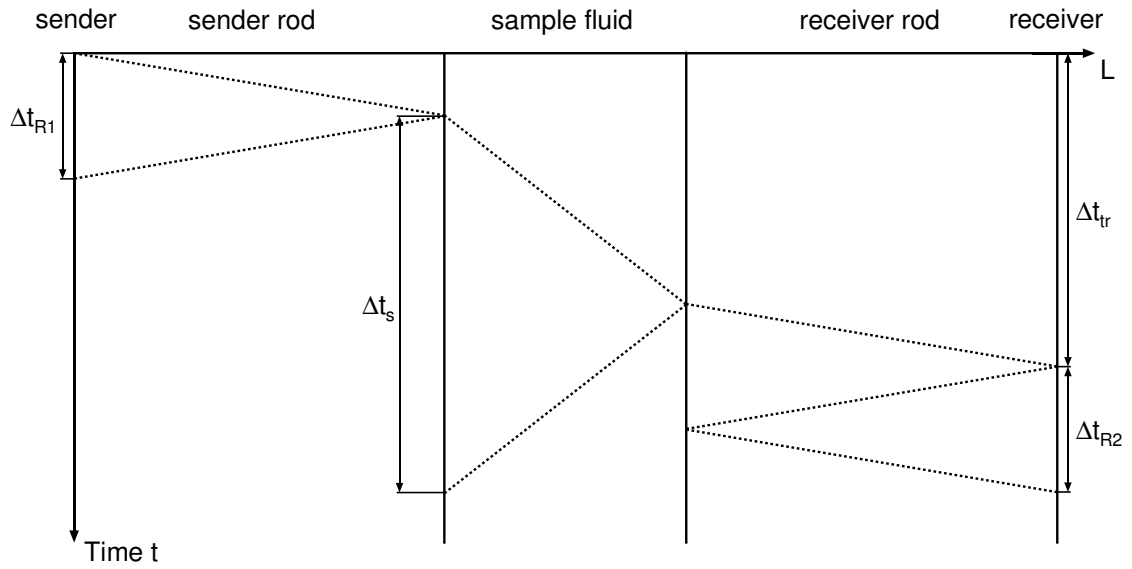

Figure 1.5. Measurement principle of the speed of sound sensor of Ye et al.[192, 193].

The accuracy of speed of sound measurements in liquids is usually not as high as for measurements in gases, ranging from 0.05 % to 0.5 %. Some notable exceptions are studies to determine the speed of sound in water at ambient pressure by Fujii and Masui [62], del Grosso and Mader [69], and Kroebel and Mahrt [99], where uncertainties between 0.001 % and 0.003 % were achieved, and in water under high pressures, for example by Aleksandrov and Larkin [5], Benedetto et al. [20], or Fujii [61] with uncertainties between 0.005 % and 0.02 %. In studies on the speed of sound in *n*-heptane and toluene [135], argon [93], helium [94], nitrogen [95], and methane [96] under high pressures up to 1000 MPa by a group at the van der Waals Laboratory in Amsterdam, uncertainties of 0.02 % were claimed.

In summary, the preceding discussion shows that there is a permanent need for accurate speed of sound measurements, especially in the liquid region. Therefore, the aim of this work was to summarize the knowledge on the pulse-echo method for measurements of the speed of sound in fluids and to develop an instrument for high-precision measurements over a wide range of temperature and under high pressures up to 100 MPa. During the course of this work, the instrument was designed and optimized, and comprehensive measurements of the speed of sound in compressed nitrogen and in the liquid and supercritical regions of propane, propene, and the refrigerants 227ea and 365mfc were carried out.

This work is organized as follows. The next chapter describes fundamentals for the design of pulse-echo speed of sound sensors. In Chapter 3, the speed of sound apparatus developed in this work is presented, and the instrumentation employed for temperature and pressure measurement and for signal generation and detection is described. Chapter 4 treats the analysis of the speed of sound measurements and the estimation of the measurement uncertainties. In order to validate the apparatus, the speed of sound in liquid water under pressure was measured. The results of these measurements are also discussed in Chapter 4. In Chapter 5, the measurements in nitrogen, propane, propene, and the refrigerants 227ea and 365mfc are discussed and compared with literature data and equation of state models. Conclusions and an outlook are presented in Chapter 6.

2 Fundamentals

In a pulse-echo experiment to measure the speed of sound in a fluid, the time of flight of a short sinusoidal burst signal over a well-known distance in the sample is measured. The way of the signal through an acoustic sensor, which realizes this measurement principle, usually consists of the following steps: A piezoelectric transducer, which acts as sender, is electrically excited by a sinusoidal burst signal and generates a sound signal in the surrounding fluid. The sound signal propagates nearly as a plane wave in the fluid, is reflected at a solid reflector, and travels back to the transducer, which now acts as a receiver. The arriving sound signal excites the piezoelectric transducer mechanically so that it generates an electric signal, which can be measured by an oscilloscope.

The aim of this chapter is to provide the fundamental theory for these basic elements of a pulse-echo sensor. First, the differential equations, which describe acoustic wave motion, are derived for pure fluids. In Sec. 2.1, the basic quantities used to describe acoustic fields are introduced. In Sec. 2.2, the acoustic field equations are first derived for idealized fluids by neglecting dissipation mechanisms from the Euler equations (Sec. 2.2.1) and, subsequently, for the more complicated case of Newtonian fluids from the Navier-Stokes equations and the energy equation by including viscous dissipation and heat conduction (Sec. 2.2.2). In order to illustrate the properties of solutions of the acoustic field equations, the propagation of plane mono-frequency harmonic waves in unbounded fluids is discussed in Sec. 2.3. The reflection of sound waves at solid surfaces is treated in Sec. 2.4, again first for ideal fluids (Sec. 2.4.1) and, subsequently, for real fluids with viscous dissipation and heat conduction (Sec. 2.4.2). In Sec. 2.5, molecular relaxation phenomena, which can result in a frequency dependence of the speed of sound and can cause additional damping of sound waves, are discussed. The last section of this chapter describes the application of piezoelectric crystals as sound transducers. First, general properties of piezoelectric materials are described in Sec. 2.6.1. In Sec. 2.6.2, the differential equation for thickness vibrations of a thin piezoelectric plate is derived. Secs. 2.6.3 and 2.6.4 treat the operation of piezoelectric transducers as sound receivers and senders. Finally, an equivalent electric circuit model for piezoelectric transducers is described in Sec. 2.6.5.

More detailed treatments of the propagation of sound waves in fluid media than

the one given in the following sections can be found in the books of Kinsler et al. [92], Morse and Ingard [134], or Trusler [177]. Reviews of experimental studies on the speed of sound in gases were published by Zuckerwar [199, 200, 201] and in organic liquids by Oakley et al. [140, 141]. A review of the role of the speed of sound in thermophysical properties research was given by van Dael [33] and Trusler [177]. Relaxation phenomena are discussed in detail in the books of Cortrell and McCoubrey [31], Herzfeld and Litowitz [76], and Lambert [106]. A fundamental account of the theory of piezoelectric transducers within the frame of continuum mechanics was given by Tiersten [175]. Useful material on piezoelectric transducers can also be found in the ANSI/IEEE standard on piezoelectricity [8] and in the books of Cady [27, 28], Ikeda [87], Mason [117], Ruschmeyer [154] and Trusler [177].

2.1 Acoustic Field Quantities

When a sound wave propagates in a fluid, it produces local changes of the pressure p, the density ρ, and the temperature T. Acoustic wave motions are described in terms of these three variables, and the velocity of the fluid $\boldsymbol{v}$ is used to describe the fluid motion. Since pressure changes can most easily be measured by some detector, the pressure is used as the primary variable to describe the acoustic wave motion, and the other variables are calculated from it by the relations which will be derived in the following sections.

The local pressure, density, and temperature are written as sums of an equilibrium contribution and an acoustic contribution:

$$p(\boldsymbol{r},t) = p_{\mathrm{eq}} + p_{\mathrm{a}}(\boldsymbol{r},t) \tag{2.1}$$

$$\rho(\boldsymbol{r},t) = \rho_{\mathrm{eq}} + \rho_{\mathrm{a}}(\boldsymbol{r},t) \tag{2.2}$$

$$T(\boldsymbol{r},t) = T_{\mathrm{eq}} + T_{\mathrm{a}}(\boldsymbol{r},t). \tag{2.3}$$

The acoustic contributions, indicated by the subscript ‘a’, describe the changes due to the presence of a sound wave. They are functions of the position vector $\boldsymbol{r}$ and time t, that is, they are local quantities. In the absence of sound, the fluid is assumed to be at rest so that the fluid velocity $\boldsymbol{v}(\boldsymbol{r},t) = \boldsymbol{v}_{\mathrm{a}}(\boldsymbol{r},t)$ consists of an acoustic contribution only[1)]. This set of acoustic variables is a convenient choice because

[1)] In the acoustic literature, $\boldsymbol{v}_{\mathrm{a}}$ is sometimes termed particle velocity. The particle velocity must be distinguished from the speed of sound, which is the speed at which acoustic waves propagate in a fluid.

they appear in the conventional form of the hydrodynamic balance equations as independent variables.

Often, the velocity potential Ψ is used to describe acoustic wave motion. It is related to the fluid velocity by

$$\boldsymbol{v}(\boldsymbol{r},t) = -\nabla\Psi(\boldsymbol{r},t). \tag{2.4}$$

The advantage of describing acoustic fields by the velocity potential lies in the fact that, in ideal fluids, both fluid velocity and pressure can unambiguously be related to the velocity potential. This reduces the number of independent variables from four – pressure and three velocity components – to one, the velocity potential. Moreover, if, in real fluids, the fluid velocity is resolved into longitudinal and transverse components, the longitudinal velocity vector field can be represented by the scalar velocity potential field.

Furthermore, it will be assumed that local equilibrium is attained instantaneously at every material point in the fluid so that the standard thermodynamic relations between state variables can be applied locally. In ordinary liquids and compressed gases, this assumption is known to be satisfied up to very high frequencies in the GHz regime [177, pp. 90]. If local equilibrium is not reached instantaneously, the speed of sound depends on the frequency of the wave, and it is no longer a thermodynamic state variable. This effect is called dispersion, and the fluid is then said to be dispersive. In the following sections, the acoustic field equations are first derived for a non-dispersive fluid. Dispersion effects will be included in the model in Sec. 2.5.

Sometimes, for example in the formulation of boundary conditions, analogies between acoustical or mechanical quantities and electrical circuit theory are useful. If the acoustic pressure is the analog of the voltage and the fluid velocity is the analog of the current, the acoustic impedance of a medium Z_a is defined as

$$Z_\mathrm{a} = p_\mathrm{a}/v. \tag{2.5}$$

In general, the acoustic impedance is a complex quantity and can be decomposed into its real part, the acoustic resistance R_a, and its imaginary part, the acoustic reactance X_a. The inverse of the acoustic impedance is the acoustic admittance Y_a. Its real part is the acoustic conductance G_a, and its imaginary part is the acoustic susceptance B_a.

A similar analogy can be formulated for mechanical quantities. In the mechanical analogy, the force is interpreted as the analog of the voltage and the velocity as the

analog of the current. The mechanical impedance is then defined as

$$Z_{\mathrm{m}} = F/v, \tag{2.6}$$

and the mechanical admittance Y_{m} is the inverse of the impedance. Furthermore, the real and imaginary parts of the mechanical impedance and admittance are interpreted in the same way as in the acoustic analogy. Acoustical and mechanical impedances are related by $Z_{\mathrm{m}} = AZ_{\mathrm{a}}$, where A is the area upon which the force F acts.

2.2 Acoustic Field Equations

In acoustic experiments for measurements of thermophysical properties, the local disturbances in the fluid due to propagating sound waves are usually kept so small in magnitude that nonlinear effects are negligible, and a treatment within linear acoustics yields an excellent description of the wave motion. Therefore, the presentation in the following sections aims at deriving the linearized acoustic field equations. The derivation starts from the hydrodynamic balance equations for mass, momentum, and energy, which are assumed to be known. Their derivation and thorough discussions of them can be found in many books on fluid or continuum mechanics, see for example [149, 165]. A treatment of nonlinear acoustic wave motion was for example given by Morse and Ingard [134, pp. 863].

2.2.1 Ideal Fluids

In the first step, the fluid is treated as an ideal fluid without viscous dissipation and heat conduction. For an ideal fluid, the mass balance equation reads

$$\frac{D\rho}{Dt} + \rho(\nabla \cdot \boldsymbol{v}) = 0, \tag{2.7}$$

where

$$\frac{D}{Dt} = \frac{\partial}{\partial t} + \boldsymbol{v} \cdot \nabla \tag{2.8}$$

represents the material time derivative. The momentum balance is represented by the Euler equation

$$\rho \frac{D\boldsymbol{v}}{Dt} + \nabla \cdot (p\boldsymbol{I}) = 0, \tag{2.9}$$

in which the symbol $\boldsymbol{I}$ denotes the identity tensor. The mass and momentum balances constitute a set of four partial differential equations – the Euler equation represents in fact three equations for the three components of the velocity vector – for the five unknown functions $p(\boldsymbol{r},t)$, $\rho(\boldsymbol{r},t)$, and $\boldsymbol{v}(\boldsymbol{r},t)$. Thus, one additional equation is required to complete the system of equations.

In an ideal fluid, all motion is adiabatic and reversible, in other words isentropic. If the entropy equation of state of the fluid is written in the form $p = p(\rho, s)$, the acoustic pressure can be related to the acoustic density by

$$p_\mathrm{a} = p - p_\mathrm{eq} \approx \left(\frac{\partial p_\mathrm{eq}}{\partial \rho_\mathrm{eq}}\right)_s (\rho - \rho_\mathrm{eq}) = \left(\frac{\partial p_\mathrm{eq}}{\partial \rho_\mathrm{eq}}\right)_s \rho_\mathrm{a}. \tag{2.10}$$

This relation is the fifth equation of the system of equations, which provides the starting point for the derivation of the acoustic field equations.

In order to linearize the mass and momentum balances, the separation of the pressure and density into equilibrium and acoustic contributions, Eqs. (2.1) and (2.2), is substituted into Eqs. (2.7) and (2.9). Since the fluid is assumed to be at rest, all gradients of equilibrium quantities vanish identically. Within the linear approximation, the material time derivative is approximated by the simple time derivative [134, p. 239], and terms of second and higher order of the acoustic contributions are neglected. The linearized mass and momentum balances read

$$\frac{\partial \rho_\mathrm{a}}{\partial t} + \rho_\mathrm{eq}(\nabla \cdot \boldsymbol{v}) = 0 \tag{2.11}$$

$$\rho_\mathrm{eq} \frac{\partial \boldsymbol{v}}{\partial t} + \nabla \cdot (p_\mathrm{a} \boldsymbol{I}) = 0. \tag{2.12}$$

In the linearized mass balance, the thermodynamic relation (2.10) is applied to replace the density derivative with respect to time by a pressure derivative

$$\left(\frac{\partial \rho_\mathrm{eq}}{\partial p_\mathrm{eq}}\right)_s \frac{\partial p_\mathrm{a}}{\partial t} + \rho_\mathrm{eq}(\nabla \cdot \boldsymbol{v}) = 0, \tag{2.13}$$

and the momentum balance is multiplied by the nabla operator, which yields

$$\rho_\mathrm{eq} \frac{\partial}{\partial t}(\nabla \cdot \boldsymbol{v}) + \nabla^2 p_\mathrm{a} = 0. \tag{2.14}$$

Eq. (2.13) is then solved for $\nabla \cdot \boldsymbol{v}$, and the result is substituted into Eq. (2.14). In order to simplify the notation, ρ_eq and p_eq are replaced by p and ρ without ambiguity so that from now on p and ρ denote the equilibrium pressure and density. One obtains

$$\left[\nabla^2 - \left(\frac{\partial \rho}{\partial p}\right)_s \frac{\partial^2}{\partial t^2}\right] p_\mathrm{a} = 0. \tag{2.15}$$

This equation is a partial differential equation of the hyperbolic type, whose solutions represent propagating pressure waves in the fluid [198]. The coefficient of the second term is the square of the speed at which these pressure waves propagate in the fluid. This speed is called the thermodynamic speed of sound and is denoted by the symbol w_0. It is related to the equation of state of the fluid by

$$w_0^2 = \left(\frac{\partial p}{\partial \rho}\right)_s . \tag{2.16}$$

The thermodynamic speed of sound is a thermodynamic state variable because it solely depends on the thermodynamic state of the fluid, but not on the amplitude and frequency of the pressure waves.

An expression for the acoustic pressure in terms of the velocity potential can be derived by inserting the definition of the velocity potential, Eq. (2.4), into Eq. (2.12). One finds

$$p_\mathrm{a}(\boldsymbol{r}, t) = \rho \frac{\partial \Psi(\boldsymbol{r}, t)}{\partial t}. \tag{2.17}$$

This relation will be used in Sec. 4.2, where diffraction in the acoustic field in front of a sound transducer will be examined.

2.2.2 Newtonian Fluids with Viscous Dissipation and Heat Conduction

In real Newtonian fluids, viscous friction and heat conduction cause the dissipation of energy. A complete description of acoustic wave motion must take these effects into account because they result in damping of sound waves. For example, the amplitude of a plane wave decreases as the wave propagates through a fluid.

The mass balance, Eq. (2.7), remains unchanged, but in the momentum balance, Eq. (2.9), the scalar pressure must be replaced by the pressure tensor, which is denoted by the symbol $\boldsymbol{P}$. The momentum balance then reads

$$\rho \frac{D\boldsymbol{v}}{Dt} + \nabla \cdot \boldsymbol{P} = 0. \tag{2.18}$$

The pressure tensor is written as a sum of two contributions

$$\boldsymbol{P} = p\boldsymbol{I} + \boldsymbol{\Pi}. \tag{2.19}$$

The first contribution is the spherical equilibrium pressure tensor. It contains the thermodynamic equilibrium pressure p in the diagonal elements, and its off-diagonal

elements are zero. The second contribution represents the symmetric viscous pressure tensor $\mathbf{\Pi}$, whose elements are in general non-zero. The momentum balance is completed by a constitutive equation, which relates the viscous pressure tensor to the velocity field. For Newtonian fluids, the viscous pressure tensor is related to the elements of the velocity gradient tensor $\nabla \otimes \boldsymbol{v}$ by the constitutive equation

$$\mathbf{\Pi} = -\left(\eta_\mathrm{b} + \frac{4}{3}\,\eta\right)(\nabla \cdot \boldsymbol{v})\boldsymbol{I} + 2\eta\left[(\nabla \cdot \boldsymbol{v})\boldsymbol{I} - \frac{1}{2}\left\{\nabla \otimes \boldsymbol{v} + (\nabla \otimes \boldsymbol{v})^t\right\}\right], \quad (2.20)$$

where the symbol '$\otimes$' denotes a dyadic product of two vectors, which, in index notation, means $(\boldsymbol{a} \otimes \boldsymbol{b})_{ij} = a_i\, b_j$. The first term describes viscous effects associated with changes of the volume of an infinitesimal volume element of the fluid at constant shape, and the second term describes viscous effects associated with changes of shape of an infinitesimal volume element of the fluid at constant volume. The coefficients η and η_b are the viscosity and bulk viscosity. Both transport coefficients are properties of the fluid and generally depend on the thermodynamic state of the fluid.

With the tensor identity

$$\nabla \cdot \left[2(\nabla \cdot \boldsymbol{v})\boldsymbol{I} - \left\{\nabla \otimes \boldsymbol{v} + (\nabla \otimes \boldsymbol{v})^t\right\}\right] = \nabla \times (\nabla \times \boldsymbol{v}), \quad (2.21)$$

the relation

$$\nabla \cdot \mathbf{\Pi} = -\left(\eta_\mathrm{b} + \frac{4}{3}\,\eta\right)\nabla \cdot (\nabla \cdot \boldsymbol{v})\boldsymbol{I} + \eta\,(\nabla \times (\nabla \times \boldsymbol{v})) \quad (2.22)$$

for the viscous pressure tensor can be established. Combining Eq. (2.22) with Eq. (2.19) and substituting the result into the momentum balance, Eq. (2.18), yields the Navier-Stokes equation

$$\rho\,\frac{D\boldsymbol{v}}{Dt} = -\nabla p + \left(\eta_\mathrm{b} + \frac{4}{3}\,\eta\right)\nabla(\nabla \cdot \boldsymbol{v}) - \eta\,(\nabla \times (\nabla \times \boldsymbol{v})). \quad (2.23)$$

Along the same line of arguments as in the preceding section, the Navier-Stokes equation is linearized, and one obtains

$$\frac{\partial \boldsymbol{v}}{\partial t} = -\frac{1}{\rho}\,\nabla\left[p_\mathrm{a} - \left(\eta_\mathrm{b} + \frac{4}{3}\,\eta\right)(\nabla \cdot \boldsymbol{v})\right] - \frac{\eta}{\rho}\,(\nabla \times (\nabla \times \boldsymbol{v})). \quad (2.24)$$

In the next step, the fluid motion is resolved into transverse and longitudinal components. This is achieved by writing the fluid velocity as a sum of a longitudinal component $\boldsymbol{v}_\mathrm{l}$ and a transverse component $\boldsymbol{v}_\mathrm{t}$,

$$\boldsymbol{v} = \boldsymbol{v}_\mathrm{l} + \boldsymbol{v}_\mathrm{t}, \quad (2.25)$$

with $\nabla \times \boldsymbol{v}_\mathrm{l} = 0$ and $\nabla \cdot \boldsymbol{v}_\mathrm{t} = 0$. This separation of the fluid velocity is advantageous for two reasons. First, since the gradient of a scalar quantity is rotation free, the gradient of the acoustic pressure contributes only to the longitudinal fluid motion. Second, the longitudinal velocity component, which is a vectorial quantity, can be represented in terms of the scalar velocity potential.

With this separation of the fluid velocity, the Navier-Stokes equation is resolved into two uncoupled equations:

$$\frac{\partial \boldsymbol{v}_\mathrm{l}}{\partial t} = -\frac{1}{\rho}\nabla p_\mathrm{a} + D_\mathrm{v}\nabla(\nabla \cdot \boldsymbol{v}_\mathrm{l}) \tag{2.26}$$

$$\frac{\partial \boldsymbol{v}_\mathrm{t}}{\partial t} = -D_\mathrm{s}\nabla \times (\nabla \times \boldsymbol{v}_\mathrm{t}) \tag{2.27}$$

The symbol $D_\mathrm{s} = \eta/\rho$ is the kinematic viscosity or viscous diffusivity, and, similarly, $D_\mathrm{v} = 4D_\mathrm{s}/3 + \eta_\mathrm{b}/\rho$ is introduced as an abbreviation. The transverse momentum balance may be rewritten by using the identity $\nabla \times (\nabla \times \boldsymbol{v}_\mathrm{t}) = -\nabla^2 \boldsymbol{v}_\mathrm{t}$, which yields

$$\frac{\partial \boldsymbol{v}_\mathrm{t}}{\partial t} = D_\mathrm{s}\nabla^2 \boldsymbol{v}_\mathrm{t}. \tag{2.28}$$

Eq. (2.28) is a partial differential of the parabolic type [198], which describes rapidly attenuated shear waves. In the following, the longitudinal momentum balance, Eq. (2.26), is further elaborated on in the first place, while the discussion of the transverse momentum balance is postponed to the following section.

First, the longitudinal fluid velocity is eliminated from the longitudinal momentum balance, Eq. (2.26). With the separation of the fluid velocity into longitudinal and transverse components, the mass balance, Eq. (2.7), becomes

$$\frac{\partial \rho_\mathrm{a}}{\partial t} + \rho(\nabla \cdot \boldsymbol{v}_\mathrm{l}) = 0. \tag{2.29}$$

Since Eq. (2.29) contains the divergence of the longitudinal fluid velocity $\nabla \cdot \boldsymbol{v}_\mathrm{l}$, the longitudinal momentum balance, Eq. (2.26), is multiplied by the nabla operator, which yields

$$\frac{\partial}{\partial t}(\nabla \cdot \boldsymbol{v}_\mathrm{l}) = -\frac{1}{\rho}\nabla^2 p_\mathrm{a} + D_\mathrm{v}\nabla \cdot (\nabla(\nabla \cdot \boldsymbol{v}_\mathrm{l})). \tag{2.30}$$

The divergence of the longitudinal velocity is then replaced by using Eq. (2.29):

$$\frac{\partial^2 \rho_\mathrm{a}}{\partial t^2} = \nabla^2 p_\mathrm{a} + D_\mathrm{v}\nabla^2\left(\frac{\partial \rho_\mathrm{a}}{\partial t}\right). \tag{2.31}$$

In the last step, the acoustic density ρ_a is eliminated in favor of the acoustic pressure and temperature. For this purpose, the acoustic density is related to the acoustic

pressure and acoustic temperature by the derivatives of the thermal equation of state $p = p(\rho, T)$

$$\rho_\mathrm{a} \approx \left(\frac{\partial \rho}{\partial p}\right)_T p_\mathrm{a} + \left(\frac{\partial \rho}{\partial T}\right)_p T_\mathrm{a}. \tag{2.32}$$

With the thermodynamic relations

$$\left(\frac{\partial \rho}{\partial p}\right)_T = \frac{c_p}{c_v}\left(\frac{\partial \rho}{\partial p}\right)_s = \frac{\kappa}{w_0^2} \tag{2.33}$$

and

$$\left(\frac{\partial \rho}{\partial T}\right)_p = -\left(\frac{\partial p}{\partial T}\right)_\rho \left[\left(\frac{\partial p}{\partial \rho}\right)_T\right]^{-1} = -\frac{\beta\kappa}{w_0^2}, \tag{2.34}$$

where $\kappa = c_p/c_v$ is the ratio of the isobaric and isochoric heat capacities and $\beta = (\partial p/\partial T)_\rho$ is the thermal pressure coefficient, Eq. (2.32) becomes

$$\rho_\mathrm{a} = \frac{\kappa}{w_0^2}\,(p_\mathrm{a} - \beta T_\mathrm{a}). \tag{2.35}$$

This result is inserted into Eq. (2.31), and one finally obtains

$$\nabla^2 p_\mathrm{a} = \frac{\kappa}{w_0^2}\left[\frac{\partial^2}{\partial t^2} - D_\mathrm{v}\frac{\partial}{\partial t}\nabla^2\right](p_\mathrm{a} - \beta T_\mathrm{a}). \tag{2.36}$$

This equation corresponds to the simple wave equation for ideal fluids derived in the last section. It is a hyperbolic partial differential equation, which describes propagating pressure waves, and is termed modified wave equation. Compared with the wave equation for ideal fluids, it additionally contains a damping term with a mixed derivative, and the pressure wave is accompanied by a temperature wave. In order to form a complete set of equations for the two unknown functions $p_\mathrm{a}(\boldsymbol{r}, t)$ and $T_\mathrm{a}(\boldsymbol{r}, t)$, an additional equation is required.

The periodic pressure changes in a propagating sound wave in a real fluid are accompanied by temperature changes because the fluid is locally compressed and expanded. Consequently, heat flows from warmer to colder regions in the fluid, and the propagation of the sound wave is no longer isentropic.

In order to account for heat conduction, the energy balance

$$\frac{D(u\rho)}{Dt} = -u\rho(\nabla \cdot \boldsymbol{v}) - \nabla \cdot \boldsymbol{q} - \nabla \cdot (\boldsymbol{P} \cdot \boldsymbol{v}) \tag{2.37}$$

is considered. In this equation, u denotes the internal energy, and $\boldsymbol{q}$ is the heat flux vector per unit area. With Fourier's constitutive relation, the heat flux is related to the temperature gradient by

$$\boldsymbol{q} = -\lambda_\mathrm{c} \nabla T, \tag{2.38}$$

where the coefficient λ_c is the thermal conductivity[2)]. As the viscosity and bulk viscosity, the thermal conductivity is a property of the fluid and depends on the thermodynamic state of the fluid. Inserting the heat flux, the separation of the fluid velocity into longitudinal and transverse components, and the separation of the pressure tensor into the equilibrium contribution and viscous pressure tensor into the energy balance and applying the product rule to evaluate the derivatives of the products, yields

$$\rho \frac{Du}{Dt} + u \frac{D\rho}{Dt} = -u\rho(\nabla \cdot \boldsymbol{v}_\mathrm{l}) + \lambda_\mathrm{c} \nabla^2 T - \nabla \cdot (p \boldsymbol{v}_\mathrm{l}) - \nabla \cdot (\boldsymbol{\Pi} \cdot \boldsymbol{v}_\mathrm{l}). \tag{2.39}$$

The energy balance can be simplified, by replacing $(\nabla \cdot \boldsymbol{v}_\mathrm{l})$ in the first term on the right hand side by the mass balance, Eq. (2.7), which cancels the second term on the left hand side. The energy balance is then linearized in the same way as the momentum balance above. The material derivative of the energy is approximated by the simple time derivative, and the last term on the right hand side is neglected because it is of second order. The linearized energy balance reads

$$\frac{\partial u_\mathrm{a}}{\partial t} = -\frac{p}{\rho} (\nabla \cdot \boldsymbol{v}_\mathrm{l}) + \frac{\lambda_\mathrm{c}}{\rho} \nabla^2 T_\mathrm{a}. \tag{2.40}$$

As before, the index 'eq' for equilibrium properties has been omitted. Small changes of the internal energy are related to small entropy changes by using the Gibbs relation

$$du = T ds - p\, dv = T ds + \frac{p}{\rho^2} d\rho \tag{2.41}$$

as

$$u_\mathrm{a} \approx T s_\mathrm{a} + \frac{p}{\rho^2} \rho_\mathrm{a}. \tag{2.42}$$

When Eq. (2.42) is substituted into Eq. (2.40), one finds

$$T \frac{\partial s_\mathrm{a}}{\partial t} + \frac{p}{\rho^2} \frac{\partial \rho_\mathrm{a}}{\partial t} = -\frac{p}{\rho} (\nabla \cdot \boldsymbol{v}_\mathrm{l}) + \frac{\lambda_\mathrm{c}}{\rho} \nabla^2 T_\mathrm{a}. \tag{2.43}$$

[2)] The index 'c' is used to distinguish the thermal conductivity from the wave length λ.

If the mass balance is used again to eliminate $(\nabla \cdot \boldsymbol{v}_\mathrm{l})$, the second term on the left hand side and first term on the right hand side cancel, and the intermediate result

$$\frac{\partial s_\mathrm{a}}{\partial t} = \frac{\lambda_\mathrm{c}}{\rho T} \nabla^2 T_\mathrm{a} \tag{2.44}$$

is obtained.

Since the pressure, the density and the temperature were selected to describe the acoustic wave motion, the entropy must be eliminated in favor of these variables. The acoustic entropy can be related to the acoustic pressure and temperature by

$$s_\mathrm{a} \approx \left(\frac{\partial s}{\partial T}\right)_p T_\mathrm{a} + \left(\frac{\partial s}{\partial p}\right)_T p_\mathrm{a}. \tag{2.45}$$

The partial derivatives in Eq. (2.45) are replaced by

$$\left(\frac{\partial s}{\partial T}\right)_p = \frac{c_p}{T} \tag{2.46}$$

and

$$\left(\frac{\partial s}{\partial p}\right)_T = \frac{1}{\rho^2} \left(\frac{\partial \rho}{\partial T}\right)_p. \tag{2.47}$$

When Eq. (2.45) together with Eqs. (2.46) and (2.47) is inserted into Eq. (2.44), one obtains

$$\frac{\partial T_\mathrm{a}}{\partial t} + \frac{T}{\rho^2 c_p} \left(\frac{\partial \rho}{\partial T}\right)_p \frac{\partial p_\mathrm{a}}{\partial t} = \frac{\lambda_\mathrm{c}}{\rho c_p} \nabla^2 T_\mathrm{a}. \tag{2.48}$$

By standard thermodynamic transformations (see Appendix A), it can be shown that the coefficient of the second term on the left hand side is

$$\frac{T}{\rho^2 c_p} \left(\frac{\partial \rho}{\partial T}\right)_p = -\frac{\kappa - 1}{\kappa \beta}. \tag{2.49}$$

The coefficient on the right hand side of Eq. (2.48) is the thermal diffusivity $D_\mathrm{h} = \lambda_\mathrm{c}/\rho c_p$. With these abbreviations, the result

$$\frac{\partial}{\partial t}\left(T_\mathrm{a} - \frac{\kappa - 1}{\kappa \beta} p_\mathrm{a}\right) = D_\mathrm{h} \nabla^2 T_\mathrm{a}. \tag{2.50}$$

is obtained. This is a second order partial differential equation of the parabolic type for the two unknown functions p_a and T_a, which must be solved simultaneously with the modified wave equation, Eq. (2.36). Some solutions, which are important for designing pulse-echo experiments, will be discussed in the following sections.

When Eqs. (2.36) and (2.50) have been solved, the longitudinal fluid velocity can be obtained as follows. The term $\nabla \cdot \boldsymbol{v}_\mathrm{l}$ on the right hand side of the longitudinal momentum balance,

$$\frac{\partial \boldsymbol{v}_\mathrm{l}}{\partial t} = -\frac{1}{\rho}\nabla p_\mathrm{a} + D_\mathrm{v}\nabla(\nabla \cdot \boldsymbol{v}_\mathrm{l}),$$

is again replaced by the mass balance equation, and one obtains

$$\frac{\partial \boldsymbol{v}_\mathrm{l}}{\partial t} = -\frac{1}{\rho}\,\nabla p_\mathrm{a} - \frac{D_\mathrm{v}}{\rho}\,\nabla\frac{\partial \rho_\mathrm{a}}{\partial t}. \tag{2.51}$$

If, furthermore, the acoustic density is replaced by Eq. (2.35), the result

$$\frac{\partial \boldsymbol{v}_\mathrm{l}}{\partial t} = -\nabla\left[\frac{p_\mathrm{a}}{\rho} + \frac{D_\mathrm{v}\kappa}{\rho w_0^2}\frac{\partial}{\partial t}(p_\mathrm{a} - \beta T_\mathrm{a})\right] \tag{2.52}$$

is found, which yields the time derivative of the longitudinal velocity in terms of the functions p_a and T_a.

It is instructive to consider two limiting cases of acoustic wave motion. If the viscosity and bulk viscosity were zero, the damping term in the modified wave equation, Eq. (2.36), would vanish. If, moreover, the thermal conductivity were zero, the fluid motion would be isentropic. In this case, the simple wave equation for ideal fluids, Eq. (2.15), would be recovered. In Eq. (2.52), the second term on the right hand side would vanish, and it would become a linearized Euler equation for the longitudinal velocity component.

If, on the other hand, the thermal conductivity were infinite, the acoustic temperature would be zero. In this case, pressure waves would propagate isothermally, and the propagation speed would be given by $w^2 = (\partial p/\partial \rho)_T$.

For intermediate cases, the acoustic pressure and temperature are coupled. The fluid tends to propagate pressure waves, while heat tends to diffuse. This coupling originates from the terms containing D_v and D_h.

In summary, acoustic wave motion is described by five variables, the acoustic pressure, the acoustic temperature, and the three components of the longitudinal velocity component. Eqs. (2.36), (2.50), and (2.52) form a system of five partial differential equations for the five unknown functions, which, for a specific problem, must be supplemented by appropriate boundary conditions.

2.3 Plane Harmonic Waves in Free Space

In order to examine the properties of solutions of the acoustic field equations, the propagation of mono-frequency harmonic plane waves in infinitely extended free

space is treated in this section as an illustration. This case is also important for the design of pulse-echo experiments because, in a first approximation, the propagating sound signals in speed of sound sensors can be viewed as plane waves.

In plane wave motion, the acoustic variables have a harmonic dependence on time, that is they contain a factor $\exp(i\omega t)$, where $\omega = 2\pi/f$ is the angular frequency of the wave. The derivatives of the acoustic pressure satisfy the relations

$$\frac{\partial p_\mathrm{a}}{\partial t} = i\omega p_\mathrm{a} \tag{2.53}$$

and

$$\frac{\partial^2 p_\mathrm{a}}{\partial t^2} = -\omega^2 p_\mathrm{a}. \tag{2.54}$$

In a mono-frequency plane harmonic wave, all acoustic variables are proportional to the acoustic pressure. With this requirement and the properties of the acoustic pressure derivatives, expressed by Eqs. (2.53) and (2.54), the modified wave equation, Eq. (2.36), can be written as

$$(\nabla^2 + k^2) p_\mathrm{a} = 0. \tag{2.55}$$

This equation is a Helmholtz equation for the acoustic pressure. The quantity k is called the propagation constant, and $-k^2$ represents the eigenvalues of the Laplace operator ∇^2. The solution of this partial differential equation requires the solution of an eigenvalue problem.

In the first step of the solution, the eigenvalues are determined, while the corresponding eigenfunctions are constructed thereafter. The method to determine the eigenvalues to be described in the following is due to Trusler [177, Sec. 2.3.4]. In order to simplify the notation, the dimensionless propagation constant

$$\Gamma = \frac{k w_0}{\omega} \tag{2.56}$$

is introduced. This definition is chosen in order that Γ takes the value unity for an ideal fluid. In that case, $w_0 = \omega/k$, where $k = 2\pi/\lambda$ represents the wave number with the wave length λ.

When $-\Gamma^2 = (w_0^2/\omega^2)\nabla^2$ and $\partial/\partial t = i\omega$ are inserted into the modified wave equation, Eq. (2.36), and the modified energy balance, Eq. (2.50), the algebraic equations

$$\left(-\Gamma^2 + \kappa - \frac{D_\mathrm{v}}{w_0^2} i\omega\kappa\Gamma^2\right) p_\mathrm{a} + \beta\kappa \left(-1 + \frac{D_\mathrm{v}}{w_0^2} i\omega\Gamma^2\right) T_\mathrm{a} = 0 \tag{2.57}$$

and

$$\left(1 - i\omega\frac{D_\mathrm{h}}{w_0^2}\Gamma^2\right) T_\mathrm{a} - \frac{\kappa - 1}{\kappa\beta}\, p_\mathrm{a} = 0 \tag{2.58}$$

result. It is convenient to introduce the viscous relaxation time

$$\tau_\mathrm{v} = \frac{D_\mathrm{v}}{w_0^2} \tag{2.59}$$

and the thermal relaxation time

$$\tau_\mathrm{h} = \frac{D_\mathrm{h}}{w_0^2}, \tag{2.60}$$

with which Eqs. (2.57) and (2.58) become

$$\left(-\Gamma^2 + \kappa - i\omega\tau_\mathrm{v}\kappa\Gamma^2\right) p_\mathrm{a} + \beta\kappa\left(-1 + i\omega\tau_\mathrm{v}\Gamma^2\right) T_\mathrm{a} = 0 \tag{2.61}$$

and

$$\left(1 - i\omega\tau_\mathrm{h}\Gamma^2\right) T_\mathrm{a} - \frac{\kappa - 1}{\kappa\beta}\, p_\mathrm{a} = 0. \tag{2.62}$$

Combining Eqs. (2.61) and (2.62), yields a quadratic equation for Γ^2:

$$\Gamma^4(\omega^2\tau_\mathrm{v}\tau_\mathrm{h}\kappa - i\omega\tau_\mathrm{h}) + \Gamma^2(1 + i\omega\tau_\mathrm{h}\kappa + i\omega\tau_\mathrm{v}) - 1 = 0, \tag{2.63}$$

which has the two exact solutions

$$\Gamma^2 = -\frac{i}{2\omega\tau_\mathrm{h}}\left(\frac{1 + i\omega\tau_\mathrm{v} + i\omega\tau_\mathrm{h}\kappa \pm D}{1 + i\omega\tau_\mathrm{v}\kappa}\right), \tag{2.64}$$

where D is an abbreviation defined by

$$D^2 = (1 - i\omega\tau_\mathrm{h}\gamma + i\omega\tau_\mathrm{v})^2 + 4i\omega\tau_\mathrm{h}(\gamma - 1). \tag{2.65}$$

As the effects of viscous dissipation and heat conduction are usually very small, an approximation to the exact solution for D can be made. For this purpose, D^2 is expanded in a binomial series [1, p. 14]

$$(1 + z)^m = 1 + \binom{m}{1} z + \binom{m}{2} z^2 + \ldots \tag{2.66}$$

with $m = 1/2$ and $z = D^2 - 1$. If only terms of first order in $\omega\tau_\mathrm{v}$ and of second order in $\omega\tau_\mathrm{h}$ are retained, the approximation

$$D \approx 1 + 2(\kappa - 1)\omega\tau_\mathrm{h}\omega(\tau_\mathrm{v} - \tau_\mathrm{h}) + i[\omega(\tau_\mathrm{v} - \tau_\mathrm{h}) + (\kappa - 1)\omega\tau_\mathrm{h}] \tag{2.67}$$

is obtained. Within this approximation, the two solutions for Γ^2 with the minus and plus sign are given by

$$\Gamma_\mathrm{p}^2 = 1 - i(\omega\tau_\mathrm{v} + (\kappa - 1)\omega\tau_\mathrm{h}) \tag{2.68}$$

$$\Gamma_\mathrm{h}^2 = -\frac{i}{\omega\tau_\mathrm{h}}. \tag{2.69}$$

The solutions of the modified wave equation corresponding to Γ_p and Γ_h are called propagational sound mode and thermal sound mode, respectively.

From Eq. (2.68), the propagation constant is obtained as

$$k_\mathrm{p} = \frac{\omega}{w_0} - \frac{i}{2}\frac{\omega}{w_0}(\tau_\mathrm{v} + (\kappa - 1)\tau_\mathrm{h}), \tag{2.70}$$

where only first-order terms have been retained. Eq. (2.70) shows that including viscous dissipation and heat conduction in the model leaves the real part of the propagation constant unchanged. The speed of sound in a real fluid with viscous dissipation and heat conduction is frequency independent and identical with the thermodynamic speed of sound. The losses due to viscous dissipation and heat conduction result in a small imaginary part of the propagation constant. Substituting the result for the propagational mode constant into Eq. (2.58) and retaining only first-order terms in $\omega\tau_\mathrm{h}$, yields the acoustic temperature T_p of the propagational mode

$$T_\mathrm{p} = \frac{\kappa - 1}{\kappa\beta}(1 + i\omega\tau_\mathrm{h})p_\mathrm{p}, \tag{2.71}$$

where p_p is the acoustic pressure of the propagational mode. The longitudinal velocity component of the propagational sound mode $\boldsymbol{v}_\mathrm{l,p}$ is similarly found by substituting the result for acoustic temperature into Eq. (2.52). If furthermore the time derivatives are replaced by $\partial/\partial t = i\omega$, one obtains

$$\boldsymbol{v}_\mathrm{l,p} = \frac{i}{\omega\rho}(1 + i\omega\tau_\mathrm{v})\nabla p_\mathrm{p}. \tag{2.72}$$

Eqs. (2.71) and (2.72) show that the propagational mode contributes to the acoustic temperature and longitudinal velocity component. As $\omega\tau_\mathrm{h}$ and $\omega\tau_\mathrm{v}$ are usually small compared with unity, the temperature and longitudinal velocity are slightly out of phase with the pressure. In the propagational mode, the fluid motion is in the direction of the propagation of the wave. Therefore, sound waves are longitudinal waves.

In the thermal sound mode, the acoustic pressure p_a is small compared with the term βT_a. Thus, Eq. (2.58) is the primary one, which describes the thermal mode. The propagation constant of the thermal mode

$$k_\mathrm{h} = \frac{\omega}{w_0}\,\Gamma_\mathrm{h} = \frac{\omega}{w_0}\,\frac{1}{\sqrt{2\omega\tau_\mathrm{h}}}\,(1-i) = \sqrt{\frac{\omega}{2D_\mathrm{h}}}\,(1-i) \tag{2.73}$$

has equal real and imaginary parts. Substituting the result for Γ_h^2, Eq. (2.69), into Eq. (2.58), yields the contribution of the thermal mode to the acoustic pressure

$$p_\mathrm{h} = -i\omega(\tau_\mathrm{h} - \tau_\mathrm{v})\beta\kappa T_\mathrm{h}, \tag{2.74}$$

and the longitudinal velocity contribution of the thermal mode is similarly found as for the propagational mode as

$$\boldsymbol{v}_\mathrm{l,h} = \frac{\beta\kappa\tau_\mathrm{h}}{\rho}\,\nabla T_\mathrm{h} \tag{2.75}$$

from Eq. (2.52). Again, only first-order terms have been retained.

A third solution arises from the transverse momentum balance, Eq. (2.27). Substituting $-\Gamma^2 = (w_0^2/\omega^2)\nabla^2$ and $\partial/\partial t = i\omega$ into Eq. (2.27), yields

$$\Gamma_\mathrm{s}^2 = -\frac{i}{\omega\tau_\mathrm{s}}, \tag{2.76}$$

where the shear relaxation time $\tau_\mathrm{s} = D_\mathrm{s}/w_0^2$ has been introduced. The solution

$$k_\mathrm{s} = \frac{\omega}{w_0}\,\Gamma_\mathrm{s} = \frac{1}{\sqrt{2\omega\tau_\mathrm{s}}}\,(1-i) = \sqrt{\frac{\omega}{2D_\mathrm{s}}}\,(1-i) \tag{2.77}$$

is the shear propagation constant and describes the shear mode. As the propagation constant of the thermal mode, k_s has equal real and imaginary parts. The shear mode does not contribute to the acoustic pressure, acoustic temperature, and longitudinal velocity component. The thermal and shear modes play an important role in vicinity of solid walls, but can usually safely be neglected in the bulk of the fluid.

With the eigenvalues for the propagational, thermal and shear mode, solutions of the modified wave equation for plane harmonic mono-frequency plane waves propagating in free space can be constructed. The direction of propagation is chosen along the positive z axis. In this case, the solutions for all acoustic variables are functions of the variable $w_0 t - z$. Since all acoustic variables contain the factor $\exp(i\omega t)$, the solutions are obtained by the method of separation of variables by choosing a

product approach of the form $f(z)\exp(i\omega t)$ for the main variable in each mode. The function $f(z)$ is an eigenfunction of the Laplace operator with the eigenvalue $-k^2$. Two solutions are given by $f(z) = A\exp(\pm ikz)$, where A is a constant, which must be determined by appropriate boundary conditions. For the purposes of this section, it is not necessary to specify the value of A.

For the propagational mode, the acoustic pressure of the wave propagating in the positive z direction is given by

$$p_\mathrm{p} = A\exp[i(\omega t - k_\mathrm{p} z)] = A\exp(-\alpha z)\exp[i(\omega t - (\omega/w_0)z)], \tag{2.78}$$

where $\alpha = -\mathrm{Im}(k_\mathrm{p})$ is the classical sound absorption coefficient. With the solution for k_p, Eq. (2.70), the absorption coefficient becomes

$$\alpha = \frac{\omega^2}{2w_0}\left[\tau_\mathrm{v} + (\kappa - 1)\tau_\mathrm{h}\right]. \tag{2.79}$$

If, furthermore, the expressions for the relaxation times, Eqs. (2.59) and (2.60), are inserted, an expression for the absorption coefficient in terms of transport coefficients and thermodynamic state variables,

$$\alpha = \frac{\omega^2}{2w_0^3}\left[D_\mathrm{v} + (\kappa - 1)D_\mathrm{h}\right] = \frac{\omega^2}{2w_0^3}\left[\frac{4}{3}\frac{\eta}{\rho} + \frac{\eta_\mathrm{b}}{\rho} + (\kappa - 1)\frac{\lambda_\mathrm{c}}{\rho c_p}\right], \tag{2.80}$$

is obtained. According to Eq. (2.78), the wave is attenuated exponentially as it propagates in the fluid, and the absorption coefficient describes the energy losses of the wave due to viscous dissipation and heat conduction. Eq. (2.80) shows that the absorption coefficient has a quadratic dependence on frequency.

The real part of k_p is the wave number, for which $\mathrm{Re}(k_\mathrm{p}) = 2\pi/\lambda$ holds. Between the wave number, the angular frequency, and the speed, at which the wave propagates, the speed of sound, the relation

$$\mathrm{Re}(k_\mathrm{p}) = \frac{\omega}{w_0} \tag{2.81}$$

holds. In the present approximation, the speed of sound in the real fluid equals that in an ideal fluid without viscous dissipation and heat conduction. These two effects only influence the attenuation of the wave, but not the speed, at which the wave propagates. Therefore, in the remainder of this work, the speed of sound will generally be denoted by w. If it is necessary to distinguish between the thermodynamic speed of sound and the actual speed of sound, the thermodynamic speed of sound will be denoted by w_0 and the actual speed of sound by w.

The temperature and longitudinal velocity contribution for the propagational mode are obtained as

$$T_\mathrm{p} = A\,\frac{\kappa-1}{\kappa\beta}\,(1+i\omega\tau_\mathrm{h})\exp(-\alpha z)\exp[i(\omega t-(\omega/w)z)] \tag{2.82}$$

$$\boldsymbol{v}_\mathrm{l,p} = \frac{A}{\rho w}\left[1+\frac{i}{2}\,(\omega\tau_\mathrm{v}-(\kappa-1)\omega\tau_\mathrm{h})\right]\exp(-\alpha z)\exp[i(\omega t-(\omega/w)z)] \tag{2.83}$$

by substituting the result for the propagational pressure into Eqs. (2.71) and (2.72).

The solution for a plane thermal wave propagating in the positive z direction is found in the same way. In this case, the eigenvalue of the Laplace operator is $-k_\mathrm{h}^2$, and the solution for the acoustic temperature is given by

$$T_\mathrm{h} = B\exp(i\omega t - ik_\mathrm{h}z) = B\exp(i\omega t-(1+i)z/\delta_\mathrm{h}), \tag{2.84}$$

where the thermal penetration length

$$\delta_\mathrm{h} = \frac{1-i}{k_\mathrm{h}} = \sqrt{\frac{2D_\mathrm{h}}{\omega}} \tag{2.85}$$

has been introduced. The exponential dependence on the term $-z/\delta_\mathrm{h}$ shows that thermal waves are attenuated rapidly, which is typical of diffusive behavior. For example, in liquid water at (300 K, 0.1 MPa) at 10 MHz, $\delta_\mathrm{h} = 0.068$ μm. The acoustic pressure and longitudinal velocity component in the thermal mode are given by

$$p_\mathrm{h} = -Bi\omega(\tau_\mathrm{h}-\tau_\mathrm{v})\beta\kappa\exp(i\omega t-(1+i)z/\delta_\mathrm{h}) \tag{2.86}$$

$$\boldsymbol{v}_\mathrm{l,h} = -B\,\frac{\beta\kappa\tau_\mathrm{h}}{\rho}\,\frac{1+i}{\delta_\mathrm{h}}\exp(i\omega t-(1+i)z/\delta_\mathrm{h}). \tag{2.87}$$

For the shear mode, the solution for $\boldsymbol{v}_\mathrm{t}$ must be a vector eigenfunction of the Laplace operator with the scalar eigenvalue $-k_\mathrm{s}^2$, and it must satisfy $\nabla\cdot\boldsymbol{v}_\mathrm{t}=0$. A solution for a wave propagating in the positive z direction, which satisfies these conditions, is

$$\boldsymbol{v}_\mathrm{t} = (C_1\boldsymbol{e}_x+C_2\boldsymbol{e}_y)\exp(i\omega t-k_\mathrm{s}z) = (C_1\boldsymbol{e}_x+C_2\boldsymbol{e}_y)\exp(i\omega t-(1+i)z/\delta_\mathrm{s}), \tag{2.88}$$

where, in analogy to the thermal penetration length, δ_s denotes the shear penetration length and $\boldsymbol{e}_\mathrm{x}$ and $\boldsymbol{e}_\mathrm{y}$ are orthogonal unit base vectors pointing in positive x and y directions, respectively. The shear penetration length is given by

$$\delta_\mathrm{s} = \frac{1-i}{k_\mathrm{s}} = \sqrt{\frac{2D_\mathrm{s}}{\omega}}. \tag{2.89}$$

As thermal waves, shear waves are attenuated rapidly. For example, the shear penetration length amounts to $\delta_s = 0.17$ μm in liquid water at the same state point (300 K, 0.1 MPa) at 10 MHz. In shear waves, the fluid motion is transverse to the direction of the wave propagation.

2.4 Reflection of Sound Waves at Solid Surfaces

In the preceding section, the fundamental equations that describe the propagation of plane mono-frequency harmonic sound waves in an infinitely extended fluid medium were derived. Another case of acoustic wave motion, which is important for the design and understanding of pulse-echo experiments, is the reflection of waves at solid surfaces. A model for this situation will be developed in three steps. First, the reflection of waves in ideal fluids is considered in the following section. In Sec. 2.4.2, the boundary conditions, which must be satisfied by sound waves in real fluids at solid surfaces, is discussed, and an approximate solution of the acoustic field equations in the immediate vicinity of a solid surface is derived. Based on these results, the reflection in real fluids is described. The expressions for the reflection coefficients, Eqs. (2.97) and (2.116), form the principle results of this section.

2.4.1 Reflection in Ideal Fluids

Suppose that a plane mono-frequency harmonic sound wave of small-amplitude is incident on a plane surface, which can be viewed as an idealized model of a wall. The geometric situation is shown in Fig. 2.1. The surface is taken to be the xy plane, with the fluid occupying the half space with $z < 0$. The incident wave originates in the fluid, is perpendicular to the y axis, and inclined at an angle φ_i to the z axis.

In general, some part of the incident wave will be reflected, and some part will be transmitted into the solid medium. The description of the transmitted wave is complicated by the possible occurrence of elastic shear waves in the solid medium. Since the main interest lies in the reflected wave in the fluid medium, the transmitted wave is not considered in detail, but a simplified model of the reflecting solid surface is adopted. It is assumed that the various parts of the surface are not coupled in the sense that the motion of a small element of the surface is caused only by the acoustic pressure acting upon that element and is independent of the motion of all other elements of the surface. Such a surface is said to be one of local reaction. The properties of the surface are described by assigning to it an acous-

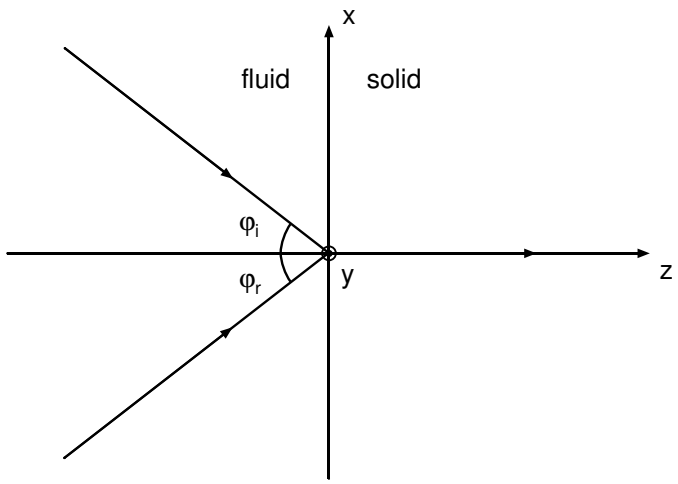

Figure 2.1. Geometry for the reflection from a plane solid surface.

tic impedance $Z_{\mathrm{a}}^{\mathrm{w}}$. This impedance is defined as the ratio of the acoustic pressure and normal fluid velocity as $Z_{\mathrm{a}}^{\mathrm{w}} = p_{\mathrm{a}}/v_z$, which provides a boundary condition at the surface. In general, the impedance may depend on frequency, on the angle of incidence, and on the spatial distribution of the wave incident on the surface. In the present model, the impedance of the surface is assumed to be constant at all points of the surface. The more complicated cases of reflection at a surface with frequency dependent impedance and at a surface of extended reaction are for example described by Morse and Ingard [134, pp. 263] or Kinsler et al. [92]. In this simplified model, the transmitted wave in the solid medium is a longitudinal wave propagating perpendicular from the surface into the solid as indicated in Fig. 2.1. Thus, the acoustic surface impedance may be approximated by $\rho_{\mathrm{w}} w_{\mathrm{w}}$, where ρ_{w} is the density of the wall material and w_{w} is the speed of longitudinal sound waves in the wall material. This assumption places no restrictions on the description of reflections of burst signals at plane solid surfaces in a pulse-echo speed of sound sensor because the signals are usually guided through the sensor so that they are normally incident on solid reflectors. Thus, the transmitted wave propagates perpendicularly to the surface in the solid medium. Since it is more convenient to work with the dimensionless specific acoustic admittance $y_{\mathrm{a}}^{\mathrm{w}} = \rho w / Z_{\mathrm{a}}^{\mathrm{w}}$ instead of the impedance, this quantity will be used to model the surface properties. The product ρw represents the acoustic impedance of the fluid.

In this section, the fluid medium is treated as an ideal fluid at the level of ap-

proximation of Sec. 2.2.1 by neglecting viscous dissipation and heat conduction. The acoustic pressure of the incident wave has the general form

$$p_{\mathrm{a}}^{\mathrm{i}} = A_{\mathrm{i}} \exp(ik[x \sin\varphi_{\mathrm{i}} - z\cos\varphi_{\mathrm{i}}]) \exp(i\omega t), \tag{2.90}$$

and the pressure of the reflected wave is given by

$$p_{\mathrm{a}}^{\mathrm{r}} = A_{\mathrm{r}} \exp(ik[x \sin\varphi_{\mathrm{r}} + z\cos\varphi_{\mathrm{r}}]) \exp(i\omega t), \tag{2.91}$$

where $k\sin\varphi_{\mathrm{i}}$ and $k\cos\varphi_{\mathrm{i}}$ are the components of the wave vector of the incident and reflected waves parallel and perpendicular to the surface. As the acoustic impedance of the surface is constant at all points of the surface, the ratio of the acoustic pressure and normal fluid velocity p_{a}/v_z is the same everywhere on the surface independent of the shape of the wave. The total acoustic pressure of the combined incident and reflected waves at the surface ($z = 0$) is given by

$$p_{\mathrm{a}} = \{A_{\mathrm{i}} \exp(ikx \sin\varphi_{\mathrm{i}}) + A_{\mathrm{r}} \exp(ikx \sin\varphi_{\mathrm{r}})\} \exp(i\omega t), \tag{2.92}$$

and, according to Eq. (2.12), the component of the fluid velocity normal to the surface at the surface is given by

$$\begin{aligned} v_{\mathrm{l},z} = \frac{1}{w\rho} \{&A_{\mathrm{i}} \cos\varphi_{\mathrm{i}} \exp(ikx \sin\varphi_{\mathrm{i}}) \\ &- A_{\mathrm{r}} \cos\varphi_{\mathrm{r}} \exp(ikx \sin\varphi_{\mathrm{r}})\} \exp(i\omega t). \end{aligned} \tag{2.93}$$

In order that the same value of the ratio p_{a}/v_z is realized everywhere on the surface, the acoustic pressures of the incident and reflected waves must have the same dependence on x at every point on the surface. Therefore, the angle of reflection φ_{r} must equal the angle of incidence φ_{i}, and p_{r} must equal p_{i} times a constant χ_{Re}. Thus, the combined pressure wave is described by

$$\begin{aligned} p_{\mathrm{a}} = A_{\mathrm{i}}\{&\exp(ik[x \sin\varphi - z\cos\varphi]) \\ &+ \chi_{\mathrm{Re}} \exp(ik[x \sin\varphi + z\cos\varphi])\} \exp(i\omega t), \end{aligned} \tag{2.94}$$

where $\varphi = \varphi_{\mathrm{i}} = \varphi_{\mathrm{r}}$ has been introduced. The constant χ_{Re} is called the reflection coefficient. An expression for the reflection coefficient in terms of the angle φ and the dimensionless acoustic impedance of the wall $y_{\mathrm{a}}^{\mathrm{w}}$ is found by substituting the acoustic pressure at the surface

$$p_{\mathrm{a}} = A_{\mathrm{i}}(1 + \chi_{\mathrm{Re}}) \exp(ikx \sin\varphi) \exp(i\omega t) \tag{2.95}$$

and fluid velocity normal to the surface at the surface

$$v_z = \frac{A_\mathrm{i}}{\rho w} \cos\varphi \, (1 - \chi_\mathrm{Re}) \, \exp(ikx \sin\varphi) \exp(i\omega t) \tag{2.96}$$

into the boundary condition $p_\mathrm{a}/v_z = Z_\mathrm{a}^\mathrm{w} = \rho w / y_\mathrm{a}^\mathrm{w}$, which must be satisfied at $z = 0$. After some algebra, the reflection coefficient is obtained as

$$\chi_\mathrm{Re} = \frac{\cos\varphi - y_\mathrm{a}^\mathrm{w}}{\cos\varphi + y_\mathrm{a}^\mathrm{w}}. \tag{2.97}$$

2.4.2 Reflection in Real Fluids

In this section, the model for the reflection of plane harmonic sound waves at a plane solid surface derived in the preceding section is extended by treating the fluid medium as a real fluid with viscous dissipation and heat conduction. This requires to include all three sound modes, and hence the acoustic temperature and transverse velocity component in the model. Moreover, additional boundary conditions for these variables must be specified. Since the thermal and shear mode are attenuated rapidly, they only contribute to the acoustic wave motion in a thin boundary layer in the immediate vicinity of the surface, whereas, in the bulk fluid, the wave motion is accurately described by the propagational mode only.

The geometric situation is the same as in the preceding section (see Fig. 2.1). In the present model, the thermal and viscous terms in the propagational wave are neglected. Thus, the wave number of the propagational wave is $k_\mathrm{p} = \omega/w$, and the acoustic pressure of the propagational sound mode is given by Eq. (2.94). The other acoustic variables of the propagational mode are then obtained as

$$\begin{aligned} T_\mathrm{p} = A_\mathrm{i} \frac{\kappa - 1}{\kappa\beta} \{ & \exp(ik_\mathrm{p} [x \sin\varphi - z \cos\varphi]) \\ & + \chi_\mathrm{Re} \exp(ik_\mathrm{p} [x \sin\varphi + z \cos\varphi]) \} \exp(i\omega t) \end{aligned} \tag{2.98}$$

$$\begin{aligned} v_{\mathrm{p},z} = A_\mathrm{i} \frac{\cos\varphi}{\rho w} \{ & \exp(ik_\mathrm{p} [x \sin\varphi - z \cos\varphi]) \\ & - \chi_\mathrm{Re} \exp(ik_\mathrm{p} [x \sin\varphi + z \cos\varphi]) \} \exp(i\omega t) \end{aligned} \tag{2.99}$$

$$\begin{aligned} v_{\mathrm{p},x} = -A_\mathrm{i} \frac{\sin\varphi}{\rho w} \{ & \exp(ik_\mathrm{p} [x \sin\varphi - z \cos\varphi]) \\ & + \chi_\mathrm{Re} \exp(ik_\mathrm{p} [x \sin\varphi + z \cos\varphi]) \} \exp(i\omega t) \end{aligned} \tag{2.100}$$

by using Eqs. (2.71) and (2.72).

Four boundary conditions must be satisfied at the surface:

$$(p_\mathrm{a}/v_z)|_{z=0} = \rho w/y_\mathrm{a}^\mathrm{w} \tag{2.101}$$

$$T_\mathrm{a}(x, z=0) = T_\mathrm{w}(x, z=0) \tag{2.102}$$

$$\boldsymbol{q}_\mathrm{a}(x, z=0) = \boldsymbol{q}_\mathrm{w}(x, z=0) \tag{2.103}$$

$$v_x(x, z=0) = 0. \tag{2.104}$$

The first boundary condition is essentially the same as for the reflection in ideal fluids. It states that the ratio of the acoustic pressure and fluid velocity normal to the surface must equal the acoustic impedance of the surface. Eqs. (2.102) and (2.103) ensure that the acoustic temperature and heat flow are continuous at the surface, and Eq. (2.104) implies that the tangential component of the fluid velocity vanishes at the surface. The propagational mode cannot, by itself, satisfy all four boundary conditions. In order to satisfy Eqs. (2.102) and (2.103), thermal waves must be generated in both the fluid and the wall. Similarly, the fourth condition demands that shear waves are generated in the fluid.

The acoustic temperature in the fluid is the sum of the contributions of the propagational and heat mode. In order to satisfy the boundary condition (2.102), the contribution of the thermal mode to the acoustic temperature must have the same dependence on x as does the propagational temperature contribution. Thus, the thermal wave must have the form

$$T_\mathrm{h} = B \exp(ik_\mathrm{p}\, x \sin\varphi + i[k_\mathrm{h}^2 - (k_\mathrm{p} \sin\varphi)^2]^{1/2} z) \exp(i\omega t), \tag{2.105}$$

where the propagation constant of the thermal wave is given by Eq. (2.73). Since k_p^2 is of order $(2\pi/\lambda)^2$, whereas k_h^2 is of order $1/\delta_\mathrm{h}^2$, the tangential component of the propagation constant $k_\mathrm{p} \sin\varphi$ is negligible in comparison with the thermal propagation constant. Hence, the thermal wave in the fluid can be approximated by

$$T_\mathrm{h} = B \exp(ik_\mathrm{p}\, x \sin\varphi + (1+i) z/\delta_\mathrm{h}) \exp(i\omega t). \tag{2.106}$$

This solution is valid, if $\lambda \gg \delta_\mathrm{h}$, which is usually satisfied in most gases and liquids at ordinary frequencies. For example, in liquid water at (300 K, 0.1 MPa) for a wave with a frequency of 10 MHz $\delta_\mathrm{h} = 0.068$ μm and $\lambda = 0.15$ mm so that the wave length is by about three orders of magnitude larger than the thermal penetration length. A thermal wave also penetrates the wall material. This wave is approximated by the function

$$T_\mathrm{w} = C \exp(ik_\mathrm{p}\, x \sin\varphi - (1+i) z/\delta_\mathrm{w}) \exp(i\omega t), \tag{2.107}$$

which has the same form as the thermal wave in the fluid, but the dependence on z is chosen so that the wave is attenuated with increasing z. The quantity δ_w is the thermal penetration length of the wall, which for example for the reflection of a wave with a frequency of 10 MHz at a stainless steel wall amounts to about 0.36 μm. As in the fluid medium, the tangential component of the propagation constant $k_\mathrm{p} \sin\varphi$ has been neglected in comparison with $1/\delta_\mathrm{w}$. The boundary condition (2.102) demands that the temperatures in the fluid and in the wall at $z = 0$ are equal, which yields a relation between the amplitudes of the two thermal waves:

$$B + A_\mathrm{i} \frac{\kappa - 1}{\kappa\beta} (1 + \chi_\mathrm{Re}) = C. \tag{2.108}$$

A second relation between B and C is provided by boundary condition (2.103), the continuity of heat flow through the surface. The analysis of this condition is much simplified by introducing two approximations. The heat flow arising from the propagational mode and, since $\lambda \gg \delta_\mathrm{h}$ and $\lambda \gg \delta_\mathrm{w}$ as above, the tangential component of the heat flow associated with the thermal mode are small compared with the normal heat flows of the two thermal modes in the fluid and in the wall. Thus, these contributions may be neglected. Applying Fourier's law, $\boldsymbol{q} = -\lambda_\mathrm{c} \nabla T$, and equating the normal heat flows associated with the two thermal modes, yields

$$C = -\frac{\delta_\mathrm{w}}{\delta_\mathrm{h}} \frac{\lambda_\mathrm{c}^\mathrm{f}}{\lambda_\mathrm{c}^\mathrm{w}}, \tag{2.109}$$

where $\lambda_\mathrm{c}^\mathrm{w}$ is the thermal conductivity of the wall material. Substituting this result into Eq. (2.108) and solving for B, yields the amplitude of the thermal wave in the fluid

$$B = -A_\mathrm{i}(1 + \chi_\mathrm{Re}) \frac{\kappa - 1}{\kappa\beta} \left(1 + \frac{\delta_\mathrm{w}}{\delta_\mathrm{h}} \frac{\lambda_\mathrm{c}^\mathrm{f}}{\lambda_\mathrm{c}^\mathrm{w}}\right)^{-1}. \tag{2.110}$$

For a typical fluid and a metal wall, the ratio $\delta_\mathrm{w}/\delta_\mathrm{h}$ is of order unity and the thermal conductivity of the wall material is much larger than that of the fluid. Consequently, according to Eq. (2.109), $C \ll B$. In this case, the two boundary conditions, Eqs. (2.102) and (2.103) reduce to a single condition, which demands that the total acoustic temperatures vanishes at the surface. Within this approximation, the temperature of the thermal mode is given by

$$T_\mathrm{h} = -A_\mathrm{i}(1 + \chi_\mathrm{Re}) \frac{\kappa - 1}{\kappa\beta} \exp(ik_\mathrm{p}\, x \sin\varphi + (1 + i)z/\delta_\mathrm{h}) \exp(i\omega t). \tag{2.111}$$

The contribution of the thermal mode to the normal component of the fluid velocity is found by substituting the result for the temperature of the thermal mode into Eq. (2.75) as

$$v_{\mathrm{h},z} = -\frac{A_\mathrm{i}(1+i)\tau_\mathrm{h}}{\rho\delta_\mathrm{h}}(\kappa-1)(1+\chi_\mathrm{Re})\exp(ik_\mathrm{p}\,x\sin\varphi+(1+i)z/\delta_\mathrm{h})\exp(i\omega t). \tag{2.112}$$

The contributions of the thermal mode to the tangential fluid velocity is negligible because, as already discussed above, the tangential propagation constant of the propagational mode is much smaller than that of the thermal mode. Similarly, the contribution of the thermal mode to the acoustic pressure, which is given by Eq. (2.74), may be neglected in gases and liquids outside the immediate vicinity of the critical point because the viscous and thermal relaxation times are usually much smaller than the periods of the sound waves at ordinary frequencies.

In order to cancel the tangential component of the fluid velocity at the surface, a shear wave must be introduced inside the boundary layer. According to Eq. (2.104), the tangential fluid velocity of the shear wave must equal $-v_{\mathrm{l},x}$ at the surface. Therefore, the x component of the velocity of the shear mode is given by

$$v_{\mathrm{s},x} = A_\mathrm{i}\,\frac{k_\mathrm{p}\sin\varphi}{\rho\omega}\,(1+\chi_\mathrm{Re})\exp(ik_\mathrm{p}\,x\sin\varphi+(1+i)z/\delta_\mathrm{s})\exp(i\omega t). \tag{2.113}$$

Furthermore, within the present geometry, the component of the fluid velocity of the shear mode in the y direction must be zero. Since the fluid velocity of the shear mode must satisfy $\nabla\cdot\boldsymbol{v}_\mathrm{s}=0$, $v_{\mathrm{s},x}$ and $v_{\mathrm{s},z}$ must satisfy the relation $\partial v_{\mathrm{s},z}/\partial z = -\partial v_{\mathrm{s},x}/\partial x$. Substituting the derivative of $v_{\mathrm{s},x}$ with respect of x into this relation and integrating over z, yields

$$v_{\mathrm{s},z} = -A_\mathrm{i}\,\frac{\delta_\mathrm{s}k_\mathrm{p}^2\sin^2\varphi}{2\rho\omega}\,(1+i)(1+\chi_\mathrm{Re})\exp(ik_\mathrm{p}\,x\sin\varphi+(1+i)z/\delta_\mathrm{s})\exp(i\omega t). \tag{2.114}$$

With Eqs. (2.114), (2.112), and (2.111) the results for the acoustic variables for the reflection of a plane mono-frequency sound wave at a solid surface are complete.

These results can now be applied to derive the expression for the reflection coefficient by using the boundary condition (2.101). Eqs. (2.99), (2.112), and (2.114) show that all three sound modes contribute to the velocity component normal to

the surface at the surface, which is given by

$$v_z(z=0) = A_\mathrm{i}\left[\frac{\cos\varphi}{\rho w}\,(1-\chi_\mathrm{Re}) - \frac{(1+i)\tau_\mathrm{h}}{\rho\delta_\mathrm{h}}(\kappa-1)(1+\chi_\mathrm{Re}) - \frac{\delta_\mathrm{s}k_\mathrm{p}^2\sin^2\varphi}{2\rho\omega}(1+i)(1+\chi_\mathrm{Re})\right]\exp(ik_\mathrm{p}\,x\sin\varphi)\exp(i\omega t). \quad (2.115)$$

Substituting this result and the pressure of the propagational mode, Eq. (2.94), into the boundary condition (2.101) and solving the resulting equation for the reflection coefficient, yields

$$\chi_\mathrm{Re} = \frac{\cos\varphi - y_\mathrm{a}^\mathrm{w} - y_\mathrm{a}^\mathrm{h} - y_\mathrm{a}^\mathrm{s}}{\cos\varphi + y_\mathrm{a}^\mathrm{w} + y_\mathrm{a}^\mathrm{h} + y_\mathrm{a}^\mathrm{s}}, \quad (2.116)$$

where the dimensionless specific acoustic admittance of the thermal boundary layer

$$y_\mathrm{a}^\mathrm{h} = (1+i)(\kappa-1)\,\frac{\omega}{2w}\,\delta_\mathrm{h} \quad (2.117)$$

and the dimensionless specific acoustic admittance of the viscous boundary layer

$$y_\mathrm{a}^\mathrm{s} = (1+i)\sin^2\varphi\,\frac{\omega}{2w}\,\delta_\mathrm{s} \quad (2.118)$$

have been introduced.

The comparison of the reflection coefficient for ideal fluids, Eq. (2.97), with Eq. (2.116) shows that effects of the thermal and viscous boundary layers on the reflection coefficient are represented by their acoustic admittances, which enter into the reflection coefficient in the same way as the wall admittance. From the viewpoint of electric circuit theory, the admittances of the thermal and viscous boundary layer are connected in parallel with the wall admittance. As the admittance of the thermal and viscous boundary layer are complex quantities with equal real and imaginary parts, the reflection coefficient is also a complex quantity. The reflection of a sound wave at solid surfaces reduces not only the amplitude of the wave, but also changes its phase. The admittance of the viscous boundary layer depends on the angle of incidence, whereas the admittance of the thermal boundary layer is independent of the angle of incidence.

In pulse-echo experiments, one is mostly interested in the reflection of waves normally incident on a solid reflector wall. In this special case, there is no viscous boundary layer, and the expression for the reflection coefficient becomes

$$\chi_\mathrm{Re} = \frac{1 - y_\mathrm{a}^\mathrm{w} - y_\mathrm{a}^\mathrm{h}}{1 + y_\mathrm{a}^\mathrm{w} + y_\mathrm{a}^\mathrm{h}}. \quad (2.119)$$

Table 2.1. Values of the reflection coefficient for the reflection of sound waves with a frequency of 10 MHz normally incident on a plane solid reflector in liquid water and gaseous argon at (300 K, 0.1 MPa).

Fluid		water		argon
ρ / kg m^{-3}		996.6		1.6025
w / m s^{-1}		1501.52		322.671
Reflector	copper	stainless steel	quartz glass	stainless steel
ρ_w / kg m^{-3}	8930	7900	2200	7900
w_w / m s^{-1}	5010	5790	5968	5790
$\chi_\mathrm{Re}^\mathrm{ideal}$	0.93527	0.93665	0.79538	0.99998
$\lvert\chi_\mathrm{Re}^\mathrm{real}\rvert$	0.93524	0.93661	0.79536	0.89829
$\varphi_\mathrm{Re}^\mathrm{real}$ / $^\circ$	$-6.70 \cdot 10^{-5}$	$-6.55 \cdot 10^{-5}$	$-2.31 \cdot 10^{-4}$	-0.331
$\Delta t_\mathrm{h}/t \cdot 10^6$	$-1.40 \cdot 10^{-3}$	$-1.37 \cdot 10^{-3}$	$-4.82 \cdot 10^{-3}$	-1.483

It remains a complex quantity, which may cause phase shifts in the reflected sound signals.

In order to examine the magnitude of the phase shift, numerical values of reflection coefficients are given for four different examples in Table 2.1. In these examples, sound waves in liquid water and gaseous argon at (300 K, 0.1 MPa) are normally incident on plane solid reflectors. In all cases, the frequency of the sound wave is 10 MHz. The symbols $|\chi_\mathrm{Re}^\mathrm{real}|$ and $\varphi_\mathrm{Re}^\mathrm{real}$ denote the modulus and phase of the complex reflection coefficient. In order to examine the influence of the thermal boundary layer on the transit time of a sound signal, which experiences a reflection at a solid wall, the propagation of a sound signal over a distance of 10 mm between a sender/receiver and reflector back and forth is considered. This situation corresponds to a typical pulse-echo experiment to measure the speed of sound. The last line in Table 2.1 reports the relative error $\Delta t_\mathrm{h}/t$ of the transit time t introduced by the phase shift due to the thermal boundary layer for this example. As can be observed from Table 2.1, the influence of the thermal boundary layer on the reflection coefficient is very small. In gaseous argon, the phase shift due to the thermal boundary layer contributes less than 1.5 ppm to the transit time of the sound signal in the chosen example. In liquid water, the contribution of the phase shift is even by about three orders of magnitude smaller. These examples demonstrate that the influence of the thermal boundary layer can safely be neglected. Hence, Eq. (2.97) provides an excellent approximation for the reflection coefficient of waves normally incident on a plane solid wall in real fluids.

2.5 Dispersion of Sound Waves

The model for the propagation of sound waves, which was developed in the preceding sections, is based on the assumption that local equilibrium is attained instantaneously in the fluid. Sometimes there are relaxation mechanisms operating in the fluid, which prevent the attainment of local equilibrium between the acoustic variables density, pressure, and temperature.

In Sec. 2.2.2, it was shown that the effects of heat conduction and viscous dissipation are described by the imaginary part of the complex propagation constant, which represents the sound absorption coefficient. From the thermodynamic point of view, these effects are irreversible transfers of kinetic and potential energy of the organized motion of the sound wave into disorganized translational motion of the molecules, which is macroscopically observed as heat. Therefore, these effects are referred to as translational relaxation. If the relaxation times characterizing these mechanisms are long compared with the inverse molecular collision frequency, the local equilibrium hypothesis is valid, and the equations derived in the preceding sections adequately describe the acoustic wave motion. In this frequency regime, the speed of sound is frequency independent and the absorption coefficient depends on the frequency squared. Only in gases at very low pressures, if the sound frequency is of the order of the molecular collision frequency, the fluid can no longer be viewed as a continuum, and translational relaxation effects must be accounted for in the model for acoustic wave motion. For example, in gaseous argon at 300 K and 0.1 MPa, the molecular collision frequency is about 5.5 GHz [77]. In compressed gases and liquids, molecular collisions occur continuously so that the molecular collision frequency is even higher. Since pulse-echo experiments are usually carried out at frequencies below 20 MHz, translational relaxation can safely be neglected for the purposes of this work.

In monatomic fluids, translational relaxation is the only possible relaxation mechanism. In diatomic or polyatomic fluids, additionally irreversible energy transfer from the collective motion of the sound wave to internal degrees of freedom of the molecules other than the translational ones can take place. If the density of the fluid is suddenly changed, the translational motion of the molecules will adjust almost instantaneously because only few collisions are required to equilibrate translational energy. Since the pressure is solely determined by the translational motion of the molecules, it also adjusts rapidly to the density change. After the compression has been completed, some of the translational energy of the molecules is transferred into

the rotational and vibrational degrees of freedom more slowly, which reduces the pressure accordingly. Since this energy transfer is an irreversible process, the fluid is heated, and the sound wave is attenuated. These effects are called rotational and vibrational relaxation. Usually, the rotational degrees of freedom equilibrate within few molecular collisions. Thus, rotational relaxation effects, as translational relaxation effects, influence the acoustic wave motion only at very high frequencies of the order of the molecular collision frequencies and can be neglected for acoustic measurements in the kHz or MHz regime. Vibrational relaxation, however, can already influence the propagation of sound waves in the kHz regime, particularly for fluids of diatomic molecules such as oxygen and nitrogen.

Besides slow energy transfer into the internal degrees of freedom of the molecules, structural rearrangements in the fluid can influence the propagation of sound waves [100, pp. 200]. Such effects arise for example in associating fluids, which are characterized by strongly ordered molecular structures due to hydrogen bonding networks. When a sound wave propagates through the fluid, the ordered structure is disturbed and relaxes towards equilibrium. If this relaxation is so slow that local equilibrium is not attained instantaneously, it is also an irreversible process, which contributes to acoustic wave motion. In this work, water is the only associating fluid, in which the speed of sound was measured. Since it is well-known from previous studies [69, 62, 99] that the speed of sound in liquid water is frequency independent up to at least 15 MHz, structural relaxation need not be considered in the remainder of this work.

If one or more of these relaxation mechanisms accompanies the acoustic wave motion, the speed of sound may become frequency dependent. This phenomenon is called dispersion, and the fluid is said to be dispersive. In a dispersive fluid, the speed of sound deviates from the thermodynamic speed of sound, which is valid for isentropic sound propagation in the limit of low frequencies. In thermophysical properties research, however, the thermodynamic speed of sound is required because only it is related to other thermodynamic properties. Therefore, if speed of sound measurements in a fluid are influenced by dispersion, the data must be corrected to the thermodynamic speed of sound. In the remainder of this section, a model for describing the effects of rotational and vibrational relaxation on the speed of sound will be developed. Rotational relaxation is included because both relaxation mechanisms can be described by the same model.

The frequency dependence of the speed of sound and the dispersive contribution to the sound absorption coefficient can most easily be described by the frequency

dependence of the specific isochoric and isobaric heat capacities. From statistical thermodynamics, it is known that the contribution of the ith internal degree of freedom of a unit mass of fluid molecules to the specific isochoric heat capacity in the ideal gas limit can be represented by an expression of the form $(R_\mathrm{m}/M)F_i(T)$ [9]. The function F_i is zero at $T = 0$, rises strongly near the characteristic temperature of the ith degree of freedom T_i, and approaches the value 1/2 for rotational degrees of freedom or unity for vibrational degrees of freedom at temperatures $T \gg T_i$. The functional form of $F_i(T)$ depends on the nature of the degree of freedom and on the structure of the molecule, but it does not need to be specified for the purposes of this section. At the temperatures of interest in this work, the functions describing the three translational degrees of freedom have reached their asymptotic values, whereas those describing electronic excitations are negligible. Furthermore, for all molecules except hydrogen, the functions F_i of the rotational degrees of freedom have also reached their asymptotic values, and the F_i's of the vibrational degrees of freedom are less than unity. Therefore, the specific isochoric heat capacity in the ideal gas limit may be written as

$$c_v^{\mathrm{iG}}(T) = \left(\frac{\partial u^{\mathrm{iG}}}{\partial T}\right)_v = \frac{R_\mathrm{m}}{M}\left(\frac{3}{2} + \sum_i F_i(T)\right). \tag{2.120}$$

The sum over i extends over all rotational and vibrational degrees of freedom of the molecule. A linear molecule has two, a nonlinear molecule has three rotational degrees of freedom. Generally, a molecule composed of N atoms has $3N-6$ vibrational degrees of freedom. Sometimes, for example in molecules of n-alkanes, one or more vibrational degrees of freedom may be degenerated to internal rotations of groups of atoms in the molecule. In such a case, the asymptotic value of the contribution of the vibrational degree of freedom to the isochoric heat capacity reduces to the value 1/2 for the internal rotation.

In the ideal gas limit, the specific isobaric heat capacity is related to the specific isochoric heat capacity by

$$c_p^{\mathrm{iG}}(T) = \left(\frac{\partial h^{\mathrm{iG}}}{\partial T}\right)_p = c_v^{\mathrm{iG}}(T) + \frac{R_\mathrm{m}}{M} = \frac{R_\mathrm{m}}{M}\left(\frac{5}{2} + \sum_i F_i(T)\right), \tag{2.121}$$

and the ratio of the two heat capacities, the isentropic exponent, is given by

$$\kappa^{\mathrm{iG}}(T) = \frac{c_p^{\mathrm{iG}}(T)}{c_v^{\mathrm{iG}}(T)} = \frac{\frac{5}{2} + \sum_i F_i(T)}{\frac{3}{2} + \sum_i F_i(T)}. \tag{2.122}$$

Next, a model must be specified, which describes the relaxation of the degrees of freedom, represented by the functions $F_i(T)$, to equilibrium. In general, the relaxation of an internal degree of freedom in a complex molecule is coupled to the relaxation of all other degrees of freedom of the molecule. In order to simplify matters, it is assumed that every degree of freedom has its individual time of response to attain equilibrium, which is called its relaxation time τ_i. Furthermore, it is assumed that the decay of the specific internal energy of the ith degree of freedom to its equilibrium value after a sudden density change obeys the simple first order differential equation

$$\frac{du_i}{dt} = -\frac{u_i - u_i^{\mathrm{le}}}{\tau_i}, \tag{2.123}$$

where u_i is the instantaneous value of the specific internal energy of the ith degree of freedom and u_i^{le} is the local equilibrium specific internal energy of the ith degree of freedom. The solution of this differential equation

$$u_i(t) = u_i^{\mathrm{le}} + (u_i^0 - u_i^{\mathrm{le}}) \exp(-t/\tau_i) \tag{2.124}$$

describes an exponential decay of the specific internal energy from the initial value u_i^0 after the change to the local equilibrium value u_i^{le}. If a harmonic sound wave propagates in the fluid, energy is alternately supplied to and released from the degree of freedom at a rate determined by the factor $\exp(i\omega t)$. If the ith degree of freedom attained local equilibrium instantaneously, the periodic variations of its specific internal energy could be approximated by

$$u_i^{\mathrm{le}} = u_i^{\mathrm{eq}} + \varepsilon_i^{\mathrm{le}} \exp(i\omega t), \tag{2.125}$$

where u_i^{eq} denotes the specific internal energy of the ith degree of freedom in the thermodynamic equilibrium state of the resting fluid and $\varepsilon_i^{\mathrm{le}}$ is the amplitude of the periodic variation of its specific internal energy. u_i^{eq} is to be distinguished from u_i^{le}, which represents the local equilibrium specific internal energy in the region of the propagating sound wave. However, since local equilibrium is not reached instantaneously, the amplitude of the specific internal energy obeys Eq. (2.123). The solution of Eq. (2.123) for the non-equilibrium amplitude ε_i is given by

$$\varepsilon_i = \frac{\varepsilon_i^{\mathrm{le}}}{1 + i\omega\tau_i}. \tag{2.126}$$

Substituting this result into Eq. (2.125), yields the periodic variation of the non-equilibrium specific internal energy

$$u_i = u_i^{\mathrm{eq}} + \frac{\varepsilon_i^{\mathrm{le}}}{1 + i\omega\tau_i} \exp(i\omega t). \tag{2.127}$$

If local equilibrium were attained instantaneously, the periodic acoustic temperature variation could be described by a function of the form $T_\mathrm{a}^\mathrm{le} \propto \exp(i\omega t)$. If, moreover, the amplitudes of the temperature and specific internal energy variations were small, the change of the local equilibrium specific internal energy could be approximated by $\varepsilon_i^\mathrm{le} \approx c_i T_\mathrm{a}^\mathrm{le}$, where c_i denotes the equilibrium contribution of the ith degree of freedom to the specific heat capacity. The actual non-equilibrium local specific internal energy change would then be given by $\varepsilon_i \approx c_i T_\mathrm{a}^\mathrm{le}/(1 + i\omega\tau_i)$. Thus, the contribution to the specific heat capacity $c_i/(1+i\omega\tau_i)$ becomes frequency dependent and represents a dynamic quantity.

If each degree of freedom is described in a similar manner, the frequency dependent isochoric heat capacity of the ideal gas is given by

$$c_v^\mathrm{iG}(T,\omega) = \frac{R_\mathrm{m}}{M}\left(\frac{3}{2} + \sum_i \frac{F_i(T)}{1+i\omega\tau_i}\right), \tag{2.128}$$

and a similar expression holds for the isobaric heat capacity. Moreover, the ratio of the frequency dependent heat capacities becomes

$$\kappa^\mathrm{iG}(T,\omega) = \frac{\dfrac{5}{2} + \sum\limits_i \dfrac{F_i(T)}{1+i\omega\tau_i}}{\dfrac{3}{2} + \sum\limits_i \dfrac{F_i(T)}{1+i\omega\tau_i}}. \tag{2.129}$$

These results can now be applied to derive an expression for the frequency dependent speed of sound in a real fluid. For a real fluid, there are additional contributions to both ideal gas heat capacities, the residual contributions c_v^Re and c_p^Re, which account for the effects of intermolecular forces. They are solely determined by the thermal equation of state and are frequency independent. The frequency dependent ratio of the heat capacities of the real fluid is given by

$$\kappa(T,\rho,\omega) = \frac{c_p^\mathrm{iG}(T,\omega) + c_p^\mathrm{Re}(\rho,T)}{c_v^\mathrm{iG}(T,\omega) + c_v^\mathrm{Re}(\rho,T)} = \frac{c_p(\rho,T,\omega)}{c_v(\rho,T,\omega)}. \tag{2.130}$$

In the low frequency limit, where dispersion is absent, the propagational sound mode is described by the propagation constant k_p as given by Eq. (2.70). If heat conduction and viscous dissipation are neglected, the propagation constant becomes $k_\mathrm{p} = \omega/w$. With the relation between the zero-frequency speed of sound, the ratio of the heat capacities, and the thermal pressure coefficient,

$$w_0^2 = \frac{c_p}{c_v}\left(\frac{\partial p}{\partial \rho}\right)_T,$$

the propagation constant can be written as

$$k_{\mathrm{p}}^2 = \frac{\omega^2}{\dfrac{c_p}{c_v}\left(\dfrac{\partial p}{\partial \rho}\right)_T}. \tag{2.131}$$

The effect of the frequency dependence of the heat capacities on the speed of sound can be introduced by replacing the zero-frequency heat capacities by the frequency-dependent heat capacities. Then, Eq. (2.131) reads

$$k_{\mathrm{p}}^2 = \frac{\omega^2}{\dfrac{c_p(\omega)}{c_v(\omega)}\left(\dfrac{\partial p}{\partial \rho}\right)_T}. \tag{2.132}$$

Since the thermal equation of state is determined by the translational degrees of freedom and intermolecular forces, it does not depend on frequency, and the derivative $(\partial p/\partial \rho)_T$ remains unchanged. Therefore, the propagation constant becomes a complex quantity. Its real part yields the frequency-dependent speed of the sound wave, while its imaginary part represents an additional contribution to the attenuation of the sound wave.

In order to illustrate the general properties of the frequency dependent speed of sound, a simple model is chosen as an example, in which it is assumed that only one degree of freedom relaxes so slowly that it does not attain equilibrium. The contribution of this degree of freedom to the equilibrium heat capacities is denoted by c^{int}, and its relaxation time is τ^{int}. The frequency dependent specific isochoric heat capacity is for this case given by

$$c_v(\omega) = c_v - c^{\mathrm{int}}\,\frac{i\omega\tau^{\mathrm{int}}}{1+i\omega\tau^{\mathrm{int}}}, \tag{2.133}$$

and a similar relation holds for c_p. In the infinite-frequency limit $\omega \to \infty$, the heat capacities take the values $c_v^\infty = c_v - c^{\mathrm{int}}$ and $c_p^\infty = c_p - c^{\mathrm{int}}$. The ratio of the heat capacities can then be written as

$$\kappa(\omega) = \frac{c_p(\omega)}{c_v(\omega)} = \frac{c_p + i\omega\tau^{\mathrm{int}}c_p^\infty}{c_v + i\omega\tau^{\mathrm{int}}c_v^\infty}. \tag{2.134}$$

Substituting this expressions into Eq. (2.132), yields

$$k_{\mathrm{p}}^2 = \frac{\omega^2}{(\partial p/\partial\rho)_T}\,\frac{c_v c_p + (\omega\tau^{\mathrm{int}})^2 c_v^\infty c_p^\infty + i\omega\tau^{\mathrm{int}}(c_v^\infty c_p - c_v c_p^\infty)}{c_p^2 + (\omega\tau^{\mathrm{int}})^2 (c_p^\infty)^2}. \tag{2.135}$$

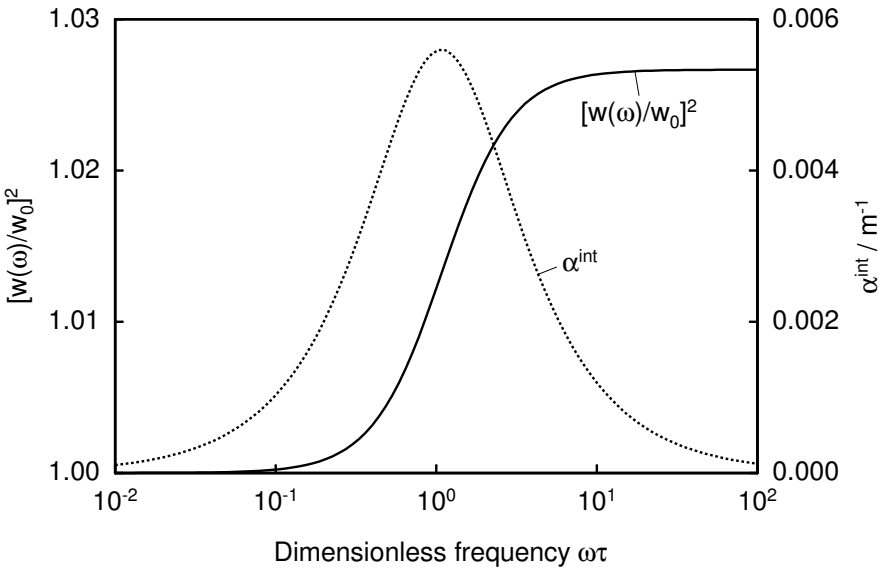

Figure 2.2. Dependence of the frequency dependent speed of sound and of the dispersive contribution to the absorption coefficient on frequency.

The propagation constant is a complex quantity, whose real part yields the speed of sound waves $w(\omega) = \omega/\mathrm{Re}(k_\mathrm{p})$ in the dispersive medium, while the negative imaginary part yields the contribution $\alpha^\mathrm{int}(\omega) = -\mathrm{Im}(k_\mathrm{p})$ to the absorption coefficient.

The dependence of the speed of sound and of the dispersive contribution to the absorption coefficient on frequency is illustrated in Fig. 2.2, which depicts the ratio $[w(\omega)/w_0]^2$ and the dispersive contribution to the absorption coefficient as a function of frequency. The curves in Fig. 2.2 are based on numerical calculations for a hypothetical fluid with $c_p = 3.75(R_\mathrm{m}/M)$, $c_v = 2.75(R_\mathrm{m}/M)$, and $c^\mathrm{int} = 0.25(R_\mathrm{m}/M)$. The dispersion takes place in a small frequency range, which depends on the relaxation time of the internal mode. In this range, the ratio $[w(\omega)/w_0]^2$ increases from unity at low frequencies to the constant value $[w_\infty/w_0]^2$ at high frequencies. The limiting value

$$w_\infty^2 = w_0^2 \, \frac{c_v}{c_p} \, \frac{c_p^\infty}{c_v^\infty} \tag{2.136}$$

is the infinite-frequency speed of sound. The dispersive contribution to the absorption coefficient passes through a peak in that range, where the speed of sound increases strongly. In the low and high frequency limit, it asymptotically approaches zero. If a fluid had more than one slowly relaxing degree of freedom with clearly distinguished relaxation times, there would be as many dispersion steps in the speed

of sound and peaks in the contribution to the absorption coefficient as there are relaxing degrees of freedom.

If measurements of the speed of sound cannot be carried out at frequencies below the dispersion step, the measured speeds of sound are most easily corrected to the thermodynamic speed of sound, if they are determined in the frequency range above the dispersion step. In this case, the contribution of the slowly relaxing degree of freedom to the heat capacities can be calculated by means of statistical thermodynamics. This contribution can then be used to calculate the infinite-frequency limits of the heat capacities, and Eq. (2.136) can be rearranged to yield

$$w_0 = w_\infty \sqrt{\frac{c_v^\infty}{c_p^\infty}\,\frac{c_p}{c_v}}. \tag{2.137}$$

If measurements are carried out in the range of the dispersion step, the relaxation time must additionally be known, and the complete real part of the propagation constant must be used to correct the measured frequency-dependent speed of sound to the thermodynamic speed of sound.

The situation is more complicated, if there are more than one slowly relaxing degree of freedom and the individual dispersion steps happen to lie in the same frequency range or if the relaxation of two or more degrees of freedom is strongly coupled. In this cases, an effective single dispersion step, whose properties are determined from measurements at several frequencies in the dispersion range, could be used to develop a correction. However, often it is not possible to obtain this information from experiment, especially, when the sound transducers are operated at their resonance frequencies only.

2.6 Piezoelectric Sound Transducers

In pulse-echo experiments, acoustic burst signals must be generated and detected in the sample fluid. For this purpose, transducers of piezoelectric materials are employed, which are either placed in direct contact with the sample fluid or are coupled to it by means of a solid buffer rod. These transducers usually consist of a thin circular piezoelectric plate with electrodes of a conducting material, such as gold, silver, or nickel, on both major faces. Some examples for piezoelectric sound transducers are shown in Fig. 2.3. Disks with with circular electrodes are often used as transducers in pulse-echo experiments. If it is difficult to connect the electrodes from both sides, one electrode can for example be wrapped around as shown in

Fig. 2.3 so that both electrodes are accessible from one side. The electrode material is coated on the surfaces of the plate by direct imprinting or by vapor-deposition.

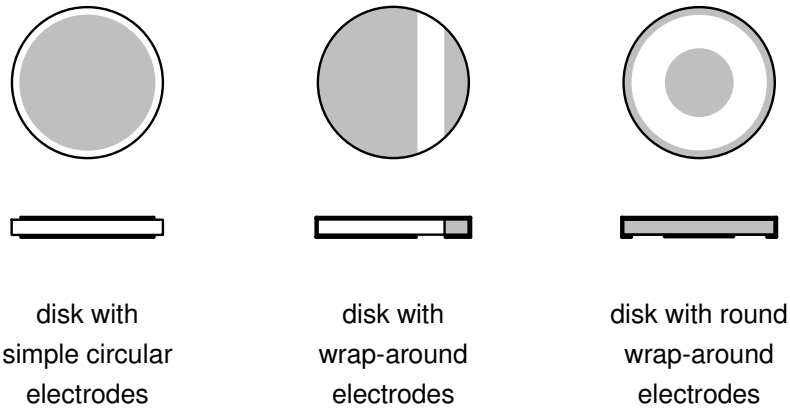

Figure 2.3. Some examples for piezoelectric sound transducers with different electrode shapes.

A solid material is said to be piezoelectric, if a mechanical deformation generates an electric field in the material. Conversely, an externally applied electric field may cause a deformation of the material. In the first case, one speaks of the piezoelectric effect, whereas the second case is called the reverse piezoelectric effect. When a piezoelectric transducer placed in direct contact with a fluid is excited electrically near its resonance frequency, longitudinal sound waves, which are coupled to the compressions and expansions of the transducer, are generated in the fluid. Viceversa, sound waves arriving at the transducer deform it mechanically and, accordingly, generate an electric field in the piezoelectric material. If piezoelectric transducers are employed to generate and detect sound waves in solids, they are usually adhered to the surface of the solid by a thin layer of viscous oil or other adhesive materials in order to provide complete mechanical coupling between the two solid materials. The piezoelectric effect is exhibited by a number of poly-crystalline and amorphous solids and by single crystals. Widely used as sound transducers are certain ceramic materials, for example lead zirconate titanate (PZT), lead titanate, lead metaniobate, or bismuth titanate and single crystals of quartz (SiO_2) or lithium niobate ($LiNbO_3$).

Since quartz transducers were used in this work, the presentation in the following sections focusses on the properties and application of quartz transducers. Nevertheless, parts of the material also apply to other piezoelectric materials. Sec. 2.6.1

presents the general linear theory of piezoelectric materials within the frame of continuum mechanics and describes the physical properties of quartz. In Sec. 2.6.2, the theory is applied to develop a one-dimensional model for thickness vibrations of thin piezoelectric plates. Based based on this model, Secs. 2.6.3 and 2.6.4 treat the operation of piezoelectric transducers as sound receivers and senders. In Sec. 2.6.5, an equivalent circuit model is introduced to describe the electrical properties of piezoelectric transducers near their resonances.

2.6.1 Linear Theory of Piezoelectric Materials

In continuum mechanics, the deformation of an elastic solid is characterized in terms of two sets of coordinates. The first one, ξ_i, defines the positions of the material points of the body in a reference configuration, and the second one, x_i, defines the positions of the material points in the actual configuration. The index i can take the values $\{1, 2, 3\}$, which represent the set of Cartesian coordinates $\{x, y, z\}$. In this section, the symbolic notation and index notation are used in parallel to represent Cartesian vectors and tensors. All equations are written in both notations in order to simplify their readability, but, at the same time, to keep the notation unambiguous. The meaning of the different mathematical operations and symbols is given in the nomenclature. A deformation of the body is described by the deformation gradient tensor $\boldsymbol{F}$, whose components are defined by

$$\boldsymbol{F} := \frac{\partial \boldsymbol{x}}{\partial \boldsymbol{\xi}}; \qquad F_{ij} := \frac{\partial x_i}{\partial \xi_j}. \tag{2.138}$$

$\boldsymbol{F}$ is a second-order tensor, and its components F_{ij} describe the transformation of a line element of the body in the reference configuration $\boldsymbol{d\xi}$ to the corresponding line element in the deformed configuration $\boldsymbol{dx}$. The deformation gradient tensor provides a complete description of the deformation of the body.

When applied as sound transducers, piezoelectric materials are only subject to small deformations so that it is appropriate to introduce a linearization. For this purpose, the displacement vector

$$\boldsymbol{u} = \boldsymbol{x} - \boldsymbol{\xi}; \qquad u_i = x_i - \xi_i \tag{2.139}$$

is introduced, which represents the displacement of a material point of the body from its position in the reference configuration to the position in the deformed configuration. With the displacement vector, the deformation gradient tensor is

written as

$$\boldsymbol{F} = \frac{\partial(\boldsymbol{\xi} + \boldsymbol{u})}{\partial \boldsymbol{\xi}} = \boldsymbol{I} + \frac{\partial \boldsymbol{u}}{\partial \boldsymbol{\xi}}; \qquad F_{ij} = \frac{\partial(\xi_i + u_i)}{\partial \xi_j} = \delta_{ij} + \frac{\partial u_i}{\partial \xi_j}. \tag{2.140}$$

For the description of piezoelectric materials, the strain tensor $\boldsymbol{S}$ is usually used instead of the deformation gradient tensor to characterize the deformations and will therefore also be used here. It is defined in terms of the deformation gradient tensor by

$$\boldsymbol{S} = \frac{1}{2}\left(\boldsymbol{F}^t \cdot \boldsymbol{F} - \boldsymbol{I}\right); \qquad S_{ij} = \frac{1}{2}\left(F_{ji}F_{ij} - \delta_{ij}\right). \tag{2.141}$$

When Eq. (2.140) is substituted into Eq. (2.141), the strain tensor becomes

$$\begin{aligned} \boldsymbol{S} &= \frac{1}{2}\left(\boldsymbol{I} + \left[\frac{\partial \boldsymbol{u}}{\partial \boldsymbol{\xi}}\right]^t\right) \cdot \left(\boldsymbol{I} + \frac{\partial \boldsymbol{u}}{\partial \boldsymbol{\xi}}\right) - \frac{1}{2}\boldsymbol{I} \\ &= \frac{1}{2}\left(\frac{\partial \boldsymbol{u}}{\partial \boldsymbol{\xi}} + \left[\frac{\partial \boldsymbol{u}}{\partial \boldsymbol{\xi}}\right]^t\right) + \frac{1}{2}\left[\frac{\partial \boldsymbol{u}}{\partial \boldsymbol{\xi}}\right]^t \cdot \frac{\partial \boldsymbol{u}}{\partial \boldsymbol{\xi}}; \end{aligned}$$

$$\begin{aligned} S_{ij} &= \frac{1}{2}\left(\delta_{ij} + \frac{\partial u_j}{\partial \xi_i}\right)\left(\delta_{ij} + \frac{\partial u_i}{\partial \xi_j}\right) - \frac{1}{2}\delta_{ij} \\ &= \frac{1}{2}\left(\frac{\partial u_i}{\partial \xi_j} + \frac{\partial u_j}{\partial \xi_i}\right) + \frac{1}{2}\frac{\partial u_j}{\partial \xi_i}\frac{\partial u_i}{\partial \xi_j}. \end{aligned} \tag{2.142}$$

Since for small displacements $|\partial u_i/\partial \xi_j| \ll 1$, products of the derivatives of the displacements are negligible. Thus, one obtains a linearized expression for the strain tensor

$$\boldsymbol{S} = \frac{1}{2}\left(\frac{\partial \boldsymbol{u}}{\partial \boldsymbol{\xi}} + \left[\frac{\partial \boldsymbol{u}}{\partial \boldsymbol{\xi}}\right]^t\right); \qquad S_{ij} = \frac{1}{2}\left(\frac{\partial u_i}{\partial \xi_j} + \frac{\partial u_j}{\partial \xi_i}\right), \tag{2.143}$$

which, in the following, will be simply be referred to as strain tensor.

The velocity and acceleration of a material point within the linear approximation are given by the first and second time derivatives of the displacement vector $\boldsymbol{v} = \dot{\boldsymbol{u}} = \partial \boldsymbol{u}/\partial t$ and $\boldsymbol{a} = \ddot{\boldsymbol{u}} = \partial^2 \boldsymbol{u}/\partial t^2$, which in index notation read $v_i = \dot{u}_i = \partial u_i/\partial t$ and $a_i = \ddot{u}_i = \partial^2 u_i/\partial t^2$.

The mechanical interactions between different portions of the body are described by the Cauchy stress tensor $\boldsymbol{T}$. The diagonal components T_{ij} with $i = j$ are the normal stresses, and the off-diagonal components T_{ij} with $i \neq j$ are the shear stresses. In a non-piezoelectric elastic body, the components of the stress tensor are related to the components of the strain tensor by the constitutive equation

$$\boldsymbol{T} = \boldsymbol{c} : \boldsymbol{S}^t; \qquad T_{ij} = c_{ijkl}S_{kl}, \tag{2.144}$$

where the c_{ijkl} are properties of the elastic material, which are called elastic constants. The set of elastic constants forms a fourth-order tensor. When Eq. (2.144) is written in inverse form,

$$\boldsymbol{S} = \boldsymbol{s} : \boldsymbol{T}^t; \qquad S_{ij} = s_{ijkl} T_{kl}, \tag{2.145}$$

the tensor of the compliances $\boldsymbol{s}$ with the components s_{ijkl} is used instead of the tensor of the elastic constants. They are related by $\boldsymbol{s} = \boldsymbol{c}^{-1}$.

In a linear solid dielectric material, the electric field vector $\boldsymbol{E}$ and electric flux density vector $\boldsymbol{D}$ are related by

$$\boldsymbol{D} = \boldsymbol{\varepsilon} \cdot \boldsymbol{E}; \qquad D_i = \varepsilon_{ij} E_j, \tag{2.146}$$

where $\boldsymbol{\varepsilon}$ represents the second-order tensor of the dielectric constants of the material. In inverse form, this relation reads

$$\boldsymbol{E} = \boldsymbol{\beta} \cdot \boldsymbol{D}; \qquad E_i = \beta_{ij} D_j. \tag{2.147}$$

In this form, the dielectric properties of the material are characterized by the impermeability tensor $\boldsymbol{\beta} = \boldsymbol{\varepsilon}^{-1}$.

For a piezoelectric material, both elastic and electric properties are coupled, and these relations must be modified. The constitutive relations for a piezoelectric material can be written in four different representations, depending on which combination of two mechanical tensors $\boldsymbol{T}$ and $\boldsymbol{S}$ and electrical vectors $\boldsymbol{E}$ and $\boldsymbol{D}$ is chosen to represent the independent variables. If $\boldsymbol{S}$ and $\boldsymbol{E}$ are chosen, the constitutive equations are given by

$$\boldsymbol{T} = \boldsymbol{c}^E : \boldsymbol{S}^t - \boldsymbol{E} \cdot \boldsymbol{e}; \qquad T_{ij} = c^E_{ijkl} S_{kl} - e_{kij} E_k \tag{2.148}$$

$$\boldsymbol{D} = \boldsymbol{e} \cdot \boldsymbol{S}^t - \boldsymbol{\varepsilon}^S \cdot \boldsymbol{E}; \qquad D_i = e_{ikl} S_{kl} + \varepsilon^S_{ij} E_j, \tag{2.149}$$

where c^E_{ijkl}, e_{ijk}, and ε^S_{ij} are the elastic constants at constant electric field, the piezoelectric constants, and the dielectric constants ε^S_{ij} at constant strain, respectively. The piezoelectric constants e_{ijk} form a third-order tensor. Since the tensor c^E_{ijkl} is symmetric with respect to the indices i and j, the indices k and l, and, furthermore, the pairs of indices ij and kl, there are only 21 unique elastic constants in the general case. Similarly, there are 18 unique piezoelectric constants and 6 unique dielectric constants.

In order to simplify the notation, a condensed matrix notation, which utilizes the symmetries of the tensors of the elastic and piezoelectric constants, is usually

Table 2.2. Relation between the indices of the piezoelectric equations in tensor and condensed matrix notation.

ij or kl	11	22	33	23 or 32	31 or 13	12 or 21
p or q	1	2	3	4	5	6

introduced to write the piezoelectric equations [8]. This matrix notation consists of replacing ij or kl by p or q, where i, j, k, and l take the values $\{1,2,3\}$ and p and q take the values $\{1,\ldots,6\}$ according to Table 2.2. Thus,

$$c^E_{ijkl} = c^E_{pq}, \quad e_{ikl} = e_{ip}, \quad \text{and} \quad T_{ij} = T_p. \tag{2.150}$$

With these identifications, the constitutive equations, Eqs. (2.148) and (2.149), take the form

$$T_p = c^E_{pq} S_q - e_{kp} E_k \tag{2.151}$$

$$D_i = e_{iq} S_q + \varepsilon^S_{ij} E_j, \tag{2.152}$$

where

$$\begin{aligned} S_{ij} &= S_p, \quad \text{if } i = j \text{ or } p = 1,2,3 \\ 2S_{ij} &= S_p, \quad \text{if } i \neq j \text{ or } p = 4,5,6. \end{aligned} \tag{2.153}$$

In condensed matrix notation, the stress tensor and strain tensor are represented by (6×1) matrices, and the elastic and piezoelectric constants are arranged in (6×6) and (3×6) matrices, respectively. Furthermore, Eqs. (2.151) and (2.152) can now be written in operator notation as

$$\boldsymbol{T} = \boldsymbol{c}^E \cdot \boldsymbol{S} - \boldsymbol{e}^t \cdot \boldsymbol{E} \tag{2.154}$$

$$\boldsymbol{D} = \boldsymbol{e} \cdot \boldsymbol{S} + \boldsymbol{\varepsilon}^S \cdot \boldsymbol{E}, \tag{2.155}$$

The other three forms of the constitutive piezoelectric equations with the pairs of independent variables $\boldsymbol{T}$ and $\boldsymbol{E}$, $\boldsymbol{T}$ and $\boldsymbol{D}$, and $\boldsymbol{S}$ and $\boldsymbol{D}$ read

$$\boldsymbol{S} = \boldsymbol{s}^E \cdot \boldsymbol{T} + \boldsymbol{d}^t \cdot \boldsymbol{E} \tag{2.156}$$

$$\boldsymbol{D} = \boldsymbol{d} \cdot \boldsymbol{T} + \boldsymbol{\varepsilon}^T \cdot \boldsymbol{E}, \tag{2.157}$$

and

$$\boldsymbol{S} = \boldsymbol{s}^D \cdot \boldsymbol{T} + \boldsymbol{g}^t \cdot \boldsymbol{D} \tag{2.158}$$

$$\boldsymbol{E} = -\boldsymbol{g} \cdot \boldsymbol{T} + \boldsymbol{\beta}^T \cdot \boldsymbol{D}, \tag{2.159}$$

and

$$\boldsymbol{T} = \boldsymbol{c}^D \cdot \boldsymbol{S} - \boldsymbol{h}^t \cdot \boldsymbol{D} \tag{2.160}$$

$$\boldsymbol{E} = -\boldsymbol{h} \cdot \boldsymbol{S} + \boldsymbol{\beta}^S \cdot \boldsymbol{D}. \tag{2.161}$$

Using the condensed matrix notation, the relations between the coefficients appearing in the four sets of constitutive equations, Eqs. (2.151), (2.152), and (2.156) to (2.161) are given by

$$\begin{aligned}
&c^E_{pr} s^E_{qr} = \delta_{pq}, && c^D_{pr} s^D_{qr} = \delta_{pq},\\
&\beta^S_{ik} \varepsilon^S_{jk} = \delta_{ij}, && \beta^T_{ik} \varepsilon^T_{jk} = \delta_{ij},\\
&c^D_{pq} = c^E_{pq} + e_{kp} h_{kq}, && s^D_{pq} = s^E_{pq} - d_{kp} g_{kq},\\
&\varepsilon^T_{ij} = \varepsilon^S_{ij} + d_{iq} e_{jq}, && \beta^T_{ij} = \beta^S_{ij} - g_{iq} h_{jq},\\
&e_{ip} = d_{iq} c^E_{qp}, && d_{ip} = \varepsilon^T_{ik} g_{kp},\\
&g_{ip} = \beta^T_{ik} d_{kp}, && h_{ip} = g_{iq} c^D_{qp},
\end{aligned}$$

where δ_{ij} represents the Kronecker δ, that is the identity tensor in index notation. In order that the relations in Eqs. (2.150) and (2.153) hold, the relations

$$s^E_{pq} = s^E_{ijkl}, \quad \text{if } i=j \text{ and } k=l,\ p,q=1,2,3, \tag{2.162}$$

$$s^E_{pq} = 2\, s^E_{ijkl}, \quad \text{if } i=j \text{ and } k\neq l,\ p=1,2,3,\ q=4,5,6, \tag{2.163}$$

$$s^E_{pq} = 4\, s^E_{ijkl}, \quad \text{if } i\neq j \text{ and } k\neq l,\ p,q=4,5,6, \tag{2.164}$$

must be satisfied, and similar relations hold for s^D_{pq}. Furthermore, the d_{iq} satisfy the relations

$$\begin{aligned}
d_{iq} &= d_{ikl}, && k=l,\ q=1,2,3\\
d_{iq} &= 2\, d_{ikl}, && k\neq l,\ q=4,5,6,
\end{aligned} \tag{2.165}$$

and similar relations hold for g_{iq}. The piezoelectric constants h_{iq} and e_{iq} and the elastic constants c^D_{pq} are simply obtained from their counterparts in tensor notation by replacing the indices according to Table 2.2.

In the acoustic sensor, which will be described in the following chapter, a quartz crystal is employed as sound transducer. Therefore, the theory is further elaborated on for this special case of a piezoelectric material. Piezoelectric devices are manufactured from single crystals of α-quartz, which is the thermodynamically stable phase of quartz below 573 °C. Only in this phase, quartz has piezoelectric properties. The physical properties and manufacturing of quartz crystals were thoroughly

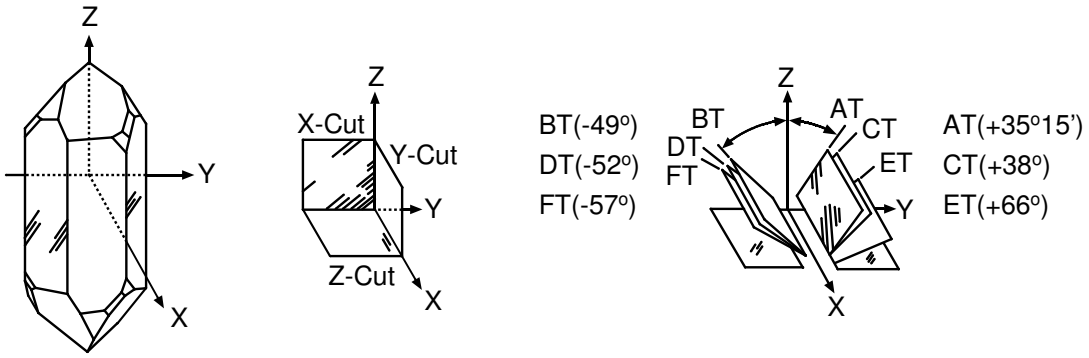

Figure 2.4. Coordinate system for describing a quartz crystal and some principal cuts.

described by Brice [26], and many books on piezoelectricity treat quartz crystals in some detail, see for example [27, 117].

In order to apply the mechanical theory to real materials like quartz, a Cartesian coordinate system with XYZ axes must be defined, in which the mathematical analysis can be carried out. This link is provided by the science of crystallography. In crystallography, properties of crystals are described in terms of the natural coordinate system formed by the edges of the unit cell of the crystal lattice. The axes of this coordinate system are termed the a, b, and c axes, and are defined in a unique way for the basic crystal systems [8]. Quartz belongs to the trigonal crystal system. It has one main axis of threefold symmetry, which is chosen to be the c axis. Moreover, there are three equivalent secondary axes of twofold symmetry, denoted by a_1, a_2, a_3, which lie in a plane perpendicular to the c axis. The Z axis of the Cartesian coordinate system is identified with the c axis of the crystallographic system, and one of the axes of twofold symmetry is taken as the X axis. The Y axis of the Cartesian system is then chosen perpendicular to the X and Z axes so that a right-handed coordinate system results as shown in Fig. 2.4. In tensor notation, the three Cartesian axes X, Y, Z correspond to the indices 1, 2, 3 (or x, y, z), which must be converted to condensed matrix notation by Table 2.2.

Quartz exists in optical right-handed and left-handed forms. In right-handed quartz, the plane of polarization of polarized light passing along the Z axis is rotated clockwise, in left-handed quartz the plane of polarization is rotated counterclockwise. In most technical applications, right-handed quartz crystals are employed. Table 2.3 summarizes the material constants c_{pq}^E, e_{kp}, and ε_{ik}^S for right-handed quartz in the

Table 2.3. Elastic, piezoelectric, and dielectric constants for right-handed quartz [26] (Units: c_{pq}^E in 10^9 Pa, e_{ip} in 10^{-2} C m^{-2}, and ε_{ij}^S in 10^{-12} F m^{-1}).

$$\begin{bmatrix} T_1 \\ T_2 \\ T_3 \\ T_4 \\ T_5 \\ T_6 \\ \hline D_1 \\ D_2 \\ D_3 \end{bmatrix} = \left[\begin{array}{cccccc|ccc} 86.74 & 6.99 & 11.91 & 17.91 & 0.0 & 0.0 & 17.1 & 0.0 & 0.0 \\ 6.99 & 86.74 & 11.91 & -17.91 & 0.0 & 0.0 & -17.1 & 0.0 & 0.0 \\ 11.91 & 11.91 & 107.2 & 0.0 & 0.0 & 0.0 & 0.0 & 0.0 & 0.0 \\ 17.91 & -17.91 & 0.0 & 57.94 & 0.0 & 0.0 & 4.06 & 4.06 & 0.0 \\ 0.0 & 0.0 & 0.0 & 0.0 & 57.94 & 35.82 & 0.0 & 0.0 & 0.0 \\ 0.0 & 0.0 & 0.0 & 0.0 & 35.82 & 39.88 & -34.2 & -34.2 & 0.0 \\ \hline 17.1 & -17.1 & 0.0 & 4.06 & 0.0 & 0.0 & 39.21 & 0.0 & 0.0 \\ 0.0 & 0.0 & 0.0 & 4.06 & 0.0 & -34.2 & 0.0 & 39.21 & 0.0 \\ 0.0 & 0.0 & 0.0 & 0.0 & 0.0 & 0.0 & 0.0 & 0.0 & 41.03 \end{array}\right] \cdot \begin{bmatrix} S_1 \\ S_2 \\ S_3 \\ S_4 \\ S_5 \\ S_6 \\ \hline E_1 \\ E_2 \\ E_3 \end{bmatrix}$$

representation of Eqs. (2.148) and (2.149) in the form

$$\left(\begin{array}{c} \boldsymbol{T} \\ \hline \boldsymbol{D} \end{array}\right) = \left(\begin{array}{c|c} \boldsymbol{c^E} & \boldsymbol{e}^t \\ \hline \boldsymbol{e} & \boldsymbol{\varepsilon^S} \end{array}\right) \cdot \left(\begin{array}{c} \boldsymbol{S} \\ \hline \boldsymbol{E} \end{array}\right). \tag{2.166}$$

Due to the symmetry properties of quartz, many of the 36 elastic constants, 18 piezoelectric constants, and 9 dielectric constants are zero, and only a few of the non-zero constants are unique. There are only 18 non-zero elastic constants, of which six are unique, five non-zero piezoelectric constants, of which two are unique, and three non-zero dielectric constants, of which two are unique.

The ability to operate a quartz crystal as a sound transducer depends on the orientation, in which the crystal is cut from the raw material. Several principal cuts are shown in Fig. 2.4. The most commonly used cut for sound transducers is the X-cut, with the acoustically active surfaces being perpendicular to the X axis. In this cut, vibrational motion in the direction of the X axis can be excited by applying an electric field in this direction. The mechanical, piezoelectric, and dielectric behavior of a quartz crystal in this mode of operation is mainly described by the variables T_{11}, S_{11}, E_1, and D_1 and the constants c_{11}^E, e_{11}, and ε_{11}^S.

2.6.2 Thickness Excitation of a Thin Piezoelectric Plate

The acoustic sensor developed in this work employs an X-cut quartz crystal disk as a sound transducer, which is operated in the thickness expander mode, that is it expands and contracts in the direction of the X axis. In this section, a model for this mode of operation will be developed. Parts of the treatment presented in this section follow closely the one given by Trusler [177, pp. 145].

The geometry for this model is depicted in Fig. 2.5. The thickness of the crystal is assumed to be $2l$ and the area of each major surface is denoted by A. The x_1 axis of

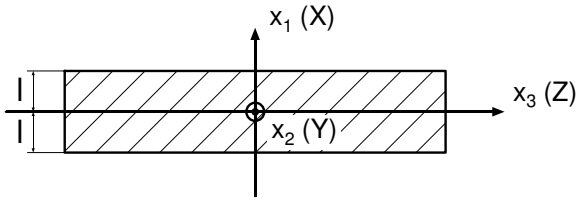

Figure 2.5. Geometry for describing the motion of a thin piezoelectric quartz plate.

the Cartesian coordinate system is perpendicular to the surfaces of the crystal with the origin at the center between the two surfaces, and the center plane of the crystal lies in the x_2x_3 plane of the coordinate system. In thickness expander mode, the compressing and expanding motion of the crystal is in the direction of the x_1 axis. It is assumed that the crystal is so thin that the lateral motion of the crystal can be neglected. This case is equivalent to the situation where the crystal is mounted by lateral clamping, which hinders lateral motion. Then the motion can be described by a one-dimensional model, in which only the elements S_1 and T_1 of the condensed strain and stress matrices are non-zero.

Since both surfaces are coated with the conducting electrode material, they form equipotential surfaces. As piezoelectric materials do not carry free charges, the electrical flux density on the lateral edge of the disk must vanish. The component of the electrical flux density perpendicular to the surfaces of the crystal D_1 is independent of the position of the surface and, according to Gauss law, it is equal to the charge density on the surface, $D_1 = Q/A$, where Q denotes the amount of charges on one surface. Furthermore, it is assumed that all dynamic variables have a harmonic dependence on time. Hence, they contain a factor $\exp(i\omega t)$.

When using the electric current I, a sign convention must be introduced [175, p. 179]. In electric circuit theory, the sign of the current is chosen so that the current has a positive sign if it flows from the plus to the minus pole of the active element of the circuit. For the present situation, which is illustrated in Fig. 2.6, the orientation of the coordinate system is chosen such that the x_1 axis points upwards. In this coordinate system, an active element is placed so that the current flows upwards through it, whereas a passive element is placed so that the current flows downwards through it. A piezoelectric crystal acts as an active element if it is operated as a receiver (see Fig. 2.6a). In this case, the current is defined by $I = dQ/dt$, and the electric flux density becomes $D_1 = I/(i\omega A)$. If a piezoelectric element is operated

as a sender, it acts as a passive element (see Fig. 2.6b). Then the current is defined by $I = -dQ/dt$, and the electric flux density is given by $D_1 = -I/(i\omega A)$.

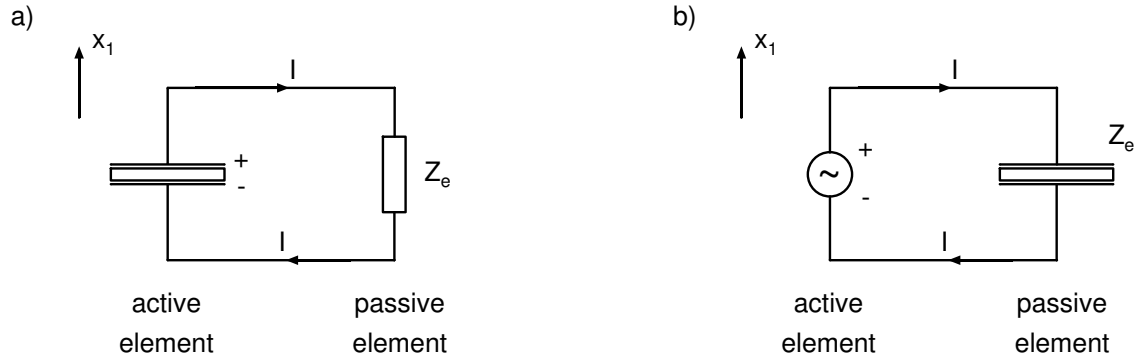

Figure 2.6. Sign convention for the electric current. a) Operation of a piezoelectric crystal as receiver and b) operation as sender.

Since the electric flux density is used to describe the electric field in the crystal, Eqs. (2.160) and (2.161) are the obvious choice to describe the piezoelectric material. For the chosen geometry, they take the form

$$T_1 = c_{11}^D S_1 - h_{11} D_1 \tag{2.167}$$

$$E_1 = -h_{11} S_1 + \beta_{11}^S D_1. \tag{2.168}$$

The numerical values of the constants in these equations for right-handed α-quartz are given by $c_{11}^D = 86.74 \cdot 10^9$ Pa, $h_{11} = 4.36 \cdot 10^9$ N C^{-1}, and $\beta_{11}^S = (\varepsilon^S)^{-1} = 39.97 \cdot 10^{-12}$ F m^{-1} [26].

In order to derive a differential equation for the motion of the crystal, the derivative of the first of these two equation with respect to x_1 is taken, and the strain is replaced by $S_1 = \partial u_1/\partial x_1$, where u_1 denotes the displacement. One obtains

$$\frac{\partial T_1}{\partial x_1} = c_{11}^D \frac{\partial^2 u_1}{\partial x_1^2}, \tag{2.169}$$

where it has been assumed that D_1 is constant within the piezoelectric material. The equation of motion, written in terms of the stress, reads [8]

$$\frac{\partial T_1}{\partial x_1} = \rho_c \frac{\partial^2 u_1}{\partial t^2}, \tag{2.170}$$

in which ρ_c denotes the density of the piezoelectric material. When both equations are combined, the differential equation for the motion of the plate is obtained as

$$\frac{\partial^2 u_1}{\partial x_1^2} - \frac{\rho_c}{c_{11}^D} \frac{\partial^2 u_1}{\partial t^2} = 0. \tag{2.171}$$

Eq. (2.171) represents a hyperbolic differential equation, which describes the propagation of longitudinal elastic waves in the piezoelectric material. The coefficient of the second term is related to the speed at which these waves propagate by $w_\mathrm{c} = (c_{11}^D/\rho_\mathrm{c})^{1/2}$, where the index '$D$' refers to the condition of constant dielectric flux density. As all variables contain the harmonic factor $\exp(i\omega t)$, the second derivative with respect to time can be replaced by $\partial^2/\partial t^2 = -\omega^2$ so that Eq. (2.171) takes the form

$$\frac{\partial^2 u_1}{\partial x_1^2} + w_\mathrm{c}^2\omega^2 u_1 = 0. \tag{2.172}$$

A general solution of this equation is given by

$$u_1(x_1, t) = [A_0 \sin(kx_1) + A_1 \cos(kx_1)] \exp(i\omega t) \tag{2.173}$$

with $k = \omega/w_\mathrm{c}$. The two constants A_0 and A_1 must be determined from appropriate boundary conditions.

Before solving Eq. (2.172) for different boundary conditions, it is useful to establish some further relations. The electromechanical coupling constant for the thickness expander mode, which provides a measure for the magnitude of the piezoelectric effect, is given by

$$K_\mathrm{t}^2 = \frac{h_{11}^2}{\beta_{11}^S c_{11}^D}. \tag{2.174}$$

In general, it is defined as the ratio of the output electrical energy delivered to an electric load and the input mechanical energy for the piezoelectric effect or, for the inverse piezoelectric effect, as the ratio of the output mechanical energy delivered to a mechanical load and the input electrical energy. With the numerical values for h_{11}, β_{11}, and c_{11}^D given above, the electromechanical coupling constant for the thickness expander mode is $K_\mathrm{t} = 0.095$. Compared with piezoelectric ceramics, which may have coupling constants up to $K_\mathrm{t} = 0.5$, the coupling constant for quartz is rather small.

Another important quantity for the describing the mechanical behavior of the plate is the relative displacement of the two surface $\Delta u_1 = u_1(l) - u_1(-l)$. With the general solution of the wave equation, Eq. (2.173), the relative displacement can be expressed as

$$\Delta u_1 = 2A_0 \sin(kl) \exp(i\omega t). \tag{2.175}$$

The electrical boundary condition, which was already introduced above, can be further elaborated on in order to derive an expression for the electric flux density.

Since the operation as a receiver is treated first in the following section, the sign convention for the current depicted in Fig. 2.6a must be applied. The potential difference between the electrodes of the plate is given by

$$V = -\int_{x_1=-l}^{x_1=l} E_1\, dx_1 = h_{11} \int_{x_1=-l}^{x_1=l} \frac{\partial u_1}{\partial x_1}\, dx_1 - 2l\beta_{11}^S D_1, \tag{2.176}$$

where Eq. (2.168) has been inserted for E_1. By substituting the general solution of the wave equation into Eq. (2.176) and using the expression for the relative displacement of the electrodes, the potential can be written as

$$V = \Delta u_1 h_{11} - 2l\beta_{11}^S D_1. \tag{2.177}$$

If the electrical impedance of the external circuit is denoted by Z_e, Ohm's law yields $V = Z_\mathrm{e} I = i\omega A D_1 Z_\mathrm{e}$ for the potential. This relation is substituted into Eq. (2.177), which can then be solved for D_1. One finds the expression

$$D_1 = \frac{h_{11}\Delta u_1}{2l\beta_{11}^S} \frac{1}{1 + i\omega Z_\mathrm{e} C_0} \tag{2.178}$$

for the electric flux density, in which $C_0 = A/2l\beta_{11}^S$ represents the static capacity of the piezoelectric plate.

After these preliminary considerations, the wave equation for the plate can now be solved for different boundary conditions. If the transducer is operated as a receiver, that is if sound waves arrive at one or both surfaces of the transducer, the relevant quantity required to describe its behavior is the mechanical input admittance. Conversely, if it is operated as a sender, that is if it is excited electrically and generates sound waves, the relevant quantity to describe its behavior is the electrical input admittance.

In order to prepare the discussion of the operation as a receiver and sender in the following sections, the mechanical input admittance is calculated for a case in which sound arrives at one surface of the transducer and the other surface is free. This result is then used to obtain the mechanical resonance frequencies of the transducer for operation in vacuum. The mechanical boundary conditions for this case are given by

$$T_1(x = -l) = 0 \tag{2.179}$$

$$T_1(x = l) = -(F/A)\exp(i\omega t). \tag{2.180}$$

F is the total force exerted by the arriving sound on the surface $x_1 = l$, and the ratio F/A represents the acoustic pressure at this surface. The minus sign arises because the stress tensor is the negative pressure tensor. The constitutive equation for the piezoelectric material, Eq. (2.167), can now be used to determine the two constants A_0 and A_1 in the general solution of the wave equation, Eq. (2.173). For this purpose, Eq. (2.173) and the result for the electric flux density, Eq. (2.178), are substituted into Eq. (2.167) for both boundary conditions, which yields a system of two linear equations for the two unknown variables A_0 and A_1. The solution of this system is given by

$$A_0 = \frac{F/(2A\rho_c w_c \omega)}{(K_t^2/kl)\sin(kl)(1+i\omega C_0 Z_e)^{-1} - \cos(kl)} \tag{2.181}$$

$$A_1 = \frac{F/(2A\rho_c w_c \omega)}{\sin(kl)}. \tag{2.182}$$

With these results, the solution of the wave equation is complete, and the mechanical input admittance is obtained as

$$\begin{aligned} Y_m &= \frac{v}{F} = -\frac{i\omega}{F}\left[A_0 \sin(kl) + A_1 \cos(kl)\right] \\ &= \frac{i/(2A\rho_c w_c)}{\cot(kl) - (K_t^2/kl)\,(1+i\omega C_0 Z_e)^{-1}} - \frac{i/(2A\rho_c w_c)}{\tan(kl)}. \end{aligned} \tag{2.183}$$

The first term on the right hand side results from the term $A_0 \sin(kx_1)$ in the solution to the wave equation, while the second term results from $A_1 \cos(kx_1)$.

First, the solution corresponding to the second term is examined more closely. Resonance occurs whenever the imaginary part of the mechanical admittance becomes infinite, that is whenever $\mathrm{Im}(Y_m) \to \infty$. Thus, the second term is resonant whenever $\tan(kl) \to 0$, which is equivalent to $kl = n(\pi/2)$ with even values of n. In this case, the first term vanishes because $\cot(kl) \to \infty$. The term $A_1 \cos(kx_1)$ is symmetric with respect to the coordinate x_1 and therefore does not contribute to the relative displacement of the transducer surfaces. At low frequencies, this term dominates, and the approximation $\tan(kl) \approx kl$ applies so that $Y_m = 1/(i\omega m)$, where $m = 2Al\rho_c$ is the mass of the transducer. Thus, the second term describes pure translations of the transducer back and forth along the x_1-axis, which are not piezoelectrically active, but are controlled by the mass of the transducer. The translational motion of the transducer is coupled to the longitudinal motion of the arriving sound wave at $x_1 = l$.

The first term in Eq. (2.183) determines the relative displacement of the transducer surfaces and therefore is responsible for thickness vibrations of the transducer.

This term is piezoelectrically active and, thus, is coupled to the electric field. From the resonance condition $\mathrm{Im}(Y_\mathrm{m}) \to \infty$, it follows that it is resonant whenever

$$\mathrm{Re}[\cot(kl) - (K_\mathrm{t}^2/kl)\,(1 + i\omega C_0 Z_\mathrm{e})^{-1}] = 0. \tag{2.184}$$

For arbitrary values of the electrical impedance of the external circuit Z_e, the resonance frequencies are determined by the solutions for kl of this equation. For the present purposes, however, it is sufficient to consider the limiting cases of open-circuit and short-circuit conditions. Under open-circuit conditions, that is for $Z_\mathrm{e} \to \infty$, the resonance condition takes the form $\cot(kl) = 0$. With $k = \omega/w_\mathrm{c}$ and $w_\mathrm{c}^2 = c_{11}^D/\rho_\mathrm{c}$, the resonance frequencies are obtained as

$$f_\mathrm{res}^\mathrm{p} = n\,\frac{w_\mathrm{c}}{4l}, \tag{2.185}$$

with $n = 1, 3, 5, \ldots$ being odd. They are called parallel resonance frequencies.

Under short-circuit conditions, that is for $Z_\mathrm{e} = 0$, Eq. (2.184) simplifies to

$$\cot(kl) = \frac{K_\mathrm{t}^2}{kl}. \tag{2.186}$$

Mason [117, p. 66] showed that for small values of K_t^2, which is satisfied for quartz with $K_\mathrm{t}^2 \approx 0.009$, this equation has the approximate solutions

$$kl = n\,\frac{\pi}{2} - \frac{K_\mathrm{t}^2}{n(\pi/2)}. \tag{2.187}$$

The resonance frequencies are given by

$$f_\mathrm{res}^\mathrm{s} = n\,\frac{w_\mathrm{c}}{4l}\left[1 - \left(\frac{2K_\mathrm{t}}{n\pi}\right)^2\right], \quad \text{with } n = 1, 2, 3, \ldots, \tag{2.188}$$

and are called series resonance frequencies. The series resonance frequencies are by $nw_\mathrm{c}(2K_\mathrm{t}/n\pi)^2/4l$ smaller than the parallel resonance frequencies.

Eq. (2.185) can be used to estimate the thickness of a piezoelectric transducer for a given resonance frequency. For an X cut quartz crystal with a resonance frequency of 10 MHz, one obtains 0.286 mm, where the value $w_\mathrm{c} = 5730\ \mathrm{m\,s^{-1}}$ for the speed of sound in quartz has been used [177].

2.6.3 Operation as a Receiver

So far the mechanical load of the fluid on the transducer has been ignored. In practise, not only the front face of the transducer, but also the back face is in

contact either with a fluid or solid medium. The mechanical load presented by the medium at the back face can be taken into account by the boundary condition

$$T_1(x_1 = -l) = Z_\mathrm{a}^\mathrm{b} \frac{\partial u_1}{\partial t}, \tag{2.189}$$

where Z_a^b represents the acoustic impedance of the medium at the back of the transducer. This boundary condition replaces Eq. (2.179). Generally, the presence of a mechanical load results in finite values of the mechanical admittance at resonance, and the resonance frequencies are changed by a small amount.

The wave equation, Eq. (2.171), must now be solved for the new boundary conditions, Eq. (2.189) and Eq. (2.180). The solution is again assumed to be of the form of Eq. (2.173), and the procedure to determine the constants A_0 and A_1 is the same as before. Although an exact treatment is possible, the solution is simplified if the approximation $|(Z_\mathrm{a}^\mathrm{b}/\rho_\mathrm{c} w_\mathrm{c}) \cot(kl)| \approx 0$ is introduced. This approximation holds at any frequency, if the backing impedance Z_a^b is small compared with the acoustic impedance of the piezoelectric material $\rho_\mathrm{c} w_\mathrm{c}$. Near the mechanical resonances, it is always satisfied because in that case $\cot(kl) \approx 0$. Since the transducer in the acoustic sensor is operated near its resonance frequency, the approximation is fully justified. Within this approximation, one obtains

$$A_0 \sin(kl) = \frac{-F/(2A\omega\rho_\mathrm{c} w_\mathrm{c})}{\cot(kl) - (K_\mathrm{t}^2/kl)(1 + i\omega C_0 Z_\mathrm{e})^{-1} + i(Z_\mathrm{a}^\mathrm{b}/2\rho_\mathrm{c} w_\mathrm{c})}. \tag{2.190}$$

The symmetric term in Eq. (2.173) with the constant A_1 can entirely be neglected because it does not contribute to the relative displacement of the transducer surfaces. The mechanical admittance for these boundary conditions is then given by

$$\begin{aligned} Y_\mathrm{m} &= \frac{v}{F} = -\frac{i\omega A_0 \sin(kl)}{F} \\ &= \frac{i/(2A\rho_\mathrm{c} w_\mathrm{c})}{\cot(kl) - (K_\mathrm{t}^2/kl)(1 + i\omega C_0 Z_\mathrm{e})^{-1} + i(Z_\mathrm{a}^\mathrm{b}/2\rho_\mathrm{c} w_\mathrm{c})}. \end{aligned} \tag{2.191}$$

Under open-circuit conditions, the first two terms in the denominator cancel at the mechanical resonance frequencies. Thus, the mechanical admittance at resonance is simply $Y_\mathrm{m} = 1/(AZ_\mathrm{a}^\mathrm{b})$. This result is useful for calculating the reflection coefficient χ_Re for plane waves normally incident at the front face of the transducer, which is given by Eq. (2.97), from the knowledge of the acoustic backing impedance. For an ideal lossless piezoelectric plate as in this model, the reflection coefficient would vanish at resonance if the plate were in contact with the same medium at the front and back.

An important quantity to characterize the transducer in receiving mode is its sensitivity, which is defined as the ratio of the generated voltage in the transducer and the acoustic pressure of the arriving sound wave at the front face of the transducer. The current flowing through the transducer is given by $I = i\omega A D_1$, and the electrical flux density D_1 is related to the relative displacement of the transducer by Eq. (2.178). Both relations can be combined to yield the current through the transducer

$$I = \frac{i\omega C_0 h_{11} \Delta u_1}{1 + i\omega C_0 Z_\mathrm{e}} \exp(i\omega t), \tag{2.192}$$

and the output voltage is given by

$$V = Z_\mathrm{e} I = \frac{i\omega C_0 h_{11} \Delta u_1 Z_\mathrm{e}}{1 + i\omega C_0 Z_\mathrm{e}} \exp(i\omega t). \tag{2.193}$$

Under short-circuit conditions ($Z_\mathrm{e} \to 0$), the current becomes

$$I = i\omega C_0 h_{11} \Delta u_1 \exp(i\omega t), \tag{2.194}$$

and the output voltage under open-circuit conditions ($Z_\mathrm{e} \to \infty$) is given by

$$V = h_{11} \Delta u_1 \exp(i\omega t). \tag{2.195}$$

For the acoustic pressure $p_\mathrm{a} = F/A$, the relative displacement of the transducer surfaces $\Delta u_1 = 2A_0 \sin(kl) \exp(i\omega t)$ is determined by Eq. (2.190). Thus, the sensitivity under open-circuit conditions at resonance is

$$V/p_\mathrm{a} = \frac{2ih_{11}}{\omega Z_\mathrm{a}^\mathrm{b}}. \tag{2.196}$$

High sensitivity is achieved if the backing impedance Z_a^b is small. However, if the transducer is in contact with the sample fluid at both faces, the backing impedance is determined by the sample fluid and cannot be used to tune the sensitivity. In general, the sensitivity of the transducer is larger for a compressed gas with a moderate density and low speed of sound than for a high density liquid with a large speed of sound. For example, for a quartz transducer with a resonance frequency of 10 MHz operating in liquid water at 300 K and 0.1 MPa $|V/p_\mathrm{a}| \approx 93\ \mu\mathrm{V\,Pa^{-1}}$, whereas in compressed gaseous argon at 300 K and 10 MPa $|V/p_\mathrm{a}| \approx 2.5\ \mathrm{mV\,Pa^{-1}}$.

2.6.4 Operation as a Sender

When the transducer is operated as a sender, a harmonic potential is applied across the two surfaces of the crystal so that it vibrates in the thickness expander mode

at the frequency of the electric field and radiates sound into the media at its front and at its back face. In this case, the electrical input impedance Z_e (or admittance Y_e) is the relevant quantity to characterize the behavior of the transducer. It can be calculated in the same way as the mechanical input impedance for operation of the transducer in the receiving mode. Again, the wave equation for the plate, Eq. (2.171), has to be solved subject to appropriate boundary conditions.

Now the medium in front of the transducer has the acoustical impedance Z_a^f, and the acoustical impedance of the medium at the back of the transducer is Z_a^b. The boundary conditions for the normal stress read

$$T_1(x_1 = -l) = Z_\mathrm{a}^\mathrm{b} \frac{\partial u_1}{\partial t} \tag{2.197}$$

$$T_1(x_1 = l) = -Z_\mathrm{a}^\mathrm{f} \frac{\partial u_1}{\partial t}. \tag{2.198}$$

As in the preceding sections, the solution of the wave equation takes the form of Eq. (2.173), and the constants A_0 and A_1 must be determined for these boundary conditions. The solution for A_0 is found to be

$$\begin{aligned} A_0 \sin(kl) &= \frac{h_{11} D_1 / \rho_\mathrm{c} w_\mathrm{c} \omega}{\cot(kl) + \dfrac{iZ_\mathrm{a}^\mathrm{f}}{\rho_\mathrm{c} w_\mathrm{c}} + \dfrac{i(Z_\mathrm{a}^\mathrm{f} - Z_\mathrm{a}^\mathrm{b})[i(Z_\mathrm{a}^\mathrm{f}/\rho_\mathrm{c} w_\mathrm{c}) \cot(kl) - 1]}{2\rho_\mathrm{c} w_\mathrm{c} + i(Z_\mathrm{a}^\mathrm{f} + Z_\mathrm{a}^\mathrm{b}) \cot(kl)}} \\ &\approx \frac{h_{11} D_1 / \rho_\mathrm{c} w_\mathrm{c} \omega}{\cot(kl) + i(Z_\mathrm{a}^\mathrm{f} + Z_\mathrm{a}^\mathrm{b})/2\rho_\mathrm{c} w_\mathrm{c}}. \end{aligned} \tag{2.199}$$

Again, the first term in the solution of the wave equation, Eq. (2.173), with the coefficient A_0 describes the thickness vibrations of the transducer, while the second term with the coefficient A_1 describes purely symmetric translational motions, which are important only at low frequencies and contribute little otherwise. Therefore, this term is negligible close to the resonances of the transducer, and A_1 need not be known for the purposes of this section. As before, the approximations $Z_\mathrm{a}^\mathrm{b}/(w_\mathrm{c}\rho_\mathrm{c}) \cot(kl) \approx 0$ and $Z_\mathrm{a}^\mathrm{f}/(w_\mathrm{c}\rho_\mathrm{c}) \cot(kl) \approx 0$ have been introduced in the second line of Eq. (2.199). The approximate expression for $A_0 \sin(kl)$ becomes exact if $Z_\mathrm{a}^\mathrm{f} = Z_\mathrm{a}^\mathrm{b}$.

The electrical input impedance can now be found by inserting the relative displacement $\Delta u_1 = 2A_0 \sin(kl)$ with $A_0 \sin(kl)$ as given by Eq. (2.199) and the electrical flux density $D_1 = -I/(i\omega A)$ into the expression for the voltage across the crystal, Eq. (2.177). The minus sign of the electric flux density is due to the sign convention for sending mode (see Sec. 2.6.2 and Fig. 2.6). The result is inserted into Ohm's law $Z_\mathrm{e} = V/I$, and one obtains for the electric input impedance

$$Z_\mathrm{e} = \frac{1}{i\omega C_0} \left(1 - \frac{K_\mathrm{t}^2 / kl}{\cot(kl) + i(Z_\mathrm{a}^\mathrm{f} + Z_\mathrm{a}^\mathrm{b})/2\rho_\mathrm{c} w_\mathrm{c}} \right). \tag{2.200}$$

The electric input admittance is given by $Y_\mathrm{e} = 1/Z_\mathrm{e}$ so that

$$Y_\mathrm{e} = i\omega C_0 \left(1 + \frac{K_\mathrm{t}^2/kl}{\cot(kl) - K_\mathrm{t}^2/kl + i(Z_\mathrm{a}^\mathrm{f} + Z_\mathrm{a}^\mathrm{b})/2\rho_\mathrm{c} w_\mathrm{c}}\right). \tag{2.201}$$

The moduli of both quantities are depicted in Fig. 2.7 as a function of frequency for a 10 MHz quartz transducer of diameter 15 mm operating in unbounded gaseous

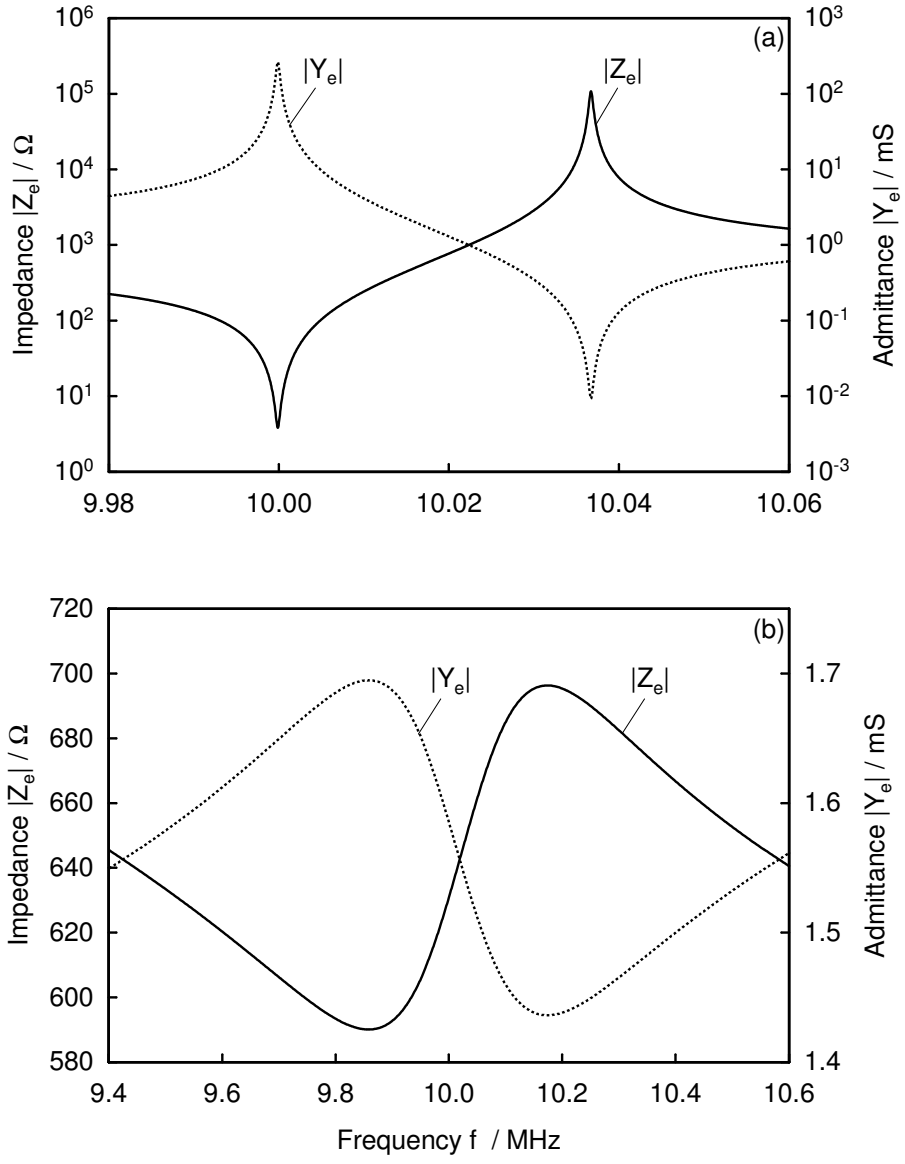

Figure 2.7. Theoretical electrical input impedance and admittance of a 10 MHz X-cut quartz transducer of diameter 15 mm operating in (a) unbounded gaseous argon at 300 K and 0.1 MPa and (b) unbounded liquid propane at 300 K and 10 MPa.

argon at 300 K and 0.1 MPa and unbounded liquid propane at 300 K and 10 MPa. In these examples, the acoustic load impedances are purely resistive and equal to the acoustic impedance of the fluid $Z_\mathrm{a} = \rho w$. When operating in gaseous argon, $|Z_\mathrm{e}|$ has a minimum close to the series resonance and a maximum close to the parallel resonance, whereas $|Y_\mathrm{e}|$ has a maximum close to the mechanical series resonance and a minimum close to the mechanical parallel resonance. Furthermore, the static capacity contributes little to the impedance and admittance in the vicinity of the resonances. With increasing acoustic impedance of the fluid, which shown here for a state in the liquid region of propane, the maxima and minima of $|Z_\mathrm{e}|$ and $|Y_\mathrm{e}|$ are shifted further away from the mechanical resonance frequencies in vacuum and the frequency range, in which the maxima and minima occur, becomes broader. Moreover, the impedance and admittance are by several orders of magnitude smaller than for the operation in a low density gas, and the static capacity yields a large contribution to the impedance and admittance in the vicinity of the resonances.

Since one is usually interested in high signal levels, the transducer should be operated at that frequency, for which the power output $P = Z_\mathrm{e} I^2 = Y_\mathrm{e} V^2$ is maximum. It is interesting to consider first the excitation by an ideal current source (zero source impedance) and ideal voltage source (infinite source impedance). In the first case, the power output is maximum when Z_e takes its largest value, that is close to the parallel resonance frequency, and, in the second case, the power output is maximum when Y_e takes its largest value, that is close to the series resonance frequency. In practice, real sources have non-zero finite impedances, and the frequency of maximum power output is between the frequencies of the maxima of Z_e and Y_e.

When the transducer is excited with a constant current source at the unloaded parallel resonance frequency, the impedance given by Eq. (2.200) is used to characterize its behavior. At the parallel resonance, the impedance becomes

$$Z_\mathrm{e} = \frac{1}{i\omega_\mathrm{res}^\mathrm{p} C_0} + \left(\frac{2h_{11}}{\omega_\mathrm{res}^\mathrm{p}}\right)^2 Y_\mathrm{m}, \tag{2.202}$$

where $Y_\mathrm{m} = (Z_\mathrm{a}^\mathrm{f} + Z_\mathrm{a}^\mathrm{b})/A$ is the mechanical admittance of the transducer. The impedance at resonance consists of a contribution due to the capacity of the transducer and a contribution due to the mechanical admittance, which represents the acoustic load impedances at the front and back faces of the transducer. The capacitance can be compensated by an inductance placed in series with the transducer. Then, the impedance is purely resistive and is simply determined by the mechanical admittance $Z_\mathrm{e} = (2h_{11}/\omega_\mathrm{res}^\mathrm{p})^2 Y_\mathrm{m}$.

Conversely, if the transducer is excited with a constant voltage source at the vacuum series resonance frequency, the admittance given by Eq. (2.201) is used to characterize its behavior. The admittance at the series resonance frequency is

$$Y_\mathrm{e} = i\omega^\mathrm{s}_\mathrm{res} C_0 + \alpha_\mathrm{t}^2 Y_\mathrm{m}, \tag{2.203}$$

where the transformation factor α_t is given by

$$\alpha_\mathrm{t} = A h_{11}/l\beta^S_{11}. \tag{2.204}$$

The expressions for α_t is obtained by combining Eqs. (2.201) and (2.191) with $\omega = \omega^\mathrm{s}_\mathrm{res}$ and using the expressions $C_0 = A/2l\beta^S_{11}$, $K^2_\mathrm{t} = h^2_{11}/(\beta^S_{11}c^D_{11})$, $w^2_\mathrm{c} = c^D_{11}/\rho_\mathrm{c}$ and Eqs. (2.187) and (2.188).

The capacitance can be compensated by an inductance placed in parallel with the transducer. The admittance is then purely resistive and determined solely by the mechanical admittance $Y_\mathrm{e} = \alpha_\mathrm{t}^2 Y_\mathrm{m}$.

2.6.5 Equivalent Circuit Model

Near a piezoelectric resonance, the electric properties of the transducer in sending mode can be represented by the equivalent circuit model depicted in Fig. 2.8. The capacitance C_0 represents the static capacitance of the transducer, and the resistance R_1, the inductance L_1, and the capacitance C_1 describe the mechanical properties of the unloaded transducer in vacuum. If dielectric losses are significant, they can be accounted for by an additional resistance R_0 in parallel with the capacitance C_0. A mechanical load on the transducer can be incorporated in the circuit by a complex impedance Z^L_e in series with the elements R_1, L_1, and C_1 in the series branch. If the transducer is surrounded by a fluid, the mechanical load on the transducer is equal to $A(Z^\mathrm{f}_\mathrm{a} + Z^\mathrm{b}_\mathrm{a})/\alpha^2_\mathrm{t}$, where the transformation factor α_t is given by Eq. (2.204). In the following, it is assumed that dielectric losses are negligible and that the transducer is operated in vacuum without mechanical loading.

By the rules of network theory, the electric admittance of the equivalent circuit can be found as

$$Y_\mathrm{e} = i\omega C_0 + \frac{R_1 - i\left(\omega L_1 - \dfrac{1}{\omega C_1}\right)}{R_1^2 + \left(\omega L_1 - \dfrac{1}{\omega C_1}\right)^2}. \tag{2.205}$$

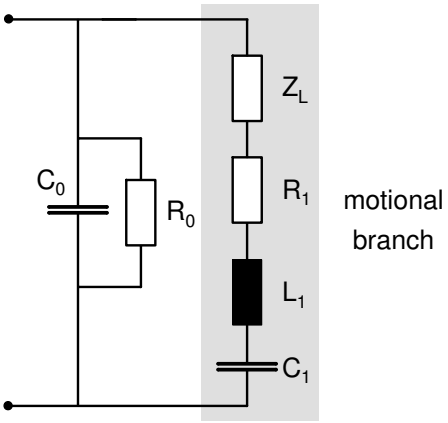

Figure 2.8. Equivalent circuit model of a thickness expander mode piezoelectric transducer near resonances.

If the admittance is split up into real and imaginary parts, the equations for the conductance and susceptance are obtained as

$$G_{\mathrm{e}} = \frac{R_1}{R_1^2 + [\omega L_1 - 1/(\omega C_1)]^2} \tag{2.206}$$

and

$$B_{\mathrm{e}} = \omega C_0 - \frac{\omega L_1 - 1/(\omega C_1)}{R_1^2 + [\omega L_1 - 1/(\omega C_1)]^2}. \tag{2.207}$$

One way of describing the behavior of electric circuits is to plot the real and imaginary parts of the admittance in the complex GB plane. By eliminating the term $\omega L_1 - 1/(\omega C_1)$ from Eqs. (2.206) and (2.207), the equation of the resonance curve in the GB plane is found to be

$$\left(G - \frac{1}{2R_1}\right)^2 + (B - \omega C_0)^2 = \left(\frac{1}{2R_1}\right)^2. \tag{2.208}$$

This equation represents a circle with the radius $1/2R_1$ and the center at $(1/2R_1, \omega C_0)$, which is depicted in Fig. 2.9. The circle is completely formed by the circuit elements of the series branch R_1, L_1, and C_1 and represents the vibration of the crystal. The term ωC_0 results in a shift of the circle along the B axis and does not affect the shape of the circle. The circle can be interpreted as a parameterized curve with ω or f as a parameter. The direction of the parametrization is clockwise.

The series resonance frequency is the frequency at which the imaginary part of the admittance of the series branch vanishes, and the parallel resonance frequency

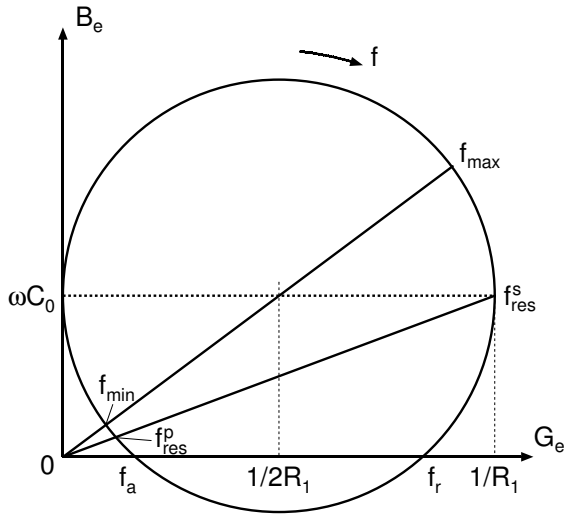

Figure 2.9. Parameterized resonance curve in the complex GB plane.

is the frequency at which the admittance of the circuit, which is formed solely by the elements C_0, C_1, and L_1 without R_1, vanishes. In terms of the circuit elements, the series resonance frequency is given by

$$f_{\mathrm{res}}^{\mathrm{s}} = \frac{1}{2\pi} \frac{1}{\sqrt{L_1 C_1}}. \tag{2.209}$$

and the parallel resonance frequency is given by

$$f_{\mathrm{res}}^{\mathrm{p}} = \frac{1}{2\pi} \sqrt{\frac{C_0 + C_1}{C_0 L_1 C_1}}. \tag{2.210}$$

In the circle diagram, the series resonance occurs at the maximum of the conductance, and the point belonging to the parallel resonance is found as the intersection of a straight line from the origin to the point of maximum conductance with the circle.

Besides the series and parallel resonance frequencies, there are further characteristic frequencies, as can be seen from the diagram. The series resonance frequency is slightly larger than the frequency $f_{\max}$, which belongs to the maximum of Y_{e}, and the parallel frequency is slightly smaller than the frequency $f_{\min}$, which belongs to the minimum of Y_{e}. The resonance frequency f_{r} and anti-resonance frequency f_{a} occur at the cuts of the circle with the G axis. These characteristic frequencies cannot be excited and, therefore, bear no significance for the present work.

Two other useful quantities to describe the electrical behavior of piezoelectric transducers are the quality factor Q and the bandwidth Δf. The quality factor is

defined as the ratio of the inductive or capacitive reactance and the resistance at the series resonance of the series branch of the circuit and is given by

$$Q = \frac{\omega_{\mathrm{res}}^{\mathrm{s}} L_1}{R_1} = \frac{1}{\omega_{\mathrm{res}}^{\mathrm{s}} C_1 R_1}. \tag{2.211}$$

The bandwidth is defined as the difference between the frequencies at which the susceptance has a minimum and a maximum or, equivalently, at which the conductance takes half the value of the maximum value. From these conditions, the bandwidth can be determined in terms of the circuit parameters as

$$\Delta f = \frac{R_1}{2\pi L_1}. \tag{2.212}$$

With this result for the bandwidth, the quality factor can be represented by

$$Q = \frac{f_{\mathrm{res}}^{\mathrm{s}}}{\Delta f}. \tag{2.213}$$

It is the ratio of the series resonance frequency and the bandwidth. The bandwidth can be interpreted as a measure for the losses of the transducer. Large quality factors are usually desired, which describe transducers with small losses.

3 The Speed of Sound Apparatus

This chapter describes the speed-of-sound apparatus developed during the course of this work in detail. Central element of the apparatus is the acoustic sensor, which materializes the pulse-echo measurement technique. The following section introduces the measurement principle, and Sec. 3.2 describes the practical realization of the acoustic sensor. The acoustic sensor resides in a pressure vessel, which is thermostatted in a circulating liquid bath thermostat. The pressure vessel and thermostat are described in Sec. 3.3, and Secs. 3.4 and 3.5 treat the temperature and pressure measurement system, respectively. Sec. 3.6 presents the electronic devices and circuitry for signal generation and detection.

3.1 Measurement Principle

The acoustic sensor employs a pulse-echo technique because this is the preferred method to measure the speed of sound in liquids. Basic principle of this technique is the measurement of the time of flight of a short sound signal over a precisely known distance in the sample liquid. If the sound signal propagates as a plane wave, the speed of sound is simply determined as the distance divided by the time the signal needs to travel the distance.

In this work, a double path length type sensor was chosen, which was first developed by Muringer et al. [135] at the van der Waals Laboratory in Amsterdam in the 1980s. This sensor was used to measure the speed of sound in n-heptane. At the same time, a similar sensor was described by Kortbeek et al. [93], also at the van der Waals Laboratory, and applied to measure the speed of sound in compressed argon [93], helium [94], nitrogen [95], and methane [96] under pressures up to 1000 MPa. More recently, similar instruments were developed by Ball and Trusler [12], Benedetto et al. [20], and Pires and co-workers [146, 147, 148].

The measurement principle of the acoustic sensor is illustrated in Fig. 3.1. A piezoelectric quartz crystal of diameter 15 mm with a resonance frequency of 8 MHz is mounted between two reflectors at distances of about $L_1 = 20\,\mathrm{mm}$ and $L_2 = 30\,\mathrm{mm}$ to the reflectors. The crystal is excited with a sinusoidal burst signal consisting of 60 to 100 cycles at its resonance frequency and radiates sound signals in both directions into the sample liquid. At the reflector faces, they are partly reflected

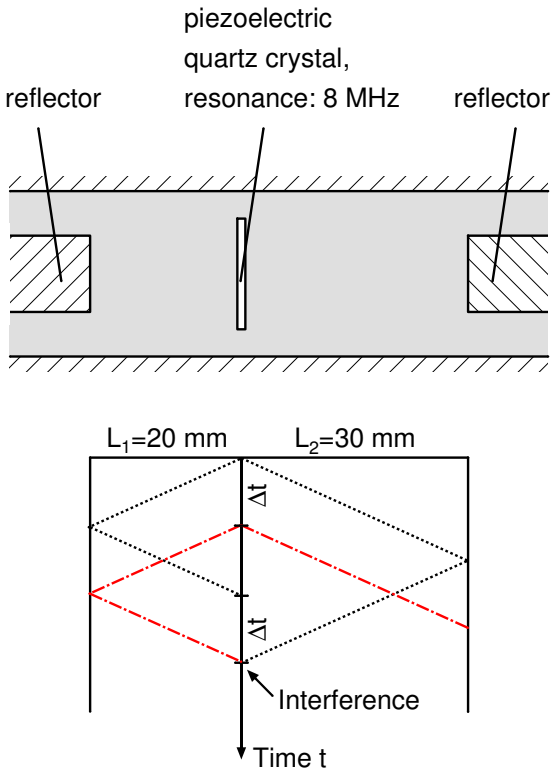

Figure 3.1. Measurement principle of the acoustic sensor.

and partly transmitted into the reflector material. The reflected signals travel back to the crystal, which now acts as a receiver. Due to the different distances, the echoes from the two reflectors arrive successively at the crystal, separated by a time difference Δt (dotted line in Fig. 3.1). With the assumption that the sound signals propagate as ideal plane waves, the speed of sound is determined by

$$w = \frac{2(L_2 - L_1)}{\Delta t}. \tag{3.1}$$

The chosen values for L_1 and L_2 ensure that the first and second received echoes are clearly separated up to speeds of sound of 2000 m s, which is sufficient for most liquids and compressed gases.

Having the sender and receiver as one and the same object between two reflectors has significant advantages over other possibilities. First, the signals radiated by the piezoelectric crystal in both directions in the sample liquid are exploited by the measurement principle. Second, as the way the signal takes through the circuitry and the mechanical branch of the sensor is the same for both signals except for the

difference of the distances between the reflectors and the crystal, the distortion of the signals and delay times in electronic devices and cables are equal for both signals and therefore exactly cancel in the measurement of the time difference Δt. This cancellation simplifies the measurement analysis to a great extend. Moreover, the crystal is in contact with the sample liquid at both major faces so that the acoustic impedance of the medium at the front and back is the same. This situation is favorable when the crystal is operated as a receiver because with the same medium in the front and back the reflection coefficient of the crystal takes the smallest possible value under resonance conditions (see Sec. 2.6.3). In practise, the propagation of the sound signals in the sample liquid deviates slightly from ideal plane wave propagation due to diffraction effects. Therefore, a small correction has to be applied to the measured time difference, which will be described in Sec. 4.2.

For the measurement of the time difference, the original method suggested by Kortbeek et al. [93] is modified. At a time Δt after the first burst signal, the piezoelectric crystal is excited by a second burst signal (dashed-dotted line in Fig. 3.1). The second signal has the same shape as the first signal, but the sign is reversed and the amplitude is reduced to account for sound attenuation. The time interval Δt and the amplitude of the second burst are adjusted so that the first echo from the second signal exactly cancels the second echo from the first signal. This cancellation can very accurately be monitored on an oscilloscope screen. If complete cancellation is achieved, the time difference between the two emitted signals equals the time difference between the arrival of the first and second echoes of the first signal at the crystal.

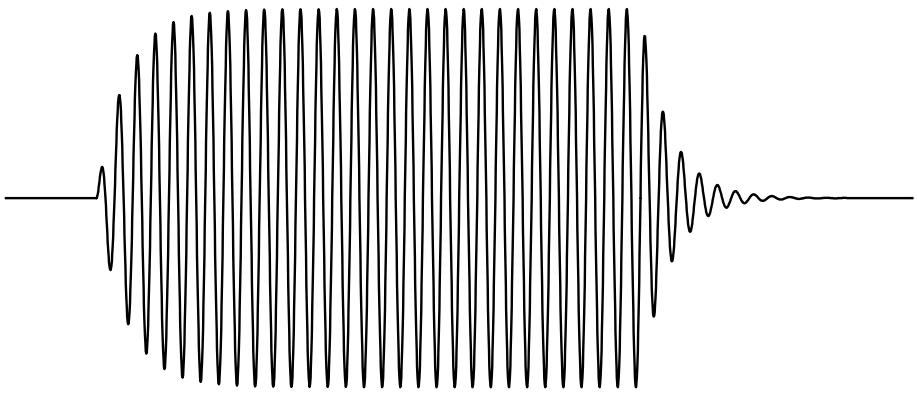

Figure 3.2. Shape of a typical received echo signal for a measurement in a water-like liquid.

Fig. 3.2 depicts an example of a typical received echo signal for a measurement in a water-like liquid. In this example, the transducer was excited by 30 sinus cycles. The signal consists of three different regions: A short transient region at the start, where the vibration amplitude increases until the maximum amplitude is reached, a long intermediate region, where the signal amplitude has reached its maximum value and is nearly constant, and a transient region at the end, where the amplitude decays to zero. The cancellation of the echoes is observed in the intermediate region, where the maximum amplitude is reached. In compressed gases, the transient regions at the start and end of the signals become longer due to the lower mechanical load.

3.2 Acoustic Sensor

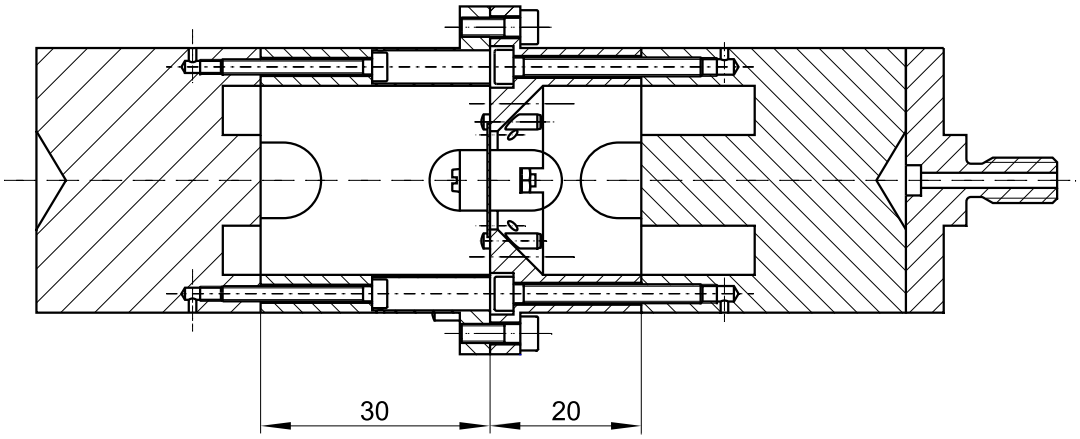

Figure 3.3. Cut through the acoustic sensor.

The acoustic sensor consists of four main parts as shown in a cut through the sensor in Fig. 3.3. All parts of the sensor are made of the highly corrosion resistant stainless steel 1.4571. The partition of the sensor is chosen in the reflector planes and in the center of the sensor in the plane where the crystal is mounted so that these surfaces are easy to access during manufacturing. In order to achieve optimal parallelism between the reflector planes and the crystal, the end planes of the four parts were finely finished on a lathe. After that they were subject to a heat treatment to remove self stresses in the material and to recrystallize the steel structure (one hour at 1050 °C in vacuum). In the last manufacturing step, all planes were lapped to a mirror-like finish. The parts of the sensor are held together by stainless steel screws (material: 1.4301). Blind holes are connected to the surrounding sample

liquid by small holes so that the blind volumes can easily be evacuated. Both end faces of the sensor are equipped with conical reflecting surfaces. The opening angle of the cones was optimized so that signals transmitted into the reflector are damped in the reflector material by multiple reflections at the side walls of the reflector. With this feature, disturbing signals from reflections at the rear faces of the reflectors could be reduced to a negligible level.

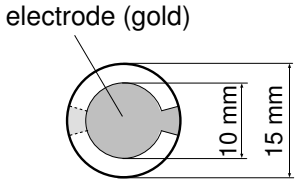

Figure 3.4. Geometry of the piezoelectric crystal electrodes.

The piezoelectric crystal has a diameter of 15 mm and is about 0.358 mm thick. Both faces are partially coated by gold electrodes, whose shape is depicted in Fig. 3.4. The main area of the electrodes has a diameter of 10 mm, and small contact areas are lead to the outer edges of the crystal with an offset angle of about 180 degrees on both sides. With this geometry, only the inner area of the crystal with 10 mm diameter is acoustically active. The reasons for the dimensioning will be discussed in Sec. 4.2, where diffractions effects in the sound field of the sensor will be examined. Electrical connections to the electrodes are made by small forks, which are clamped on the crystal in the regions of the contact areas. The crystal is held on the center plane of the sensor by four small stainless steel tabs in the outer electrode-free region. One electrode is connected to ground potential via the stainless steel parts of the acoustic sensor. The second electrode is lead to the exterior of the pressure vessel by a high pressure electrical feed through (see Sec. 3.3). The connection to the feed through is provided by a nickel wire, whose ends are welded to the contact fork and to the stainless steel wire of the electrical feed through.

Figs. 3.5 and 3.6 show photos of the sensor. In Figures 3.5a and 3.5b, both sides of the sensor with the high-potential and grounded electrodes are shown. Fig. 3.6 additionally shows the sensor as mounted at the closure of the pressure vessel and the nickel wire used to lead the signal to the exterior of the pressure vessel. The sensor is mounted at the closure of the vessel for easy access when opening the vessel. The required sample volume amounts to about 0.25 liters, which includes the inner volume of all high-pressure parts of the system.

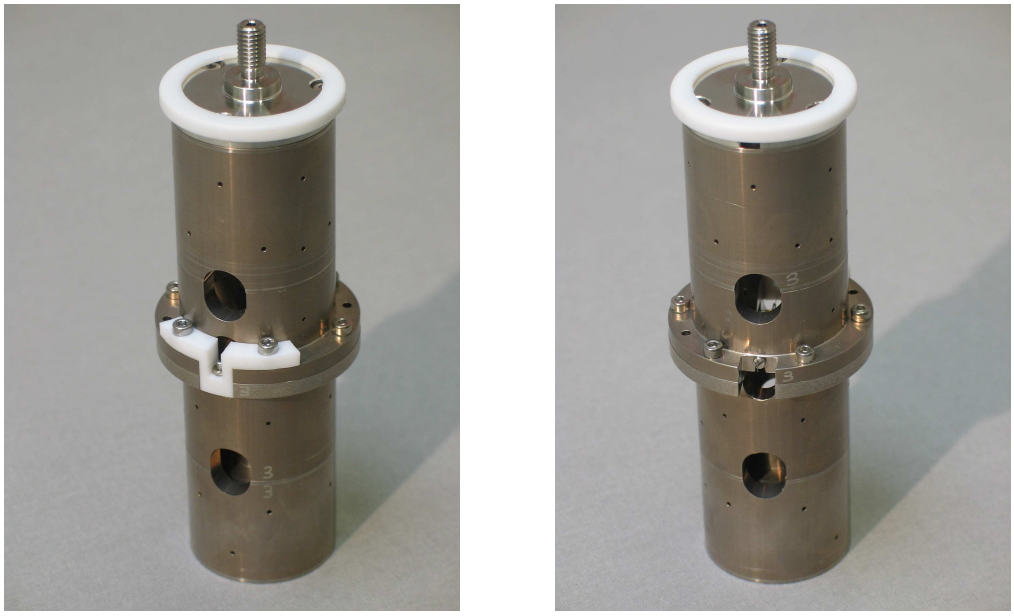

Figure 3.5. Photo of the acoustic sensor. a) high-potential electrode visible, b) grounded electrode visible.

Figure 3.6. Photo of the acoustic sensor mounted at the closure of the pressure vessel with electrical connections.

3.3 Thermostat and Pressure Vessel

The thermostat of the speed of sound apparatus is depicted in Fig. 3.7. The acoustic sensor resides in the pressure vessel, which is filled with the sample liquid. The pressure vessel is mounted in the center of a circulating liquid bath thermostat. An inclined blade stirrer mounted above the pressure vessel provides an downwards

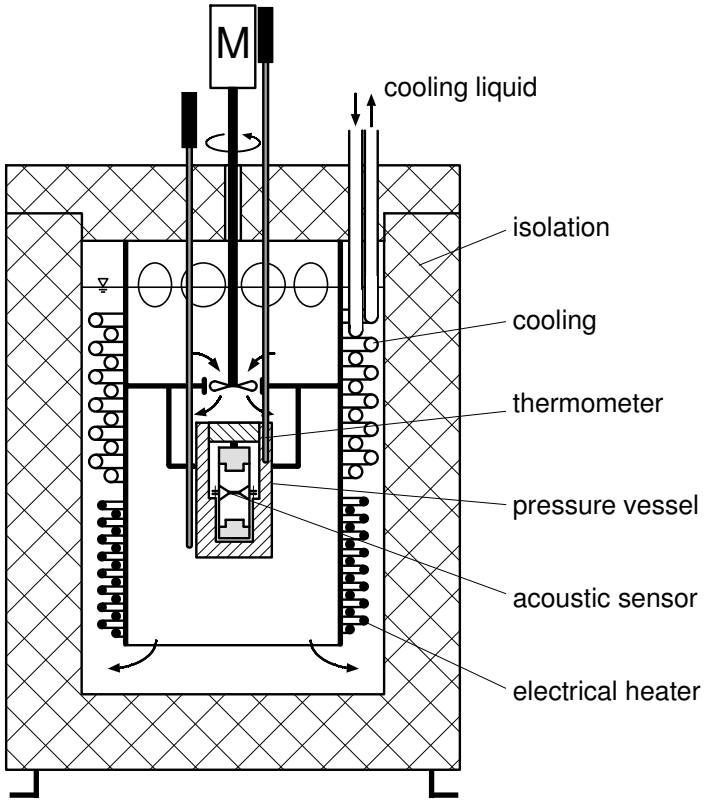

Figure 3.7. The circulating liquid bath thermostat.

directed flow in the center of the thermostat and a upwards directed flow in the outer ring volume, which is formed by a cylindrical baffle plate and the cylindrical surface of the thermostat container. The pressure vessel is placed below the stirrer, where the thermostatting fluid[1)] is optimally mixed to ensure homogeneity of the temperature field in the vessel. In order to avoid splashing of the thermostatting liquid and formation of a rotation paraboloid, a circular plate is mounted above the stirrer, and radial baffle plates ensure that the flow is directed radially towards the outer ring volume in the upper part of the thermostat.

In the upper part of the ring volume, the thermostatting liquid passes along heat exchanger pipes, which form part of the secondary circuit of a liquid bath cryostat (Lauda, type KRYOMAT RUK 90) filled with ethanol. In the lower part, the fluid flows along electrical heaters, which are used for temperature control above ambient temperature and for fine tuning the temperature below ambient temperature. The

[1)] Silicone oil, Lauda, type Thermo 180 (above ambient temperature) and Kryo 85 (below ambient temperature).

electrical heater is operated by a PID controller (Julabo, type LC 6). The controller thermometer measures the temperature in the thermostatting liquid in the region below the stirrer, where the liquid is optimally mixed. The apparatus is operated in an air-conditioned laboratory room, in which the temperature is kept constant within 1 K over a day. During the course of the measurements, it was found that the temperature set by the PID controller drifted by up to 15 mK over a day. In order to avoid this drift, the controller was placed in an air-conditioned isolated wooden box, in which the temperature was kept constant at 25 °C within 0.1 K. With this control mechanism, the temperature inside the pressure vessel was kept constant within 0.5 mK over a few hours, which ensures that the temperature is constant in the pressure vessel for at least the time it takes to measure the speed of sound at one state point. The temperature is measured by a Pt25 sensor (Chino, type R800-2) in the upper part of the wall of the pressure vessel (see Fig. 3.7). Furthermore, a second Pt25 sensor (Tinsley, type 5187SA) and several industry-type Pt100 sensors are used to measure the temperature in the thermostatting liquid in the immediate vicinity of the pressure vessel. The temperature in the region of the speed of sound measurement in the sample liquid is assumed to be equal to the temperature measured by the Pt25 sensor in the wall of the pressure vessel.

The pressure vessel is shown in Fig. 3.8. Its body and the parts of the closure are fabricated of stainless steel type 1.4418. The sealing of the closure is provided by a polymer seal. First, o-rings of different materials (NBR, Viton, silicone encapsulated by FEP) were used. With water as a sample liquid, NBR o-rings could be used over a wide temperature range between 273 K and 353 K and pressures up to 100 MPa. However, with the other liquids examined in this work (propane, propene, partially flourinated hydrocarbons), NBR and Viton o-rings dissolved in the sample liquid causing the speed of sound of the sample to change with time. In this case, silicone o-rings encapsulated by the highly chemically resistant polymer FEP proved to be more suitable. However, after being subject to 100 MPa for a few times, they had to be exchanged because the FEP protection had been deformed and extruded into the free space behind the o-ring and small gaps between the pressure vessel body and the closure. Second, special sealing rings were tested, which consist of a stainless steel spring with c-shape cross section, whose outer face is encapsulated by PTFE. The spring ensures that the PTFE encapsulation is always tightly pressed against the faces of the groove, even during evacuation. Furthermore, the sample liquid enters the inner volume of the ring and supports the sealing under pressure. With this sealing ring, the most chemically resistant and most durable sealing was achieved.

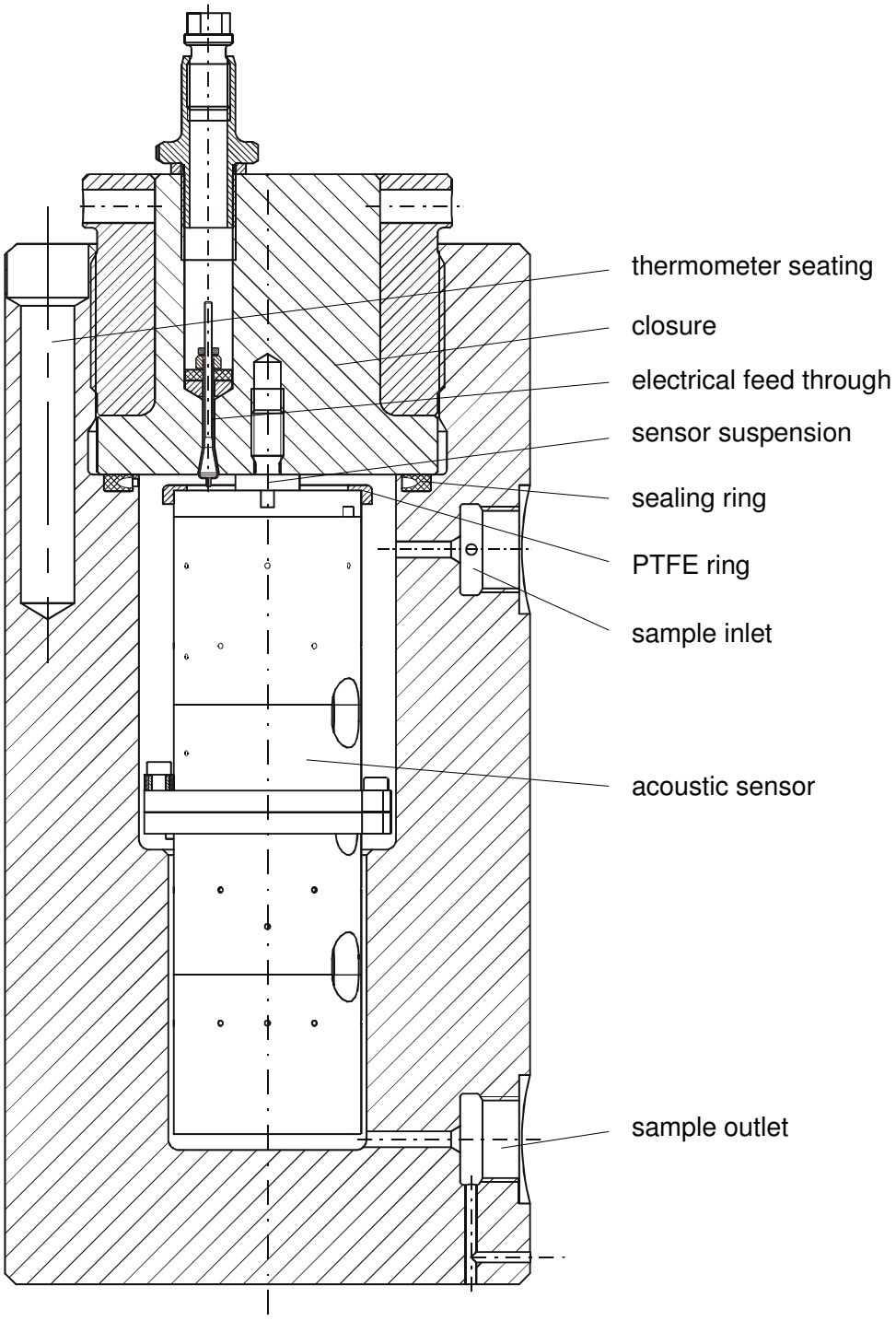

Figure 3.8. Cut through the pressure vessel with the acoustical sensor.

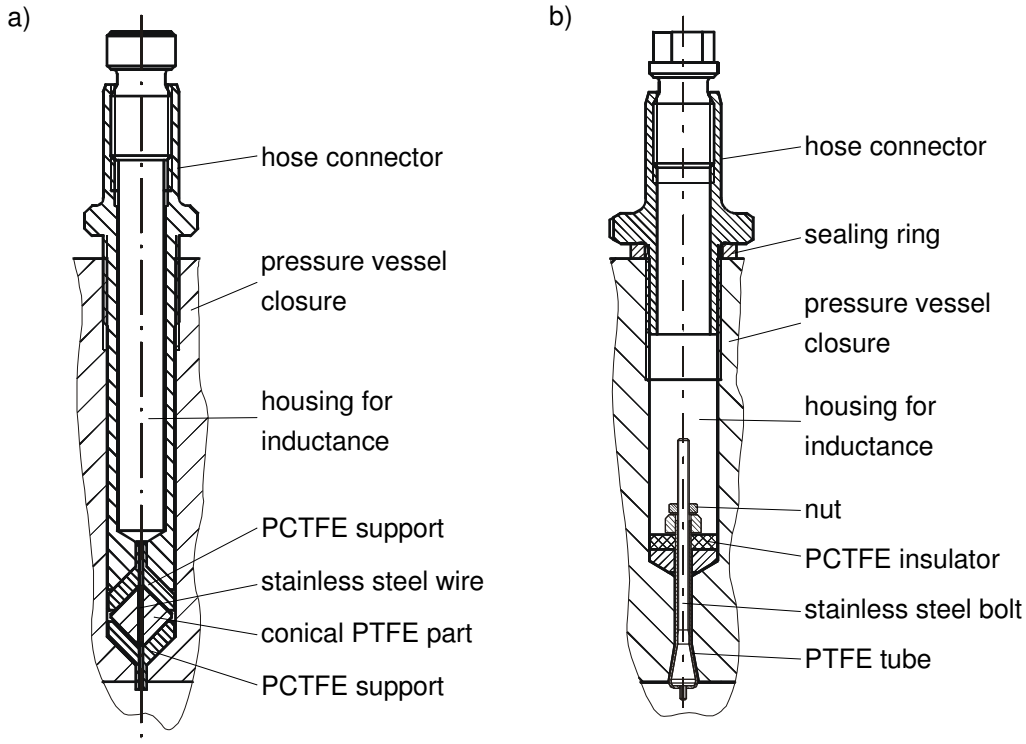

Figure 3.9. Cut through the electrical feed through in the closure of the pressure vessel. a) Homemade feed through; b) Commercial feed through (SITEC, type 770.8350).

The pressure vessel is connected to ground potential. Since one electrode of the piezoelectric crystal is connected via the acoustic sensor to the pressure vessel, the pressure vessel acts as an electric shield against external noise. The other electrode has to be connected to the center conductor of a coaxial cable at the exterior of the pressure vessel, which connects the acoustic sensor to the signal generation and detection devices. For the transmission of the signal through the closure of the pressure vessel, an electrical feed through is required. Constructive solutions for this problem are described in the literature [155, 168] or are commercially available.

In the first instance, the feed through described by Straty [168] was adopted and modified. A cut through the feed through is shown in Fig. 3.9a. The conductor is a stainless-steel wire of diameter 0.5 mm. A PTFE part with conical shape on both ends provides the electrical insulation and the high-pressure seal. At both ends, conical supports made of PCTFE, which has better mechanical properties than PTFE, prevent the PTFE from extruding under the high-pressure load. The PCTFE parts have small tubes at their ends, which serve as insulations between the

stainless-steel wire and the grounded closure of the pressure vessel.

The liquid-filled interior of the pressure vessel and the feed through present a large capacitance to the electric signal. Since, at the operation frequency of 8 MHz, high-frequency effects already play a dominant role, the electric impedance of the whole arrangement comprising the pressure vessel, acoustic sensor, and feed through must match the impedance of the coaxial cable, which connects the feed through with the devices for signal generation and detection. Since the coaxial cable must withstand the temperature in the thermostat, the cable type RG 188 with PTFE dielectric and jacket was chosen. The characteristic wave impedance of this cable type is $50\,\Omega$. In order to match the impedance of the cable, an inductance, which compensates for the large capacitance of the pressure vessel, is placed between the center conductor of the cable and the wire of the feed through. The value of the inductance is optimized manually so that the signal amplitude takes its highest possible value. For the optimization process, the pressure vessel was filled with liquid water and mounted in the thermostat in its final position.

The inductance for impedance matching is located as close as possible to the inner wall of the closure just at the outer end of the electrical feed through so that the cable ends as close as possible to the piezoelectric crystal. The inductance is soldered to the center conductor of the cable at one end and to the center conductor of a standard SMA connector at the other end. The whole arrangement is housed in a small tube, which is held by a hollow screw in the closure of the pressure vessel. The screw assures that the connector is plugged into the stainless-steel wire of the feed through and that the outer conductor of the cable is connected to the grounded closure of the pressure vessel.

This electrical feed through was used for the water, propane, propene and R227ea measurements. It provided a tight seal at high temperatures up to 420 K and under pressures up to 100 MPa, but sometimes it failed at low temperatures (240 K, 260 K). Moreover, after being subject to 420 K and 100 MPa for a few times, the tube end of the inner PCTFE part had extruded and the nickel wire had been shifted towards the suspension of the acoustic sensor. In the worst case, short circuits occurred.

Second, a commercially available electrical feed through was used (SITEC, type 770.8350), which is also shown in Fig. 3.9. The conductor is made of stainless steel, and the insulation and sealing is provided by a heat shrinkable PTFE tubing. The stainless steel conductor has a conical extension at the high pressure side, which is pressed in a conical depression of the same shape in the closure of the pressure

vessel by fastening the nut at the exterior of the feed through. Since the vertex of the cone is directed outwards, the high pressure inside the pressure vessel acts upon the bottom of the cone and supports the sealing. The inductance for impedance matching is arranged in a similar way as for the homemade feed through between the conductor of the feed through and the center conductor of the cable.

The nitrogen and R365mfc measurements were carried out with the commercial feed through. After being subject to 100 MPa pressure for about 10 times, the PTFE tubing had extruded outwards, and short circuits occurred. Then, the feed through had to be demounted, and the tubing had to be renewed. Sometimes the sealing failed, especially when the apparatus was cooled from a high to a low temperature. However, in such cases, it was often possible to restore the sealing by imposing it to high pressure. With the commercial feed through, longer durabilities over the whole temperature range of the apparatus could be achieved.

3.4 Temperature Measurement System

The resistances of the thermometers are measured with an alternating current bridge system, which consists of the bridge (ASL, type F18), a multi-channel switch box (ASL, type SB148/SB158), and a reference resistor module (ASL, type FR4) with four resistors with resistance values of 10 Ω, 25 Ω, 100 Ω, and 300 Ω. The resistors are housed in a thermostat, with which the temperature of the resistors is kept constant at 30 °C.

The two Pt25 sensor were calibrated at the national metrology institute, the PTB in Berlin, according to the ITS-90 [150], and the Pt100 sensors were calibrated against the Pt25 sensors. The reference resistors were calibrated at the PTB in Brunswick. In order to keep long term drift and hysteresis effects of the resistances to a minimum, the resistors were permanently kept at constant temperature by the built-in thermostat from the calibration procedure on, during the transport from the PTB to the laboratory room and all measurements undertaken during the course of this work. The bridge measures the ratio of the thermometer resistance and the reference resistance. The resistances of the Pt25 sensors were measured with the 100 Ω reference resistors and the resistances of the Pt100 sensors with the 300 Ω reference resistors.

The total uncertainty of the temperature measuring chain consists of the uncertainty of the thermometer calibration, the uncertainty of the reference resistors and the uncertainty of the measurement of the resistance ratio. The uncertainties of

the thermometers and the reference resistors are taken from the PTB calibration certificates. The absolute uncertainty of the Chino Pt25 thermometer amounts to 1.5 mK between -40 °C and 30 °C (2.0 mK between 30 °C and 420 °C), and the relative uncertainty of the 100 Ω resistor is $4 \cdot 10^{-7}$. The absolute uncertainty of the resistance ratio measurement is reported in the factory calibration certificate of the bridge and amounts to $1 \cdot 10^{-7}$. This corresponds to an uncertainty of about 0.1 mK in the temperature measurement. The absolute uncertainty of the temperature measuring chain adds up to 1.7 mK (2.2 mK). The total uncertainty of the temperature measurement must additionally include the stability of the temperature in the thermostat, which is estimated to be better than 0.5 mK, and the homogeneity of the temperature field inside the pressure vessel. Thus, the total absolute uncertainty of the temperature inside the pressure vessel u_T is estimated to be better than 3 mK over the whole temperature range covered by the apparatus.

3.5 Pressure Measurement and Filling System

Figs. 3.10 and 3.11 depict the sample liquid and nitrogen branches of the pressure measurement and filling system. The different components of the system are connected by a high-pressure tubing system[2)]. The two branches of the tubing system are coupled by a differential pressure indicator (DPI). One branch contains the sample liquid, and serves for filling the pressure vessel with the sample liquid and setting the pressure in the pressure vessel. The other branch is filled with nitrogen and couples the pressure measurement devices to the sample liquid via the DPI.

Before the sample liquid is filled into the apparatus, the pressure vessel and the tubing system are evacuated. A rotary slide-valve vacuum pump (Pfeiffer, type DUO 10) is connected to the high-pressure tubing system by a vacuum tubing system. In order to prevent oil vapor from the vacuum pump from entering the high-pressure tubing system and the pressure vessel, a cold trap operated with liquid nitrogen is located in the vacuum system near the vacuum pump. During evacuation, the pressure is measured near the transition piece between the vacuum and high-pressure tubing system by a Pirani gauge (Pfeiffer, type TPR 261). The filling process is started after the pressure has decreased below 0.05 Pa. Usually this state is reached after evacuating the system for about an hour. Since, in this pressure range, the fluid flow in the high-pressure tubes is in the molecular flow regime, the remaining fluid particles in the high-pressure side of the system are no longer transported towards

[2)] SITEC, type Micro 1000 bar, internal tube diameter: 2.4 mm.

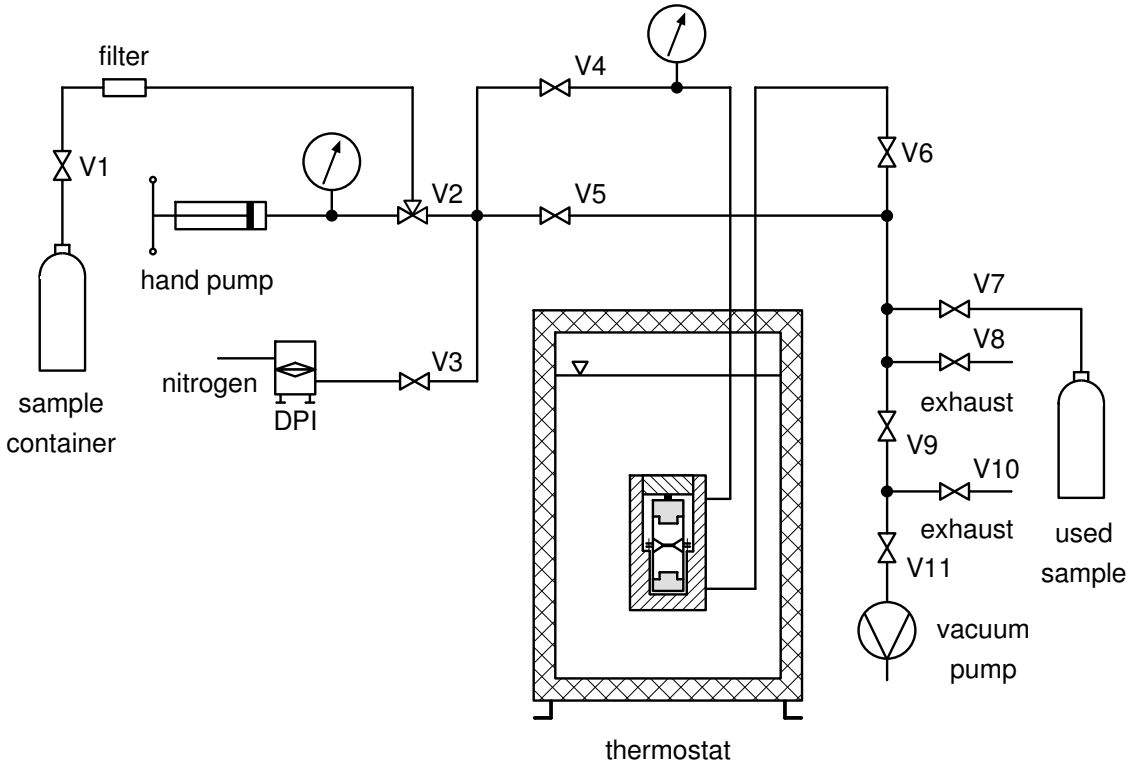

Figure 3.10. The sample liquid branch of the pressure measurement and filling system.

the vacuum pump by the pressure gradient. For this reason, the pressure in the pressure vessel and the high pressure tubes remains of the order 1 Pa and decreases only extremely slowly. In this pressure regime, the ideal gas equation of state can be applied to estimate the mass of the fluid remaining inside the system, which has an internal volume of approximately 0.25 liters. If it is assumed that the remaining fluid is air, the mass in the system is about $3.5 \cdot 10^{-9}$ kg at the temperature 293 K, which is negligibly small compared with a sample mass of about 0.25 kg, when the system is filled with liquid water at ambient temperature and pressure.

In order to fill the sample liquid into the apparatus, the sample container is heated by a temperature controlled heating pad wrapped around it. When the vapor pressure in the container is higher than the vapor pressure of the sample liquid at the highest temperature in the liquid branch of the tubing system, the pressure difference between the container and tubing system ensures that sample liquid streams into the apparatus. The sample liquid can then be pressurized within the apparatus up to 100 MPa with a variable-volume hand pump (SITEC, type 750.1100). If additional

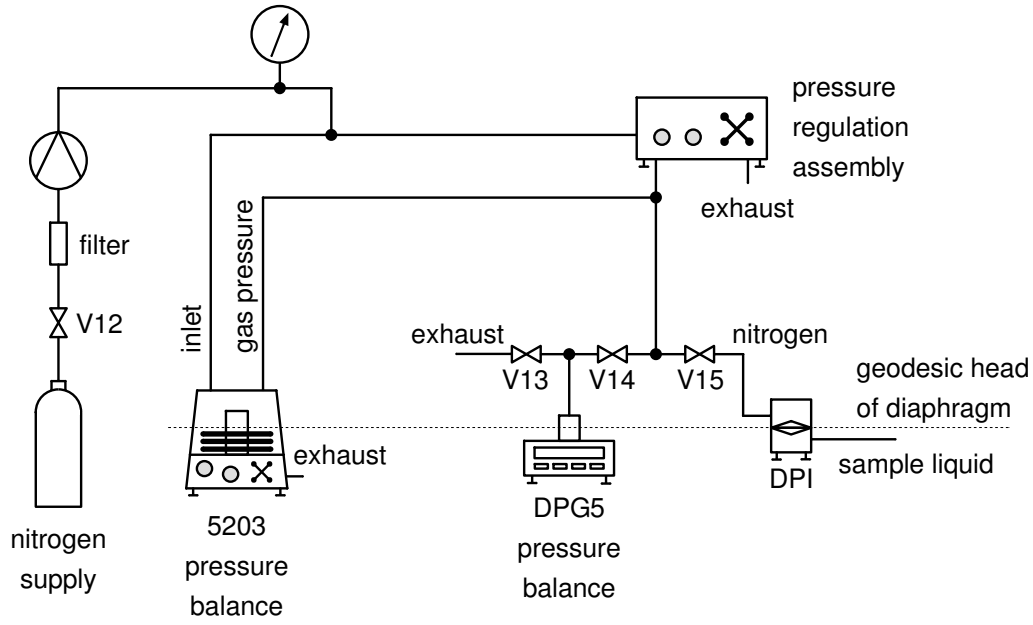

Figure 3.11. The nitrogen branch of the pressure measurement and filling system.

sample liquid must be refilled to reach the highest pressures, the pressure vessel and the liquid branch of the differential pressure indicator cell can be disconnected by closing valves V3, V4, and V5, and the pressure in the hand pump can be reduced below the vapor pressure in the heated sample container. Then sample liquid can be refilled into the internal volume of the hand pump. After that the sample liquid in the hand pump can be pressurized again and the valves V3, V4, and V5 can be opened.

The pressure inside the pressure vessel is measured by two nitrogen operated pressure balances with measurement ranges 5 MPa (Degrange & Huot, type DPG5) and 100 MPa (Degrange & Huot, type 5203). The nitrogen branch of the system is coupled to the liquid branch by a differential pressure indicator (Ruska, type 2413-705). The differential pressure indicator cell consists of two conical chambers, which are separated by a thin stainless steel diaphragm. At the top side of the diaphragm, the movable core of a differential transformer is welded on. The transformer yields an electrical signal once a pressure difference between the two chambers occurs. This signal is evaluated by an indicator. If the indicator is calibrated to zero with equal pressures on both sides of the membrane, it can be used to adjust the pressures in the nitrogen and in the liquid branch. In the nitrogen branch, pressures higher than the nitrogen container pressure are generated by a pneumatically controlled

compressor (Maximator, type DLB 75-2-GG). Fine adjustment of the pressure is made by the built-in variable-volume hand pump of the pressure balance and an additional hand pump (Degrange & Huot, type 42302).

The basic component of a pressure balance is a piston-cylinder system, in which an oil-lubricated piston rotates within a cylindrical cavity. The pressure is measured by balancing the force of the nitrogen pressure acting upon the bottom face of the piston and the gravitational force of calibrated masses acting upon the top of the piston to static equilibrium. The pressure is then obtained as

$$p_{\mathrm{PB}} = \frac{g_{\mathrm{loc}} \sum_{i=1}^{n} m_i (1 + \rho_{\mathrm{air}}/\rho_{\mathrm{m}})}{A_{\mathrm{p}}(p, \vartheta)}, \tag{3.2}$$

where g_{loc} is the local gravitational acceleration in the laboratory room, the m_i denote the masses on the pressure balance, and A_{p} is the area of the piston face. The term in the parentheses represents the correction for the buoyancy of the masses in the air of the laboratory room. In this term, ρ_{air} is the density of air, and ρ_{m} is the density of the stainless steel masses.

The piston area changes with temperature and pressure so that small corrections have to be applied:

$$A_{\mathrm{p}}(p, \vartheta) = A_{\mathrm{p}}(p_0, \vartheta_0)[1 + (\alpha_{\mathrm{cyl}} + \alpha_{\mathrm{p}})(\vartheta - \vartheta_0)][1 + \lambda_{\mathrm{p}}(p + p_0)]. \tag{3.3}$$

In this equation, A_0 denotes the piston area at the reference state ($\vartheta_0 = 20$ °C, $p_0 = 1$ bar), α_{cyl} and α_{p} are the thermal expansion coefficients of the cylinder and the piston, respectively, and λ_{p} is the pressure coefficient.

When Eq. (3.3) is inserted into Eq. (3.2), a quadratic equation for the pressure results, which has the solution

$$p_{\mathrm{PB}} = \frac{1}{2\lambda_{\mathrm{p}}} \left(-1 + \sqrt{1 + 4\lambda_{\mathrm{p}}[1 + (\alpha_{\mathrm{cyl}} + \alpha_{\mathrm{p}})(\vartheta - \vartheta_0)]} \right). \tag{3.4}$$

The values of the masses, the piston area and the pressure coefficient for the two pressure balances were determined by a calibration at the PTB in Brunswick. The local gravitational acceleration g_{loc} in the laboratory room was determined experimentally by the Institute of Geophysics at the University Hamburg to $g_{\mathrm{loc}} = 9.8137627\ \mathrm{m\,s^{-2}}$ with an uncertainty $u_g = 1 \cdot 10^{-7}\ \mathrm{m\,s^{-2}}$ [37]. The pressure measured by the balances is the pressure in the system minus the ambient pressure, which has to be added to obtain the total pressure in the system. The ambient pressure in

the laboratory room is measured at the geodesic head of the pressure balances by a capacitive pressure transducer (Vaisala, type PTB220).

As the pressure balances and the acoustic sensor are located at different geodesic heads in the laboratory room, the pressure measured by the pressure balances differs from the pressure in the pressure vessel. In order to obtain the pressure in the pressure vessel, a correction must be applied. The hydrostatic pressure difference between two points in a fluid at different geodesic heads is generally given by

$$\Delta p_{\mathrm{hydro}} = \rho g_{\mathrm{loc}} \Delta h, \tag{3.5}$$

where ρ is the fluid density and Δh denotes the difference between the geodesic heads.

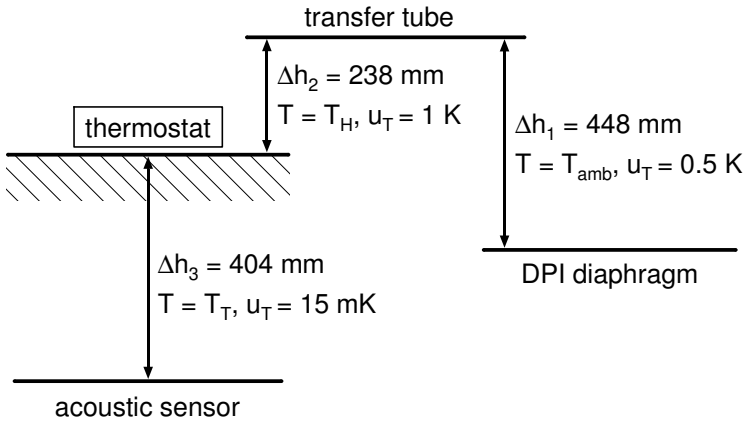

Figure 3.12. Separation of the pressure transfer system for the calculation of the hydrostatic pressure correction.

The pressure balances and the ambient pressure transducer are placed at the same geodesic head as the diaphragm of the differential pressure indicator cell so that no hydrostatic pressure correction is required for the nitrogen branch of the system and the ambient pressure measurement. For the sample liquid branch, the hydrostatic pressure correction is separated into three contributions, which correspond to three regions with different temperatures as shown in Fig. 3.12. The tubes inside the thermostat have the same temperature as the pressure vessel (uncertainty: u_T = 15 mK). If the thermostat temperature is higher than the ambient temperature the high pressure tubes above the thermostat are heated by electrical heaters at a temperature slightly larger than the thermostat temperature (uncertainty: $u_T = 1$

K). If the thermostat temperature is lower than the ambient temperature, the tubes above the thermostat are kept at ambient temperature. The tube leading down to the differential pressure indicator is also at ambient temperature. The ambient temperature was measured by a simple mercury thermometer (uncertainty: $u_T = 0.5$ K). The differences between the geodesic heads were measured with an uncertainty $u_{\Delta h_i} = 1$ mm. The hydrostatic pressure correction becomes

$$\Delta p_{\mathrm{hydro}} = g_{\mathrm{loc}}[-\rho(T_{\mathrm{amb}}, p)\Delta h_1 + \rho(T_{\mathrm{H}}, p)\Delta h_2 + \rho(T_{\mathrm{T}}, p)\Delta h_3], \tag{3.6}$$

and the pressure is given by

$$p = p_{\mathrm{amb}} + p_{\mathrm{PB}} + \Delta p_{\mathrm{hydro}}. \tag{3.7}$$

The total uncertainty of the pressure measurement is the sum the the uncertainties of the three contributions $u_{p_{\mathrm{amb}}}$, $u_{p_{\mathrm{PB}}}$, and $u_{\Delta p_{\mathrm{hydro}}}$ and the uncertainty of the pressure transmission by the differential pressure indicator u_{DPI}.

The uncertainty of the pressure balances $u_{p_{\mathrm{PB}}}$ are reported in the PTB calibration certificates[3)]. The ambient pressure transducer was calibrated by the manufacturer, and the uncertainty of the ambient pressure measurement is reported in the calibration certificate as $u_{p_{\mathrm{amb}}} = 7$ Pa. According to the specifications of the manufacturer, the uncertainty of the differential pressure indicator is given by $u_{\mathrm{DPI}} = \max(70\,\mathrm{Pa}, 5 \cdot 10^{-6} p)$ after calibration of the zero position of the indicator.

The uncertainty of the hydrostatic pressure correction consists of several contributions, which are due to the uncertainty of the local gravitational acceleration u_g, the uncertainty of the measured differences between the geodesic heads $u_{\Delta h_i}$, and the uncertainty of the density of the sample fluid u_ρ. The uncertainty of the density generally depends on the accuracy of the equation of state, from which it is calculated. Since for all measured fluids accurate equations of state were available or became available during the course of this work, the uncertainty of the density is conservatively estimated to be 0.1 %. For some fluids, for example water, it is even much better than 0.1 %. The uncertainty of the local gravitational acceleration can be neglected because it is several orders of magnitude smaller than the uncertainties of the other variables. The influence of the remaining variables on the hydrostatic pressure correction must be estimated by the error propagation law and is given by

$$u_{\Delta p_{\mathrm{hydro}}} \approx \left(\frac{\partial \Delta p_{\mathrm{hydro}}}{\partial \rho}\right) u_\rho + \sum_i \left(\frac{\partial \Delta p_{\mathrm{hydro}}}{\partial \Delta h_i}\right) u_{\Delta h_i}, \tag{3.8}$$

[3)] The uncertainty $u_{p_{\mathrm{PB}}}$ is given by $(0.27 \cdot 10^{-5}\,\mathrm{bar}^2 + 0.16 \cdot 10^{-8} p_{\mathrm{PB}}^2 + 0.42 \cdot 10^{-15}\,\mathrm{bar}^{-2} \cdot p_{\mathrm{PB}}^4)^{1/2}$ for the Degranges & Huot 5203 pressure balance and by $(1.6 \cdot 10^{-7}\,\mathrm{bar}^2 + 1.6 \cdot 10^{-9} p_{\mathrm{PB}}^2)^{1/2}$ for the Degranges & Huot DPG5 pressure balance.

where it has been assumed that the uncertainties are due to systematic measurement errors.

The uncertainty of pressure measurements is usually reported in terms of the relative uncertainty ε_p, which is therefore also used here. The relative uncertainty of the pressure measurement system with resolution of the different contributions to the total uncertainty is shown for both pressure balances in Fig. 3.13. The main contribution to the uncertainty is due to uncertainty of the pressure balances with constant magnitude of about 0.0045 % over large parts of pressure range of the apparatus. At pressures above 10 MPa, the uncertainty of the differential pressure indicator contributes 0.0005 %, while the contributions due to the uncertainty of the ambient pressure measurement and of the hydrostatic pressure correction are negligible. Thus, the total uncertainty of the measured pressures above 10 MPa is 0.005 %. At lower pressures, the relative uncertainties of the ambient pressure measurement, the hydrostatic pressure correction, and the differential pressure indicator increase because their absolute uncertainty is constant. At pressures below 1 MPa, the relative uncertainty of the pressure measurement can be as high as 0.02 %, mainly due to the uncertainty of the transmission of the pressure by the DPI and the uncertainty of the pressure balances, but it decreases to about 0.006 % at 5 MPa. Since the D&H 5203 pressure balance has a constant absolute uncertainty of 430 Pa below 10 MPa, the uncertainty of the pressure measurement decreases between 5 MPa and 10 MPa from 0.01 % near 5 MPa to 0.005 % at 10 MPa.

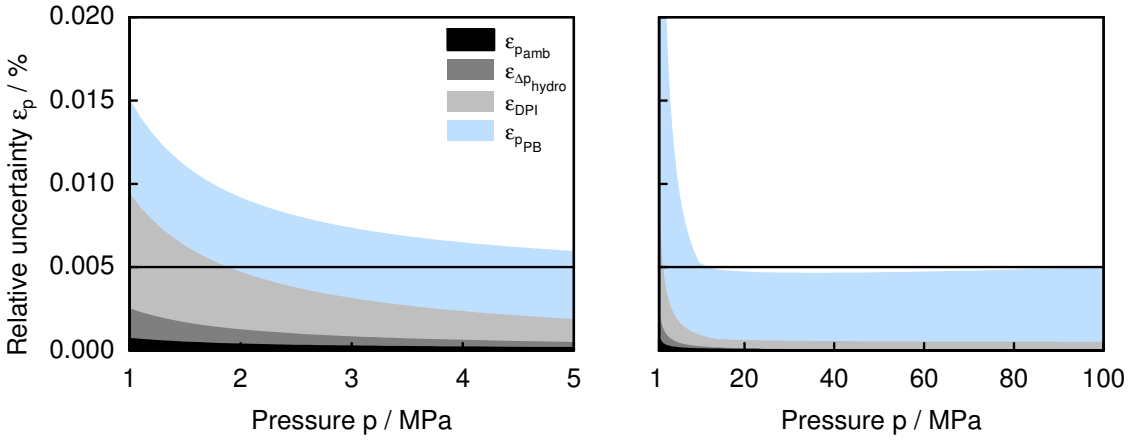

Figure 3.13. Contributions to the relative measurement uncertainties of the pressure for the pressure balance DPG5 (left) and for the pressure balance 5203 (right). In both cases, the sample liquid is propane at 260 K.

3.6 Signal Generation and Detection

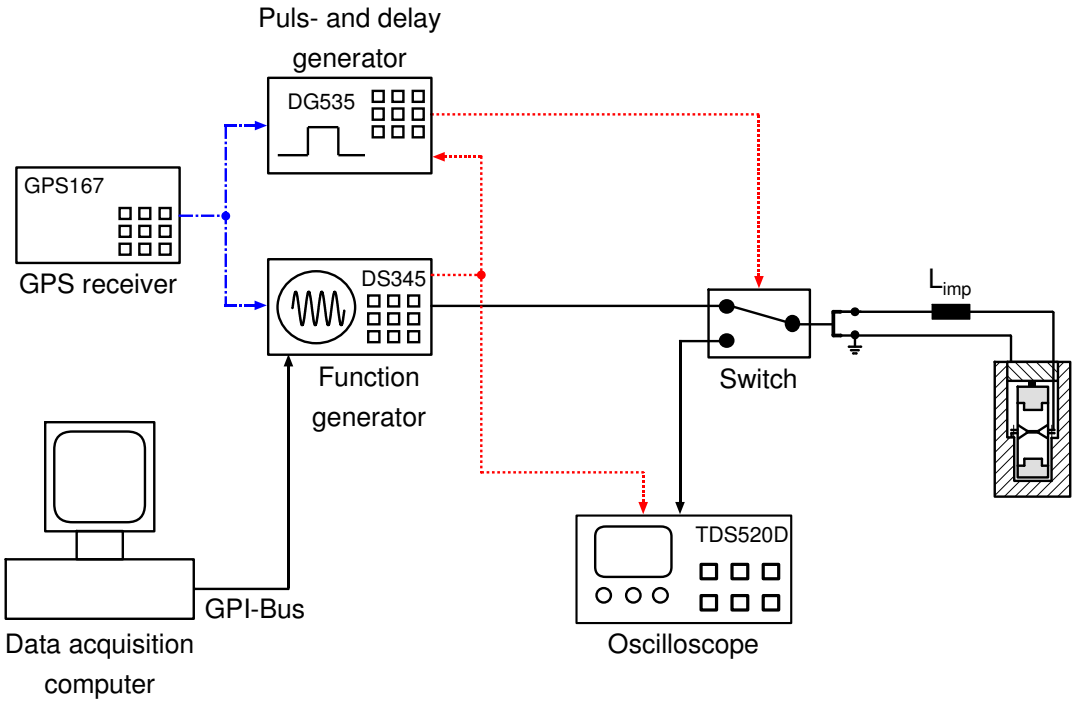

Figure 3.14. Arrangement of electronic devices and circuitry for signal generation and detection.

Fig. 3.14 depicts the arrangement of the electronic devices and circuitry for signal generation and detection. The arbitrary wave function of a function generator (Stanford Research Systems, type DS345) with a sampling frequency of 40 MHz is employed to generate the electric signals, with which the piezoelectric crystal is excited. The points of the signals are calculated on the data acquisition computer and transferred into the internal memory of the function generator via the GPIB interface of the computer. The function generator generates a digitized signal, which is transformed into an analog signal by a built-in low pass filter at the output of the function generator. The function generator also triggers a pulse and delay generator (Stanford Research Systems, type DG535) and a digital storage oscilloscope (Tektronix, type TDS520D), on which the signal cancellation is monitored. The function generator itself is triggered by the internal trigger rate generator with a repetition rate of 10 Hz. With this repetition rate it is ensured that all echoes from the previous experiment have decayed to a negligible level. The pulse and delay generator

is employed to control an electronic switch (Mini-Circuits, type ZYSWA-2-50DR, absorptive), which either directs the generated signal towards the acoustic sensor or, in the other position, directs the received pulse-echo pattern to the oscilloscope. A GPS (Global Positioning System) receiver with roof antenna (Meinberg, type GPS167TGP) serves as a frequency standard. It is equipped with a oven-controlled rubidium oscillator, which is frequency-locked to the received GPS signal, and delivers several highly accurate 10 MHz TTL compatible square wave reference signals, which are connected to the time bases of the function and pulse and delay generators. When the receiver is synchronized to the GPS system, the frequency of the 10 MHz reference signals, and thus the frequency of the time basis of the function generator, has a relative uncertainty of $1 \cdot 10^{-12}$.

All electronic devices are connected by standard RG58 coaxial cables with 50 Ω characteristic wave impedance. At the operating frequency of 8 MHz, high frequency effects already become important and must be taken into account. This means that all impedances the signal passes on its way through the system must match the 50 Ω characteristic wave impedance of the cables. Therefore, the input resistance of the oscilloscope is set to 50 Ω. Furthermore, the complex impedance of the mechanical part of the system, formed by the acoustic sensor, the pressure vessel and the electrical feed through, must be transformed close to the real impedance of 50 Ω. This is achieved by placing an inductance as close as possible at the exterior of the pressure vessel between the center conductor of the cable and the conductor of the electrical feed through as was described in Sec. 3.3.

With an excitation signal of 4 V peak-to-peak amplitude – the signal amplitude is limited to 5 V peak-to-peak due to the electronic switch –, the amplitude of the first two echoes of the received pulse-echo pattern is about 20 to 40 mV depending on the sample liquid and the pressure and temperature of the state point. If the amplitude of the received signal is not large enough to observe the cancellation with high resolution, an amplifier (amplifier research, type 1W1000A) is placed between the switch and the oscilloscope. This is particularly required at supercritical low density states, where the sound signals in the sample fluid are strongly attenuated. With the amplifier, the signal amplitude is increased by a factor of about 60.

For the generation of the signal cancellation, the time difference between the two generated bursts is adjusted manually in the data acquisition software and transferred to the function generator so that changes in the received signal can be observed immediately on the oscilloscope screen. The cancellation of the signals can be observed with high accuracy so that a resolution of at least 5 ppm in the measured

time difference is achieved. Since the cancellation depends on the amplitudes, but not on the time difference between the two signals, the resolution increases with larger time differences, that is with decreasing speeds of sound, and is as small as 1 ppm at time differences of 50 μs. Since the relative uncertainty of the frequency of the time basis of the function generator is by some orders of magnitude smaller than the resolution of the time difference measurement, the uncertainty of the measured time difference is essentially equal to the resolution.

The data acquisition computer is used to perform the time, temperature and pressure measurements and to store the measured data digitally. The function generator and the ASL bridge system are connected to the data acquisition computer via a GPIB interface, while the ambient pressure transducer and the pressure balance DPG5 are connected via serial RS232 interfaces. The data acquisition software was developed within the graphical programming environment Labview (National Instruments, Version 6i).

4 Measurement Analysis

If the acoustic sensor were perfectly rigid and the sound signals propagated as plane waves, the working equation for the determination of the speed of sound would be given by

$$w = \frac{2(L_2 - L_1)}{\Delta t} = \frac{\Delta L}{\Delta t}.$$

In practice, there are small deviations from this simple model, which must be accounted for in the analysis of the measurements. The stainless steel material of the acoustic sensor and the piezoelectric crystal expand and contract with temperature and are compressed under pressure, changing the distances between the crystal and the reflectors. Moreover, the propagation of the sound signals deviates from plane wave propagation because of diffraction of the emitted signals at the edges of the acoustically active area of the crystal. This effect results in measured time differences which are smaller than in the case of plane wave propagation. Additionally, if the fluid is dispersive, the measured speeds of sound must be corrected to the thermodynamic speeds of sound. This latter correction generally depends on the fluid and therefore will be discussed individually for each measured fluid in Chap. 5.

The behavior of the sensor material and the piezoelectric crystal under the influence of temperature and pressure is described in the following section and a diffraction correction for the time difference is developed in Sec. 4.2. Sec. 4.3 describes the determination of the acoustic path length ΔL by calibration measurements in pure liquid water at ambient pressure. Based on this acoustic model of the sensor and on the calibration measurements, an estimate for the uncertainty of the speed of sound measurement is derived in Sec. 4.4. Sec. 4.5 reports measurements of the speed of sound in liquid water under pressure, which were carried out to validate the apparatus.

4.1 Variation of the Acoustic Path Length with Temperature and Pressure

The frame for modelling thermal expansion and deformation of a solid under pressure is provided by continuum mechanics [25, 171]. As the material of the acoustic

sensor and the piezoelectric crystal is deformed only elastically in the temperature and pressure range of the apparatus, linear elastic theory can be applied. The deformation of a solid is described in terms of the strain $S = \delta L/L_0$, which measures the change of the length δL relative to the length L_0 at a reference state with temperature T_0 and p_0. Here, the state ($T_0 = 273.15$ K, $p_0 = 0.1$ MPa) is chosen as the reference state.

Changes of the acoustic path length with temperature and pressure can be calculated by

$$\Delta L(T,p) = [\Delta L(T_0,p_0) + L_\mathrm{c}(T_0)] \left[1 + \alpha_\mathrm{th}^\mathrm{AS}(T-T_0) + \frac{1}{E}(1-2\nu)(p-p_0)\right] - L_\mathrm{c}(T_0)[1 + \alpha_\mathrm{th}^\mathrm{c}(T-T_0)], \qquad (4.1)$$

where $\alpha_\mathrm{th}^\mathrm{AS}$ and $\alpha_\mathrm{th}^\mathrm{c}$ represent the thermal expansion coefficients of the sensor material and the piezoelectric crystal, L_c is the thickness of the crystal and E and ν are the elastic modulus and the Poisson number of the sensor material.

The change of length due to thermal expansion is described by the average thermal expansion coefficient α_th. The differential thermal expansion coefficient β_th is defined by

$$\beta_\mathrm{th} = \left(\frac{\partial S(T)}{\partial T}\right)_p, \qquad (4.2)$$

and the average thermal expansion coefficient α_th is obtained by integrating β_th between T_0 and T as

$$\alpha_\mathrm{th} := \frac{1}{T-T_0}\int_{T_0}^{T} \beta_\mathrm{th}(T)\,dT. \qquad (4.3)$$

Values for the elastic modulus and the Poisson number of the sensor material, the stainless steel 1.4571, are taken from the database FEZEN [72]. The Poisson number is $\nu = 0.3$, independent of temperature. The reference values for the elastic modulus as a function of temperature are summarized in Table 4.1. For practical calculations, the temperature dependence of E is represented by a linear fit of the form

$$E(T) = e_0 + e_1\left(\frac{T}{T_0} - 1\right) \qquad (4.4)$$

to the data in Table 4.1. The values of the coefficients e_0 and e_1 are reported in Table 4.2. The relative uncertainties of the elastic modulus ε_E as calculated from Eq. (4.4) and of the Poisson number ε_ν are estimated to be 5 %.

Table 4.1. Reference data for the elastic modulus E, the average thermal expansion coefficient α_{th} between 0 °C and the given temperature, and the differential thermal expansion coefficient β_{th} of the stainless steel 1.4571 [72].

ϑ / °C	E / 10^3 N/mm^2	α_{th} / 10^{-6} K^{-1}	β_{th} / 10^{-6} K^{-1}
-100	206	14.9	13.3
0	198	16.0	15.8
20	196	16.1	16.1
100	190	16.7	17.2
200	182	17.2	18.1
300	174	17.7	18.8
400	166	18.1	19.5
500	158	18.4	20.1
600	150	18.8	20.7
700	142	19.1	21.3
800	134	19.4	21.9
900	127	19.7	22.4
1000	120	20.0	22.9

Table 4.2. Numerical values of the coefficients e_i of Eq. (4.4), b_i of Eq. (4.5), and c_i of Eq. (4.6) as obtained from polynomial fits.

i	e_i / 10^3 N/mm^{-2}	b_i / 10^{-6} K^{-1}	c_i / 10^{-6} K^{-1}
0	197.9137	17.7656	13.0874
1	21.797	5.08059	7.2112
2		-3.7448	-0.87369
3		1.8672	
4		-0.34148	

The reference values for the thermal expansion coefficient from the database FEZEN [72], which are also reported in Table 4.1, are not accurate enough to predict the thermal expansion of the sensor accurately because the properties of the stainless steel may vary considerably depending on the charge it was taken from and the conditions of the manufacturing processes it was subject to. In order to keep the properties as close as possible to the reference specifications, all parts of the sensor were subject to a heat treatment after the major steps of the manufacturing process as was described in Sec. 3.2.

For the pre-analysis of the calibration measurements, the data for the differential thermal expansion coefficient β_{th} reported in Table 4.1 were represented by a fourth

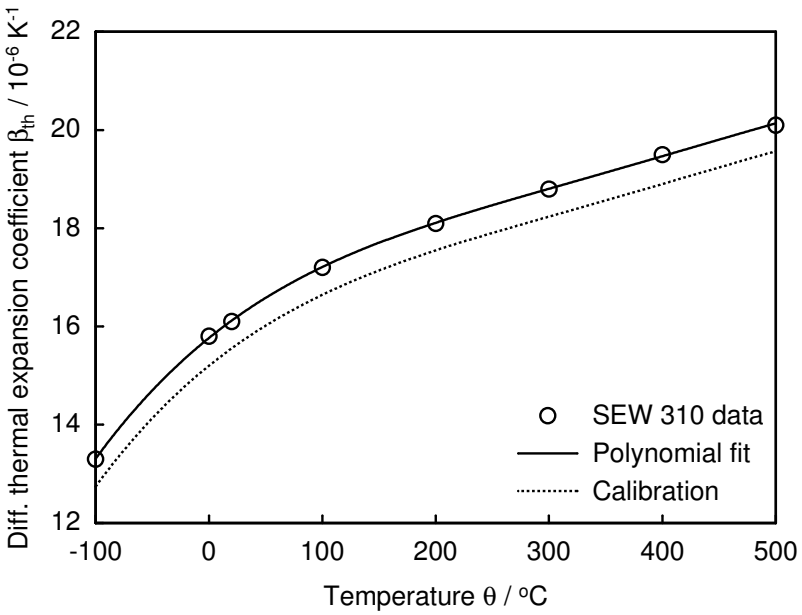

Figure 4.1. The differential thermal expansion coefficient of stainless steel 1.4571 as a function of temperature.

order polynomial as

$$\beta_{\mathrm{th}} = \sum_{i=0}^{4} b_i \left(\frac{T}{T_0} - 1 \right)^i \tag{4.5}$$

in the temperature range between 173 K (-100 °C) and 873 K (600 °C). The numerical values of the coefficients b_i are reported in Table 4.2, and the fitting function together with the data from Table 4.1 is shown in Fig. 4.1. During the calibration procedure, which will be described in Sec. 4.3, the coefficient b_0 was adjusted so that the temperature dependence of the speed of sound in liquid water at ambient pressure is optimally represented by the calibration measurements. Since the working temperature range of the apparatus (240 K to 420 K) is larger than the range of the calibration measurements (274 K to 368 K), the thermal expansion coefficient must be extrapolated below 273 K and above 368 K. Therefore, the higher coefficients of the polynomial, which especially describe the nonlinear behavior below 273 K, are retained unchanged as obtained from the fit after the calibration.

The thermal expansion coefficient of α-quartz as a function of temperature was reported by Brice [26]. Since α-quartz is a crystalline material with different properties in different spatial directions, the thermal expansion coefficient depends on the

Table 4.3. Reference data for the differential thermal expansion coefficient $\beta_\perp$ perpendicular and $\beta_\parallel$ parallel to the optical Z-axis as reported by Brice [26].

ϑ / °C	$\beta_{\text{th}}^{\perp}$ / 10^{-6} K^{-1}	$\beta_{\text{th}}^{\parallel}$ / 10^{-6} K^{-1}
-100	10.3	4.9
-50	11.8	6.0
0	13.1	7.0
25	13.7	7.5
100	15.6	8.8
200	17.9	10.4

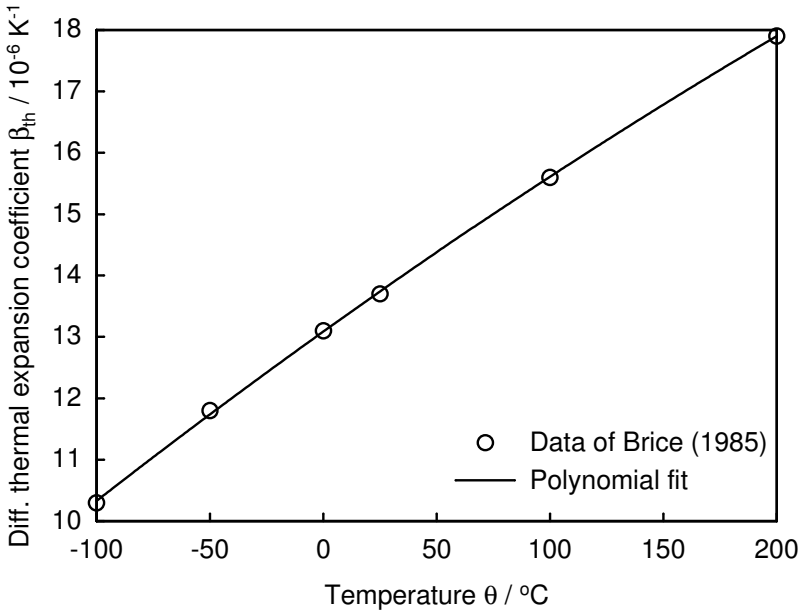

Figure 4.2. The differential thermal expansion coefficient of α-quartz perpendicular to the optical Z-axis as a function of temperature.

orientation, in which the crystal is cut from the raw material. Table 4.3 presents the data reported by Brice for the differential thermal expansion coefficient of α-quartz in the directions perpendicular and parallel to the Z-axis. The relative uncertainties of the data were estimated by Brice to be lower than 2 %. For an X-cut α-quartz, which is applied in the acoustic sensor, the thermal expansion parallel to the X-axis, that is perpendicular to the Z-axis, contributes to the acoustic path length.

Therefore, the data for $\beta_{\mathrm{th}}^{\perp}$ were fitted to a second order polynomial of the form

$$\beta_{\mathrm{th}}^{\mathrm{c}} = \beta_{\mathrm{th}}^{\perp} = \sum_{i=0}^{2} c_i \left(\frac{T}{T_0} - 1 \right)^i . \tag{4.6}$$

The numerical values of the coefficients are also reported in Table 4.2, and the data and the fitted polynomial function are depicted in Fig. 4.2. The compression of the quartz crystal under pressure is neglected because it contributes only little to the total change of the acoustic path length.

With the temperature dependent elastic modulus and thermal expansion coefficient of stainless steel 1.4571, Eqs. (4.4) and (4.5), and the temperature dependent thermal expansion coefficient of α-quartz, Eq. (4.6), changes of the acoustic path length can be calculated by Eq. (4.1). It is instructive to examine the magnitude of influences of temperature and pressure. A temperature change of 20 K changes the acoustic path length by about 0.03 %. The influence of the pressure is much smaller, amounting to only 0.02 % for the highest measured pressures of 100 MPa.

4.2 Diffraction Effects

The working equation for the determination of the speed of sound with the acoustic sensor, $w = \Delta L/\Delta t$, is based on the assumption that the sound signals propagate as plane waves in the sample fluid. However, diffraction due to the finite size of the piezoelectric crystal, which generates the sound waves, cause deviations of the real wave propagation from this simplified model. This effect results in small phase shifts of the received echoes, which are evaluated in the measurement of the time difference Δt, compared with plane wave propagation. In order to apply the simple working equation correctly, a model must be developed, with which the difference between the time differences of plane wave and real wave propagation can be estimated.

From a physical point of view, the sound field in front of a piezoelectric transducer can be calculated by applying Huygens' principle. Every point of the sound source is viewed as a point source emitting an outgoing spherical sound wave. The field at an arbitrary point in front of the source can then be constructed from a superposition of the waves emitted from all points of the source by an integration over the surface of the source.

If the surface of the sound source vibrated with a uniform amplitude distribution, in a first approximation, the sound field in front of the source could be viewed as composed of two contributions as illustrated in Fig. 4.3. In front of the center of

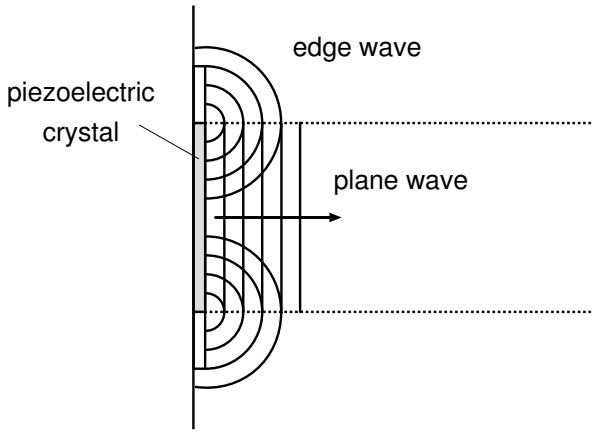

Figure 4.3. Contributions to the sound field in front of a piezoelectric disk.

the source, the spherical waves originating from all points on the source surface superimpose to form a plane wave. However, the spherical waves originating from the points on the edges of the surface, the edge waves, superimpose this plane wave so that the wave, which a finite-size receiver placed at some distance in front of the source would measure, has a small phase shift compared with the plane wave. The edge wave contribution to the sound field can be minimized by using sound sources with non-uniform vibration amplitude distributions. For this reason, a piezoelectric quartz crystal with the electrode forms shown in Fig. 3.4 was chosen. Since the electrodes cover only the inner circular area with 10 mm diameter of the piezoelectric crystal with 15 mm diameter, the amplitude of the crystal vibration has a Gaussian-like distribution (see also Fig. 4.8 below). With this electrode geometry, edges waves are reduced, but diffraction still influences the sound field and must be accounted for.

Diffraction effects in the sound field in front of sound transducers and their influence on the results of measurements of the speed and absorption of sound have been investigated by many authors before. A review of different methods to calculate diffraction effects in pulse-echo experiments was published by Gitis and Khimunin [65]. Often an expression derived by Williams [189] is applied. This expression provides the velocity potential field in front of a circular plane piston source with uniform vibration amplitude distribution for continuous sinusoidal excitation. For example, Khimunin [90] applied the result of Williams to calculate diffraction corrections for pulse-echo measurements of the speed of sound. Subsequently, Khimunin [91] extended the model by including sound absorption. A historical review of dif-

ferent methods for the calculation of the transient sound field in front of a planar piston source with uniform vibration amplitude was given by Harris [73]. In a second article, Harris [74] introduced a model for the calculation of the sound field in front of planar piston sources with non-uniformly vibration amplitude distributions and transient excitation.

In the remainder of this section, a model based on the work of Harris [74] will be developed, which provides a correction for diffraction effects within the geometry of the acoustic sensor. First, the model of a baffled point source will be derived. This result is then used to construct the Rayleigh integral [153], which – in the form given below – describes the transient sound field in front of a non-uniformly vibrating sound source in terms of the velocity potential. After that, the average acoustic pressure measured by a circular receiver, which is placed at a distance in front of the source, is calculated. These results are finally applied to calculate a diffraction correction for the time difference measurement within the geometry of the acoustic sensor. As was shown by Khimunin [91], the absorption of sound on the diffraction correction is negligible. Therefore, the theory for the propagation of sound in ideal fluids derived in Sec. 2.2.1 can be applied, which simplifies the analysis greatly.

First, the velocity potential field of a baffled point source radiating sound into an ideal fluid will be derived. For this purpose, the solution of the wave equation for outgoing spherical waves is required. The wave equation for an ideal fluid, Eq. (2.15), reads

$$\nabla^2 p_\mathrm{a} - \frac{1}{w^2}\frac{\partial^2 p_\mathrm{a}}{\partial t^2} = 0,$$

and the Laplace operator in spherical coordinates is given by

$$\nabla^2 = \frac{1}{r^2}\frac{\partial}{\partial r}\left(r^2\frac{\partial}{\partial r}\right), \tag{4.7}$$

where the dependencies on the polar and azimuthal angle have been omitted because the field of a spherical wave depends only on the radial coordinate r. Inserting the Laplace operator into the wave equation, yields

$$\frac{1}{r^2}\frac{\partial}{\partial r}\left(r^2\frac{\partial p_\mathrm{a}}{\partial r}\right) - \frac{1}{w^2}\frac{\partial^2 p_\mathrm{a}}{\partial t^2} = 0. \tag{4.8}$$

The solution of this partial differential equation for the acoustic pressure p_a can easily be derived by introducing the new dependent variable [198]

$$P = r p_\mathrm{a}. \tag{4.9}$$

In terms of P, the wave equation takes the form

$$\nabla^2 P - \frac{1}{w^2}\frac{\partial^2 P}{\partial t^2} = 0, \tag{4.10}$$

which has the same structure as the wave equation for plane waves. Therefore, the general solution for P can be written in analogy with the solution for plane waves (see Sec. 2.3) as

$$P = P(t \pm r/w) \tag{4.11}$$

The minus sign describes an outgoing spherical wave, and the plus sign represents an incoming spherical wave. Thus, the solution for p_a is

$$p_\mathrm{a} = \frac{P(t - r/w)}{r}, \quad r \neq 0, \tag{4.12}$$

where only the outgoing wave has been considered.

With this result, the velocity potential and pressure field of a point source in free space can be constructed (see also Morse and Ingard [134, Secs. 7.1 and 7.4]). A finite spherical source with radius a placed at the origin is considered, which can be viewed as a vibrating sphere. The surface of the sphere moves with the velocity $v(t) = v_r(t, r = a)$ and generates the volume flow $\dot{V}(t) = 4\pi a^2 v(t)$ at the surface. At the surface, the radial component of the momentum balance in spherical coordinates reads

$$\rho \frac{\partial v_r}{\partial t} = -\frac{\partial p_\mathrm{a}}{\partial r}, \tag{4.13}$$

in which ρ denotes the fluid density. With the volume flow $\dot{V}$ and the transformation $P = r p_\mathrm{a}$, it becomes

$$\frac{\rho}{4\pi a^2}\frac{\partial \dot{V}}{\partial t} = -\frac{1}{r}\frac{\partial P}{\partial r} + \frac{P}{r^2}. \tag{4.14}$$

If the radius of the sphere is negligible compared with the wave length of the emitted sound waves, that is if $a \ll \lambda$, the derivative $\partial P/\partial r$ is much smaller than the term P/r and can safely be neglected. This condition is satisfied here because the result for the point source will be derived from the one for the finite source below by taking the limit $a \to 0$. Hence, the momentum balance simplifies to

$$\frac{\rho}{4\pi a^2}\frac{\partial \dot{V}}{\partial t} = \frac{P}{r^2}. \tag{4.15}$$

The pressure on the surface of the sphere is therefore given by

$$p_{\mathrm{a}}(t,r) = \frac{\rho}{4\pi r}\frac{\partial \dot{V}}{\partial t}. \tag{4.16}$$

At a distance r from the source, the wave arrives by a time r/w later so that the pressure there is given by

$$p_{\mathrm{a}}(t,r) = \frac{\rho}{4\pi r}\left.\frac{\partial \dot{V}}{\partial t}\right|_{t=t-r/w}, \tag{4.17}$$

where the derivative has to be taken at the time $t - r/w$. By using the relation between the velocity potential and the acoustic pressure, $p_{\mathrm{a}} = \rho\,(\partial\Psi/\partial t)$, the expression

$$\Psi(t,r) = \frac{\dot{V}(t-r/w)}{4\pi r} \tag{4.18}$$

for the velocity potential is obtained.

In the following, the velocity potential is used as the primary variable to describe the sound field. This simplifies numerical calculations because derivatives with respect to time need not be evaluated when calculating the velocity potential. The acoustic pressure can be found after the solution for the velocity potential field has been obtained by $p_{\mathrm{a}} = \rho\,(\partial\Psi/\partial t)$.

In the next step, a point source is considered in the presence of an infinite plane wall, which is assumed to be perfectly rigid. The fluid medium is confined to one

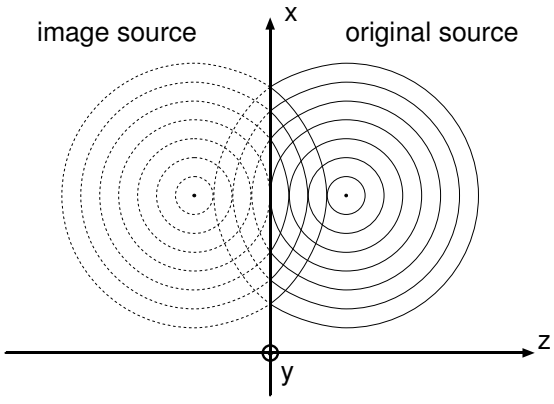

Figure 4.4. Construction of the sound field of a point source in the presence of an infinite plane wall.

side of the wall. At the surface of the wall, the normal fluid velocity is zero. Then, according to Eq. (2.12), the pressure gradient on the surface is also zero. The field of the source can be constructed by imagining that the boundary plane is replaced by a continuation of the fluid into the region behind the plane. In order to retain the boundary condition of zero pressure gradient on the plane, the effect of the boundary is replaced by an image source, which is placed symmetrically with respect to the plane in the continuation of the fluid medium as shown in Fig. 4.4, where the surface of the wall corresponds to the xy plane at $z = 0$. Both, the original source and the image source radiate into free space. The superposition of the parts of the waves from the original source and from the image source in the half space of the original source constitutes the sound field of the original source in the presence of the infinite rigid wall. The part from the image source represents the reflected wave from the boundary surface. The parts of both waves in the half space of the image source have no physical reality.

If the distance of the original source from the wall is much smaller than the wave length of the radiated sound wave, the original and image source can be viewed as if they coincided on the surface of the wall. Then, the influence of the distance of the source from the wall on the sound field is negligible and the source and its image are close enough together so that they can be considered as a single source with double strength. In this limiting case, the reflected wave adds to the original wave yielding a source with strength $2\dot{V}$. Such a source is called baffled point source. The velocity potential field in front of the wall is given by

$$\Psi(t, r) = \frac{\dot{V}(t - r/w)}{2\pi r}, \tag{4.19}$$

where r is the distance from the source as before.

With the model of the baffled point source, the field in front of a sound source, which forms a portion of the plane wall, can now be constructed. The geometry for this situation is depicted in Fig. 4.5. At every point of the surface of the source, a baffled point source is placed. The distance of a point P_0 on the surface of the source with respect to the origin is represented by the vector $\boldsymbol{r}_0$, the vector $\tilde{\boldsymbol{r}}$ describes the position of a point P in front of the source with respect to the origin, and R represents the distance between P and P_0. In order to keep the model as general as possible, it is assumed that the velocity distribution on the source surface is non-uniform and that it can produce an arbitrary transient wave form. The velocity potential field in front of the source can be viewed as a superposition of the fields of baffled point sources placed at every point of the surface of the source.

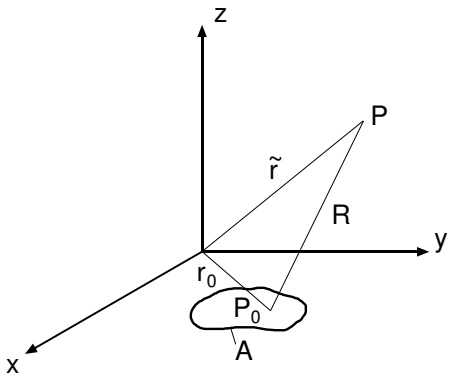

Figure 4.5. Geometry for evaluation of the transient sound field of a sound source with non-uniform vibration amplitude at a point P.

Mathematically, every infinitesimal surface element dA represents a baffled point source with source strength $2v_0dA$, v_0 is the velocity of the element normal to the surface. An integration of the velocity potential over the entire surface of the source yields [73]

$$\Psi(\tilde{\boldsymbol{r}}, t) = \int_A \frac{v_0(\boldsymbol{r}_0, t - R/w)}{2\pi R}\, dA. \tag{4.20}$$

This expression is known as the Rayleigh integral [153]. It describes the transient velocity potential at a point P due to the motion of a source with surface area A, which is located in the plane $z = 0$ and radiates into the positive z half space containing an isotropic, homogeneous, ideal fluid medium. The non-uniform source velocity is in a direction normal to the source plane and is described by the function $v_0(\boldsymbol{r}_0, t)$.

In the present acoustic sensor, the piezoelectric crystal is excited by a sinusoidal burst signal of 60–100 cycles. A typical received echo signal consists of a short transient region at the start, where the vibration amplitude increases to its maximum, a long intermediate region, where the signal amplitude is nearly constant, and a transient region at the end, where the amplitude decays to zero (see Fig. 3.2). Since the cancellation of the echoes is observed in the intermediate region, the signals can be viewed as continuous sinusoidal signals for the purposes of the diffraction correction. The source velocity function for non-uniform vibration can therefore be written as

$$v_0(\boldsymbol{r}_0, t) = v_0(\boldsymbol{r}_0) \exp(i\omega t), \tag{4.21}$$

where it has been assumed that the dependence on time and on position can be separated. $v_0(\boldsymbol{r}_0)$ is the distribution of the surface velocity, which depends on the position on the surface. With this source velocity function, the Rayleigh integral becomes

$$\Psi(\tilde{\boldsymbol{r}}, t) = \exp(i\omega t) \int\limits_A \frac{v_0(\boldsymbol{r}_0) \exp(-ikR)}{2\pi R}\, dA, \tag{4.22}$$

in which $k = \omega/w$ represents the wave number.

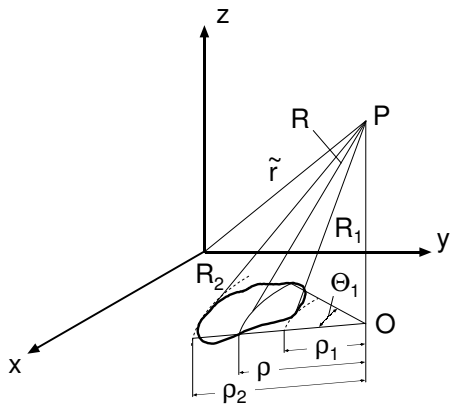

Figure 4.6. Geometry for determining the velocity potential at a point P.

For the evaluation of the integral over the surface of the source, the geometry shown in Fig. 4.6 is introduced. If the source were excited by a δ impulse at time $t = 0$, then at the later time R/w only points on the source with a distance R from the point P would contribute to the velocity potential at P. The set of these points forms the segment of a circle, whose center coincides with the point O and whose radius ρ satisfies $\rho^2 + z^2 = R^2$. ρ_1 and ρ_2 are the radii of the circles with centers at O, which touch the surface of the source first and last, respectively. Θ_1 is the angle with vertex at O formed by the segment of the circle with radius ρ, which lies within the source boundary. Θ_1 changes with R and is zero for $\rho < \rho_1$ and $\rho > \rho_2$. The origin of the coordinate system is shifted to the point O and cylindrical coordinates are introduced. With $dA = \rho\, d\rho\, d\Theta$, Eq. (4.22) becomes

$$\Psi(\tilde{\boldsymbol{r}}, t) = \exp(i\omega t) \int\limits_{\rho_1}^{\rho_2} \int\limits_0^{\Theta_1(\rho)} \frac{v_\sigma(\rho, \Theta) \exp(-ikR)}{2\pi R}\, d\Theta\, \rho\, d\rho. \tag{4.23}$$

In order to distinguish the velocity in the different reference frames, v_0 refers to coordinates with respect to the origin of the space-fixed Cartesian coordinate system and v_σ to observer-based coordinates. Substitution of ρ by the new integration variable R by using the relation $R^2 = \rho^2 + z^2$ yields

$$\Psi(\tilde{\boldsymbol{r}}, t) = \exp(i\omega t) \int_{R_1}^{R_2} \int_{0}^{\Theta_1(R)} \frac{v_\sigma(R, \Theta) \exp(-ikR)}{2\pi} \, d\Theta \, dR. \tag{4.24}$$

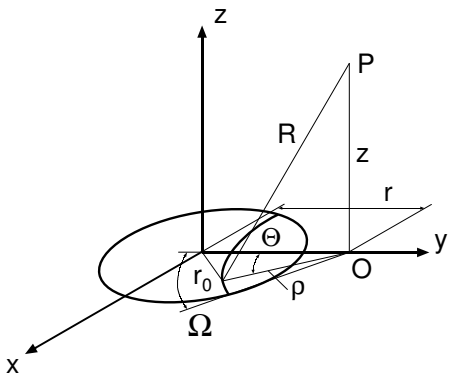

Figure 4.7. Geometry for determining the velocity potential field in front of a finite circular source with radius a located at the origin.

The acoustically active region of the piezoelectric crystal, that is the area of the surface covered by the electrodes, forms a circle (see Fig. 3.4). It is assumed that the source velocity distribution is symmetric with respect to the center of the crystal. Therefore, the sound field in front of the crystal is symmetric with respect to the center axis of the crystal, and the geometry can be described by cylindrical coordinates as shown in Fig. 4.7. The origin is located in the center of the source, the radius of the source is denoted by a, and r_0 refers to the distance between a point on the source surface and the center of the source. Because of the symmetry, the point receiver can always be placed vertically above the y axis at the point (r, z). At this position, the velocity potential field is symmetric with respect to the yz plane so that the integration over Θ between 0 and Θ_1 can be replaced by an integration between 0 and the half angle Ω of the circle segment. The result of this integration must then be multiplied by a factor of two. Thus, the Rayleigh integral for the

circular source geometry takes the form

$$\Psi(r,z,t) = \frac{\exp(i\omega t)}{\pi} \int_{R_1}^{R_2} \int_{0}^{\Omega(R)} v_\sigma(R,\Theta) \exp(-ikR)\, d\Theta\, dR. \tag{4.25}$$

Table 4.4. Models for source velocity distributions.

Model	Functional Form
Polynomial distribution	$v_0(r_0) = A[1-(r_0/a)^2]^n; \quad r_0 < a$
Uniformly vibrating source	$v_0(r_0) = A; \quad r_0 < a$
Simply supported source	$v_0(r_0) = A[1-(r_0/a)^2]; \quad r_0 < a$
Clamped source	$v_0(r_0) = A[1-(r_0/a)^2]^2; \quad r_0 < a$
Gaussian distribution	$v_0(r_0) = A\exp(-br_0^2/a^2)$

In order to evaluate Rayleigh integral, the velocity distribution on the surface of the source must be specified. Different models have been described in the literature [73, 134], from which a selection is summarized in Table 4.4. For each model, the source velocity normal to the surface is specified as a function of the radial coordinate r_0. The uniformly vibrating source, simply supported source, and clamped source are special cases of the polynomial source velocity distribution with $n = 0$, 1, and 2, respectively.

Graphs of the velocity distributions for the geometry of the piezoelectric crystal are depicted in Fig. 4.8. The functional form of the polynomial distributions is limited to the acoustically active surface of the source, while the Gaussian distribution extends to infinity. With this assumption, the evaluation of the Rayleigh integral for the Gaussian distribution is simplified, while changing the result for the velocity potential only little, because the distribution decays to zero rapidly outside the source surface. The Gaussian distribution with $b = 2$ is assumed to provide the closest description of the crystal vibration and will therefore be used to calculate the diffraction correction. The acoustically active area of the source is the circular area of the crystal covered by the electrodes. Its motion is described by the peak of the Gaussian distribution. The crystal is clamped in the outer ring area without electrodes, which is modelled by the tail of the distribution. Diffraction corrections will also be calculated for the other distributions in order to examine the influence of the source velocity distribution on the sound field in the sensor.

The Rayleigh integral, Eq. (4.25), is evaluated in the the observer-based coordinate system with the coordinates $R = wt$ and Θ, whereas the source velocity

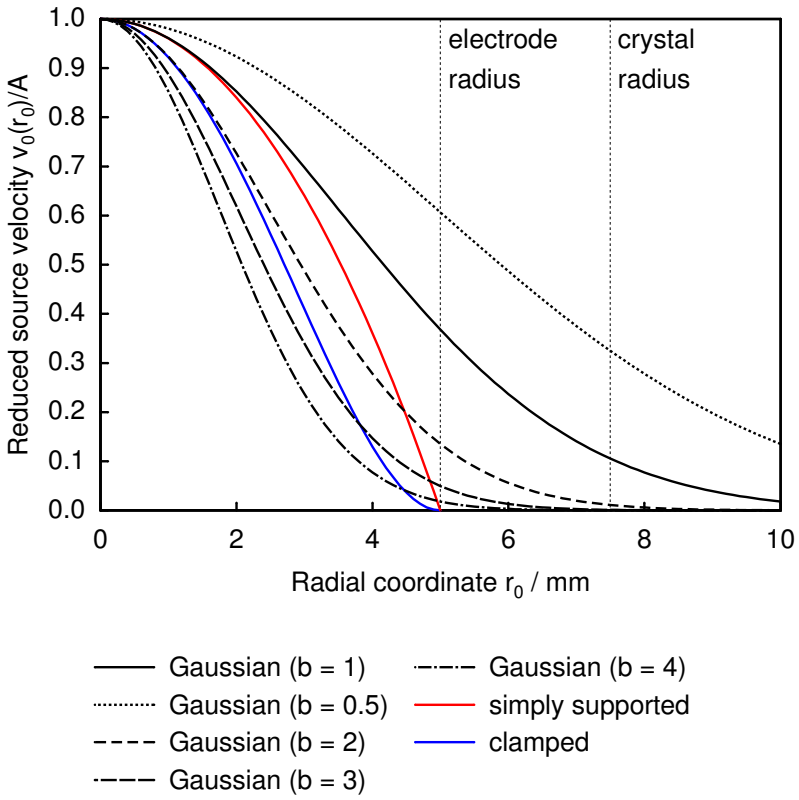

Figure 4.8. Graphs of the source velocity distributions given in Table 4.4 within the geometry of the piezoelectric crystal.

distributions in Table 4.4 are formulated in the source-centered frame. Thus, the source velocity distributions must be written in terms of observer-based coordinates. The relation between source-centered to observer-based coordinates is established by applying the law of cosine to the triangle formed by the distances r, r_0, and $(R^2 - z^2)^{1/2}$ and the angle Θ in Fig. 4.7:

$$r_0^2 = R^2 - z^2 + r^2 - 2(R^2 - z^2)^{1/2} r \cos\Theta. \tag{4.26}$$

With the new variables

$$\gamma = R^2 - z^2 + r^2 - a^2 \tag{4.27}$$

and

$$\eta = 2(R^2 - z^2)^{1/2} r, \tag{4.28}$$

one finds

$$\cos\Theta = (a^2 - r_0^2 + \gamma)/\eta. \tag{4.29}$$

Thus,

$$\left(\frac{r_0}{a}\right)^2 = 1 - \frac{\eta\cos\Theta - \gamma}{a^2}. \tag{4.30}$$

With this result, the polynomial distribution takes the form

$$v_\sigma(R,\Theta) = A[(\eta\cos\Theta - \gamma)/a^2]^n \tag{4.31}$$

in observer-based coordinates, and the result for the Gaussian distribution is

$$v_\sigma(R,\Theta) = A\exp\{-(\gamma + a^2)/a^2\}\exp\{\eta\cos\Theta/a^2\}. \tag{4.32}$$

In both cases, the integration over Θ in Eq. (4.25) can be carried out analytically. For the polynomial distribution with $n = 0$, 1, and 2, one obtains

$$\Psi(r,z,t) = \frac{A\exp(i\omega t)}{\pi}\int_{R_1}^{R_2}\Omega\exp(-ikR)\,dR, \tag{4.33}$$

$$\Psi(r,z,t) = \frac{A\exp(i\omega t)}{\pi a^2}\int_{R_1}^{R_2}[\eta\sin\Omega - \gamma\Omega]\exp(-ikR)\,dR, \tag{4.34}$$

$$\Psi(r,z,t) = \frac{A\exp(i\omega t)}{\pi a^4}\int_{R_1}^{R_2}\left[\left(\frac{\eta^2}{2} + \gamma^2\right)\Omega - 2\gamma\eta\sin\,\Omega + \frac{\eta^2}{4}\,\sin\,2\Omega\right]\exp(-ikR)\,dR, \tag{4.35}$$

respectively.

Since the Gaussian distribution extends to infinity, the upper integration limit is the angle π, and the integral can also be solved analytically with the result

$$\begin{aligned}\Psi(r,z,t) &= \frac{A\exp(i\omega t)}{\pi}\int_{R_1}^{R_2}\exp\{-(\gamma + a^2)/a^2\}\int_0^\pi\exp\{\eta\cos\Theta/a^2\}\,d\Theta\,dR \\ &= A\exp(i\omega t)\int_{R_1}^{R_2}\exp\{-(\gamma + a^2)/a^2\}I_0(\eta/a^2)\,dR,\end{aligned} \tag{4.36}$$

where I_0 is the modified Bessel function of the first kind of order zero, for which the relation

$$I_0(z) = \frac{1}{\pi}\int_0^\pi\exp\{z\cos\Theta\}\,d\Theta \tag{4.37}$$

Table 4.5. Values for the lower and upper integration limits R_1 and R_2, and the angle Ω in Eqs. (4.33) to (4.36) in regions I and II.

	R_1	R_2	Ω
Region I	$[z^2+(r-a)^2]^{1/2}$	$[z^2+(r+a)^2]^{1/2}$	$\cos\Omega = \dfrac{r^2-a^2+R^2-z^2}{2r(R^2-z^2)^{1/2}}$
Region II $\rho > a-r$ $R > [z^2+(r+a)^2]^{1/2}$	z	$[z^2+(r+a)^2]^{1/2}$	$\cos\Omega = \dfrac{r^2-a^2+R^2-z^2}{2r(R^2-z^2)^{1/2}}$
Region II $\rho \leq a-r$ $R \leq [z^2+(r+a)^2]^{1/2}$	z	$[z^2+(r+a)^2]^{1/2}$	$\Omega = \pi$

holds for arbitrary values of z [1, p. 376].

In order that Eqs. (4.33)-(4.36) yield the velocity potential Ψ as a function of the coordinates r and z and time t, the limits of the integration R_1 and R_2 must be expressed in terms of r and z, and the angle Ω must be written as a function of R, r, and z. These relations can be derived by simple geometrical considerations. Three different cases can be distinguished, depending on the position of the point receiver relative to the source. The half space $z \geq 0$ in front of the source plane is partitioned into two regions, one with $r > a$ (denoted by I), which is the volume in front of the source plane without the cylindrical volume in front of the source, and one with $r \leq a$ (denoted by II), which forms the cylindrical volume in front of the source.

If the point receiver is placed somewhere in region I (see Fig. 4.7), the lower and upper integration limits are given by $R_1 = [z^2+(r-a)^2]^{1/2}$ and $R_2 = [z^2+(r+a)^2]^{1/2}$. For a point receiver placed in region II, $R_1 = z$, and $R_2 = [z^2+(r+a)^2]^{1/2}$. The angle Ω is found by considering a projection of the three-dimensional situation depicted in Fig. 4.7 onto the source plane as shown in Fig. 4.9 for the regions I and II. An expression for Ω is obtained by applying the law of cosine to the triangle formed by Ω, the source radius a, the distance between the center of the source and the origin r, and the projection of R into the source plane, which is denoted by $\rho = (R^2-z^2)^{1/2}$. If $\rho \leq a-r$, $\Omega = \pi$. The results for R_1, R_2 and Ω are summarized in Table 4.5.

With the velocity potential field of a circular source, the pressure measured by a circular receiver can now be constructed. A finite circular receiver with surface A_h, which is placed at a distance h in front of and parallel to the source, detects

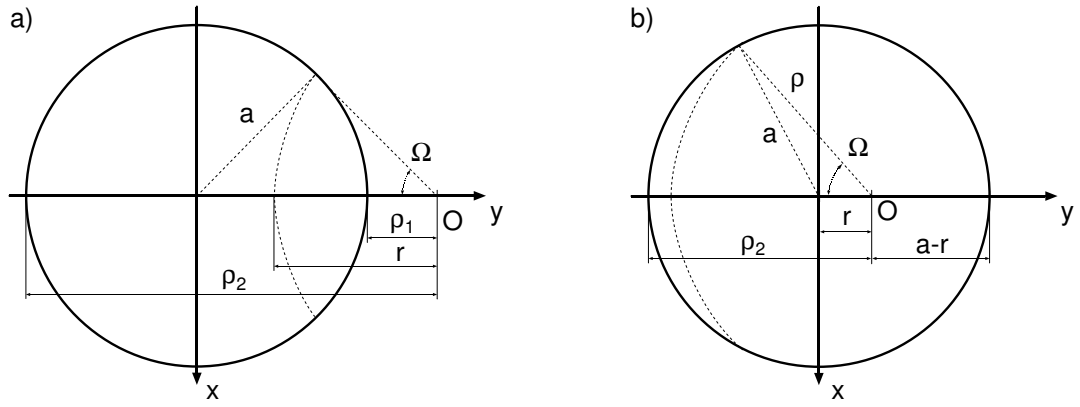

Figure 4.9. Geometry for determining the angle Ω a) in region I and b) in region II.

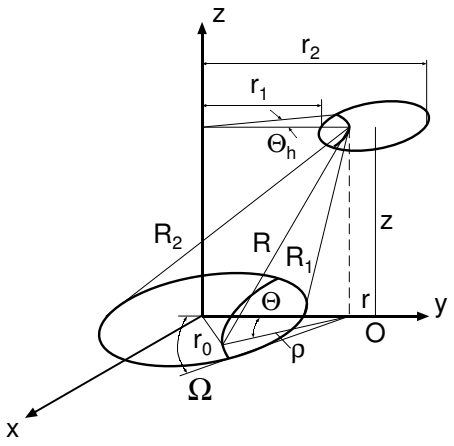

Figure 4.10. Geometry for determining the average velocity potential detected by a finite circular receiver in front of a circular source.

the average pressure acting on its surface. The average pressure is related to the average velocity potential by

$$\langle p(r,z,t)\rangle = \rho\,\frac{\partial\langle\Psi(r,z,t)\rangle}{\partial t} = \rho\,\frac{\partial}{\partial t}\int\limits_{A_h}\Psi(r_h,z,t)\,dA_h, \tag{4.38}$$

where the angular brackets denote an average over the receiver surface, r and z specify the center of the receiver and $\Psi(r_h,z,t)$ is the local velocity potential at the point (r_h,z) on the receiver surface at time t. The geometry for this situation is depicted in Fig. 4.10. The receiver is located at a distance z in parallel with

the source plane, has a radius h, and the distance between the projection of its center onto the source plane and the source center is denoted by r. The position of a surface element $dA_h = r_h\, dr_h\, d\Theta_h$ on the receiver surface is described by the cylindrical coordinates r_h and Θ_h with the origin in the source center. Within this geometry, the average velocity potential on the receiver surface is given by

$$\langle \Psi(r,z,t) \rangle = \frac{2}{\pi h^2} \int_{r_1}^{r_2} \int_{0}^{\Theta_h(r_h)} \Psi(r_h,z,t) r_h \, d\Theta_h \, dr_h \tag{4.39}$$

The factor of two arises because the angle Θ_h measures only half circle segments on the surface.

For axisymmetric source distributions, the integrand $\Psi(r_h,z,t)$ is independent of the angle Θ_h, and Eq. (4.39) simplifies to

$$\langle \Psi(r,z,t) \rangle = \frac{2}{\pi h^2} \int_{r_1}^{r_2} \Psi(r_h,z,t) \Theta_h(r_h) r_h \, dr_h. \tag{4.40}$$

The function $\Psi(r_h,z,t)$ is determined by one of the Eqs. (4.33)-(4.36), depending on the source velocity distribution, where the variable r must be replaced by r_h, because r_h represents the positions on receiver surface and r refers to the center of the circular receiver.

As for the integration over the source surface, the values of the integration limits r_1 and r_2 must be expressed in terms of r and h, and the angle $\Theta_h(r_h)$ must be expressed in terms of r, r_h, and h. Again, three different cases must be distinguished, which depend on the size and position of the receiver relative to the source. Case I refers to the situation in which $r > h$, while in case II $r \leq h$. In case II, two different subcases arise with $r_h > h - r$ and $r_h \leq h - r$. The geometry for these three situations is depicted in Fig. 4.11, and the results for r_1, r_2, and $\Theta_h(r_h)$ are summarized in Table 4.6. The results for r_1 and r_2 can easily be extracted from Fig. 4.11. The value of the angle Θ_h is determined by applying the law of cosine to the triangle formed by r_h, r, and h as

$$\cos \Theta_h(r_h) = \frac{r_h^2 + r^2 - h^2}{2 r r_h}, \tag{4.41}$$

in case I and in the subcase $r_h > h - r$ of case II. In case II, if $r_h \leq h - r$, $\Theta_h = \pi$.

With the results collected in Table 4.6, the average velocity potential detected by a circular receiver can be calculated by Eq. (4.40). The solution of the integral

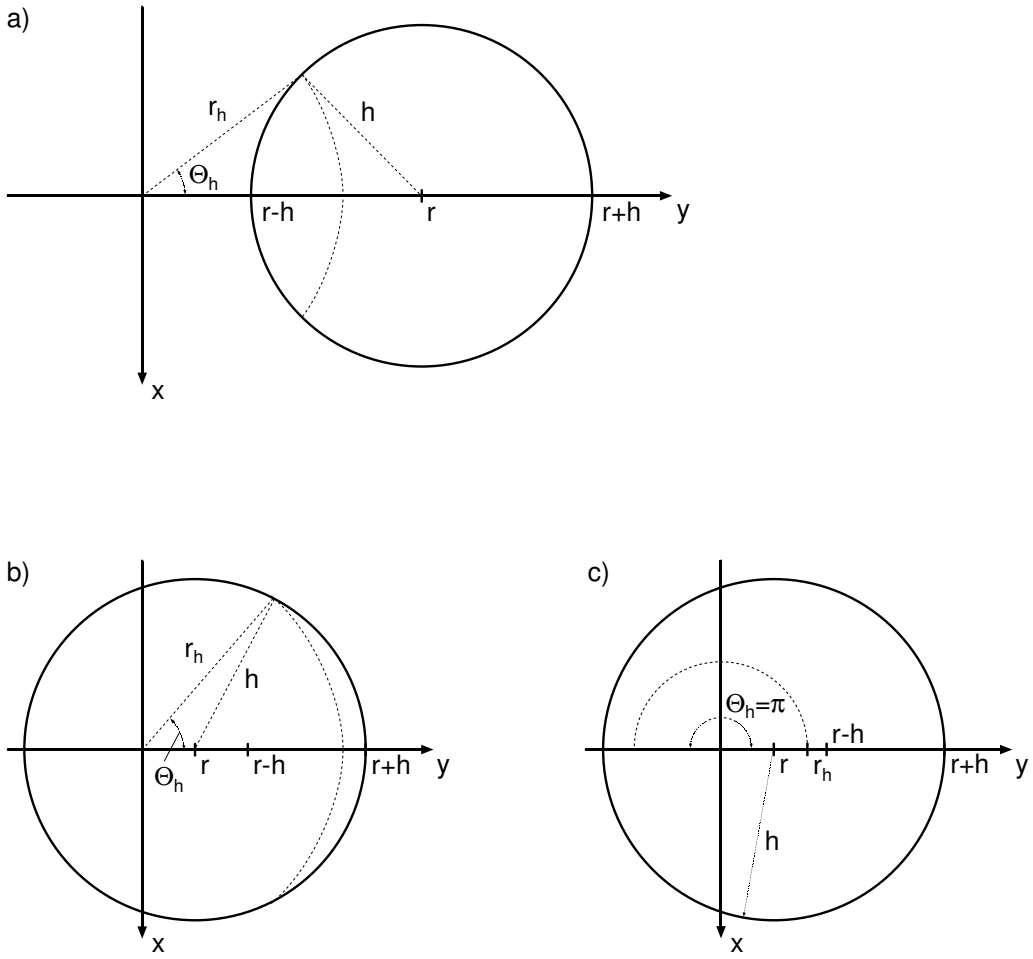

Figure 4.11. Geometry for the integration over a finite circular receiver located at r.

requires a twofold integration, which, in general, must be carried out numerically. For all numerical calculations described below, the twofold integration was carried out with an algorithm published by Press et al. [151, pp. 155].

These general results can now be applied to the geometry of the acoustic sensor. The time difference is measured by adjusting the time difference between two exciting burst signals so that the second echo from the first excitation signal cancels the first echo from the second excitation signal (see Sec. 3.1). Since this time difference exactly equals the time difference between the arrival of the first echoes from each reflector, if only one burst is applied to excite the piezoelectric crystal, the diffraction correction is derived for this latter situation because it is simpler to model than the cancellation of two echo signals. The model of the acoustic sensor, for which the

Table 4.6. Values for the lower and upper integration limits r_1 and r_2 and the angle Θ_h in the integration over a circular receiver.

Case	r_1	r_2	Θ_h
I	$r-h$	$r+h$	$\cos\Theta_h = \dfrac{r_h^2+r^2-h^2}{2rr_h}$
II $r_h > h-r$	0	$r+h$	$\cos\Theta_h = \dfrac{r_h^2+r^2-h^2}{2rr_h}$
II $r_h \leq h-r$	0	$r+h$	$\Theta_h = \pi$

diffraction correction will be derived, is depicted in Fig. 4.12. In the acoustic sensor, sender and receiver are both realized by the piezoelectric crystal, and therefore both have circular geometry and the same size. The reflections at the stainless steel reflectors are assumed to be ideal so that – as for the point source in front of a plane wall in the beginning of this section – the spaces behind the reflector planes can be viewed as a continuation of the sample fluid. The detection of the first two echo signals by the piezoelectric crystal is modelled as a separate detection of each echo by two receivers, which are placed on an axis with the reflectors and sender at distances L_1 and L_2 in the continuation of the fluid behind the reflectors.

Within this model, diffraction corrections are derived for the transit times the two signals need to travel the distances $2L_1$ and $2L_2$. The diffraction correction for the time difference between the arrival of the first two echoes is then the difference of the diffractions corrections for the two transit times.

If a signal propagated as a plane wave, the longitudinal velocity and velocity

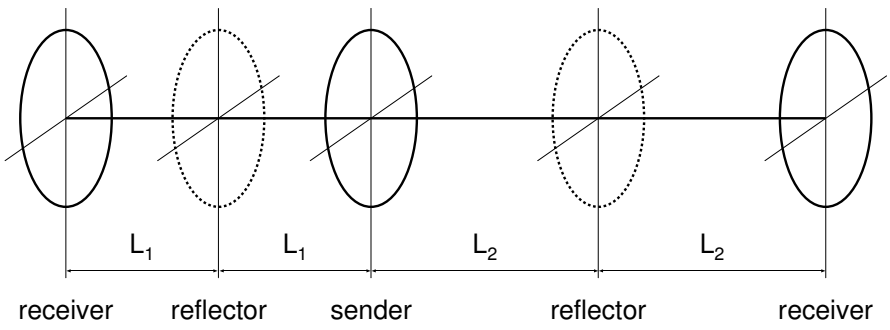

Figure 4.12. Model of the acoustic sensor for the calculation of the diffraction correction.

potential at a distance z from the source would be given by

$$v_1^{\mathrm{pw}}(z,t) = A_0 \exp(i\omega t) \exp(-ikz), \tag{4.42}$$

and

$$\Psi^{\mathrm{pw}}(z,t) = \frac{A_0}{ik} \exp(i\omega t) \exp(-ikz). \tag{4.43}$$

The acoustic pressure detected by a receiver placed at this distance in parallel and on an axis with the source would be

$$p_{\mathrm{a}}^{\mathrm{pw}} = A_0 \rho w \exp(i\omega t) \exp(-ikz) = A_0 \rho w \exp(i\omega t)[\cos(kz) - i \sin(kz)], \tag{4.44}$$

where the relation $w = \omega/k$ has been used.

On the other hand, the average acoustic pressure of the sound field in front of a finite circular source with non-uniform vibration amplitude measured by a circular receiver placed at the distance z in parallel and on an axis with the source is in general given by Eq. (4.38). In order to evaluate this equation, the expression for the velocity potential field of the source must be inserted, and the geometry of the sensor model must be adapted. These steps are exemplified here for the case of a simply-supported source with polynomial velocity distribution with $n = 1$. If the sender and receiver have the same size and are located on an axis, the integration over the angular coordinate on the receiver surface Θ_h yields π, independent of the source velocity distribution, and the average velocity potential detected by the receiver becomes

$$\langle \Psi(z,t) \rangle = A_0 \exp(i\omega t) \frac{2}{\pi a^4} \int_0^a \int_z^{R_2(r_h)} (\eta \sin\Omega - \gamma\Omega) \cdot(\cos(kR) - i \sin(kR)) r_h \, dR \, dr_h. \tag{4.45}$$

This expression may be written in the form

$$\langle \Psi(z,t) \rangle = A_0 \exp(i\omega t)(C + iD) \tag{4.46}$$

with

$$C = \frac{2}{\pi a^4} \int_0^a \int_z^{R_2(r_h)} (\eta \sin\Omega - \gamma\Omega) \cos(kR) r_h \, dR \, dr_h \tag{4.47}$$

and

$$D = -\frac{2}{\pi a^4} \int_0^a \int_z^{R_2(r_h)} (\eta \sin\Omega - \gamma\Omega) \sin(kR) r_h \, dR \, dr_h. \tag{4.48}$$

The average pressure is then given by

$$\langle p_\mathrm{a}(z,t)\rangle = \rho \frac{\partial\langle\Psi\rangle}{\partial t} = A_0 \rho w k \exp(i\omega t)(-D + iC), \tag{4.49}$$

and the ratio of the pressure and the plane wave pressure is given by

$$\begin{aligned} \frac{\langle p_\mathrm{a}(z,t)\rangle}{p_\mathrm{a}^\mathrm{pw}(z,t)} &= \frac{k(-D+iC)}{\cos(kz) - i\sin(kz)} \\ &= -k[D\cos(kz) + C\sin(kz)] + ik[-D\sin(kz) + C\cos(kz)] \\ &= A + iB \end{aligned}$$

with

$$A(z) = -k[D\cos(kz) + C\sin(kz)] \tag{4.50}$$

and

$$B(z) = k[-D\sin(kz) + C\cos(kz)]. \tag{4.51}$$

The phase advance of the real wave $\varphi(z)$ due to diffraction compared with the plane wave is determined by

$$\tan\varphi(z) = B(z)/A(z). \tag{4.52}$$

The difference due to diffraction between transit times of the plane wave and real wave is given by

$$\Delta t_\mathrm{dc}(z) = \frac{\varphi(z)}{2\pi} T_\mathrm{p} = \frac{\varphi(z)}{2\pi f} = \frac{\varphi(z)}{\omega}, \tag{4.53}$$

where $T_\mathrm{p} = 1/f$ denotes the period of the wave.

Applying this result to the model of the sensor, one obtains

$$\Delta t_\mathrm{dc} = [\varphi(2L_2) - \varphi(2L_1)]/\omega \tag{4.54}$$

for the diffraction correction to the measured time difference. The time difference for plane wave propagation, which must be inserted into the working equation of the sensor $w = \Delta L/\Delta t^\mathrm{pw}$, is then found as

$$\Delta t^\mathrm{pw} = \Delta t^\mathrm{m} + \Delta t^\mathrm{dc}. \tag{4.55}$$

The diffraction correction depends on the geometry of the sensor, that is the radius of the piezoelectric crystal and the distances between the crystal and the reflectors, and the frequency and the wave number of the sound waves. Since the frequency is fixed at $f = 8$ MHz, the dependence on the wave number can be replaced by a dependence on the value of the speed of sound. As the geometry is also fixed, the diffraction correction can be represented solely as a function of the speed of sound. For the following calculations, the source and receiver radius was set to $a = h = 5\,\mathrm{mm}$, which is the radius of the electrode area on the crystal, and the values $L_1 = 19.9430\,\mathrm{mm}$ and $L_2 = 29.8025\,\mathrm{mm}$ measured by the coordinate measuring machine were used for the distances between the crystal and the reflectors. Small changes of the acoustic path length, for example due to thermal expansion or compression of the sensor under pressure, have only a very small influence on the diffraction correction and are therefore neglected.

With this model, the diffraction correction was calculated as a function of the speed of sound in the sample fluid for the different source velocity distributions listed in Table 4.4. For the Gaussian distribution, the four different values 1, 2, 3, and 4 of the width of the distribution b were considered. The results of these calculations are depicted in Fig. 4.13, which displays the percentage contribution of the diffraction correction to the measurement value of the speed of sound as a function of the speed of sound. For all source velocity distributions, the diffraction correction increases from values between 0 % and 0.001 % for a speed of sound of 500 $\mathrm{m\,s^{-1}}$ to values between 0.006 % and 0.01 % for a speed of sound of 2000 $\mathrm{m\,s^{-1}}$. Thus, the diffraction correction contributes only little to the measurement value of the speed of sound. However, for high precision measurements, this small contribution cannot be neglected. The diffraction corrections for the source with Gaussian amplitude distribution and for the model of a clamped source increase monotonically with the speed of sound, whereas for the planar piston source with uniform vibration amplitude and for the model of a simply-supported source the increase is superimposed by a pattern of local maxima and minima. This oscillating behavior is due to the edge wave contributions to the sound field, which are most pronounced for the planar piston source with uniform vibration amplitude and for the model of a simply-supported source because, in these cases, the source velocity distribution decays to zero very rapidly at the edge of the source. The behavior of the piezoelectric crystal in the sensor is approximated by the Gaussian distribution with width $b = 2$. As all speeds of sound measured in this work were smaller than 1700 $\mathrm{m\,s^{-1}}$, the diffraction correction is always smaller than 0.006 %.

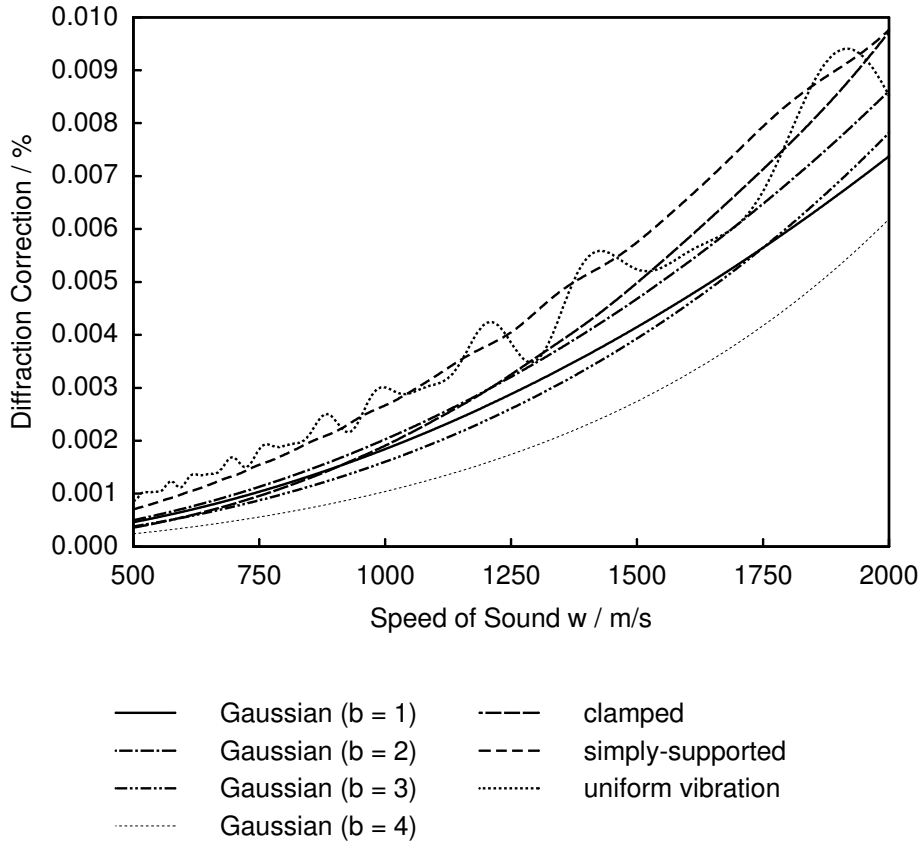

Figure 4.13. Percentage contribution of the diffraction correction to the measured time difference as a function of the speed of sound in the sample fluid for different source velocity distributions.

For the integration of the diffraction correction in the measurement analysis, the contribution to the measured time difference is represented by a third-order polynomial function, whose coefficients were fitted to the results for the Gaussian distribution with $b = 2$. The polynomial representation has the form

$$\frac{\Delta t^{\mathrm{dc}}}{\mu\mathrm{s}} = 3.886503 \cdot 10^{-7} \left(\frac{w}{\mathrm{m\,s^{-1}}}\right) + 3.165669 \cdot 10^{-12} \left(\frac{w}{\mathrm{m\,s^{-1}}}\right)^2 + 7.158732 \cdot 10^{-15} \left(\frac{w}{\mathrm{m\,s^{-1}}}\right)^3, \quad (4.56)$$

which ensures that the diffraction correction vanishes in the limit $w \to 0$. It represents the correction to the measured time difference within 1 % for values of the speed of sound between $50\,\mathrm{m\,s^{-1}}$ and $2000\,\mathrm{m\,s^{-1}}$. The uncertainty of the diffraction correction is estimated to be smaller than 0.001 %, which accounts for the incomplete knowledge of the amplitude distribution of the source vibration.

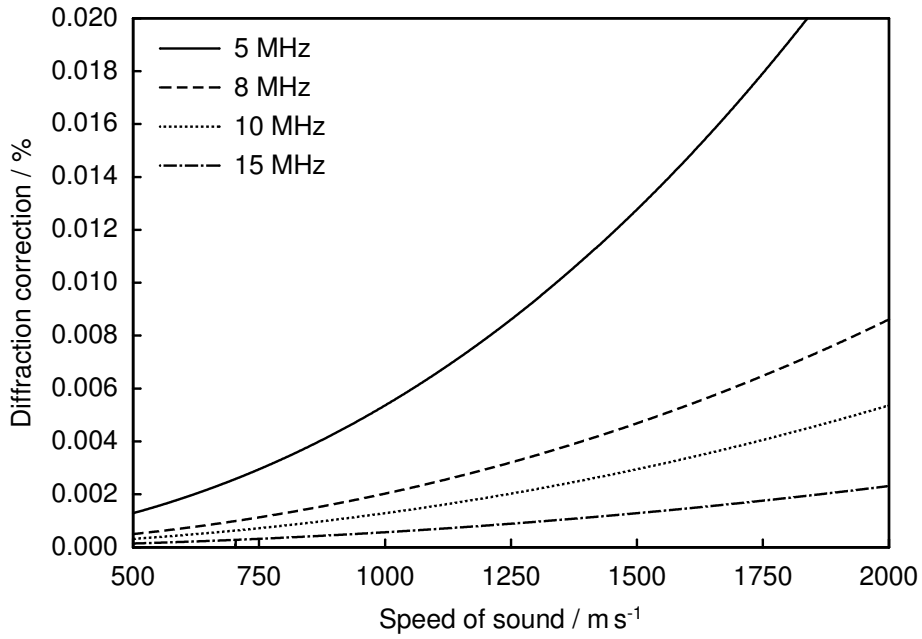

Figure 4.14. Percentage contribution of the diffraction correction to the measured time difference as a function of the speed of sound in the sample fluid for different excitation frequencies.

As the final point in this section, it is instructive to examine the influence of the frequency and transducer radius on the diffraction correction. Figs. 4.14 and 4.15 show the percentage contribution of the diffraction correction to the measured time difference as a function of the speed of sound for selected values of the frequency and transducer radius. In Fig. 4.14, the transducer radius was held constant at $a =$ 5 mm, while in Fig. 4.15 the frequency was fixed at 8 MHz. As can be observed from Figs. 4.14 and 4.15, the diffraction correction decreases with increasing frequency and increasing transducer radius. With the present choice of 5 mm for the radius of the acoustically active area and 8 MHz for the frequency, the diffraction correction is always smaller than 0.01 % for measured speeds of sound up to $2000\,\mathrm{m\,s^{-1}}$.

4.3 Calibration Procedure

For the determination of the speed of sound at a given temperature and pressure with the acoustic sensor by the working equation $w = \Delta L/\Delta t^{\mathrm{pw}}$, two quantities must be measured, the acoustic path length ΔL and the time difference Δt between the two emitted burst signals. Since the acoustic path length is determined by

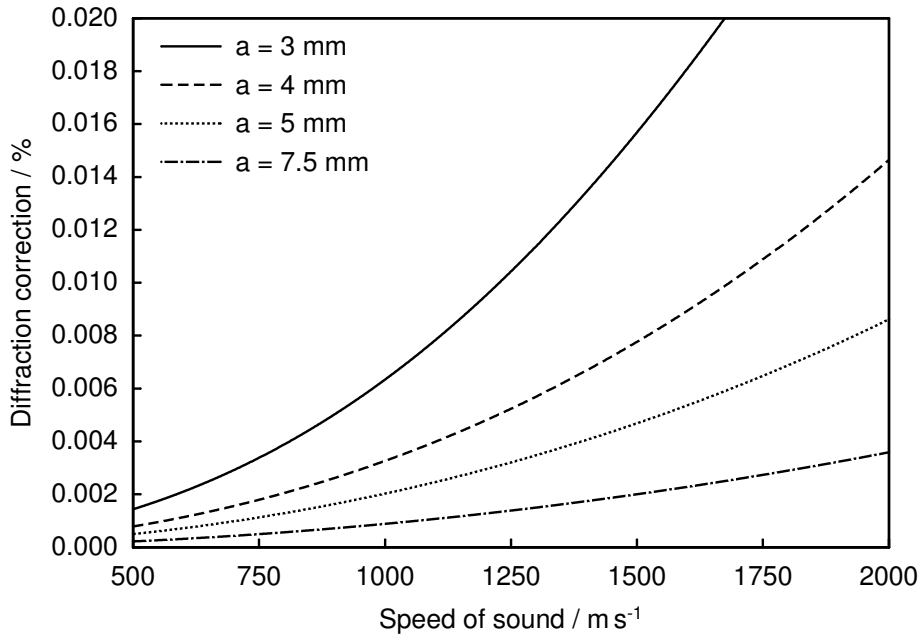

Figure 4.15. Percentage contribution of the diffraction correction to the measured time difference as a function of the speed of sound in the sample fluid for different transducer radii.

the geometry of the sensor, it is fixed during a series of measurements except for changes due to thermal expansion and compression under pressure, which, however, can accurately be predicted with the model developed in Sec. 4.1. Therefore, the acoustic path length is usually determined only once before starting a series of measurements, whereas the time difference must be measured at every state point. There are two different ways of determining the acoustic path length: either by measuring it directly by means of a length measurement device or by calibration measurements with a fluid, for which the speed of sound is accurately known. In principle, the first method is the most desirable because it avoids the uncertainties introduced by calibration measurements, for example uncertainties due to impurities of the sample of the calibration fluid or the uncertainties of the reference values of the speed of sound in the calibration fluid. For this reason, it was first tried to measure the distances between the crystal and the reflectors by a coordinate measuring machine. It turned out that this method was not reliable because, when touching the crystal surface with the sensor of the coordinate measuring machine, the crystal was deformed. Therefore, it was decided to develop a calibration procedure

for the determination of the acoustic path length.

Water was chosen as the calibration liquid because it is the liquid for which the speed of sound is most accurately known. Several authors have measured the speed of sound in liquid water at ambient pressure in the temperature range between 273 K and 373 K with high accuracy, see for example [13, 62, 68, 69, 78, 99, 120, 190], and, furthermore, with the 'IAPWS formulation 1995 for the thermodynamic properties of ordinary water substance for general and scientific use' by Wagner and Pruß [187] an accurate fundamental equation of state is available, from which reference values for the speed of sound can be calculated.

Table 4.7. Literature data sets for the speed of sound in liquid water at ambient pressure (0.101325 MPa). Abbreviations: PE: pulse-echo, IF: interferometer.

Author	Year	Method	Data	T	Uncertainty
Aleksandrov [4]	1976	PE	9	273–373 K	< 0.008 %
Barlow [13]	1967	PE	43	296–353 K	< 0.01 %
Del Grosso [69]	1972	IF	148	273–368 K	< 0.001 %
Fujii [62]	1993	IF	41	293–348 K	< 0.001 %
Greenspan [68]	1957	PE	100	274–373 K	< 0.03 %
Holton [78]	1968	PE	2	323 K	< 0.2 %
Kroebel [99]	1976	IF	20	276–307 K	< 0.003 %
McSkimin [120]	1965	PE	37	296–352 K	< 0.03 %
Petitet [143]	1983	PE	12	253–295 K	< 0.05 %
Wilson [190]	1959	PE	11	274–364 K	< 0.05 %

Details of the literature data sets are summarized in Table 4.7. In order to identify the best reference values for the speed of sound in liquid water at ambient pressure, the literature data from the different sources listed in Table 4.7 are compared with the IAPWS formulation in Fig. 4.16[1)]. The data sets of Del Grosso and Mader [69] and of Fujii and Masui [62] show the highest internal consistency and agree among each other and with the IAPWS formulation within 0.004 %. The data of Greenspan and Tschiegg [68] are also very consistent, but lie by about 0.025 % above the IAPWS formulation. The data of Aleksandrov and Larkin [4], Barlow and Yazgan [13], Kroebel and Mahrt [99], McSkimin [120], Petitet et al. [143], and Wilson [190] show higher scatter than the other data sets, with the data of Kroebel

[1)] For this and all other comparisons in the remainder of this work, the temperatures reported in older publications, which were measured according to the IPTS-48 temperature scale [166, 167] and IPTS-68 temperature scales [30, 145], were converted to the current practical temperature scale ITS-90 [150] by the procedures described by Blanke [23, 24], Douglas [39], and Fay [56].

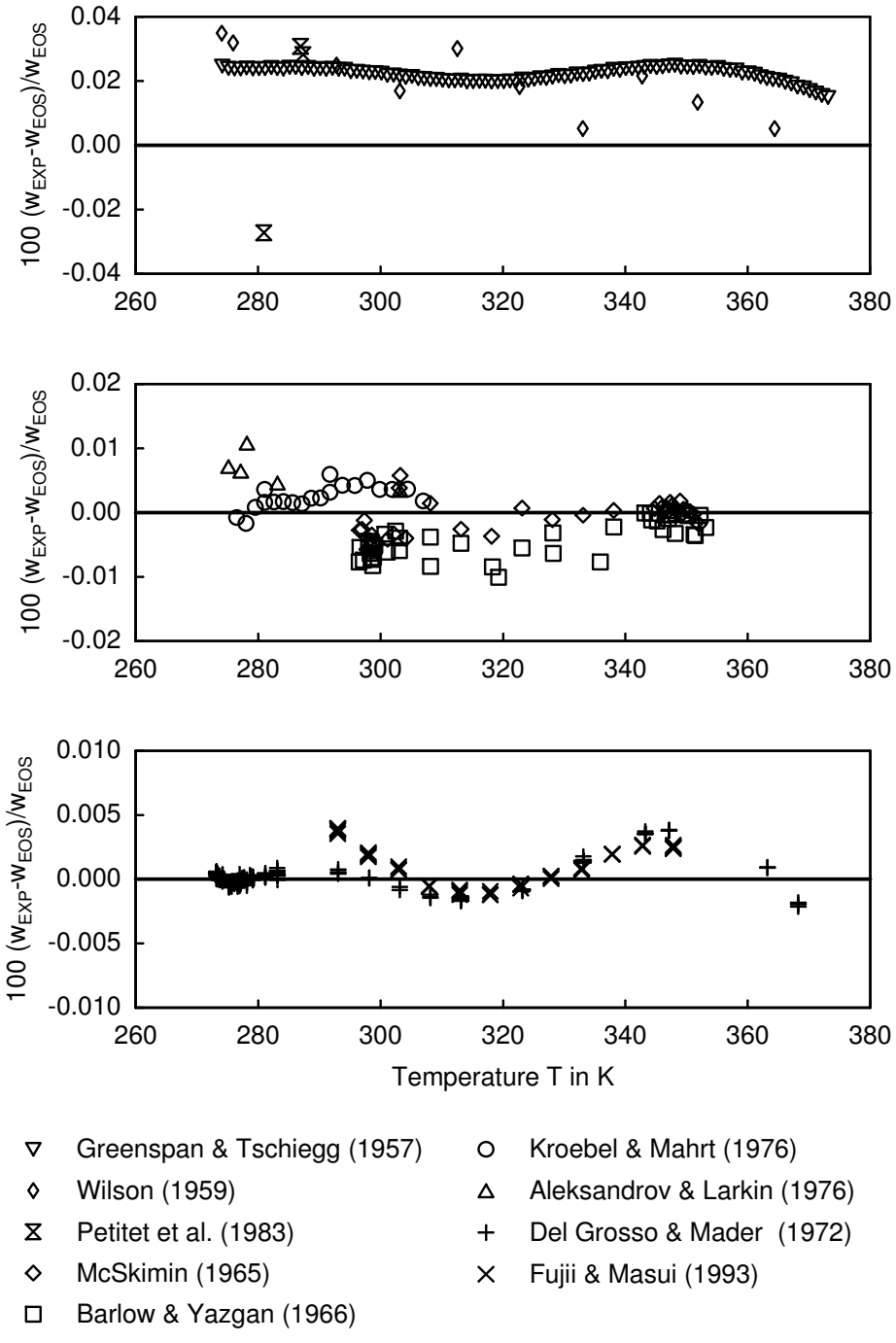

Figure 4.16. Percentage deviations of literature data for the speed of sound in liquid water at ambient pressure from the IAPWS formulation as a function of temperature.

and Mahrt having the highest internal consistency. With the exception of the data of Petitet et al. and of Wilson, these data sets agree with the IAPWS formulation within 0.01 %. From this comparison, it is evident that the data sets of Del Grosso and Mader [69] and of Fujii and Masui [62] are the most accurate data available. For this reason, these two data sets were chosen as reference data for the calibration of the acoustic sensor. As the IAPWS formulation represents the most accurate density data for liquid water at ambient pressure in the low temperature range up to about 315 K within 1 ppm and the speed of sound data of Del Grosso and Mader agree with the IAPWS formulation within their quoted uncertainty of 0.001 % in this temperature range, they are chosen as the primary reference data in the low temperature range between 273.15 K and 315 K.

A thorough discussion of the differences between the data sets of Del Grosso and Mader, Fujii and Masui, and Kroebel and Mahrt was given by Marczak [116]. He concluded that small differences between the three data sets at low temperatures, which were attributed to temperature measurement errors by Fujii and Masui [62], cannot be due to such errors, because the influence of the temperature measurement uncertainties reported by the authors of the three data sets is lower than the difference between the data. Marczak suggested that differences in the purity of the water samples might be the most likely reason for the differences between the data.

Purified water for the calibration measurements was available from two different sources: a deionization station (Wasseraufbereitung und Regenerierstation GmbH, type Reinstwassersystem Ultra Clear UV Plus) and a double distillation apparatus (Heraeus Quarzglas, type Destamat Bi 18 E). Before filling the water sample into the apparatus, it was carefully degassed. For this purpose, the sample container was connected to a vacuum pump so that gas phase was continuously removed. By mechanically knocking at the container, the formation of gas bubbles was initiated. This procedure was applied until the bubble formation had decreased to a negligible level. Before disconnecting the sample container from the vacuum pump, it is closed by a high pressure valve so that the water remains under vapor pressure in the container until it is filled into the apparatus.

The influence of dissolved air on the speed of sound in liquid water was examined by Greenspan and Tschiegg [66]. They prepared water samples, which were 10 % and 100 % saturated with air, and measured the difference in the speed of sound at 0 °C and 31.8 °C. They concluded that the effect of dissolved air on the speed of sound is less than 10 ppm at both temperatures, even for fully saturated water. Since the solubility of air in water is greatest at 0 °C, it can be safely concluded that the

dissolved gases, which remain after the degassing process, have a negligible effect on the speed of sound in the whole temperature range of the calibration measurements between 1 °C and 95 °C. In a different publication, Greenspan and Tschiegg [68] reported that even using local tap water increased the speed of sound only by 30 ppm compared with distilled water.

Before filling the water sample into the apparatus, the thermostat temperature is set to 20 °C, and the pressure vessel and the high pressure tubing system are evacuated. The water is then filled in by sucking it from the sample container at vapor pressure into the evacuated system. Ambient pressure in the pressure vessel is maintained by opening the nitrogen branch of the high pressure tubing system to ambient pressure and adjusting the pressure in the sample liquid branch to ambient pressure by using the differential pressure indicator.

When performing the calibration measurements for the first time for the sensor in

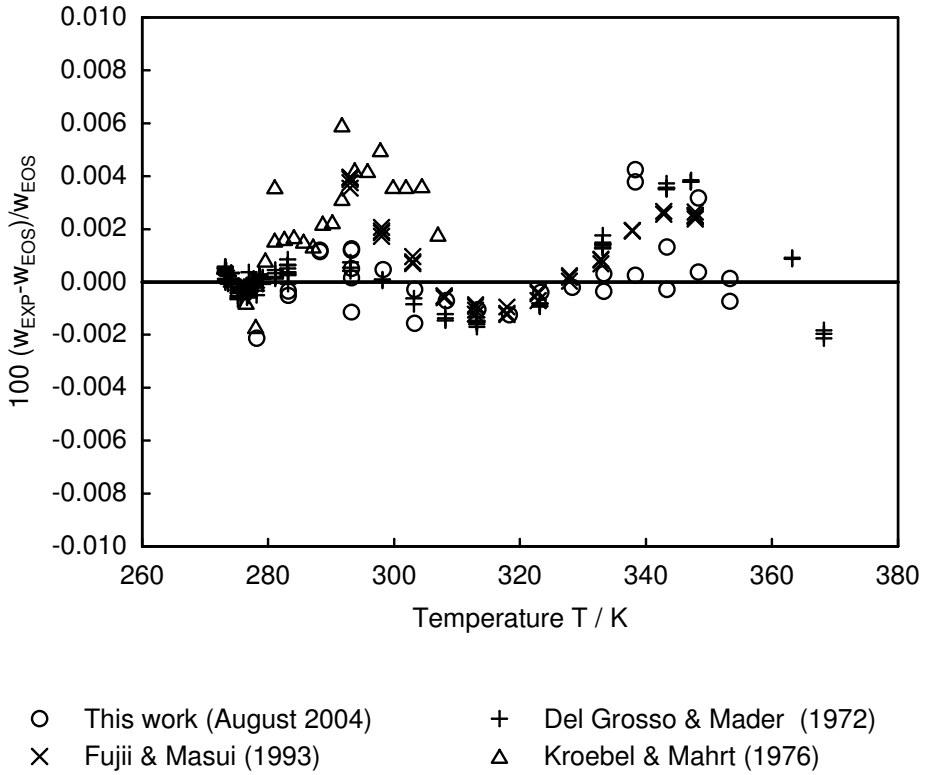

Figure 4.17. Percentage deviations of speed of sound data in liquid water at ambient pressure measured in August 2004 and of literature data from the IAPWS formulation for water [187] as a function of temperature.

August 2004, the temperature was simply changed in steps of 5 K in either direction, that is to lower and higher temperatures. In this first calibration, measurements were taken in the temperature range between 5 °C and 80 °C. Initially, the acoustic path length $\Delta L = 2(L_2 - L_1)$ as measured by the coordinate measuring machine at ambient temperature and the thermal expansion coefficient of the stainless steel 1.4571 as given in the database FEZEN [72] was used in the measurement analysis. The results of this pre-analysis were compared with the IAPWS formulation [187] and with the data of Del Grosso and Mader [69] and of Fujii and Masui [62] by plotting the deviations of the speed of sound data and the two literature data sets from the IAPWS formulation against temperature. The acoustic path length ΔL at (T_0, p_0) and the thermal expansion coefficient were then adjusted so that the deviation pattern of the data agreed optimally with that of the two literature data sets. In this first calibration, the thermal expansion coefficient was assumed to be constant and the different thermal expansion of the quartz crystal and the stainless steel material of the sensor was neglected. The two parameters were determined as

$$\Delta L(T_0, p_0) = 0.0197222\,\mathrm{m} \tag{4.57}$$

and

$$\alpha_{\mathrm{th}} = 15.7 \cdot 10^{-6}\,\mathrm{K}^{-1}. \tag{4.58}$$

The results of these calibration measurements after adjustment the two parameters are shown in Fig. 4.17. The diagram shows percentage deviations of the measured speeds of sound and of the chosen reference data from the IAPWS formulation as a function of temperature. All data agree with the literature data and the equation of state within 0.005 %. The data are very consistent at low temperatures, with the exception of a few data points at 293.15 K. Above 330 K, they tend to scatter, but still agree among each other within 0.004 %. At low temperatures, the deviation pattern is similar to that of the literature data, whereas at high temperatures the data lie mainly between the equation of state and the literature data.

With this calibration, measurements on propane and propene were carried out. During the course of these measurements taken after August 2004, it was found that the direction, in which the temperature is changed, has a small influence of up to about 50 ppm on the result of the speed of sound. This effect is illustrated by measurement results for the speed of sound in liquid propene in Fig. 4.18, which shows percentage deviations of speed of sound data at the state point (300 K, 30.1 MPa) measured over a period of five days. Percentage deviations instead of the

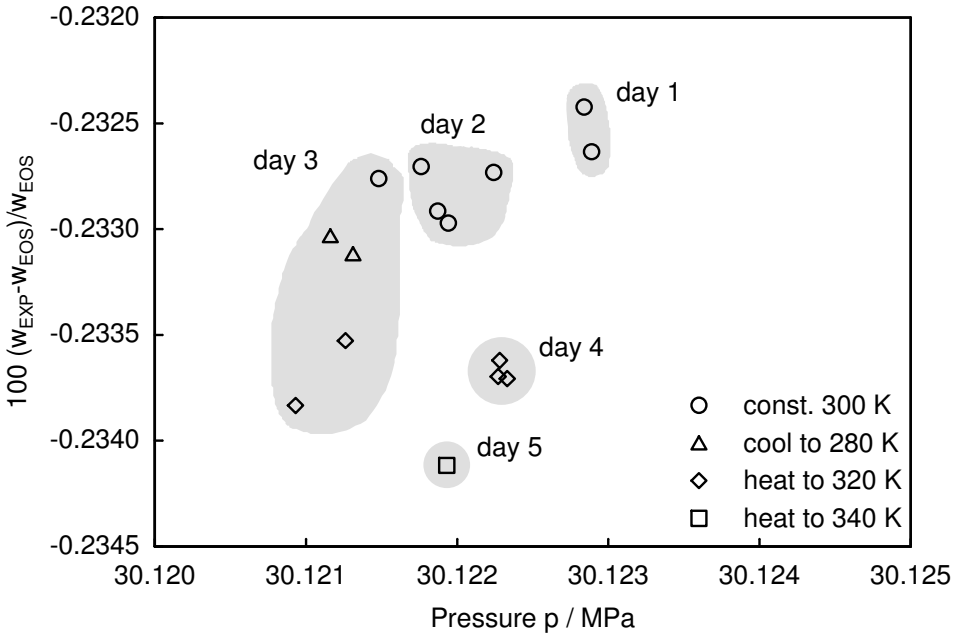

Figure 4.18. Percentage deviations of measured speed of sound data in liquid propene at 300 K under 30.1 MPa from the fundamental equation of state of Angus et al. [7] as a function of pressure.

absolute speed of sound data are used to compare the data because measurements are generally not taken at exactly the same state point due to changes in the ambient temperature and pressure in the laboratory room. Before the first measurement, the temperature was set by heating the system to 300 K. The first 7 measurements were then taken without changing the temperature and pressure. Before the other measurements, the temperature was changed to 280 K, 320 K and 340 K, and then it was set to 300 K again by heating the system up to or cooling it down to 300 K. Since the pressure in the apparatus depends on the ambient pressure in the laboratory room, one can clearly identify the days on which the measurements were taken. The groups of data with nearly the same pressure were measured on the same day. As one can see from Fig. 4.18, the first data taken while the temperature was not changed agree within 6 ppm. The data taken after a temperature change to 280 K lie below the data taken at constant temperature, but the agreement is still within 8 ppm. The results of the measurements, before which the temperature was increased lie by about 10 ppm (20 K increase) or 15 ppm (40 K increase) lower on the average.

From this investigation, it was concluded that the apparent difference acoustic path length ΔL depends on the way the temperature is changed. It is well reproducible, when the temperature is increased in the system from a lower to the desired temperature, but it is lowered when the temperature is decreased from a higher temperature to the desired temperature. The same effect was observed when the calibration with water was repeated in August 2005.

Is is assumed that this hysteresis effect is due to the different thermal expansion of the stainless steel material of the acoustic sensor and the quartz crystal. The quartz crystal has different thermal expansion coefficients in the direction of the optical Z-axis of the crystal lattice ($\alpha_{\mathrm{th}}^{\perp} \approx 13 \cdot 10^{-6}$ K^{-1}) and perpendicular to this axis ($\alpha_{\mathrm{th}}^{\parallel} \approx 7 \cdot 10^{-6}$ K^{-1}). In the acoustic sensor, the Z-axis is perpendicular to the axis of the sensor. Thus, the thermal expansion of the sensor material ($\alpha_{\mathrm{th}} \approx 16 \cdot 10^{-6}$ K^{-1}) is approximately two times higher than that of the crystal perpendicular to the sensor axis. This is not a problem if the temperature is increased because the crystal can slide over the stronger expanding stainless steel surface even though it is clamped. However, if the temperature is decreased, the contracting stainless steel material might prevent the crystal from sliding on it so that the crystal is bent. In this case, the acoustic path length ΔL and thus the speed of sound changes. This would explain the effect observed in Fig. 4.18. In order to obtain the best reproducibility, the thermostat must be heated from a lower to the desired temperature, when setting a new temperature.

In August 2005, the calibration was repeated. In this second calibration, the temperature range was extended down to 1 °C and up to 95 °C with measurements taken in steps of 5 °C. When the temperature had to be decreased by 5 °C, it was first decreased by about 10 °C, except for the measurement at 1 °C and 5 °C, and then increased by 5 °C to the desired temperature. With this procedure, the reproducibility of the speed of sound data over the whole temperature range was within 20 ppm. The apparatus was filled every day with newly prepared water to avoid changes of the water purity by corrosion. After a change of the thermostat temperature, the system was allowed to equilibrate for about two to three hours before a measurement was taken.

The measurements were first analyzed by applying the calibration function determined in August 2004. These results are depicted in Fig. 4.19. With the experience of the influence of temperature changes, the new data are very consistent over the whole temperature range of the measurements. As one can observe, the speed of sound data are by about 0.005 % higher than the data taken in August 2004. This

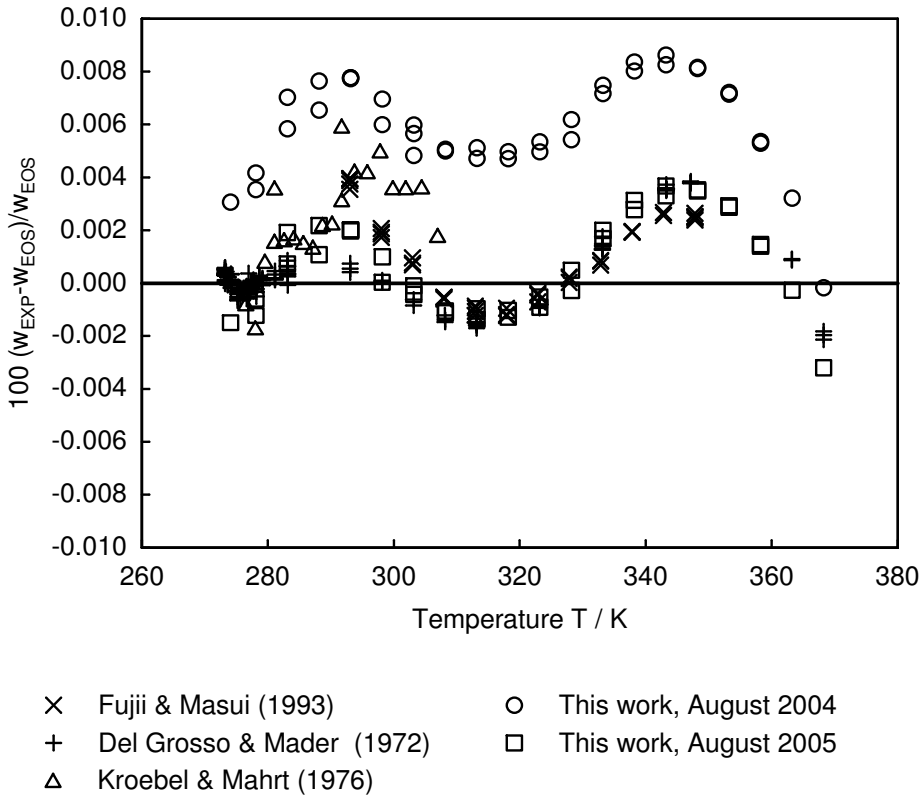

Figure 4.19. Percentage deviations of speed of sound data in liquid water at ambient pressure measured in August 2005 and of literature data from the IAPWS formulation for water [187] as a function of temperature.

means that the sensor material or the mounting of the sensor pieces must have changed between August 2004 and August 2005. For this reason, a new calibration function was determined. When adjusting the acoustic path length ΔL at (T_0, p_0) and the thermal expansion coefficient, it turned out that it is not possible to exactly reproduce the deviation pattern of the literature data over the full temperature range. Therefore, it was decided to include the full temperature dependence of the thermal expansion coefficient of the sensor material as described by Eq. (4.5). Only the coefficient b_0 of the polynomial was adjusted to match the deviation pattern of the literature data, while the remaining coefficients were taken as reported in Table 4.2. It is believed that retaining the higher terms improves the extrapolation behavior of the calibration function below 1 °C and above 95 °C. Furthermore, the different thermal expansion behavior of the quartz crystal and the stainless steel over the thickness of the crystal is included as given by Eq. (4.1). The crystal

thickness was determined by measurement with a coordinate measuring machine as $L_C = 0.3575$ mm, and the parameters of the calibration function were determined as

$$\Delta L(T_0, p_0) = 0.01972102\,\mathrm{m}, \quad b_0 = 15.2 \cdot 10^{-6}\,\mathrm{K}^{-1}. \tag{4.59}$$

The data after the parameter optimization are depicted by the squares in Fig. 4.19. Compared with the first calibration, the deviations of the speed of sound data from the IAPWS formulation now agree much better with the deviation pattern of the chosen reference data from the literature. The agreement with the reference data is within 0.002 % over the complete temperature range of the calibration. The influence of temperature measurement errors on the speed of sound will be discussed more closely in the following section. With these results, it appears convincing that the calibration measurements show the correct temperature dependence at high temperatures. Beside the present data, the literature data of Fujii and Masui [62], of Del Grosso and Mader [69], and even the data of Greenspan and Tschiegg [68], although having a constant systematic error of about 0.02 %, show similar dependencies on temperature at high temperatures (see Fig. 4.16), while the IAPWS formulation deviates by up 0.004 %, which, however, is within the uncertainty of 0.005 % of the IAPWS formulation reported by the authors. This observation justifies the choice of the literature data sets of Del Grosso and Mader [69] and of Fujii and Masui [62] instead of the IAPWS formulation as the reference for the calibration.

The difference between the two calibrations performed in August 2004 and 2005 raises the question, which calibration is to be used in the analysis of the propene and propane measurements. Therefore, measurements in both fluids at some state points were repeated after the calibration in August 2005. Based on these measurements, it was concluded that the change in the sensors must have occurred between the measurements of the two fluids. Therefore, the propene measurements were analyzed according to the August 2004 calibration, and the propane measurements according to the August 2005 calibration.

4.4 Assessment of Measurement Uncertainty

One speed of sound measurement triple consists of a temperature measurement, a pressure measurement, and a speed of sound measurement. A complete measurement value must also include estimates for the uncertainty of each measurement. The uncertainties of the temperature and pressure measurement were already dis-

cussed in Secs. 3.4 and 3.5 so that only the uncertainty of the speed of sound measurement remains to be determined.

There are two possibilities to describe the uncertainty of the speed of sound measurement. First, it can simply be reported as the uncertainty of the measured speed of sound value. Second, an additional contribution due to the uncertainty of the temperature and pressure measurement can be included. This additional contribution to the uncertainty is called state point assignment error because it describes the influence of the temperature and pressure measurement uncertainties on the speed of sound measurement value, which vary with the temperature and pressure dependence of the speed of sound. In this section, only the first contribution to the uncertainty is discussed. Since the state point assignment error generally depends on the sample liquid, it is discussed individually for each measured fluid in the following chapter.

The measurement value of the speed of sound is determined by $w = \Delta L/\Delta t$, and the uncertainty of the speed of sound according to the error propagation law is given by

$$u_w = \frac{1}{\Delta t}\, u_{\Delta L} + \frac{\Delta L}{(\Delta t)^2}\, u_{\Delta t}, \tag{4.60}$$

and the relative uncertainty is determined by

$$\varepsilon_w = \frac{u_w}{w} = \varepsilon_{\Delta L} + \varepsilon_{\Delta t}. \tag{4.61}$$

The uncertainty of the acoustic path length ΔL must be determined from the calibration measurements described in the preceding section, while the uncertainty of the measurement value of the time difference is simply the sum of the uncertainty of the time difference measurement and the uncertainty of the diffraction correction. The uncertainty of the time measurement was estimated to be $u_{\Delta t_\mathrm{m}} = 50 \cdot 10^{-12}\,\mathrm{s}$ in Sec. 3.6. The largest relative uncertainty of the time difference measurement occurs for the measurement of the shortest time difference. If a speed of sound of about 2000 $\mathrm{m\,s^{-1}}$ were measured, the measurement value of the time difference would be $\Delta t_\mathrm{m} = 10 \cdot 10^{-6}$ s. Therefore, an estimate of the relative uncertainty of the measurement value of the time difference is given by $\varepsilon_{\Delta t_\mathrm{m}} < 5$ ppm. The relative uncertainty of the diffraction correction was estimated in Sec. 4.2 to be $\varepsilon_{\Delta t_\mathrm{d}} < 0.001$ %. Thus, the total uncertainty of the time difference measurement becomes

$$\varepsilon_{\Delta t} < 0.0015\,\%. \tag{4.62}$$

The uncertainty of the acoustic path length is mainly determined by the calibration measurements and depends on several influence factors: the uncertainty of the time difference measurement, the uncertainty of the reference speed of sound data, the difference between the calibration measurements and the reference data for the speed of sound in water, the uncertainty of the temperature measurement, and the uncertainty, with which the ambient pressure can be realized in the apparatus. For measurements under pressure, the uncertainty of the change of the acoustic path length due to the compression of the sensor must additionally be included.

The uncertainty of the reference values for the speed of sound were reported by both Del Grosso and Mader [69] and Fujii and Masui [62] as 0.001 %, although larger differences of about 0.003 % between the two data sets exist at low temperatures. For the reasons discussed in the preceding section, the data of Del Grosso and Mader [69] were chosen as reference data in the temperature range between 273.15 K and 315 K. With this choice, the uncertainty of the reference data is estimated to be 0.001 % over the complete temperature range of the calibration, and the agreement between the calibration measurements and the two literature data sets is estimated from Fig. 4.19 to be within at least 0.002 %.

The influence of the temperature and pressure measurement uncertainty can be estimated from the IAPWS formulation. The measurement uncertainty of the pressure consists of three contributions, which are due to uncertainty of the ambient pressure measurement, the uncertainty of the zero pressure indicator, and the uncertainty of the hydrostatic pressure correction. For liquid water these uncertainties amount to 7 Pa, 69 Pa, and 35 Pa, respectively. This yields a total uncertainty of 111 Pa for the pressure measurement. Relative changes in the speed of sound due to this pressure measurement error as calculated from the IAPWS formulation are smaller than $1 \cdot 10^{-7}$ over the whole temperature range of the measurements and can safely be neglected.

Fig. 4.20 depicts the influence of small errors in the temperature measurement on the speed of sound at 0.103125 MPa in the temperature range between 273.15 K and 373.15 K. The influence of small temperature measurement errors vanishes at 347.30 K because the speed of sound has a maximum at this temperature. The largest influence occurs at the lowest temperature, amounting to 0.001 % for an uncertainty of 3 mK of the temperature measurement. With this contribution, the total uncertainty of the acoustic path length at ambient pressure becomes 0.0055 %.

For measurements under high pressures, the relative uncertainty of the change of the acoustic path length due to compression can be estimated by applying the error

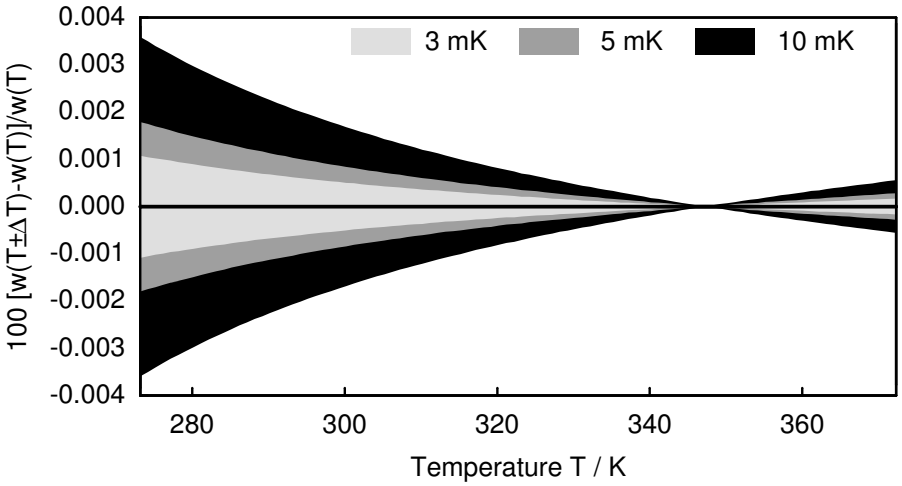

Figure 4.20. Influence of small temperature measurement errors on the speed of sound in liquid water at 0.101325 MPa in the temperature range between 273.15 K and 373.15 K. Calculations are based on the IAPWS formulation.

propagation law to the last term of the first line of Eq. (4.1):

$$\varepsilon_{\Delta L(p)} \approx \varepsilon_{\Delta L(p_0)} + \frac{(1-2\nu)p}{E}\,\varepsilon_E + \frac{2\nu p}{E}\,\varepsilon_\nu. \tag{4.63}$$

The relative uncertainties of the elastic modulus and the Poisson number are both estimated to be 5 %. Both additional terms depend linearly on pressure. The highest contribution occurs at the highest measured pressure 100 MPa and amounts to 0.001 % for the term due to the uncertainty of the elastic modulus and 0.0015 % for the term due to the uncertainty of the Poisson number.

The total relative uncertainty of the acoustic path length can be expressed as

$$\varepsilon_{\Delta L}(p) = 0.0055\% + 2.5 \cdot 10^{-5}\,\frac{\%}{\mathrm{MPa}} \cdot p, \tag{4.64}$$

where the pressure has to be inserted in MPa. The uncertainty increases from 0.0055 % at ambient pressure to 0.008 % at 100 MPa.

With the uncertainty of the time difference measurement and of the acoustic path length, the uncertainty of the speed of sound measurement value becomes

$$\varepsilon_w(p) = 0.007\% + 2.5 \cdot 10^{-5}\,\frac{\%}{\mathrm{MPa}} \cdot p\,. \tag{4.65}$$

Besides the contributions to the uncertainty of the speed of sound discussed in this section, sample impurities can also contribute significantly to the uncertainty.

Such contributions individually depend on the purity of the samples used for the measurements. Furthermore, the reproducibility of the speed of sound measurements at the same state point also contributes to the uncertainty. These contributions will be discussed separately for every investigated liquid in the following chapter.

4.5 Measurements in Liquid Water under Pressure

In order to validate the instrument, the speed of sound in liquid water was measured under pressure. Water is one of the best investigated fluids concerning its thermophysical properties, and the speed of sound under pressure was measured by many authors before. Table 4.8 summarizes details of literature data sets, and Fig. 4.21 shows their distribution in the T,p plane.

From Table 4.8 it is evident that the data of Fujii [61] are the most accurate data for the speed of sound in liquid water presently available with a quoted uncertainty of 0.005 %. Fujii measured the three isotherms 303.15 K (30 °C), 313.15 K (40 °C),

Table 4.8. Literature data sets for the speed of sound in water. Data already listed in Table 4.7 are not considered here. Abbreviations: PE: pulse-echo, IF: interferometer, PA: photo-acoustic, sat. liq.: saturated liquid.

Author	Year	Method	Data	T / K	p / MPa	Uncertainty
Aleksandrov [4]	1976	PE	186	270–647	70	< 0.02 %
Aleksandrov [5]	1979	PE	60	266–423	100	< 0.03 %
Aleksandrov [6]	1980	PE	37	473–673	50	< 0.14 %
Barlow [14]	1967	PE	72	290–367	80	< 0.02 %
Benedetto [20]	2003	PE	90	274–394	90	< 0.05 %
Chávez [29]	1985	PE	54	273–535	sat. liq.	< 0.05 %
Erokhin [41]	1979	IF	238	453–653	50	< 1.9 %
Erokhin [42]	1980	IF	219	648–773	50	< 0.1 %
Evstefeev [48]	1979	PE	53	423–573	10	< 0.2 %
Fujii [61]	1994	PE	47	313–323	200	< 0.005 %
Holton [78]	1968	PE	32	323	1000	< 0.2 %
Mamedov [114]	1979		93	273–623	70	< 0.3 %
Novikov [139]	1968	IF	99	423–583	9.7	< 1.0 %
Petitet [143]	1983	PE	93	252–293	350	< 0.05 %
Petitet [144]	1986	PE	73	479–973	300	< 0.5 %
Wilson [190]	1959	PE	77	274–365	97	< 0.05 %
Wiryana [191]	1998	PA	42	353–473	3500	< 0.1 %
Ye [193]	1990	PE	45	290–343	47	< 0.06 %

and 323.15 K (50 °C), under pressures up to 200 MPa. Therefore, these three temperatures were chosen for the test measurements. The measurements were carried starting at ambient pressure in steps of 10 MPa up to 100.1 MPa. The measurement results are reported in Appendix B, Table B.1.

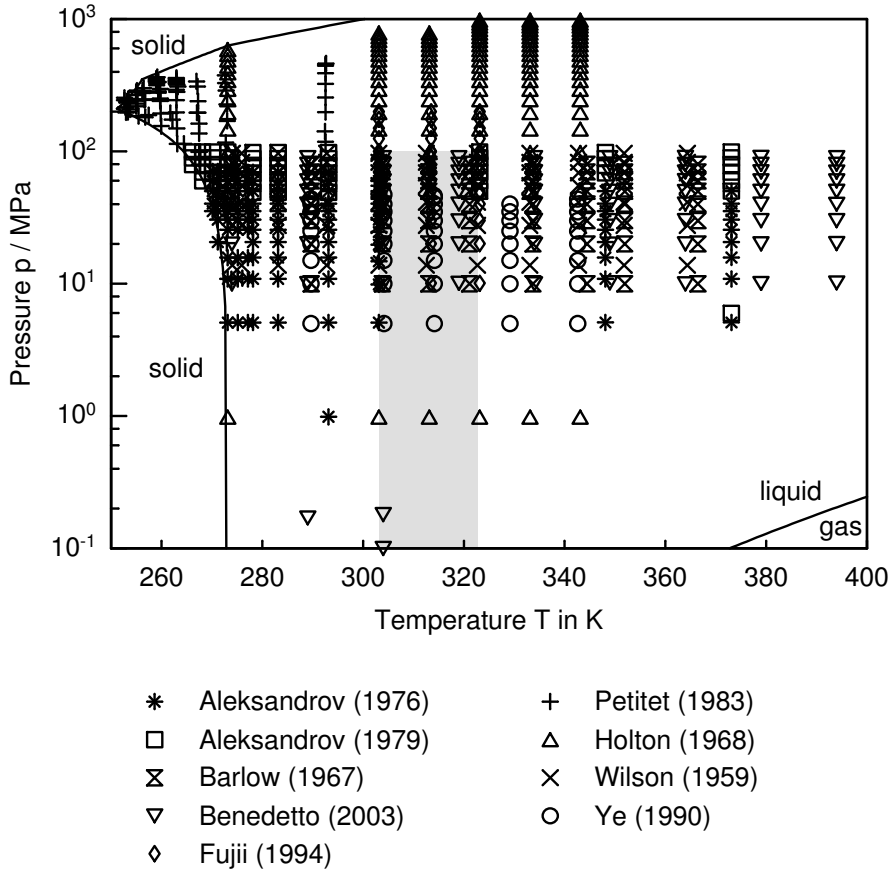

Figure 4.21. Distribution of literature data for the speed of sound in water in the p,T plane. The lines are the phase boundaries [186, 187].

In this special case, the speed of sound measurements at ambient pressure on every isotherm are directly calibrated against the data of Fujii and Masui [62] at ambient pressure. The acoustic path length is optimized so that the deviation of the data from the IAPWS formulation is exactly equal to the deviation of the data of Fujii and Masui from the IAPWS formulation at the same temperature. The direct calculation of the acoustic path length from the reference data of Fujii and Masui is not possible because they were measured at slightly different temperatures. With this procedure, the uncertainty of the acoustic path length is reduced consid-

erably. In this temperature range, the reference data sets of Del Grosso and Mader and of Fujii and Masui show the best agreement among each other (see Fig. 4.19). Therefore, the quoted uncertainty 0.001 % of the data of Fujii and Masui appears reasonable. Since the calibration measurements exactly match the reference data, there is no contribution to the uncertainty from a difference between the present data and the data of Fujii and Masui in this special case. The contributions to the uncertainty due to time difference measurement errors is the same as that for the calibration described in the preceding section. The influence of the temperature measurement error is estimated from Fig. 4.20 to be 5 ppm within the temperature range of the measurements. The total uncertainty also includes the uncertainty of the change of the acoustic path length under pressure and is given by

$$\varepsilon_w = 0.003\% + 2.5 \cdot 10^{-10} \frac{\%}{\mathrm{MPa}} \cdot p \tag{4.66}$$

Fig. 4.22 depicts percentage deviations of the present data and of the data of Fujii from the IAPWS formulation for the three measured isotherms. Both data sets agree with the IAPWS formulation within 0.02 %. They show the same systematic deviations from the IAPWS formulation and agree among each other within 0.01 %. Our data show less scatter than the data of Fujii and are more consistent. Observing the scatter of the data at this fine resolution, Fujii's estimation of 0.005 % for the uncertainty of his data appears to be too optimistic. The comparison shows that the present data are even more accurate than the data of Fujii, and it demonstrates the capability of the instrument for highly accurate speed of sound measurements. Unfortunately, the high accuracy cannot be transferred to measurements in other fluids because then the calibration has the higher uncertainty discussed in the last section, and additional allowances due to sample impurities have to be included in the uncertainty.

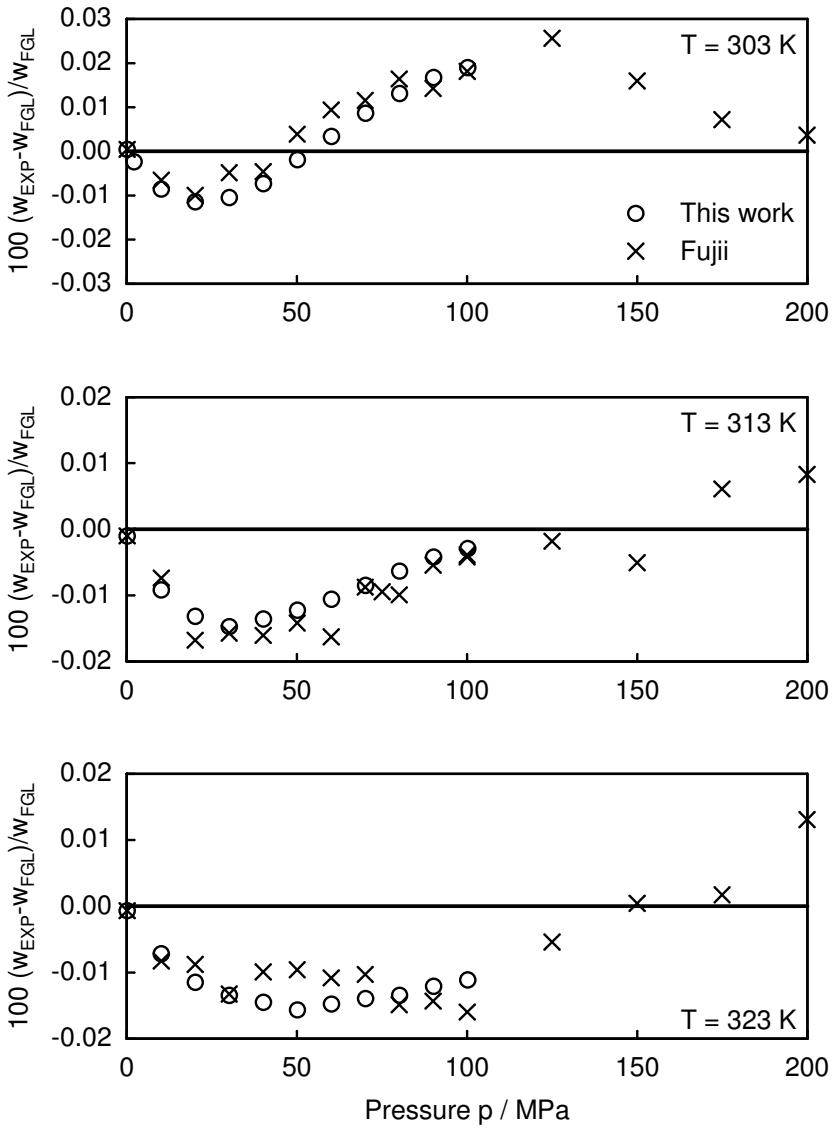

Figure 4.22. Percentage deviations of measured speed of sound in liquid water at 303.15 K, 313.15 K, and 323.15 K under pressures up to 100 MPa and the data of Fujii [61] from the IAPWS formulation as a function of pressure.

5 Measurements in Pure Fluids

With the instrument described in the preceding chapters, the speed of sound in compressed nitrogen and in the liquid and supercritical region of the pure fluids propane, propene (propylene), and the refrigerants 227ea (1,1,1,2,3,3,3-heptafluoropropane) and 365mfc (1,1,1,3,3-pentafluorobutane) was measured in the temperature range between 240 to 420 K and under pressures up to 100 MPa. In this chapter, the results of these measurements are presented, discussed, and compared with literature data and equation of state models. These comparisons are carried out on the basis of the NIST Reference Database RefProp [108], in which the most accurate fundamental equations of state for each fluid presently available are implemented.

The following section describes the sample preparation, and then each of the Secs. 5.2 to 5.6 reports and discusses the measurement results for one fluid.

5.1 Sample Preparation

Accurate measurements of the speed of sound require samples with high purity. Therefore, the liquid samples were degassed from eventually dissolved low boiling gases, such as nitrogen or oxygen, and then their purity was analyzed with a gas chromatograph (Perkin Elmer, type Clarus 500), which was equipped with a thermal conductivity detector and a packed column (Porapak Q 80/100 Mesh). In the analysis of the chromatograms, peak areas were approximately interpreted as mole fractions of the components. Nitrogen, oxygen and water impurities and the main component could unambiguously be detected, while no attempt was made to identify the peaks of other than these substances. The resolution of the purity analysis with the gas chromatograph was better than 0.001 %.

For the degassing procedure, the sample container was placed in an ultrasonic bath and heated at the bottom to about 50 °C. While the container was continuously being treated with ultrasound, its valve was opened several times to remove the gas phase from the container.

Before a sample is filled into the apparatus, the pressure vessel and tubing system are carefully evacuated. Then, the temperature in the thermostat is set to about 20 °C. For sample fluids with a vapor pressure below ambient pressure, the sample container is mounted upside down on top of the thermostat and heated to about

50 °C. After opening the container valve, the liquid flows into the apparatus. For sample fluids with vapor pressure larger than ambient pressure, the sample container is placed in upright position on top of the thermostat. The container is heated to about 50 °C, which is higher than the temperature in any other part of the high pressure system. After opening the container valve, the gas phase in the sample container flows into the high pressure system, where it condenses.

After a new sample had been filled in or the pressure had been changed, the pressure vessel was allowed to equilibrate for at least an hour before a measurement was taken.

5.2 Nitrogen

Besides the measurements in liquid water, which were reported in Sec. 4.5, the speed of sound in compressed nitrogen was measured in order to validate the apparatus. Moreover, these measurements serve to examine the capability of the apparatus, which was primarily designed for liquid samples, for measurements in compressed gases. Nitrogen is well suited for this purpose because it is readily available in high purity. Furthermore, the speed of sound in nitrogen has been measured by many authors before, for example [32, 95, 197], and with the fundamental equation of state developed by Span et al. [161] an accurate basis for comparisons is available. Costa Gomez and Trusler [32] measured the speed of sound in nitrogen with a spherical resonator on the four isotherms 250 K, 275 K, 300 K, and 350 K under pressures up to 30 MPa. This data set enables a comparison of the present pulse-echo technique with the spherical resonator. In the pressure range, where the data sets overlap, they should agree within the uncertainties of the two completely different methods. The data set of Kortbeek et al. [95] covers the temperature range between 123 K to 298 K under pressures from 85 MPa to 1000 MPa. Kortbeek et al. claimed an uncertainty of 0.02 % for their data. Further literature data sets for the speed of sound in nitrogen were reviewed by Span et al. [161].

The nitrogen sample was purchased from Westfalen AG with a manufacturer specified purity of 99.999 vol. %. The sample purity was checked with the gas chromatograph, and no impurities were detected within the resolution of the chromatograph, which is about 0.001 %.

The speed of sound was measured along six isotherms in the temperature range between 275 K and 400 K in steps of 25 K under pressures up to 100 MPa. The lowest pressure on an isotherm was chosen as the lowest pressure at which the

two successive echoes relevant for the time difference measurement could clearly be distinguished. At lower pressures, the slow decay of the first echo extended too far into the second echo for the cancellation to occur. On the four isotherms 275 K, 300 K, 325 K, and 350 K, the lowest pressure was 20.1 MPa, whereas at 375 K and 400 K it was 25.1 MPa. The reproducibility of the data at the same state point after temperature and pressure cycles was better than 0.001 %.

According to Costa Gomez and Trusler [32], the propagation of sound waves in nitrogen is already influenced by dispersion phenomena at very low frequencies in the audio regime because the vibrational relaxation time for the nitrogen molecule is significantly longer than the period of the sound waves. Costa Gomez and Trusler argued that the vibrational mode of the nitrogen molecules does not participate in the propagation of sound waves, if the relation $f/p \geq 30\ \mathrm{Hz{\cdot}MPa^{-1}}$ is satisfied. Since the present measurements were carried out at 8 MHz, it can safely be concluded that the vibrational mode is not excited at all. This means that the frequency of the present measurements lies in the infinite frequency regime above the dispersion step in Fig. 2.2. Thus, the present data can easily be corrected to the thermodynamic speed of sound by Eq. (2.137), which requires only the correction of the ideal gas heat capacities.

The contribution of the vibration to the ideal gas heat capacities can be calculated by means of statistical thermodynamics. If the vibration is described by the model of the linear oscillator, the contribution to the ideal gas heat capacities is given by [9]

$$c^{\mathrm{vib}} = \frac{R_{\mathrm{m}}}{M} \left\{ \frac{T^{\mathrm{vib}}/T \, \exp(-T^{\mathrm{vib}}/2T)}{1 - \exp(-T^{\mathrm{vib}}/T)} \right\}^2 , \tag{5.1}$$

where T^{vib} represents the characteristic temperature of the vibrational mode. The thermodynamic speed of sound w_0 is obtained from the measured speed of sound w by applying the correction

$$w_0 = w \sqrt{\frac{c_p}{c_v} \frac{c_v - c^{\mathrm{vib}}}{c_p - c^{\mathrm{vib}}}} \tag{5.2}$$

with c^{vib} according to Eq. (5.1). Eq. (5.2) corresponds to Eq. (2.137) in Sec. 2.5. All measured speed of sound data were corrected according to Eq. (5.2). Values for the isochoric and isobaric heat capacities were calculated from the fundamental equation of state of Span et al., and the characteristic temperature of the vibration was taken from the work of Laher and Gilmore [103] as $T^{\mathrm{vib}} = 3352.2$ K. The measurement results are reported in Table B.2 in Appendix B.

Since the nitrogen sample is of very high purity, the influence of impurities on the measurement uncertainty is negligible. The uncertainty of the data is given by Eq. (4.65) plus an additional contribution introduced by the reproducibility. The total uncertainty of the speed of sound measurement becomes

$$\varepsilon_w(p) = 0.008\% + 2.5 \cdot 10^{-5} \, \frac{\%}{\mathrm{MPa}} \cdot p \, . \tag{5.3}$$

The state point assignment error due to the uncertainties of the temperature and pressure was estimated by the equation of state of Span et al. [161]. It amounts to 3 ppm for the temperature measurement and 0.0025 % for the pressure measurement. The uncertainty of the speed of sound data including the state point assignment error is given by

$$\varepsilon_w(p) = 0.011\% + 2.5 \cdot 10^{-5} \, \frac{\%}{\mathrm{MPa}} \cdot p \, . \tag{5.4}$$

In Figs. 5.1 and 5.2, the present data are compared with the fundamental equation of state of Span et al. and literature data. The plots show percentage deviations of the data from the equation of state as a function of pressure. The present data are very consistent and agree with the equation of state within at least 0.02 % over the entire temperature and pressure range of the measurements. The agreement of the present data and the data of Costa Gomes and Trusler is generally within 0.01 %, in most cases even better. At the lowest measured pressures, the present data approach the equation of state and the data of Costa Gomez and Trusler and agree with them within 0.005 % or better. This comparison shows that the pulse-echo technique of the present apparatus yields essentially the same results as the spherical resonator method within the uncertainty of both methods.

From the data set of Kortbeek et al. [95] only four data overlap with the present measurements, namely at 275 K and 298 K at the pressure 85 MPa and 100 MPa. They are by about 0.2 % larger than the prediction of the equation of state and therefore lie outside the range of Fig. 5.1. Since the present data agree well with the data of Costa Gomes and Trusler at low pressures and the pressure dependence of the speed of sound was shown to be correctly resembled by the water data in Sec. 4.5, the data of Kortbeek et al. are probably too high.

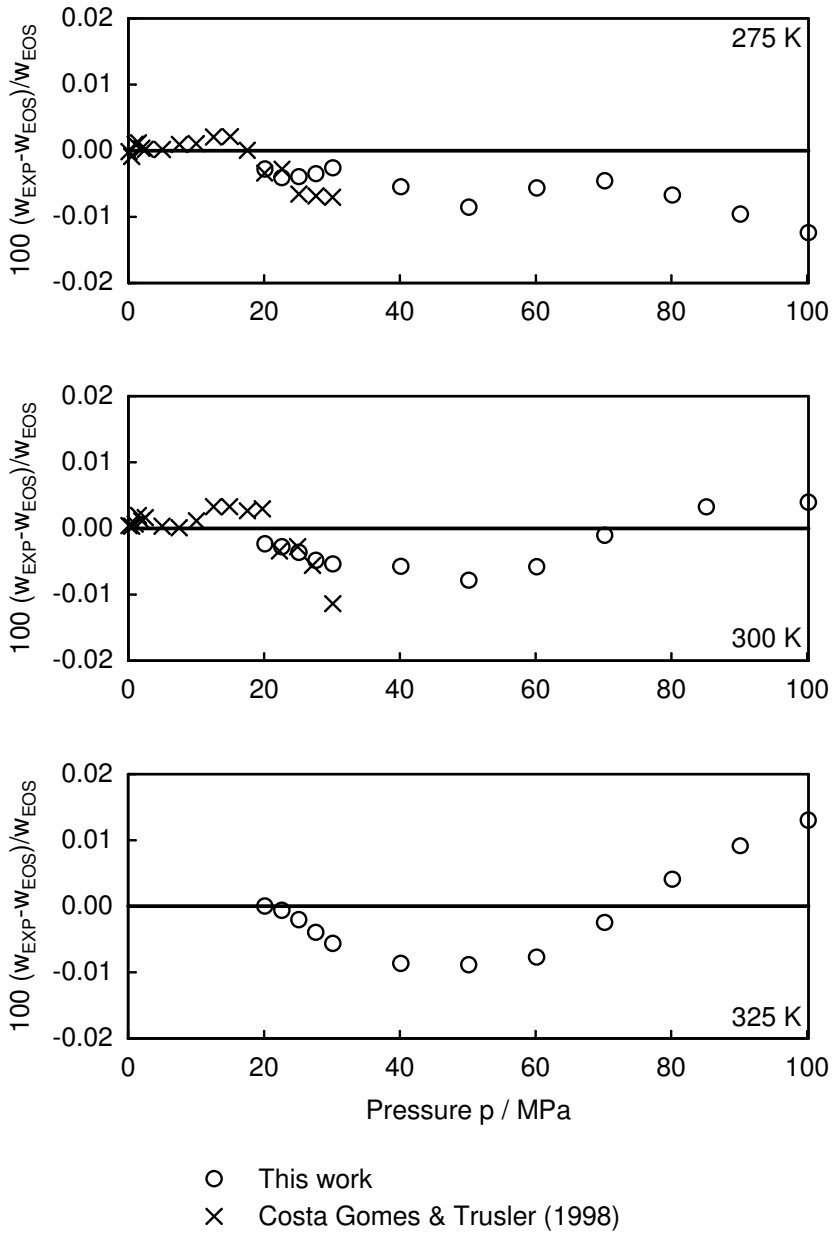

Figure 5.1. Percentage deviations of measured speeds of sound in compressed nitrogen and literature data from the fundamental equation of state of Span et al. [161] as a function of pressure at 275 K, 300 K, and 325 K.

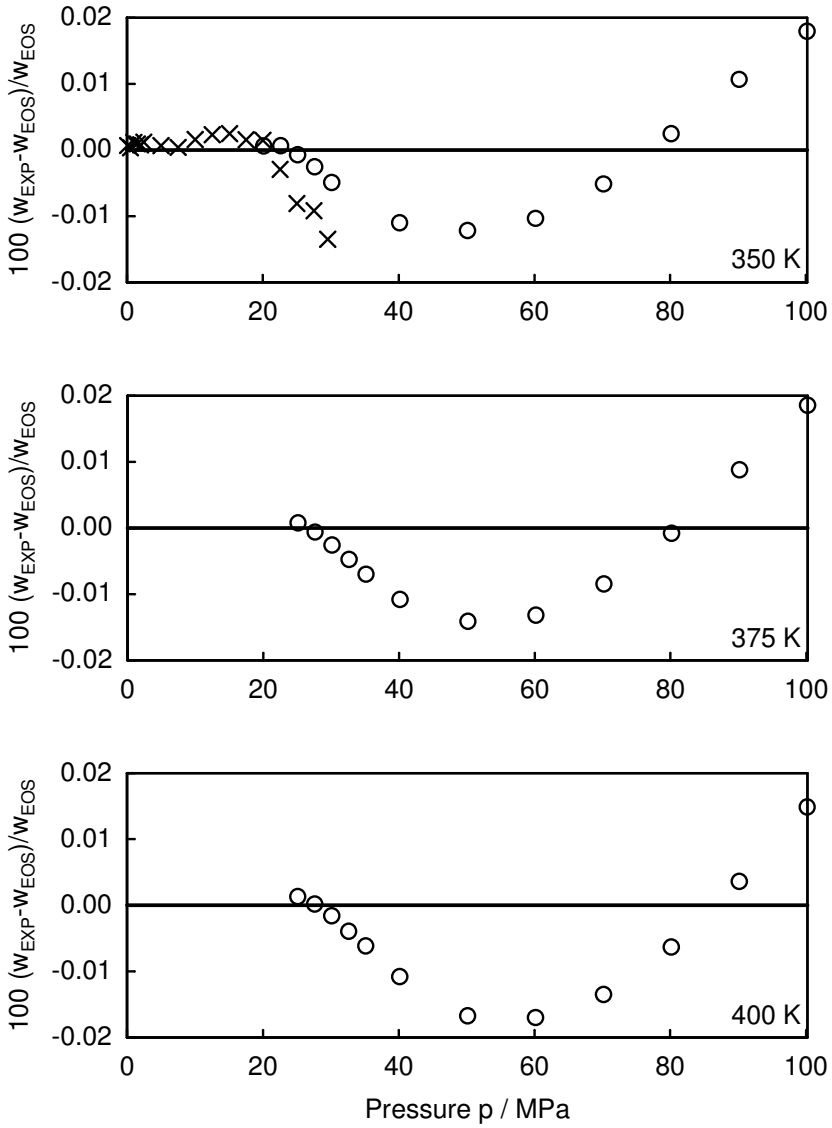

Figure 5.2. Percentage deviations of measured speeds of sound in compressed nitrogen and literature data from the fundamental equation of state of Span et al. [161] as a function of pressure at 350 K, 375 K, and 400 K. Symbols are the same as in Fig. 5.5.

5.3 Propane

Propane is a fluid with a wide range of technical applications. For example, it is used as a basic ingredient in many production processes in the chemical industry or as a working fluid in refrigeration cycle processes, and it occurs as a secondary component in natural gas mixtures. Therefore, an accurate fundamental equation of state for the description of the thermodynamic properties of propane is desirable, which requires accurate speed of sound data as part of the experimental data set for the optimization process. Although the speed of sound in propane under high pressures was measured by several authors before, there are considerable differences between the different data sets, and it is not known which one is correct. New accurate speed of sound data can help to decide between the different data sets and extend the data basis for a new fundamental equation of state. For these reasons, it was decided to measure the speed of sound in propane.

The propane sample was purchased from Scott Specialty Gases with a manufacturer specified purity better than 99.993 vol. %. A gas chromatograph analysis revealed two peaks with 0.009 area % and 0.003 area % besides the main propane peak. The first peak was identified as water, while the nature of the second peak could not be identified. This impurity is probably another hydrocarbon, which is a remain of the production process. No nitrogen or oxygen was detected. The purity of the sample is estimate to be 99.988 %. For the remaining impurities, an additional allowance of 0.005 % is added to the uncertainty of the speed of sound data.

Experimental data for the speed of sound in propane were published by seven

Table 5.1. Literature data for the speed of sound in propane. Abbreviations: PE: pulse-echo, SR: spherical resonator, DL: diffraction of light by ultrasound, SP: spectroscopically pure in the infrared regime.

Author	Year	Method	Data	T / K	p / MPa	Purity	Uncertainty
He [75]	2002	SR	24	293–323	0.7	> 99.95 %	< 0.004 %
Lacam [102]	1956	DL	200	298–498	100	SP	< 1 %
Niepmann [137]	1984	PE	241	200–323	60	> 99.95 %	< 0.2 %
Noury [138]	1954	DL	118	348–398	15	SP	< 1.5 %
Terres [173]	1957	IF	99	293–448	10	> 96 %	< 1 m/s (g) < 5 m/s (l)
Trusler [180]	1996	SR	68	225–375	0.85	> 99.95 %	< 0.01 %
Younglove [195]	1981	PE	180	90–300	35	> 99.95 %	< 0.05 %

groups. Details of these literature data sets are summarized in Table 5.1. He et al. [75], Terres et al. [173], and Trusler and Zarari [180] measured the speed of sound in the gas phase, while the data of Noury [138] cover the vicinity of the critical point in the supercritical region. Data in the liquid region were published by Lacam [102], Niepmann [137], and Younglove [195].

Fundamental equations of state in terms of the Helmholtz free energy as a function of density and temperature were developed by Miyamoto and Watanabe [128], Span and Wagner [163], and Lemmon, McLinden, and Wagner [109]. Younglove and Ely [196] published a thermal equation of state of the MBWR-type, which together with an equation for the isochoric ideal gas heat capacity can be represented as a fundamental equation of state.

The distribution of the present measurements and the literature data in the p,T plane is shown in Fig. 5.3. The present data cover the subcritical liquid region from

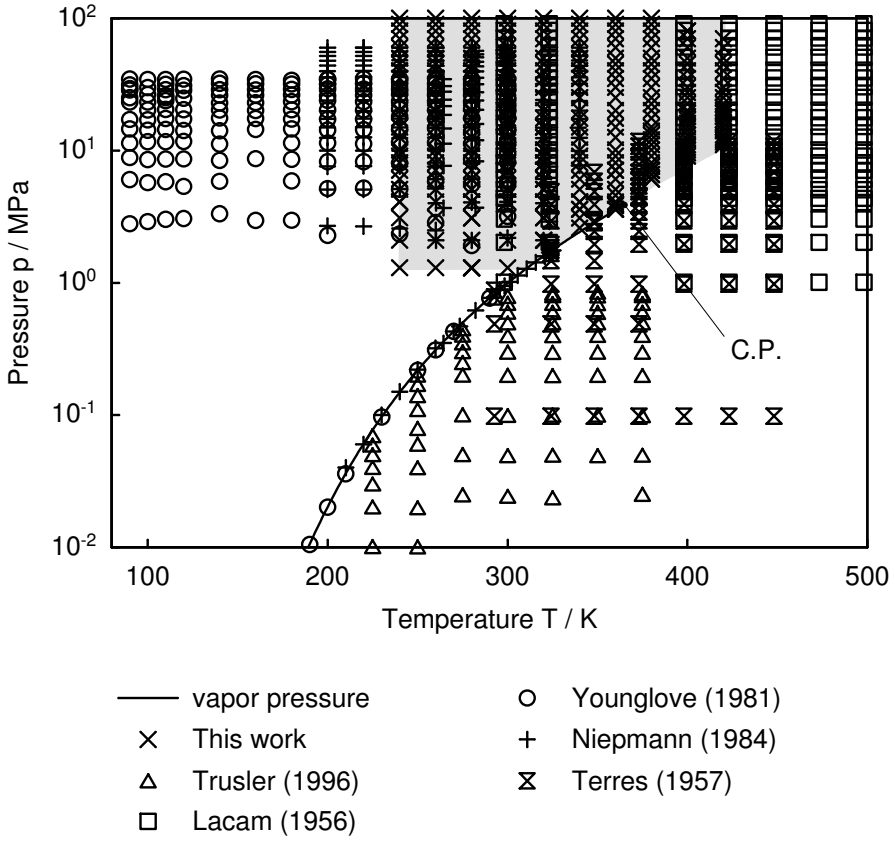

Figure 5.3. Distribution of the present measurements and literature data for the speed of sound in propane in the p,T plane.

240 K upwards and extend up to 420 K into the supercritical region under pressures up to 100 MPa. On subcritical isotherms, the lowest pressures, at which measurements were carried out, were chosen close to the vapor pressure. On supercritical isotherms, measurements were started at the lowest pressure where a clear signal cancellation could be observed. The measurement results are reported in Appendix B, Table B.3.

The reproducibility of the speed of sound, when repeating measurements at the same state point after pressure and temperature cycles, was within 0.002 %. Thermal relaxation phenomena do not significantly influence the propagation of sound waves in propane in the frequency range of the present measurements [200, p. 472] so that no dispersion correction is required. With the reproducibility and the additional contribution due to sample impurities, the total uncertainty of the speed of sound measurement is given by

$$\varepsilon_w(p) = 0.014\,\% + 2.5 \cdot 10^{-5}\,\frac{\%}{\mathrm{MPa}} \cdot p\,. \tag{5.5}$$

The state point assignment error due to the uncertainties of the temperature and pressure was estimated by the equation of state of Lemmon et al. [109]. It amounts to 0.003 % for the temperature measurement and 0.002 % for the pressure measurement. For the lowest measured pressures on the supercritical isotherms, the influence of the pressure is larger because the isotherms are rather flat in this state region, and it amounts to 0.005 %. When taking theses additional contributions into account, the uncertainty of the speed of sound measurement becomes

$$\varepsilon_w(p) = 0.019\,\% + 2.5 \cdot 10^{-5}\,\frac{\%}{\mathrm{MPa}} \cdot p\,. \tag{5.6}$$

At the lowest pressures on supercritical isotherms, 0.019 % has to be replaced by 0.022 %.

Fig. 5.4 shows the speed of sound data for the ten measured isotherms as a function of pressure. In the measured state region, the speed of sound ranges from about 250 $\mathrm{m\,s^{-1}}$ to 1700 $\mathrm{m\,s^{-1}}$.

In the remainder of this section, the present data are compared with the literature data and equation of state models. The equation of state of Lemmon et al. [109] is chosen as a reference for these comparisons. In the optimization process of this equation of state, the present speed of sound data were already used. Figs. 5.5, 5.6, and 5.7 show percentage deviations of the present data, literature data at similar temperatures, and the three other equation of state models from the equation of state of Lemmon et al.

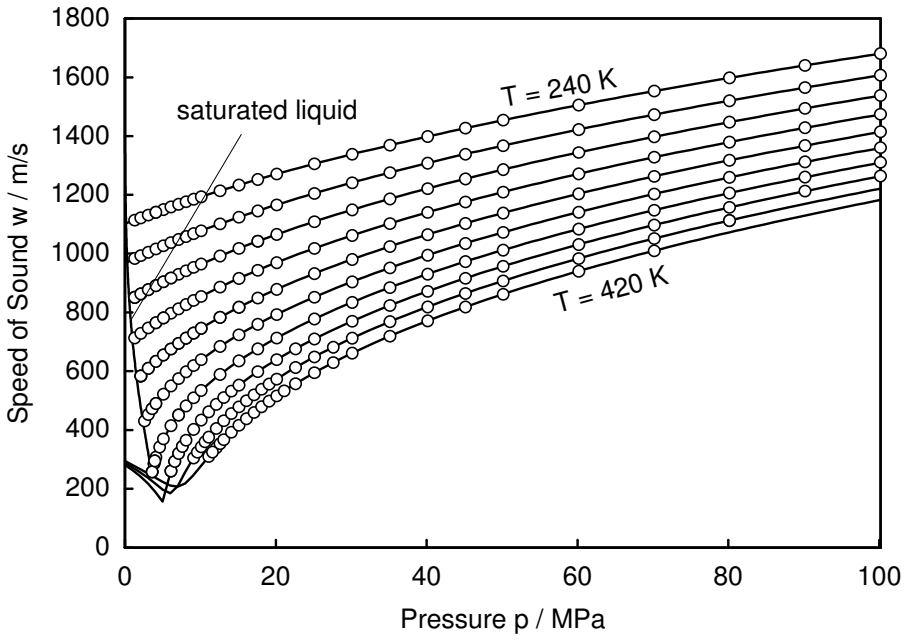

Figure 5.4. The speed of sound in propane as a function of pressure for all measured isotherms.

The present data agree with the equation of state within 0.06 % over the whole range of temperatures and pressures. This excellent agreement is due to the fact that they were used by Lemmon et al. in the optimization process of the equation of state. From the three literature data sets, the data of Younglove at 240 K, 260 K, 280 K, and 300 K agree best with the present data. They are slightly lower than the present data, but the agreement is within 0.04 % except for a few data, where the differences are slightly larger. Younglove reported an uncertainty of 0.05 % for his data. Thus, both data sets agree among each other within the uncertainty quoted by Younglove.

The data of Niepmann show some scatter and lie about 0.2 to 0.8 % below the present data. The differences between the data of Niepmann and the present data are similar on all isotherms except for the highest isotherm, which was measured by Niepmann, 340 K, and generally increase with pressure. At 340 K, the percentage deviations from the equation of state range from 0.5 % to 1 %.

The data of Lacam also show some scatter and systematic deviations of up to 2 % from the equation of state. At 300 K, the data agree with the present data within 0.5 %, but the deviations increase up to 2 % at 420 K, which is the highest

temperature measured in this work.

This comparison shows that the present data and the data of Younglove are the most accurate data for the speed of sound in the liquid phase of propane presently available, and they are well represented by the equation of state of Lemmon et al. Without the present speed of sound data, it was not possible to identify which one of the three literature data sets is correct. The present data could not only help to identify the data set of Younglove as the most accurate, but they are even more accurate than all previously available literature data for the speed of sound in liquid propane.

Among the three other equation of state models, the oldest equation of state of Younglove and Ely provides the best representation of the speed of sound over a wide range of temperatures, only at high temperatures the deviations increase up to 0.5 %. The equation of state of Span and Wagner represents the speed of sound with 0.5 % except for the lowest measured isotherm 240 K, while the equation of state of Miyamoto and Watanabe shows larger deviations of up to 1 % over the whole temperature range of the present measurements.

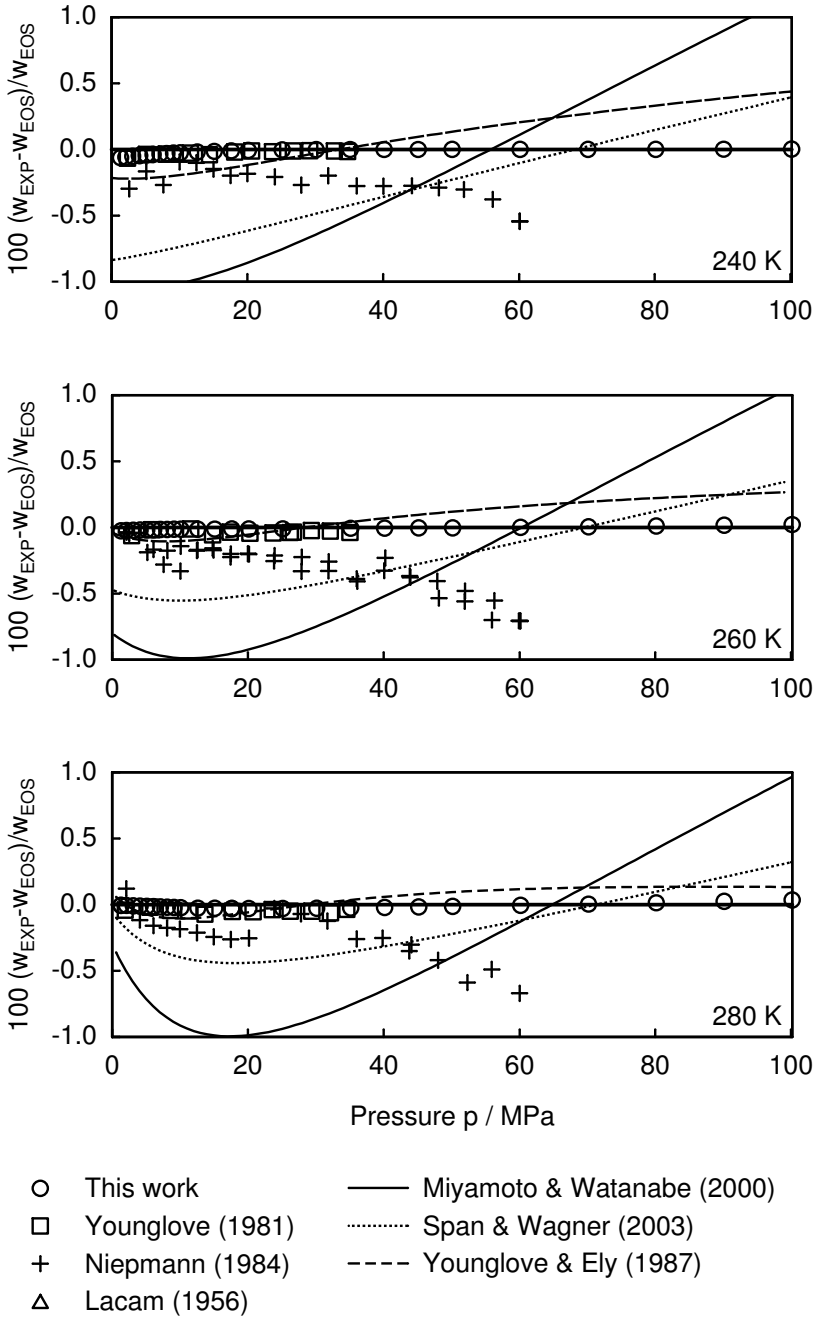

Figure 5.5. Percentage deviations of measured speeds of sound in liquid propane, literature data, and three equation of state models from the fundamental equation of state of Lemmon et al. [109] as a function of pressure at 240 K, 260 K, and 280 K.

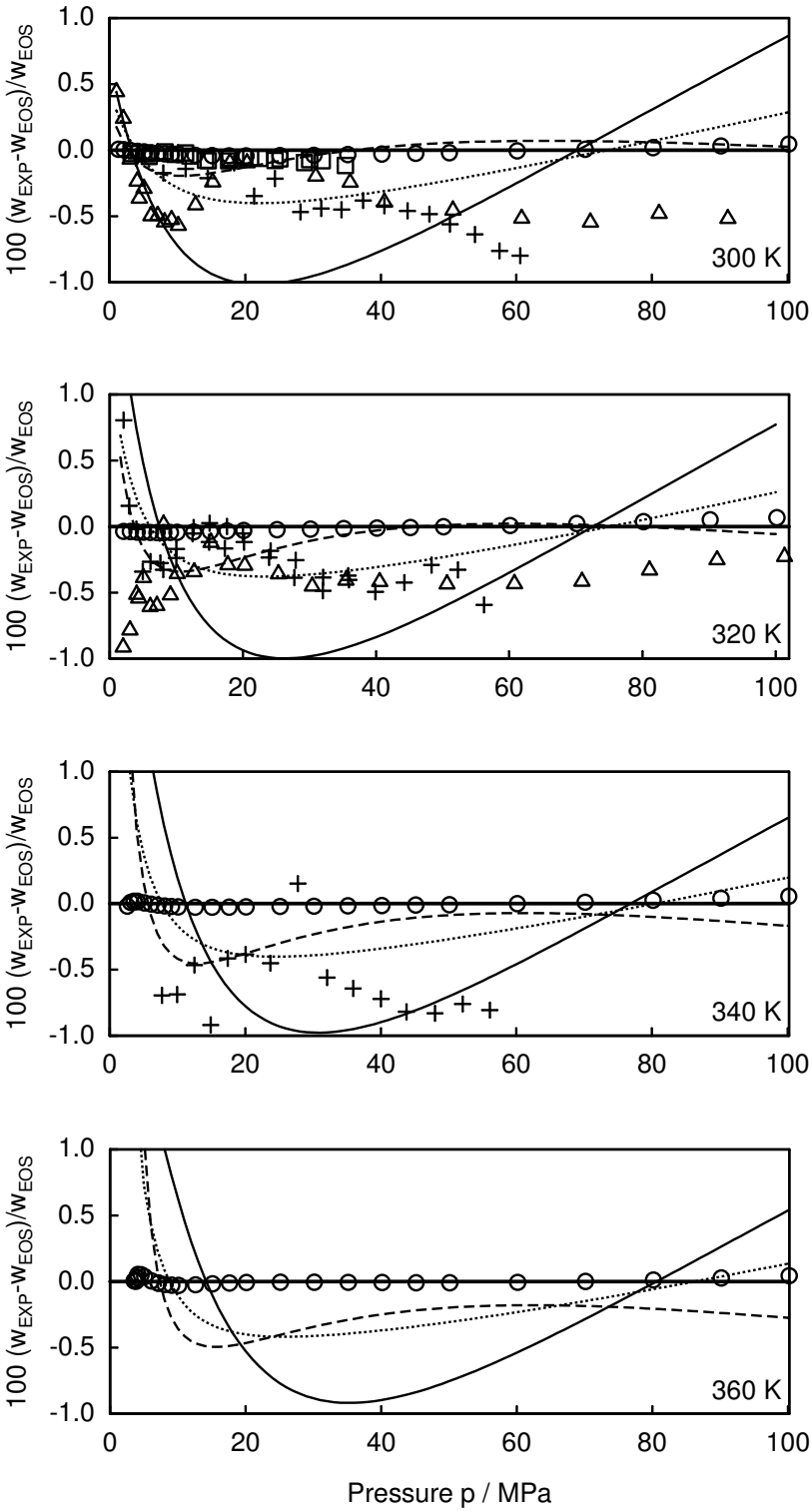

Figure 5.6. Percentage deviations of measured speeds of sound in liquid propane, literature data, and three equation of state models from the fundamental equation of state of Lemmon et al. [109] as a function of pressure at 300 K, 320 K, 340 K, and 360 K. Symbols are the same as in Fig. 5.5.

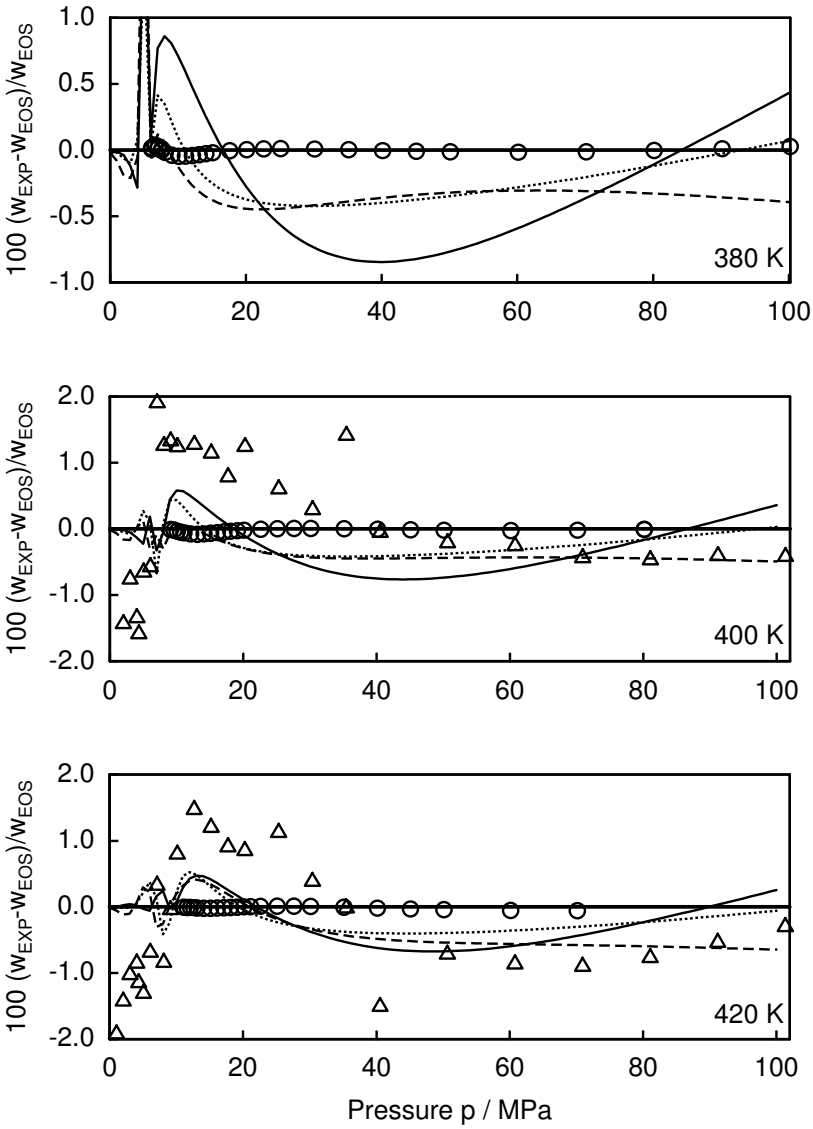

Figure 5.7. Percentage deviations of measured speeds of sound in liquid propane, literature data, and three equation of state models from the fundamental equation of state of Lemmon et al. [109] as a function of pressure at 380 K, 400 K and 420 K. Symbols are the same as in Fig. 5.5.

5.4 Propene

As propane, propene is a fluid with applications in many technical areas. A review of the thermodynamic properties of propene was published by Angus et al. [7] in 1980. In this volume, the most recent fundamental equation of state for propene was published. Only two rather old data sets for the speed of sound in propene exist in the literature, which were published by Soldatenko and Dregulyas in 1970 [158] and Terres et al. in 1957 [173]. The 100 data of Soldatenko and Dregulyas were measured with an interferometer and cover parts of the gas and supercritical region between 193–473 K under pressures up to 10 MPa. The sample purity was better than 99.5 %, and the uncertainty of the data was estimated to be lower than 0.15 %. The 224 data of Terres et al. were also measured with an interferometer and cover the gas region between 293–448 K under pressures up to 10 MPa. A few data were measured in the liquid region. The sample purity was reported to be approximately 100 %, and the uncertainty was estimated to be 1 $\mathrm{m\,s^{-1}}$ for data in the gas region and 5 $\mathrm{m\,s^{-1}}$ for data in the liquid region. The distribution of both data sets in the p,T plane is shown in Fig. 5.8. The measurements of this work fill a gap by providing data in the liquid and supercritical region under high pressures.

The propene sample was purchased from Deutsche Air Liquide with a manufacturer specified purity better than 99.95 %. After degassing the sample as described above, two impurities with 0.008 area % and 0.002 area % besides the main propene peak were detected by the gas chromatograph, whose nature could not be identified. They are probably other hydrocarbons, which are remains of the production process. This leads to the conclusion that the purity of the sample was 99.990 %. As for propane, an additional allowance of 0.005 % is added to the uncertainty of the measured speeds of sound to account for influence of the impurities.

Measurements were taken on ten isotherms between 240 K and 420 K under pressures up to 100 MPa. The distribution of the measurements in the p,T plane is included in Fig. 5.8. Below 300 K, a Viton o-ring was used to seal the closure of the pressure vessel, while at higher temperatures FEP encapsulated silicone o-rings were used. At the lowest and highest temperatures, the o-rings did not withstand the highest pressures. Therefore, the data at 240 K extend only up to 50 MPa and at 420 K only up to 80 MPa. At moderate pressures in the supercritical region, the present data overlap with the data of Soldatenko and Dregulyas. The measurement results are reported in Appendix B, Table B.4.

Since the propene measurements were analyzed with the calibration function for

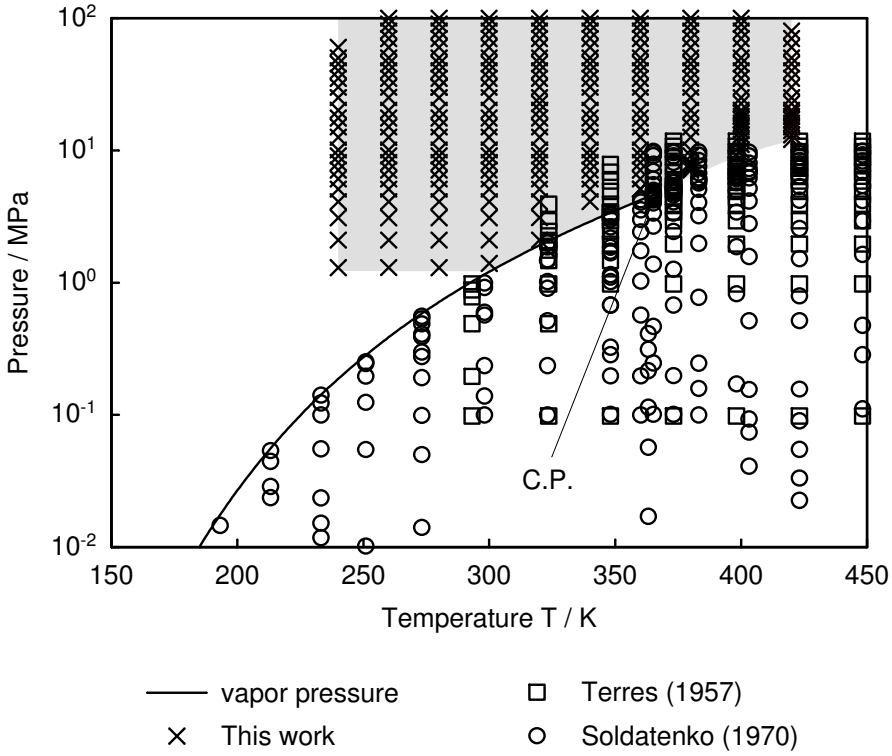

Figure 5.8. Distribution of the present measurements and literature data for the speed of sound in propene in the p,T plane.

the acoustic path length determined by the August 2004 calibration measurements, the basic uncertainty of the speed of sound measurement is slightly higher than the one given by Eq. (4.65). In Eq. (4.65), the value 0.007 % is therefore replaced by 0.009 %. The reproducibility of the speed of sound data for repeated measurements at the same state point after temperature and pressure cycles was better than 0.002 %. On the subcritical isotherms 340 K and 360 K and on supercritical isotherms, the reproducibility at the states with low pressures was somehow larger, amounting to 0.005 %. As for propane, thermal relaxation phenomena do not significantly influence the propagation of sound waves in the frequency range of the present measurements [200, p. 471] so that no dispersion correction is required. When the reproducibility and the additional contribution due to sample impurities are included, the total uncertainty of the speed of sound measurement is given by

$$\varepsilon_w(p) = 0.016\,\% + 2.5 \cdot 10^{-5}\,\frac{\%}{\mathrm{MPa}} \cdot p\,. \tag{5.7}$$

The state point assignment error due to the uncertainties of the temperature and

pressure was estimated by the equation of state of Angus et al. [7] to be 0.003 % for the temperature measurement and 0.002 % for the pressure measurement. For the lowest measured pressures on the supercritical isotherms, the influence of the pressure is larger, amounting to 0.005 %. When taking these additional contributions into account, the uncertainty of the speed of sound measurement becomes

$$\varepsilon_w(p) = 0.021\,\% + 2.5 \cdot 10^{-5}\,\frac{\%}{\mathrm{MPa}} \cdot p\,. \tag{5.8}$$

At the lowest pressures on the on supercritical isotherms, 0.019 % has to be replaced by 0.027 %.

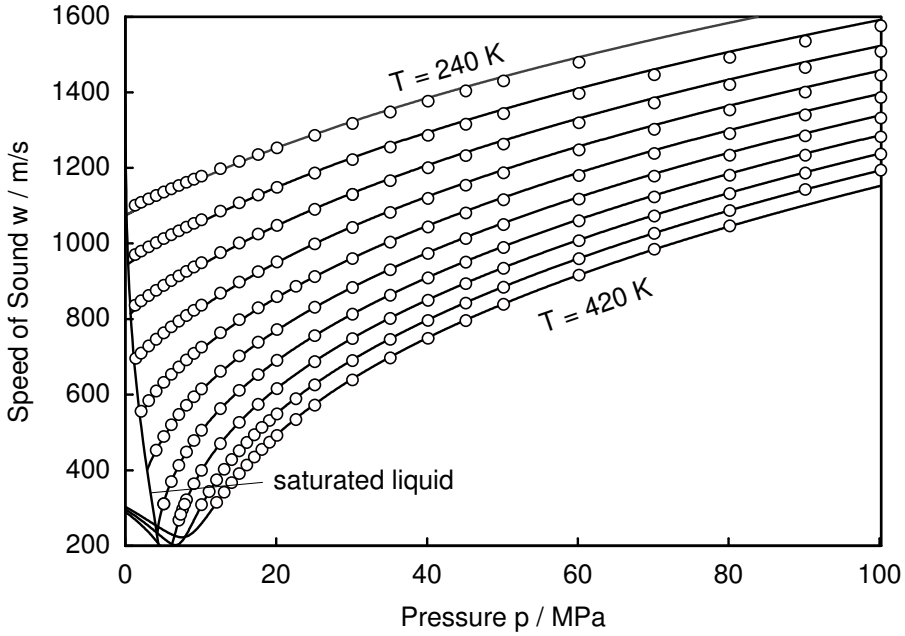

Figure 5.9. The speed of sound in propene as a function of pressure for all measured isotherms.

Fig. 5.9 shows the speed of sound data for the ten isotherms as a function of pressure. In the region of the measurements, the speed of sound ranges from about 250 $\mathrm{m\,s^{-1}}$ to 1700 $\mathrm{m\,s^{-1}}$ and is of similar magnitude as for propane, which is not surprising because the propene and propane molecules are very similar.

Figs. 5.10 and 5.11 show percentage deviations of the present data and the two literature data sets from the fundamental equation of state of Angus et al. [7]. The present data are very consistent and are represented by the equation of state on all isotherms within 1.5 %. The two literature data sets generally show similar

deviations, but scatter more than the present data. On some isotherms, for example at 340 K or 360 K, the data of Terres et al. in the liquid are by about 1.5 % higher than the present data. Except for these cases, the agreement among the data sets is within 1 % in the region where they overlap. The present data will be useful for establishing a more accurate fundamental equation of state for propene in the future.

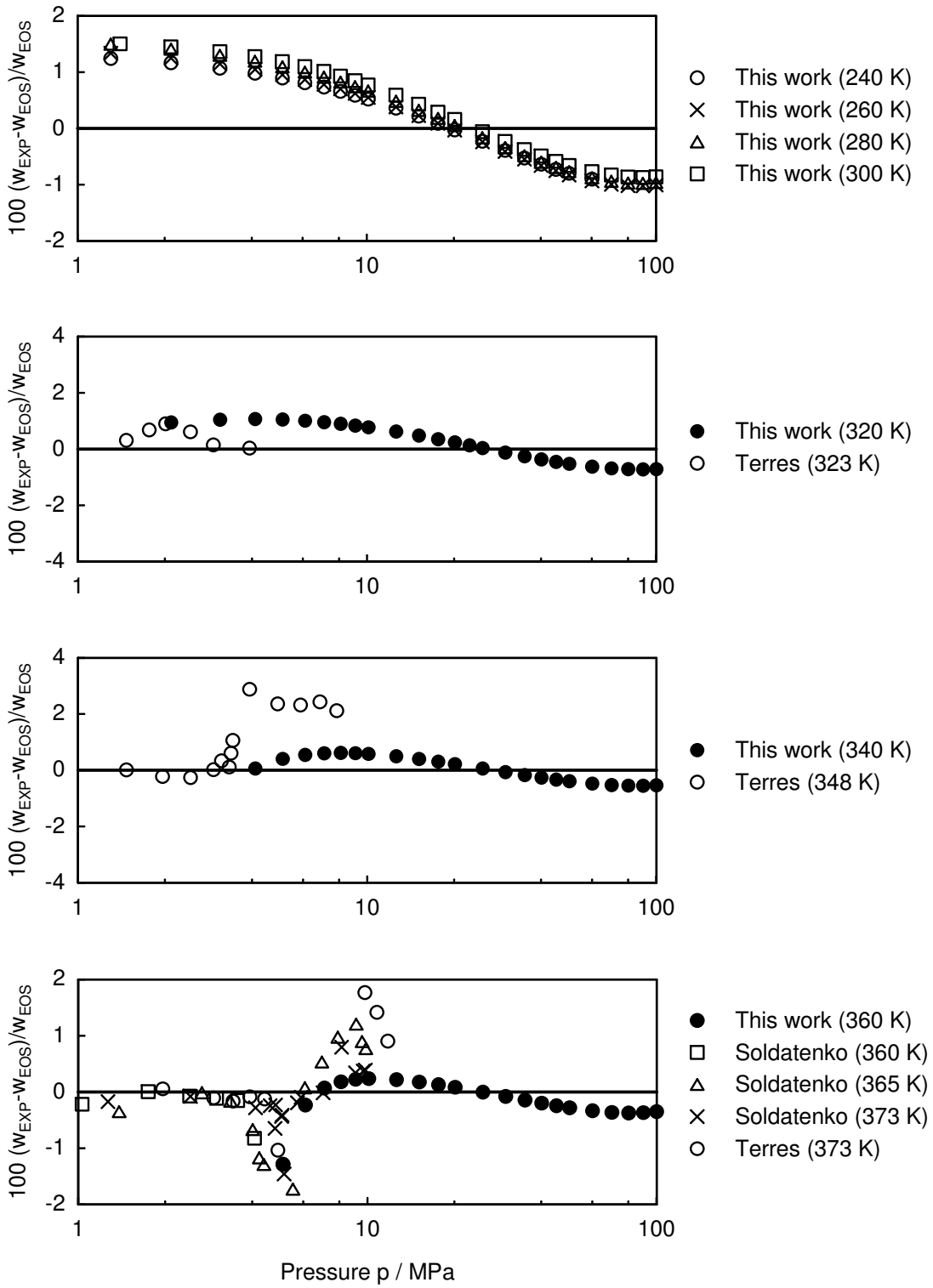

Figure 5.10. Percentage deviations of measured speeds of sound in liquid propene and literature data from the fundamental equation of state of Angus et al. [7] as a function of pressure at temperatures between 240 K and 360 K.

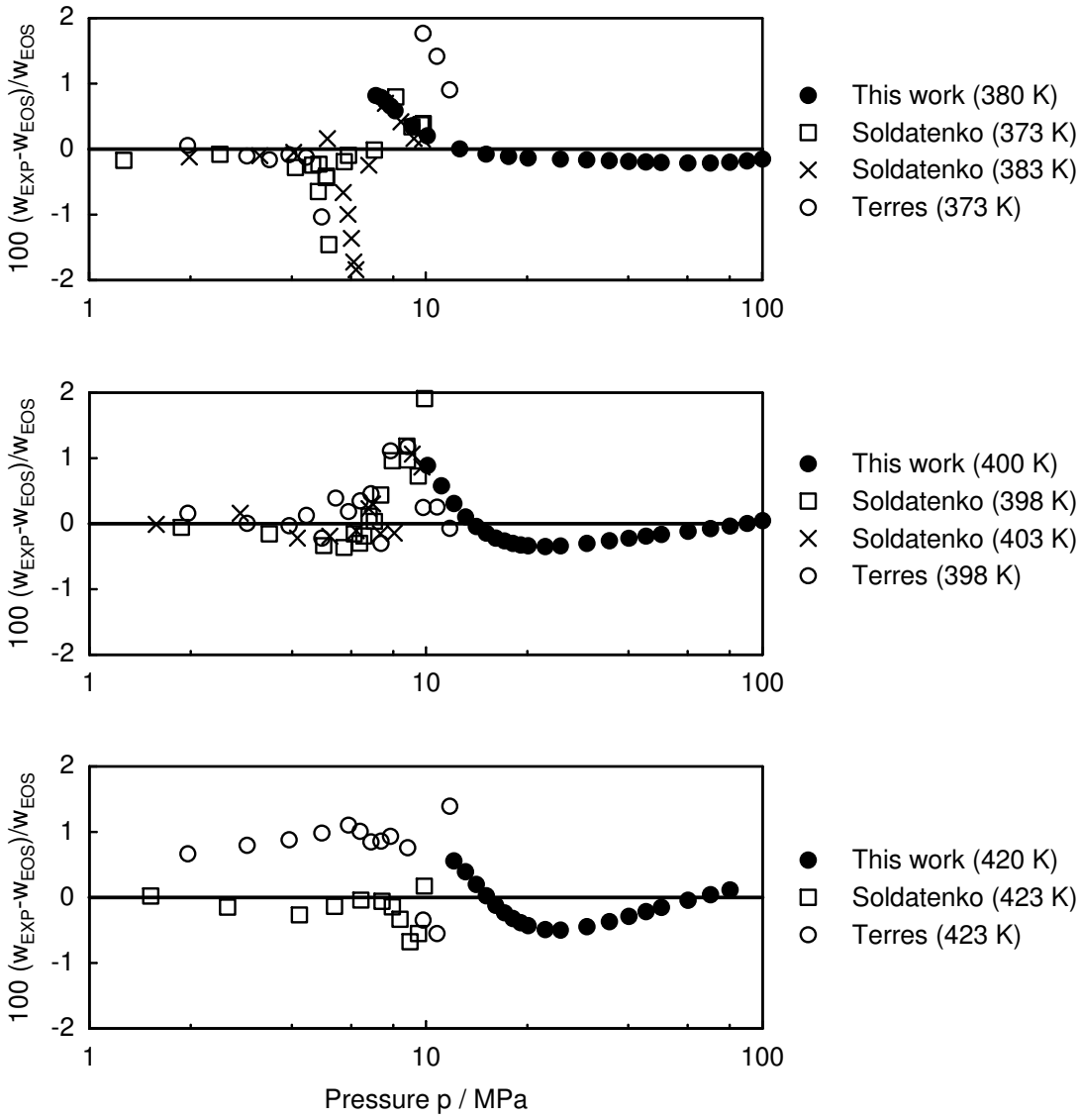

Figure 5.11. Percentage deviations of measured speeds of sound in liquid propene and literature data from the fundamental equation of state of Angus et al. [7] as a function of pressure at 380 K, 400 K, and 420 K.

5.5 Refrigerant 227ea

The refrigerant 227ea (1,1,1,2,3,3,3-heptafluoropropane) is a non-flammable hydrofluorocarbon without ozone depletion potential. It is mainly used as a pure substance as a propellant in aerosol sprays in medical technology. R227ea is employed as the secondary component in mixtures with R365mfc with 7 or 13 % by weight, which are used as blowing agents in the production of polyurethane foams for insulation purposes. Furthermore, R227ea can be used as a low vapor pressure refrigerant in refrigeration and air-conditioning applications with high condensation temperatures. Another possible application for mixtures of R365mfc with R227ea as a secondary component, which is presently being discussed, is the use as a working fluid in high temperature heat pumps with condensation temperatures of about 100 °C [89]. With the addition of R227ea, the flammability of R365mfc is reduced.

Table 5.2. Literature Data for the Speed of Sound in R227ea. Abbreviations: PE: Pulse-echo, IF: Cylindrical Interferometer, LS: Dynamic Light Scattering, sat. line: Saturated Gas and Liquid.

Author	Year	Method	Data	T / K	p / MPa	Purity	Uncertainty
Benedetto [18]	2001	SR	78	270–370	0.5	> 99.99 %	< 0.01 %
Fröba [60]	2005	LS	33	293–375	sat. line	> 99.9 %	< 0.5 %
Gruzdev [70]	2002	IF	66	273–383	3.5	> 99.99 %	< 0.2 %
Pires [148]	2000	PE	259	248–333	65	> 99.98 %	< 0.8 %

Four data sets for the speed of sound in R227ea are published in the literature. The details of these data sets are summarized in Table 5.2 and the distribution of the data in the p,T plane is depicted in Fig. 5.12. The data set of Benedetto et al. [18] covers a larger part of the gas region at subcritical temperatures. Fröba et al. [60] measured the speed of sound in saturated vapor and liquid R227ea, whereas the data of Gruzdev et al. [70] and Pires et al. [148] cover parts of the liquid region. The data set of Pires et al. extends up to 65 MPa, but the temperature range is limited by 333 K. The data of Gruzdev et al. cover a larger temperature range, but are restricted to moderate pressures below 3.5 MPa. At present, there are no data for the speed of sound in the liquid phase at high pressures above 333 K, and also the speed of sound at supercritical temperatures has not yet been measured. A fundamental equation of state for R227ea was developed by Lemmon and Span [112]. The functional form of the equation is of the so-called short type, which was originally developed by Span and Wagner [162, 163, 164] for several polar and non-polar fluids before. According

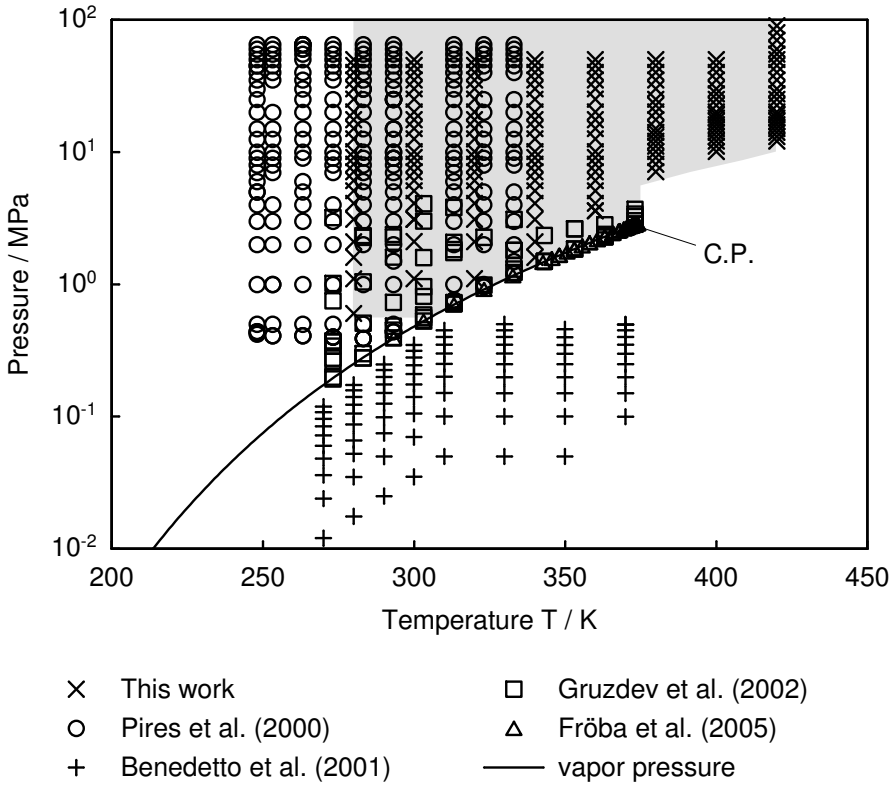

Figure 5.12. Distribution of the present measurements and literature data for the speed of sound in R227ea in the p,T plane.

to the authors, this equation of state represents the speed of sound in the liquid region only within 3 %. The present measurements were undertaken to extend the range of speed of sound measurements to higher temperatures and pressures.

The R227ea sample was provided by Solvay Fluor & Derivate GmbH in Hanover and had a purity better than 99.5 % according to the manufacturer's specification. The purity of the sample was examined by gas chromatography and found to be better than 99.975 %. Besides the main R227ea peak, four peaks with 0.010 area %, 0.008 area %, 0.006 area %, and 0.001 area % were detected. The peak with 0.008 area % could be identified as water, and no nitrogen or oxygen was detected. The nature of the remaining impurities was not identified. It is assumed that they are other hydrofluorocarbons, which occur as by-products in the production process. The contribution of the impurities to the uncertainty of the speed of sound data is estimated to be smaller than 0.01 %.

The present measurements cover the temperature range between 280 K and 420

K under pressures up to 50 MPa. Only the highest isotherm extends up to 90 MPa. During these measurements, the pressure vessel was sealed with an FEP encapsulated silicon o-ring. Since this type of o-ring fails after having been exposed to 100 MPa about four times, it was decided to measure only up to 50 MPa starting from the lowest to the highest temperature. At 420 K, measurements were also taken at higher pressures until the sealing failed at 100 MPa. The distribution of the present measurements in the p,T plane is also shown in Fig. 5.12.

The reproducibility of the speed of sound measurements at the same state point after pressure and temperature cycles was within 0.01 %, which is much higher than that for the propane and propene measurements. This is probably due to the use of a Viton o-ring in the hand pump. R227ea dissolves in the elastomer material and increases the size of a free Viton o-ring considerably [159]. It is assumed that small amounts of the elastomer material also dissolve in the R227ea or even react with it, which causes changes of the speed of sound in the R227ea.

Contrary to nitrogen, propane, and propene, it is not known if thermal relaxation phenomena influence the propagation of sound waves in R227ea. However, one can conclude from the comparison of the present data with the data of Gruzdev et al., which were measured at 1 MHz, and the data of Fröba et al., which were measured by a dynamic light scattering technique, given below that the influence of thermal relaxation on the speed of sound is negligible for the present measurements.

Due to the sample impurities and the reduced reproducibility, the uncertainty of the speed of sound data is higher than that for the propane and propene data. It is estimated to be

$$\varepsilon_w(p) = 0.027\,\% + 2.5 \cdot 10^{-5}\,\frac{\%}{\mathrm{MPa}} \cdot p\,. \tag{5.9}$$

The state point assignment errors due to the uncertainties of the temperature and pressure measurements are estimated from the preliminary equation of state of Lemmon. They are lower than 0.003 % and 0.002 %, respectively. For the measurements at the lowest pressures on the supercritical isotherms, the error due to the uncertainty of the pressure measurement is higher, amounting to 0.01 %. Including the state point assignment error, the uncertainty becomes

$$\varepsilon_w(p) = 0.032\,\% + 2.5 \cdot 10^{-5}\,\frac{\%}{\mathrm{MPa}} \cdot p\,. \tag{5.10}$$

At the lowest pressures on the highest subcritical isotherms and on supercritical isotherms, 0.032 % has to be replaced by 0.04 %.

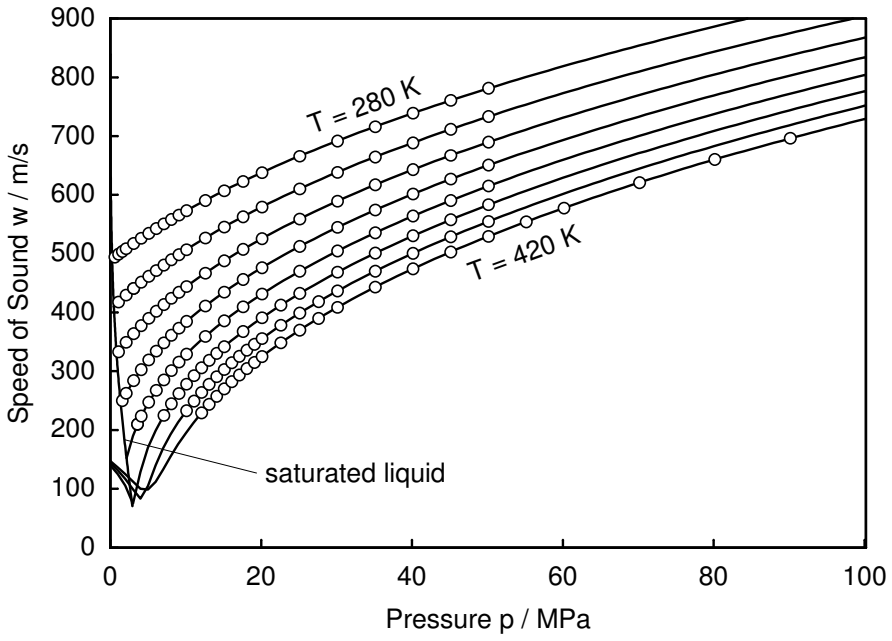

Figure 5.13. The speed of sound in R227ea as a function of pressure for all measured isotherms.

Fig. 5.13 shows the speed of sound data for all measured isotherms as a function of pressure. Generally, the speed of sound in R227ea is lower than in propane and propene. In the range of the measurements, it takes values between 200 m/s to 800 m/s.

The new data are currently being used by Lemmon [110] to establish a new fundamental equation of state for R227ea. In the following, the present data are compared with a preliminary equation of state for R227ea provided by Lemmon. Figs. 5.14 and 5.15 show percentage deviations of the present data and of selected literature data reviewed in Table 5.2 from the fundamental equation of state.

The present data are represented by the equation of state within 0.1 % in the entire temperature and pressure range of the measurements. They agree with the data of Gruzev et al. mostly within 0.5 %. The present data are very consistent, whereas the data of Gruzdev et al. scatter considerably. The data of Pires et al. at 280 K and 320 K are systematically lower than the present data by about 0.8 %. This large systematic difference is probably due to the different calibration procedures. Pires et al. determined the acoustic path length in their sensor by a calibration measurement at 298.15 K and 10 MPa with pure CCl_4, for which the speed of sound

is not as accurately known as for water, which was used as the calibration fluid in this work. Good agreement between the present data and the data of Fröba et al. is observed within the quoted uncertainty of 0.5 %. As for propane, the accurate present data allow to decide which one of the literature data sets is correct. In this case, the data of Pires et al. are too low by about 0.8 %.

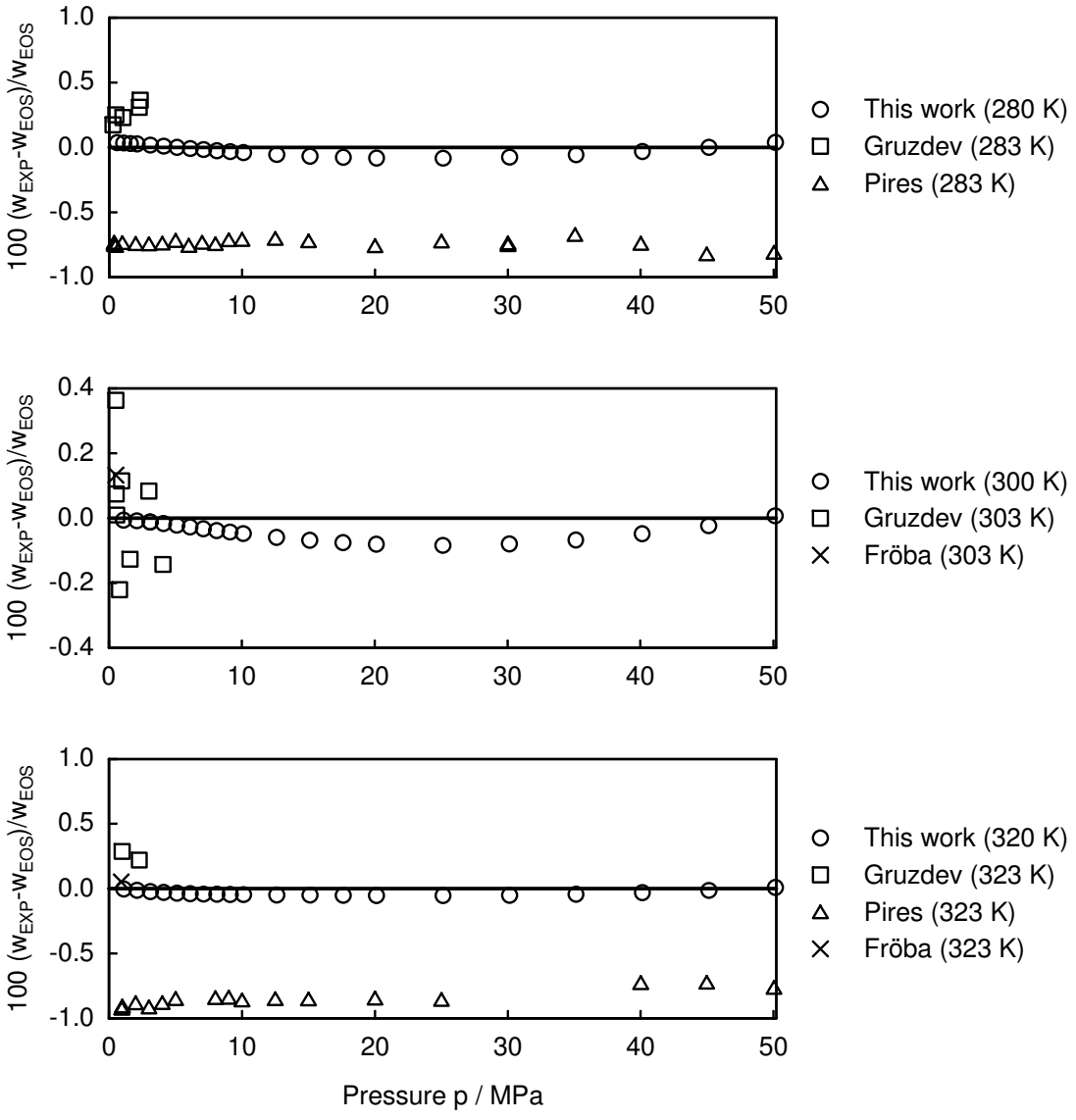

Figure 5.14. Percentage deviations of the present speed of sound data for R227ea and literature data from the preliminary fundamental equation of state of Lemmon [110] as a function of pressure at temperatures at 280 K, 300 K, and 320 K.

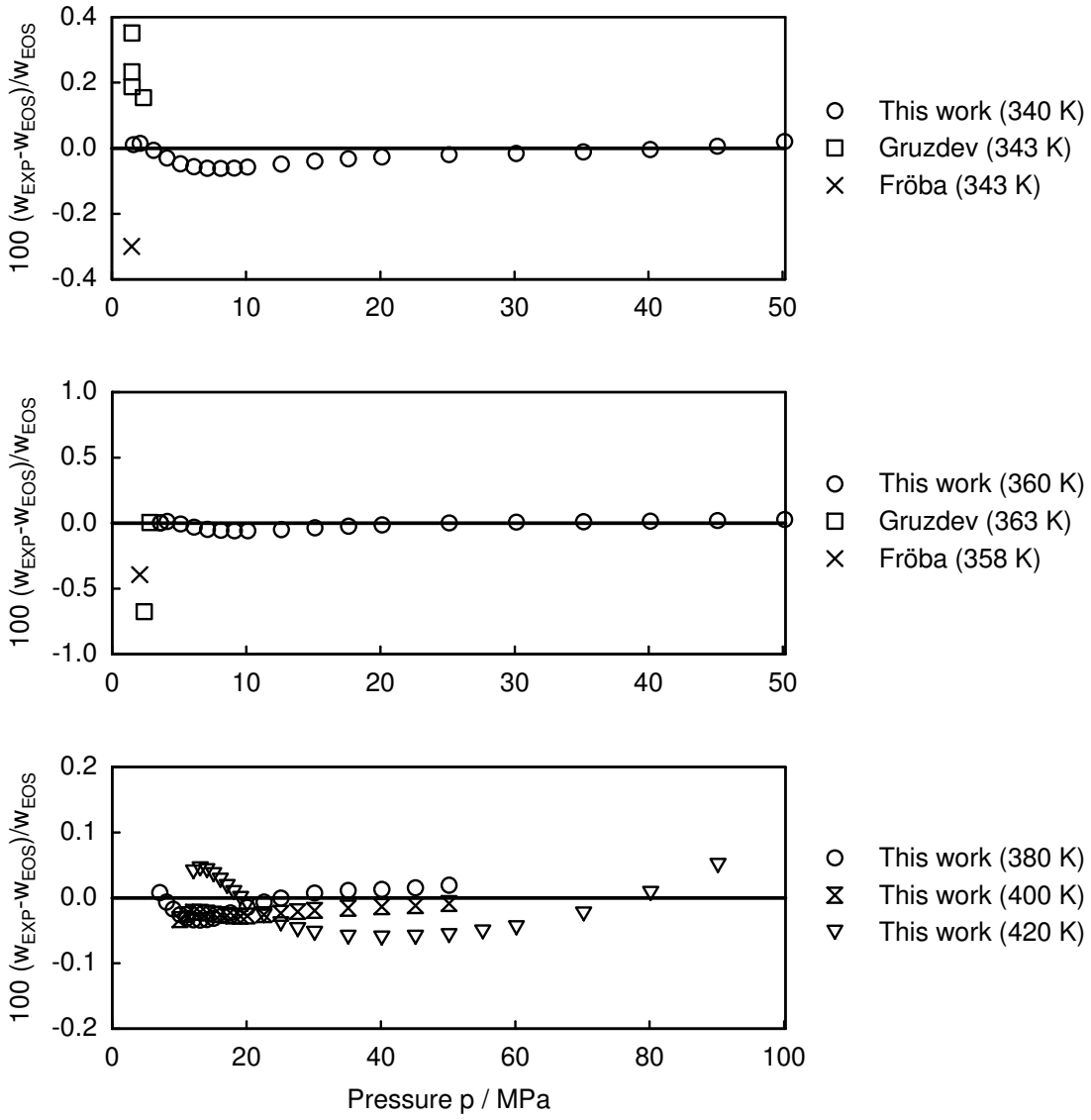

Figure 5.15. Percentage deviations of the present speed of sound data and literature data for R227ea from the preliminary fundamental equation of state of Lemmon [110] as a function of pressure between 340 K and 420 K.

5.6 Refrigerant 365mfc

R365mfc (1,1,1,3,3-pentafluorobutane) is a flammable hydrofluorocarbon, which has no impact on the ozone layer. It is predominantly used as the main component in binary mixtures with 7 % or 13 % by weight R227ea in the production of polyurethane foams for insulation purposes, where a liquid foaming agent with low thermal conductivity and high vapor pressure is required. Besides, mixtures of R365mfc and R227ea are considered as possible working fluids in high temperature heat pump systems with condensation temperatures of about 100 °C.

In spite of these practical applications, only a very limited number of data for the thermophysical properties of R365mfc is available in the literature. In particular, only one data set has been published for the speed of sound in R365mfc by Fröba et al. [59]. In that work, the dynamic surface light scattering technique was employed to measure the speed of sound in the saturated gas and liquid. Altogether, 29 data were reported in the temperature range between 298 K and 460 K. The sample had a purity better than 99.5 %, and the uncertainty of the speed of sound data was estimated to be 0.5 %. The speed of sound in the single phase liquid region has not yet been measured.

The R365mc sample was provided by Solvay Fluor & Derivate GmbH in Hanover. It had a stated purity better than 99.5 % and was degassed in an ultrasonic bath before it was filled into the apparatus. Since the vapor pressure of R365mfc at ambient temperature is lower than the ambient pressure, the sample container was heated up to at least 50 °C, where the vapor pressure amounts to about 0.14 MPa, during the degassing process.

The purity of the sample was analyzed by gas chromatography, and two peaks with 0.001 area % and 0.006 area % besides the main R365mfc peak were detected. The nature of these peaks could not be identified. The purity of the sample is assumed to be 99.993 %. The contribution of the impurities to the uncertainty of the speed of sound data is estimated to be lower than 0.004 %.

Fig. 5.16 depicts the distribution of the present data and the data of Fröba et al. [59] in the p,T plane. The present measurements cover the temperature range between 250 K and 420 K under pressures up to 100 MPa. Due to the high critical point of R365mfc at about (460 K, 3.252 MPa), the data cover only a part of the liquid region. It was first tried to start the measurements at 240 K because the NIST Reference Database RefProp [108] reports the triple point temperature 239 K. During the cooling process the sample was kept at about 40 MPa and froze before

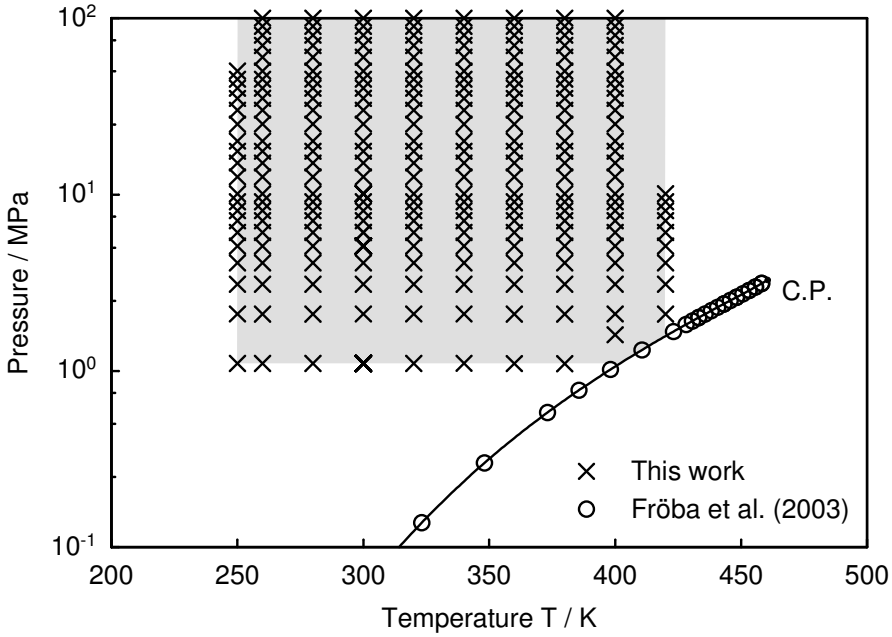

Figure 5.16. Distribution of the present measurements and the data of Fröba et al. [59] for the speed of sound in R365mfc in the p,T plane.

240 K were reached. Therefore, it was decided to start measurements at 250 K. At this temperature, measurements were taken up to 50 MPa. When it was tried to increase the pressure from 50 MPa to 60 MPa, the sample froze again. Then the measurements were continued at 260 K, where it was possible to take measurements over the full pressure range of the apparatus up to 100 MPa. The measurement results are reported in Appendix B, Table B.6.

Measurements on the isotherm 300 K were repeated several times with new samples filled into the apparatus to assess the reproducibility. It was observed that the reproducibility initially decreased with time by about 0.003 % over a day, indicating that the sample changes in the apparatus. This is probably due to interactions between the R365mfc and the polymer materials PTFE and PVDF used inside the system. Also, interactions between R365mfc and a Viton o-ring used as a seal in the hand pump could be the cause for these changes. For this reason, the sample was removed from the apparatus after two complete isotherms were measured (about up to 10 days), and the apparatus was refilled with R365mfc from the sample container.

When the apparatus was evacuated after it had been filled with R365mfc, it was observed that it took considerably longer than usual to reach 0.05 Pa, which is the

lowest pressure indicated by the vacuum pressure gauge. It is believed that the R365mfc dissolves in the PTFE parts in the pressure vessel and the PTFE seals of the high pressure valves. Although this provides no problem for the measurements described in this section, the apparatus must be carefully cleaned and evacuated before a different sample is filled in.

As for R227ea, it is not known, if thermal relaxation phenomena influence the propagation of sound waves in R365mfc. However, one can conclude from the comparison of the present data with the data of Fröba et al. below that the influence of thermal relaxation on the speed of sound can be neglected for the present measurements. Since the Fröba et al. data were measured by a dynamic light scattering technique, they should not be influenced by dispersion effects.

The uncertainty of the speed of sound data is higher than that for the propane and propene data due to the reduced reproducibility. It is estimated to be

$$\varepsilon_w(p) = 0.02\,\% + 2.5 \cdot 10^{-5}\,\frac{\%}{\mathrm{MPa}} \cdot p\,. \tag{5.11}$$

The state point assignment errors were estimated from a preliminary equation of state of Lemmon [111] and amounts to 0.002 % and 0.003 % for the influence of the temperature and pressure. On the highest isotherms near the vapor pressure, the influence of the uncertainty of the temperature measurement is larger, amounting to 0.005 %. Including the state point assignment errors, the uncertainty of the speed of sound data becomes

$$\varepsilon_w(p) = 0.025\,\% + 2.5 \cdot 10^{-5}\,\frac{\%}{\mathrm{MPa}} \cdot p\,. \tag{5.12}$$

For the state points on the highest isotherms near the vapor pressure, 0.025 % must be replaced by 0.028 %.

Fig. 5.17 shows the measured speed of sound data on all isotherms as a function of pressure. The speed of sound in R365mfc ranges from about 250 $\mathrm{m\,s^{-1}}$ to about 1250 $\mathrm{m\,s^{-1}}$, which is considerably lower than the speed of sound in propane or propene. For example, the speed of sound in propane in the vicinity of the triple point is larger than 2000 $\mathrm{m\,s^{-1}}$, while in R365mfc it is about 1000 $\mathrm{m\,s^{-1}}$.

As for R227ea, the new data are currently being used by Lemmon [111] to establish a new fundamental equation of state for R365mfc. Fig. 5.18 compares the present measurements with a preliminary equation of state provided by Lemmon [111] and with the data of Fröba et al. [59]. The equation of state represents the present data generally within 0.1 %, only few data at the highest measured pressure 100.1 MPa on some isotherms show slightly larger deviations. The data of Fröba

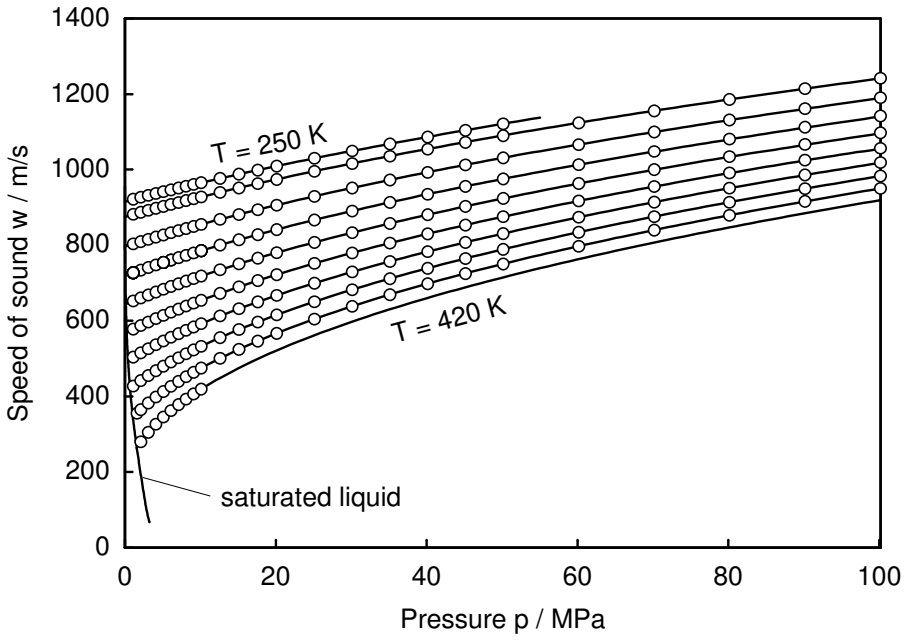

Figure 5.17. The speed of sound in R365mfc as a function of pressure for all measured isotherms.

et al. are represented within 0.4 % by the equation of state in the temperature range of the present measurements, but at higher temperatures their deviations increase. This comparison shows that the present data agree with the data of Fröba et al. within the quoted uncertainties.

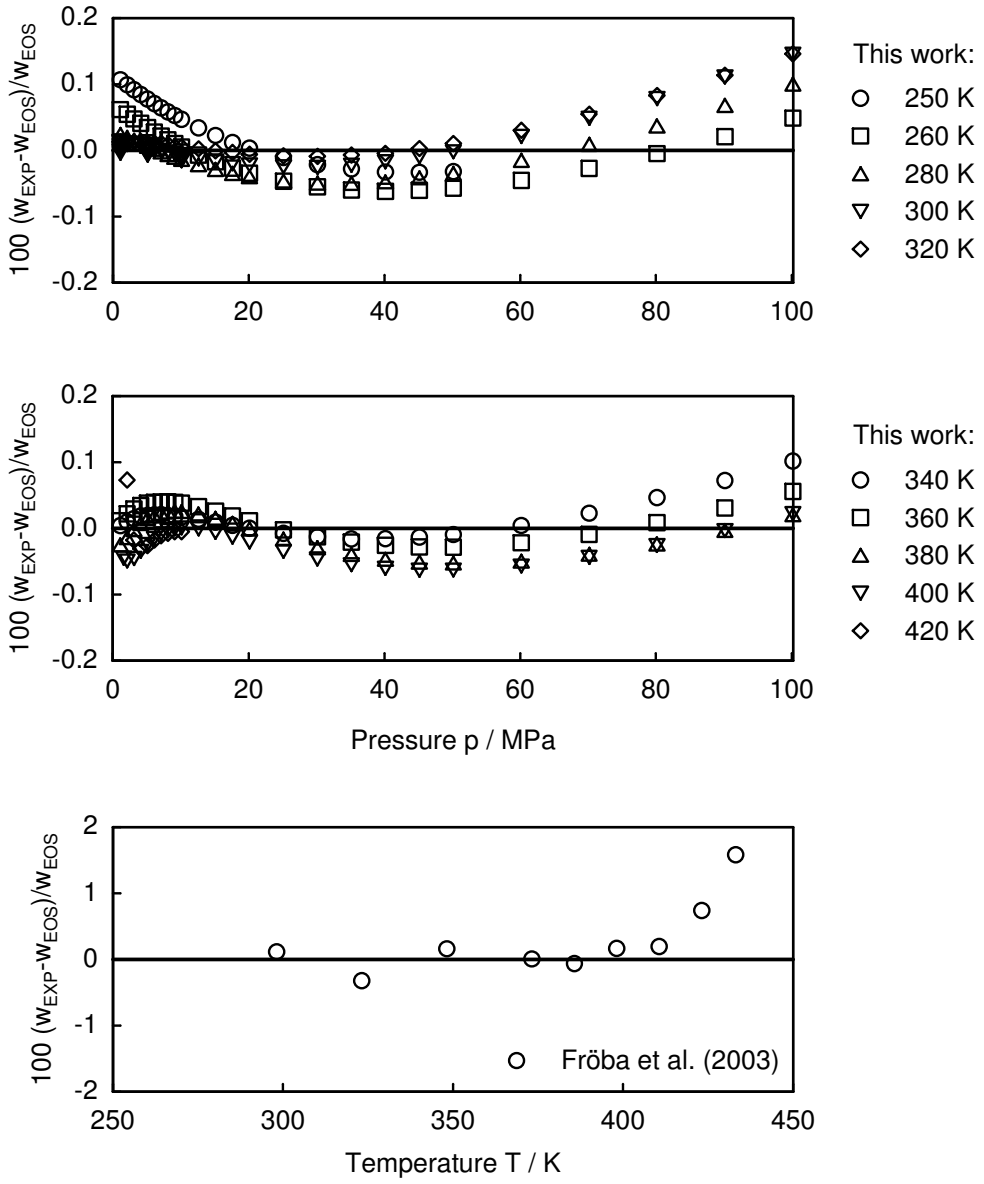

Figure 5.18. Percentage deviations of the speeds of sound data in liquid R365mfc from the preliminary fundamental equation of state of Lemmon [111] as a function of pressure for all measured isotherms (top figures). The bottom figure shows percentage deviations of the data of Fröba et al. [59] from the equation of state as a function of temperature.

6 Conclusions and Outlook

In the limit of low frequencies and small amplitudes, the speed at which sound waves propagate in a fluid is a function of its thermodynamic state only. Since the square of the speed of sound is the derivative of pressure with respect to density at constant entropy, accurate speed of sound data sets are useful for developing equations of state for pure fluids and mixtures, especially under high pressures where many thermodynamic properties depend strongly on density.

In this work, a new instrument for high-precision measurements of the speed sound in liquids and compressed gases in the temperature range between 240 K and 420 K and under high pressures up to 100 MPa was developed. The measurement principle of the acoustic sensor is based on a pulse-echo technique. A piezoelectric quartz crystal is mounted asymmetrically at distances of 20 mm and 30 mm between two stainless steel reflectors. The crystal is excited by a sinusoidal burst signal of 60–100 cycles and emits sound signals in both directions into the sample liquid. The speed of sound is obtained as two times the difference of the distances between the crystal and the reflectors divided by the difference of the transit times the signals need to travel these distances. For the extraction of the time difference from the received pulse-echo pattern, a phase-comparison technique originally developed by Kortbeek et al. [93] was modified, with which a resolution of the time difference measurement of at least 5 ppm is achieved.

The acoustic sensor resides in a pressure vessel, which is mounted in a circulating liquid bath thermostat, whose temperature is kept constant by a PID controller. The temperature is measured in the wall of the pressure vessel with a calibrated Pt25 platinum resistance thermometer employing a high-precision alternating current bridge system. Measurements of the pressure are performed by two gas pressure balances operated with nitrogen with measurement ranges of 5 MPa and 100 MPa, which are coupled to the sample liquid via a membrane-type differential pressure indicator. The measurement uncertainties are estimated to be smaller than 3 mK for the temperature and smaller than 0.01 % below 10 MPa or smaller than 0.005 % between 10 and 100 MPa for the pressure.

The acoustic path length and the thermal expansion coefficient of the sensor material were determined by calibration measurements with distilled and deionized liquid water at ambient pressure. Corrections for the variation of the acoustic path

length with temperature and pressure and for diffraction effects are applied in the measurement analysis.

In order to validate the instrument, the speed of sound in liquid water was measured on the three isotherms 303 K, 313 K, and 323 K under pressures up to 100 MPa. These speed of sound data have uncertainties smaller than 0.005 % and are even more accurate than the best literature data for liquid water. Moreover, the speed of sound in compressed nitrogen was measured on six isotherms between 275 K and 400 K and under pressures between 20 MPa and 100 MPa. These data set partially overlaps with a very accurate data set measured by Costa Gomez and Trusler [32] with a spherical resonator, whose accuracy was estimated to be better than 0.01 %. In the region where the two data sets overlap, their agreement is within at least 0.01 %. These results demonstrate that the instrument is capable of highly accurate speed of sound measurements.

Furthermore, the speed of sound in the liquid and supercritical region of propane, propene, and the refrigerants 227ea and 365mfc was measured in the temperature range between 240 K and 420 K under pressures up to 100 MPa. The uncertainty of the speed of sound data is generally estimated to be smaller than 0.01 %. Including contributions due to the state point assignment error and due to sample impurities, increases the uncertainty for each fluid. The uncertainties of the data for propane and propene are estimated to be 0.025 %, whereas the uncertainties of the data for R227ea and R365mfc are larger and amount to 0.035 %. The data for propane, R227ea, and R365mfc were used by Lemmon et al. [109] and Lemmon [109, 110] to develop new accurate fundamental equations of state for these fluids. The high accuracy of the data is demonstrated by comparisons with literature data and equation of state models.

Future research projects on speed of sound measurements in liquids and compressed gases could develop in two directions: First, besides pure fluids, mixtures could be examined. This requires containers, in which mixtures can be set up gravimetrically from the pure substances and stored under pressure in the liquid phase until they are filled into the apparatus.

Second, the speed of sound apparatus could be extended by a sensor for accurate density measurements under moderate pressures. With speed of sound measurements over the full pressure range of the apparatus up to 100 MPa and additional density measurements at moderate pressures, fundamental equations of state, which cover the complete pressure range, could be developed as follows. With the density and speed of sound data and additional data for the vapor pressure and the

density and speed of sound in the gas phase, a fundamental equation of state could be established which describes the moderate pressure regime accurately. From this intermediate fundamental equation of state, initial values for the integration method described in the introduction could be calculated. Furthermore, the speed of sound data could be represented by a correlation over the full pressure range. Then the integration method could be applied to determine the thermal equation of state up to 100 MPa. Finally, the speed of sound data and the derived thermal data could be used to establish a fundamental equation of state, from which all thermodynamic properties could be calculated under pressures up to 100 MPa.

Appendix

A Relations Between Thermodynamic State Variables

In this appendix, relations between thermodynamic state variables, which have been used in the main text without prove, will be derived. In particular, relations between the thermodynamic speed of sound and the thermal equation of state and the fundamental equation of state will be considered.

In Sec. 2.2.1, it was shown that, under the assumption that the compression and expansion cycles within a sound wave are almost isentropic processes, the speed of sound is a thermodynamic state variable and related to the thermal equation of state by

$$w^2 = \left(\frac{\partial p}{\partial \rho}\right)_s . \tag{A.1}$$

For the calculation of the speed of sound, the entropy equation of state in the form $p = p(\rho, s)$ must be known. However, usually the thermal equation of state is either given as $p = p(\rho, T)$ or $\rho = \rho(p, T)$ with the temperature in place of the entropy as an independent variable. In order to relate the speed of sound to the thermal equation of state, the partial derivative $(\partial p/\partial \rho)_s$ must be replaced by derivatives of the thermal equation of state. This procedure is exemplified here for the case that the equation of state is given in the form $p = p(\rho, T)$.

Assume that an arbitrary function Φ depends on two independent variables x and y, which themselves are function of two variables u and v, that is $\Phi = \Phi(x(u, v), y(u, v))$. The derivative of Φ with respect to u is then given by the chain rule as

$$\left(\frac{\partial \Phi}{\partial u}\right)_v = \left(\frac{\partial \Phi}{\partial x}\right)_y \left(\frac{\partial x}{\partial u}\right)_v + \left(\frac{\partial \Phi}{\partial y}\right)_x \left(\frac{\partial y}{\partial u}\right)_v . \tag{A.2}$$

If $u = x$, Eq. (A.2) reduces to

$$\left(\frac{\partial \Phi}{\partial x}\right)_v = \left(\frac{\partial \Phi}{\partial x}\right)_y + \left(\frac{\partial \Phi}{\partial y}\right)_x \left(\frac{\partial y}{\partial x}\right)_v . \tag{A.3}$$

Setting $\Phi = p$, $v = s$, $x = \rho$, and $y = T$, yields

$$\left(\frac{\partial p}{\partial \rho}\right)_s = \left(\frac{\partial p}{\partial \rho}\right)_T + \left(\frac{\partial p}{\partial T}\right)_\rho \left(\frac{\partial T}{\partial \rho}\right)_s . \tag{A.4}$$

The derivative $(\partial T/\partial \rho)_s$ can be expressed in terms of the isochoric heat capacity and the derivative $(\partial p/\partial T)_\rho$. First, an infinitesimal entropy change is represented by the total differential of the entropy equation of state $s = s(\rho, T)$

$$ds = \left(\frac{\partial s}{\partial T}\right)_\rho dT + \left(\frac{\partial s}{\partial \rho}\right)_T d\rho = 0, \tag{A.5}$$

which must be zero since the sound propagation is assumed to be isentropic. Dividing by dT, yields

$$\left(\frac{\partial s}{\partial T}\right)_\rho = -\left(\frac{\partial s}{\partial \rho}\right)_T \left(\frac{\partial \rho}{\partial T}\right)_s, \tag{A.6}$$

which can be rewritten as

$$\left(\frac{\partial T}{\partial \rho}\right)_s = -\left(\frac{\partial T}{\partial s}\right)_\rho \left(\frac{\partial s}{\partial \rho}\right)_T. \tag{A.7}$$

By using the relations

$$\left(\frac{\partial s}{\partial T}\right)_\rho = \left(\frac{\partial s}{\partial u}\right)_\rho \left(\frac{\partial u}{\partial T}\right)_\rho = \frac{c_v}{T} \tag{A.8}$$

and

$$\left(\frac{\partial s}{\partial \rho}\right)_T = -\frac{1}{\rho^2}\left(\frac{\partial p}{\partial T}\right)_\rho, \tag{A.9}$$

one finds

$$\left(\frac{\partial T}{\partial \rho}\right)_s = \frac{T}{\rho^2 c_v}\left(\frac{\partial p}{\partial T}\right)_\rho. \tag{A.10}$$

By substituting Eq. (A.10) into Eq. (A.4) and the result into Eq. (A.1), the desired expression for the speed of sound in terms of derivatives of the thermal equation of state

$$[w(\rho, T)]^2 = \left(\frac{\partial p}{\partial \rho}\right)_T + \frac{T}{\rho^2 c_v}\left[\left(\frac{\partial p}{\partial T}\right)_\rho\right]^2 \tag{A.11}$$

is obtained.

In Eq. (A.8), the definitions of the thermodynamic temperature, $T = (\partial u/\partial s)_\rho$, and of the isochoric heat capacity, $c_v = (\partial u/\partial T)_\rho$, have been used. Eq. (A.9) is

a Maxwell relation, which can be derived by equating the mixed second partial derivatives of the Helmholtz free energy

$$\left[\frac{\partial}{\partial v}\left(\frac{\partial a}{\partial T}\right)_v\right]_T = \left[\frac{\partial}{\partial T}\left(\frac{\partial a}{\partial v}\right)_T\right]_v . \tag{A.12}$$

With the identifications $s = -(\partial a/\partial T)_v$ and $p = -(\partial a/\partial v)_T$, and $\partial\rho/\partial v = -\rho^2$, Eq. (A.9) is established.

If the thermal equation of state is given in the form $\rho = \rho(p, T)$, a similar derivation leads to the representation

$$[w(p,T)]^{-2} = \left(\frac{\partial\rho}{\partial p}\right)_T - \frac{T}{\rho^2 c_p}\left[\left(\frac{\partial\rho}{\partial T}\right)_p\right]^2 \tag{A.13}$$

for the speed of sound.

An expression for the speed of sound in terms of derivatives of the fundamental equation of state $a = a(\rho, T)$ can be derived from Eq. (A.11) by replacing the pressure by $p = \rho^2(\partial a/\partial\rho)_T$ and the isochoric heat capacity by $c_v = -T(\partial^2 a/\partial T^2)_\rho$. One finds

$$[w(\rho,T)]^2 = 2\rho\left(\frac{\partial a}{\partial\rho}\right)_T + \rho^2\left(\frac{\partial^2 a}{\partial\rho^2}\right)_T - \rho^2\frac{\left(\dfrac{\partial}{\partial T}\left[\dfrac{\partial a}{\partial\rho}\right]_T\right)^2_\rho}{\left(\dfrac{\partial^2 a}{\partial T^2}\right)_\rho} \tag{A.14}$$

Similarly, when the Gibbs free energy is used as a fundamental equation of state, Eq. (A.13) becomes

$$[w(p,T)]^2 = \frac{-\left[\left(\dfrac{\partial g}{\partial p}\right)_T\right]^2\left(\dfrac{\partial^2 g}{\partial T^2}\right)_p}{\left(\dfrac{\partial^2 g}{\partial p^2}\right)_T\left(\dfrac{\partial^2 g}{\partial T^2}\right)_p - \dfrac{\partial}{\partial p}\left(\dfrac{\partial g}{\partial T}\right)^2_\rho}. \tag{A.15}$$

For the integration scheme for the determination of the thermal equation of state from speed of sound data, the relation

$$\left(\frac{\partial c_v}{\partial\rho}\right)_T = -\frac{T}{\rho^2}\left(\frac{\partial^2 p}{\partial T^2}\right)_\rho \tag{A.16}$$

is required as part of the system of differential equation, which has to be solved. This relation can be derived by equating the mixed third partial derivatives of the Helmholtz free energy

$$\left(\frac{\partial}{\partial\rho}\left[\frac{\partial^2 a}{\partial T^2}\right]_\rho\right)_T = \left(\frac{\partial^2}{\partial T^2}\left[\frac{\partial a}{\partial\rho}\right]_T\right)_\rho , \tag{A.17}$$

in which the isochoric heat capacity $c_v = -T(\partial^2 a/\partial T^2)_\rho$ is inserted on the left hand side and the pressure $p = \rho^2(\partial a/\partial\rho)_T$ on the right hand side.

In Sec. 2.2.2 and 2.5, the relation

$$\left(\frac{\partial p}{\partial \rho}\right)_s = \frac{c_p}{c_v}\left(\frac{\partial p}{\partial \rho}\right)_T \tag{A.18}$$

was introduced. In order to establish it, Eq. (A.3) is applied to the entropy by setting $\Phi = s$, $x = T$, $y = p$, and $v = \rho$, which yields

$$\left(\frac{\partial s}{\partial T}\right)_\rho = \left(\frac{\partial s}{\partial T}\right)_p + \left(\frac{\partial s}{\partial p}\right)_T \left(\frac{\partial p}{\partial T}\right)_\rho . \tag{A.19}$$

Multiplying by T and using Eq. (A.8) and the similar relation

$$\left(\frac{\partial s}{\partial T}\right)_p = \left(\frac{\partial s}{\partial h}\right)_p \left(\frac{\partial h}{\partial T}\right)_p = \frac{c_p}{T} \tag{A.20}$$

for the isobaric heat capacity, leads to the expression

$$c_v = c_p + T\left(\frac{\partial s}{\partial p}\right)_T \left(\frac{\partial p}{\partial T}\right)_\rho . \tag{A.21}$$

The derivative $(\partial s/\partial p)_T$ must be replaced by derivatives of the thermal equation of state. First, the equality of the second mixed derivatives of the Gibbs free energy $g = g(T, p)$ is used to establish the Maxwell relation

$$\left(\frac{\partial s}{\partial p}\right)_T = -\left(\frac{\partial v}{\partial T}\right)_p = \frac{1}{\rho^2}\left(\frac{\partial \rho}{\partial T}\right)_p . \tag{A.22}$$

Second, the derivative of the density with respect to temperature must be replaced by derivatives of the pressure.

If an arbitrary function $\Phi(x, y)$ of two independent variables x and y is held constant, the total differential of Φ is given by

$$d\Phi = \left(\frac{\partial \Phi}{\partial x}\right)_y dx + \left(\frac{\partial \Phi}{\partial y}\right)_x dy = 0. \tag{A.23}$$

Dividing by dx and rearranging the result, yields

$$\left(\frac{\partial y}{\partial x}\right)_\Phi = -\left(\frac{\partial \Phi}{\partial x}\right)_y \left[\left(\frac{\partial \Phi}{\partial y}\right)_x\right]^{-1} . \tag{A.24}$$

With the identifications $\Phi = p$, $x = T$, and $y = \rho$, one finds

$$\left(\frac{\partial \rho}{\partial T}\right)_p = -\left(\frac{\partial p}{\partial T}\right)_\rho \left[\left(\frac{\partial p}{\partial \rho}\right)_T\right]^{-1} . \tag{A.25}$$

Substituting Eq. (A.25) into Eq. (A.22) and the result into Eq. (A.21), leads to

$$c_p = c_v + \frac{T}{\rho^2}\left(\frac{\partial p}{\partial T}\right)_\rho^2 \left[\left(\frac{\partial p}{\partial \rho}\right)_T\right]^{-1} \tag{A.26}$$

Combining Eqs. (A.26) and (A.11), finally yields Eq. (A.18).

All other thermodynamic relations, which were used in the main text, but not explicitly proved in this appendix, appear as intermediate results in the above derivations.

B Measurement Results

Table B.1. Measurement results for the speed of sound in liquid water under pressure.

T / K	p / MPa	w / $\mathrm{m\,s^{-1}}$	T / K	p / MPa	w / $\mathrm{m\,s^{-1}}$
		T = 303.15 K			
303.1538	0.102784	1509.172	303.1530	50.1370	1593.201
303.1538	2.10411	1512.526	303.1544	60.1435	1609.939
303.1540	10.1096	1525.983	303.1544	70.1505	1626.624
303.1541	20.1165	1542.805	303.1544	80.1575	1643.242
303.1538	30.1233	1559.621	303.1542	90.1645	1659.784
303.1535	40.1301	1576.418	303.1546	100.172	1676.236
		T = 313.15 K			
313.1576	0.102441	1528.904	313.1578	60.1445	1630.908
313.1578	10.1094	1546.163	313.1575	70.1516	1647.528
313.1577	20.1164	1563.323	313.1573	80.1587	1664.035
313.1575	30.1233	1580.374	313.1574	90.1658	1680.426
313.1576	40.1302	1597.336	313.1572	100.173	1696.684
313.1576	50.1373	1614.178			
		T = 323.20 K			
323.2085	0.103686	1542.635	323.2086	60.1449	1646.465
323.2078	10.1106	1560.409	323.2087	70.1519	1663.164
323.2081	20.1174	1577.979	323.2089	80.1588	1679.692
323.2081	30.1242	1595.370	323.2089	90.1659	1696.071
323.2085	40.1311	1612.576	323.2089	100.173	1712.283
323.2085	50.1380	1629.593			

Table B.2. Measurement results for the speed of sound in compressed nitrogen.

T / K	p / MPa	w / m s^{-1}	T / K	p / MPa	w / m s^{-1}
		$T = 275$ K			
274.9983	20.1142	415.4929	274.9984	50.1358	609.2602
274.9982	22.6159	431.0634	274.9983	60.1430	667.4263
274.9982	25.1176	447.1885	274.9983	70.1502	721.1118
274.9985	27.6194	463.6605	274.9985	80.1574	770.7800
274.9986	30.1211	480.3151	274.9982	90.1646	816.9420
274.9983	40.1286	546.5025	274.9987	100.172	860.0509
		$T = 300$ K			
300.0045	20.1136	426.5639	300.0059	50.1348	601.5197
300.0058	22.6152	440.2877	300.0059	60.1420	656.2306
300.0056	25.1170	454.5060	300.0058	70.1492	707.4303
300.0059	27.6188	469.0756	300.0058	85.1599	778.0554
300.0057	30.1205	483.8758	300.0062	100.171	842.2103
300.0061	40.1276	543.5779			
		$T = 325$ K			
325.0054	20.1139	438.3118	325.0045	50.1357	598.2718
325.0053	22.6158	450.7279	325.0048	60.1429	649.7057
325.0054	25.1176	463.5672	325.0049	70.1501	698.4085
325.0055	27.6194	476.7270	325.0047	80.1572	744.3508
325.0053	30.1212	490.1177	325.0049	90.1643	787.6845
325.0053	40.1284	544.5768	325.0050	100.172	828.6303
		$T = 350$ K			
349.9986	20.1160	450.1779	349.9988	50.1376	598.1073
349.9987	22.6179	461.6341	349.9983	60.1447	646.5658
349.9987	25.1196	473.4440	349.9987	70.1517	692.8898
349.9984	27.6214	485.5354	349.9987	80.1586	736.9342
349.9989	30.1231	497.8378	349.9987	90.1656	778.7510
349.9985	40.1303	548.0729	349.9987	100.173	818.4696
		$T = 375$ K			
374.9970	25.1176	483.6345	374.9978	50.1356	600.0579
374.9971	27.6193	494.8944	374.9984	60.1472	645.8771
374.9974	30.1211	506.3425	374.9984	70.1543	689.9961
374.9971	32.6229	517.9314	374.9991	80.1612	732.2254
374.9974	35.1246	529.6183	374.9993	90.1682	772.5474

Continued on next page.

Continued from previous page.

T / K	p / MPa	w / $\mathrm{m\,s^{-1}}$	T / K	p / MPa	w / $\mathrm{m\,s^{-1}}$
374.9977	40.1283	553.1456	374.9992	100.175	811.0293
		T = 400 K			
399.9978	25.1206	493.9124	399.9999	50.1384	603.4887
399.9981	27.6223	504.5069	400.0003	60.1456	646.9374
399.9984	30.1240	515.2653	400.0004	70.1528	689.0421
399.9983	32.6257	526.1493	400.0006	80.1601	729.5711
399.9986	35.1274	537.1280	400.0005	90.1673	768.4592
399.9994	40.1310	559.2445	400.0005	100.175	805.7315

Table B.3. Measurement results for the speed of sound in the liquid and supercritical region of propane.

T / K	p / MPa	w / m s^{-1}	T / K	p / MPa	w / m s^{-1}
		T = 240 K			
239.9981	1.30427	1113.773	239.9951	17.6162	1252.105
239.9977	2.10477	1121.560	239.9948	20.1179	1270.402
239.9974	3.10535	1131.115	239.9947	25.1214	1305.296
239.9977	4.10604	1140.476	239.9939	30.1250	1338.195
239.9948	4.10602	1140.490	239.9941	35.1285	1369.391
239.9977	5.10662	1149.656	239.9939	40.1319	1399.077
239.9978	6.10773	1158.650	239.9937	45.1353	1427.443
239.9971	7.10853	1167.507	239.9937	50.1387	1454.628
239.9967	8.10964	1176.200	239.9935	60.1456	1505.905
239.9967	9.11030	1184.736	239.9931	70.1526	1553.690
239.9967	10.1110	1193.134	239.9927	80.1598	1598.505
239.9960	12.6128	1213.535	239.9923	90.1668	1640.824
239.9952	15.1144	1233.173	239.9923	100.174	1680.930
		T = 260 K			
259.9956	1.30258	983.5414	259.9974	35.1262	1275.005
259.9958	2.10221	992.9805	259.9975	40.1297	1307.347
259.9957	3.10375	1004.492	259.9976	45.1332	1338.081
259.9961	4.10435	1015.695	259.9973	50.1368	1367.388
259.9960	5.10507	1026.614	259.9973	60.1444	1422.350
259.9963	6.10593	1037.264	259.9972	70.1514	1473.220
259.9962	7.10663	1047.671	259.9973	80.1584	1520.712
259.9966	8.10702	1057.836	259.9974	90.1655	1565.338
259.9964	9.10776	1067.785	259.9964	100.173	1607.495
259.9967	10.1085	1077.522	260.0024	1.30362	983.5120
259.9966	12.6102	1101.019	260.0022	4.10533	1015.672
259.9965	15.1120	1123.434	260.0020	10.1098	1077.492
259.9968	17.6141	1144.893	260.0017	20.1167	1165.454
259.9971	20.1158	1165.484	260.0012	30.1235	1240.761
259.9970	25.1193	1204.427	260.0019	40.1305	1307.321
		T = 280 K			
280.0026	1.30337	851.1622	280.0014	40.1310	1220.837
280.0013	1.30177	851.1420	280.0011	45.1345	1253.962
280.0015	2.10178	862.9531	280.0009	50.1381	1285.389

Continued on next page.

Continued from previous page.

T / K	p / MPa	w / m s^{-1}	T / K	p / MPa	w / m s^{-1}
280.0014	3.10256	877.1979	280.0011	60.1451	1343.972
280.0013	4.10327	890.9078	280.0009	70.1521	1397.843
280.0013	5.10402	904.1486	280.0008	80.1590	1447.870
280.0013	6.10483	916.9569	280.0009	90.1660	1494.687
280.0012	7.10557	929.3663	280.0013	100.173	1538.777
280.0016	8.10769	941.4215	280.0029	1.30200	851.1567
280.0018	9.10852	953.1253	280.0028	2.10252	862.9644
280.0018	10.1092	964.5196	280.0033	3.10304	877.1960
280.0016	12.6111	991.7596	280.0036	4.10371	890.9118
280.0016	15.1129	1017.445	280.0032	5.10427	904.1507
280.0014	17.6148	1041.794	280.0034	6.10502	916.9547
280.0016	17.6148	1041.794	280.0009	1.30358	851.1860
280.0015	20.1170	1064.973	280.0019	4.10552	890.9460
280.0019	25.1205	1108.346	280.0020	10.1097	964.5291
280.0014	30.1239	1148.415	280.0019	20.1165	1064.973
280.0013	35.1274	1185.771	280.0014	30.1235	1148.405
		$T = 300$ K			
300.0003	1.30344	713.1675	300.0013	35.1265	1101.932
300.0003	2.10401	728.7452	300.0015	40.1301	1139.761
300.0002	3.10451	747.1668	300.0016	45.1335	1175.264
300.0001	4.10512	764.5879	300.0016	50.1370	1208.788
300.0001	5.10562	781.1330	300.0014	60.1440	1270.888
300.0005	6.10613	796.9184	300.0013	70.1509	1327.618
300.0003	7.10668	812.0294	300.0015	80.1578	1380.042
300.0004	8.10732	826.5404	300.0013	90.1649	1428.911
300.0004	9.10793	840.5093	300.0010	100.172	1474.785
300.0011	10.1088	853.9889	300.0038	1.30369	713.1418
300.0017	12.6107	885.8170	299.9961	4.10571	764.6086
300.0020	15.1124	915.3732	300.0039	4.10565	764.5701
300.0020	17.6142	943.0456	299.9963	5.10643	781.1515
300.0016	20.1159	969.1237	300.0035	10.1098	853.9778
300.0016	25.1194	1017.346	300.0033	20.1168	969.1165
300.0016	30.1230	1061.330			
		$T = 320$ K			
320.0044	2.10294	583.6663	320.0049	50.1374	1137.653
320.0046	3.10370	609.7187	320.0038	60.1432	1203.103
320.0044	4.10490	633.3770	320.0039	70.1502	1262.540

Continued on next page.

Continued from previous page.

T / K	p / MPa	w / m s^{-1}	T / K	p / MPa	w / m s^{-1}
320.0041	5.10503	655.1577	320.0038	80.1572	1317.199
320.0045	6.10569	675.4144	320.0040	90.1642	1367.955
320.0048	7.10634	694.4133	320.0041	100.171	1415.464
320.0048	8.10700	712.3431	320.0481	2.10395	583.3329
320.0050	9.10775	729.3534	319.9973	2.10355	583.7163
320.0051	10.1084	745.5574	319.9975	3.10422	609.7592
320.0050	12.6102	783.1402	319.9976	4.10478	633.4115
320.0045	15.1124	817.3411	319.9977	5.10545	655.1838
320.0048	17.6143	848.8521	319.9974	6.10606	675.4455
320.0051	20.1162	878.1859	319.9974	7.10672	694.4474
320.0050	25.1196	931.6528	319.9988	8.10788	712.3790
320.0050	30.1232	979.7358	319.9993	9.10859	729.3843
320.0049	35.1267	1023.657	319.9993	10.1093	745.5897
320.0049	40.1302	1064.246	319.9994	12.6111	783.1681
320.0051	45.1338	1102.098	319.9996	15.1129	817.3579
		T = 340 K			
339.9981	3.60491	472.3191	339.9992	35.1268	951.0826
339.9983	4.10532	490.1540	339.9994	40.1299	994.3739
339.9980	5.10610	521.8832	340.0000	45.1332	1034.493
339.9982	6.10682	549.7903	340.0013	50.1367	1071.971
339.9984	7.10849	574.9377	340.0014	60.1437	1140.589
339.9983	8.10921	597.9274	340.0012	70.1506	1202.519
339.9983	9.10981	619.2067	340.0014	80.1575	1259.233
339.9984	10.1105	639.0842	340.0014	90.1644	1311.719
339.9989	12.6116	683.9772	340.0015	100.171	1360.706
339.9990	15.1132	723.7071	340.0027	2.60267	430.5995
339.9987	17.6148	759.6089	340.0022	3.10303	452.6182
339.9991	20.1165	792.5288	340.0022	3.60340	472.2474
339.9993	25.1199	851.5827	340.0027	4.10370	490.0798
339.9991	30.1235	903.8535			
		T = 360 K			
359.9973	3.60291	257.6805	359.9967	12.6105	588.7943
360.0044	3.60440	257.7428	359.9967	15.1123	635.0486
359.9986	3.60427	257.8319	359.9968	17.6141	675.8414
359.9987	3.85408	285.6228	359.9967	20.1158	712.6103
360.0004	3.85464	285.6703	359.9977	25.1200	777.4150
359.9994	3.95413	294.9441	359.9974	30.1235	833.8579

Continued on next page.

Continued from previous page.

T / K	p / MPa	w / m s^{-1}	T / K	p / MPa	w / m s^{-1}
359.9973	3.95462	295.0009	359.9976	35.1270	884.2941
359.9971	4.10337	307.5336	359.9977	40.1304	930.1574
359.9974	4.60361	342.1046	359.9978	45.1338	972.3991
359.9972	5.10390	369.8770	359.9974	50.1371	1011.686
359.9967	6.10488	414.5481	359.9977	60.1441	1083.207
359.9981	7.10523	450.8153	359.9986	70.1513	1147.408
359.9985	7.10518	450.8102	359.9988	80.1584	1205.953
359.9986	8.10596	481.9503	359.9987	90.1654	1259.987
359.9987	9.10667	509.5395	359.9985	100.172	1310.303
359.9987	10.1073	534.4932			
		T = 380 K			
380.0005	6.10522	260.5611	379.9969	15.1127	552.6023
379.9985	6.10531	260.5566	379.9976	17.6149	598.5089
379.9994	6.60555	293.1744	379.9977	20.1166	639.1515
379.9978	6.60568	293.1741	379.9980	22.6183	675.8861
379.9991	7.10592	320.3950	379.9983	25.1200	709.5603
379.9976	7.10610	320.3854	379.9980	30.1234	769.9383
379.9994	7.60631	344.0499	379.9982	35.1268	823.3510
379.9974	7.60654	344.0337	379.9980	40.1302	871.5634
379.9973	8.10695	365.1269	379.9985	45.1337	915.7338
379.9976	9.10812	401.9056	379.9987	50.1371	956.6329
379.9972	10.1089	433.6051	379.9989	60.1441	1030.754
379.9974	11.1097	461.7497	379.9993	70.1510	1096.962
379.9971	12.1104	487.2257	379.9996	80.1579	1157.136
379.9970	13.1112	510.6099	380.0000	90.1649	1212.528
379.9969	14.1120	532.3047	379.9996	100.172	1263.994
		T = 400 K			
400.0014	9.10726	305.1686	399.9999	20.1160	573.1887
400.0012	9.60768	324.6554	400.0005	22.6179	612.6424
400.0009	10.1081	342.7712	400.0004	25.1197	648.5354
400.0006	10.6085	359.7224	400.0010	27.6215	681.6036
400.0009	11.1090	375.6702	400.0011	30.1232	712.3548
400.0003	12.1099	404.9945	400.0013	35.1267	768.3406
399.9994	13.1111	431.5800	400.0012	40.1302	818.5892
399.9996	14.1118	455.9723	400.0012	45.1337	864.4167
400.0001	15.1125	478.5858	400.0018	50.1373	906.7101
399.9997	16.1132	499.7120	400.0020	60.1442	983.0535

Continued on next page.

Continued from previous page.

T / K	p / MPa	w / $\mathrm{m\,s^{-1}}$	T / K	p / MPa	w / $\mathrm{m\,s^{-1}}$
399.9995	17.1139	519.5723	400.0020	70.1511	1050.994
399.9997	18.1146	538.3518	400.0021	80.1579	1112.570
399.9996	19.1153	556.1850	400.0017	80.1585	1112.567
		T = 420 K			
420.0024	11.1087	309.8123	420.0051	21.1157	532.9916
420.0029	11.6090	324.8857	420.0051	22.6167	557.3006
420.0024	12.1101	339.4703	420.0050	25.1183	594.8296
420.0016	12.6104	353.4865	420.0050	27.6199	629.2926
420.0015	13.1107	366.9725	420.0055	30.1214	661.2565
420.0031	14.1108	392.4713	420.0053	35.1260	719.2603
420.0032	15.1115	416.2572	420.0051	40.1295	771.1205
420.0036	16.1122	438.5179	420.0051	45.1331	818.2800
420.0039	17.1130	459.4621	420.0047	50.1367	861.6980
420.0042	18.1137	479.2519	420.0048	60.1438	939.8517
420.0049	19.1143	498.0271	420.0048	70.1508	1009.203
420.0050	20.1150	515.9086			

Table B.4. Measurement results for the speed of sound in the liquid and supercritical region of propene.

T / K	p / MPa	w / m s^{-1}	T / K	p / MPa	w / m s^{-1}
		T = 240 K			
240.0057	1.30295	1101.202	240.0047	15.1127	1216.781
240.0060	2.10360	1108.744	240.0041	17.6138	1235.087
240.0060	3.10434	1117.998	240.0042	20.1155	1252.765
240.0056	4.10503	1127.067	240.0041	25.1187	1286.478
240.0054	5.10572	1135.965	240.0043	30.1221	1318.241
240.0052	6.10644	1144.689	240.0043	35.1255	1348.340
240.0049	7.10733	1153.262	240.0044	40.1289	1376.978
240.0048	8.10806	1161.667	240.0046	45.1323	1404.324
240.0050	9.10871	1169.931	240.0048	50.1358	1430.518
240.0048	10.1093	1178.057	240.0047	60.1439	1479.926
240.0045	12.6110	1197.797			
		T = 260 K			
259.9987	1.30335	970.6291	260.0000	20.1177	1148.429
259.9984	2.10391	979.8933	260.0001	25.1208	1186.307
259.9984	3.10455	991.1856	260.0000	30.1242	1221.648
259.9983	4.10529	1002.171	260.0001	35.1276	1254.849
259.9985	5.10605	1012.868	260.0003	40.1309	1286.219
259.9979	6.10661	1023.305	260.0001	45.1343	1315.998
259.9980	7.10725	1033.480	260.0001	50.1377	1344.374
259.9986	8.10779	1043.420	260.0001	60.1447	1397.546
259.9983	9.10824	1053.137	259.9999	70.1517	1446.717
259.9976	10.1086	1062.649	259.9967	80.1583	1492.587
260.0000	12.6127	1085.604	259.9965	90.1654	1535.645
259.9999	15.1143	1107.466	259.9967	100.172	1576.307
259.9999	17.6160	1128.374			
		T = 280 K			
279.9970	1.30164	836.3986	279.9964	20.1166	1047.835
279.9967	2.10240	848.1942	279.9976	25.1181	1090.313
279.9970	3.10325	862.3939	279.9967	30.1221	1129.512
279.9971	4.10404	876.0488	279.9970	35.1256	1165.981
279.9970	5.10490	889.2062	279.9966	40.1291	1200.192
279.9966	6.10580	901.9185	279.9966	45.1326	1232.453
279.9958	7.10730	914.2363	279.9963	50.1375	1263.071

Continued on next page.

Continued from previous page.

T / K	p / MPa	w / m s^{-1}	T / K	p / MPa	w / m s^{-1}
279.9955	8.10806	926.1576	279.9958	60.1445	1319.985
279.9955	9.10875	937.7314	279.9959	70.1514	1372.261
279.9954	10.1095	948.9836	279.9951	80.1571	1420.770
279.9953	12.6112	975.8555	279.9952	90.1638	1466.086
279.9954	15.1129	1001.146	279.9954	100.171	1508.742
279.9978	17.6130	1025.043			
		T = 300 K			
299.9991	1.40274	696.0120	299.9978	17.6129	925.4777
299.9996	1.40249	696.0083	299.9977	20.1145	951.3116
299.9995	2.10273	709.9875	299.9970	25.1179	998.9391
299.9991	3.10318	728.8510	299.9952	30.1210	1042.272
299.9989	4.10379	746.6052	299.9950	35.1245	1082.155
300.0005	5.10416	763.4029	299.9951	40.1279	1119.247
300.0003	6.10472	779.3698	299.9953	45.1313	1154.004
299.9980	7.10716	794.6580	299.9953	50.1347	1186.785
300.0005	8.10602	809.2216	299.9955	60.1416	1247.384
300.0004	9.10668	823.2508	299.9952	70.1486	1302.660
300.0006	10.1074	836.7571	299.9948	80.1564	1353.646
299.9984	12.6110	868.5846	299.9950	90.1634	1401.119
299.9984	15.1128	898.0102	299.9952	100.170	1445.617
		T = 320 K			
319.9995	2.10438	556.2000	319.9919	22.6161	886.7207
319.9995	3.10515	584.4313	319.9989	25.1191	912.5247
319.9990	4.10581	609.6381	319.9985	30.1226	960.1870
319.9989	5.10644	632.5567	319.9987	35.1261	1003.581
319.9994	6.10710	653.6882	319.9986	40.1295	1043.588
319.9994	7.10776	673.3606	319.9989	45.1330	1080.811
319.9995	8.10842	691.8179	319.9993	50.1364	1115.713
319.9998	9.10844	709.2476	319.9993	60.1433	1179.853
319.9996	10.1090	725.7791	319.9986	70.1503	1237.937
320.0000	12.6108	763.9051	319.9990	80.1573	1291.257
319.9999	15.1124	798.3761	319.9992	90.1643	1340.698
319.9998	17.6142	829.9978	319.9943	100.172	1386.940
319.9999	20.1159	859.3233			
		T = 340 K			
340.0053	4.10499	453.1630	340.0096	25.1187	831.3953
340.0052	5.10568	489.4973	340.0098	30.1222	883.5413

Continued on next page.

Continued from previous page.

T / K	p / MPa	w / m s^{-1}	T / K	p / MPa	w / m s^{-1}
340.0052	6.10634	520.3822	340.0097	35.1257	930.4603
340.0052	7.10701	547.5948	340.0097	40.1292	973.3267
340.0052	8.10768	572.1210	340.0099	45.1327	1012.950
340.0055	9.10821	594.5722	340.0100	50.1362	1049.889
340.0055	10.1092	615.3671	340.0102	60.1432	1117.347
340.0052	12.6111	661.8336	340.0099	70.1501	1178.057
340.0052	15.1130	702.4873	340.0159	80.1572	1233.521
340.0051	17.6149	738.9419	340.0166	90.1641	1284.784
340.0052	20.1167	772.1766	340.0168	100.171	1332.553
		T = 360 K			
360.0003	5.10503	311.2643	360.0032	30.1225	812.8071
360.0008	6.10574	370.1519	360.0030	35.1266	863.1363
360.0002	7.10648	413.2797	360.0029	40.1303	908.7234
360.0010	8.10712	448.5406	360.0031	45.1338	950.5863
360.0009	9.10783	478.9229	360.0031	50.1372	989.4236
360.0012	10.1086	505.8924	360.0026	60.1442	1059.933
360.0022	12.6102	563.3230	360.0027	70.1512	1123.026
360.0026	15.1120	611.3745	360.0026	80.1582	1180.434
360.0026	17.6138	653.2634	360.0028	90.1653	1233.311
360.0027	20.1155	690.7209	360.0030	100.172	1282.467
360.0022	25.1190	756.2051			
		T = 380 K			
380.0038	7.10608	268.3348	380.0026	25.1193	687.4354
380.0019	7.35745	283.4849	380.0025	30.1228	748.2255
380.0038	7.60654	297.2930	380.0020	35.1264	801.6876
380.0023	7.85819	310.3191	380.0017	40.1299	849.7467
380.0035	8.10693	322.3461	380.0022	45.1336	893.6294
380.0036	9.10764	364.5605	380.0019	50.1372	934.1597
380.0032	10.1084	399.8435	380.0020	60.1442	1007.381
380.0033	12.6102	470.5522	380.0019	70.1519	1072.586
380.0030	15.1120	526.7289	380.0018	80.1590	1131.695
380.0027	17.6127	574.2597	380.0021	90.1662	1185.989
380.0026	20.1156	615.9309	380.0020	100.173	1236.366
		T = 400 K			
400.0020	10.1084	309.3025	400.0045	25.1167	625.8160
400.0029	11.1090	343.8377	400.0040	30.1207	690.1665
400.0027	12.1096	374.7503	400.0042	35.1243	746.2953

Continued on next page.

Continued from previous page.

T / K	p / MPa	w / $\mathrm{m\,s^{-1}}$	T / K	p / MPa	w / $\mathrm{m\,s^{-1}}$
400.0029	13.1102	402.6860	400.0043	40.1280	796.4613
400.0031	14.1108	428.2118	400.0041	45.1317	842.0603
400.0032	15.1114	451.7604	400.0044	50.1353	884.0318
400.0041	16.1112	473.6317	400.0042	60.1425	959.5630
400.0042	17.1099	494.1526	400.0051	70.1484	1026.551
400.0044	18.1116	513.4875	400.0052	80.1555	1087.114
400.0043	19.1123	531.7942	400.0052	90.1626	1142.621
400.0043	20.1131	549.2023	400.0052	100.170	1194.032
400.0045	22.6148	589.4138			
		T = 420 K			
419.9962	12.1073	315.0035	419.9961	25.1197	572.2424
419.9965	13.1082	341.8473	419.9961	30.1231	639.0934
419.9963	14.1090	367.2941	419.9960	35.1268	697.1959
419.9962	15.1096	391.2515	419.9963	40.1303	748.9608
419.9960	16.1105	413.7938	419.9963	45.1339	795.8954
419.9963	17.1131	435.0771	419.9968	50.1375	839.0007
419.9962	18.1142	455.1779	419.9967	60.1451	916.3810
419.9960	19.1149	474.2448	419.9969	70.1523	984.8320
419.9961	20.1157	492.3914	419.9969	80.1594	1046.588
419.9960	22.6176	534.3229			

Table B.5. Measurement results for the speed of sound in the liquid and supercritical region of the refrigerant 227ea.

T / K	p / MPa	w / m s^{-1}	T / K	p / MPa	w / m s^{-1}
		T = 280 K			
280.0035	0.603720	494.0994	280.0040	10.1114	572.8336
280.0038	1.10441	498.9191	280.0048	12.6131	590.2924
280.0035	1.60474	503.6375	280.0043	15.1148	606.8035
280.0037	2.10500	508.2652	280.0040	17.6165	622.4986
280.0043	3.10575	517.2645	280.0044	20.1182	637.4782
280.0044	4.10622	525.9501	280.0056	25.1217	665.6044
280.0042	5.10705	534.3512	280.0053	30.1253	691.6937
280.0038	6.10793	542.4911	280.0046	35.1289	716.1062
280.0042	7.10930	550.3978	280.0047	40.1324	739.0993
280.0043	8.11003	558.0738	280.0048	45.1359	760.8830
280.0047	9.11073	565.5499	280.0048	50.1394	781.6133
		T = 300 K			
299.9941	1.10305	417.6094	299.9986	12.6125	526.4965
299.9946	1.60341	423.6098	299.9989	15.1141	545.0872
299.9941	2.10383	429.4536	299.9992	17.6158	562.5674
299.9971	3.10645	440.6634	299.9996	20.1175	579.1068
299.9974	4.10719	451.3011	299.9990	25.1221	609.8477
299.9974	5.10793	461.4509	299.9991	30.1255	638.0380
299.9973	6.10865	471.1733	299.9991	35.1289	664.1886
299.9976	7.10936	480.5089	299.9993	40.1323	688.6585
299.9978	8.11009	489.5019	299.9994	45.1357	711.7107
299.9985	9.11014	498.1811	299.9992	50.1391	733.5536
299.9988	10.1108	506.5817			
		T = 320 K			
320.0031	1.10417	332.9553	320.0043	12.6116	466.6571
320.0033	2.10489	349.1085	320.0046	15.1133	487.6095
320.0025	3.10547	363.8180	320.0044	17.6150	507.0584
320.0030	4.10565	377.3858	320.0044	20.1168	525.2728
320.0039	5.10635	390.0383	320.0044	25.1203	558.7145
320.0039	6.10705	401.9342	320.0041	30.1241	589.0279
320.0041	7.10773	413.1778	320.0041	35.1276	616.8973
320.0043	8.10837	423.8657	320.0040	40.1313	642.7960
320.0046	9.10899	434.0623	320.0047	45.1349	667.0608

Continued on next page.

Continued from previous page.

T / K	p / MPa	w / $\mathrm{m\,s^{-1}}$	T / K	p / MPa	w / $\mathrm{m\,s^{-1}}$
320.0042	10.1098	443.8331	320.0051	50.1384	689.9481
		T = 340 K			
339.9964	1.60311	249.9750	339.9974	12.6115	410.8389
339.9966	2.10344	262.3829	339.9972	15.1133	434.4304
339.9974	3.10408	283.9615	339.9978	17.6148	455.9974
339.9975	4.10477	302.5891	339.9980	20.1166	475.9591
339.9977	5.10541	319.1677	339.9980	25.1201	512.1510
339.9974	6.10600	334.2301	339.9980	30.1236	544.5403
339.9976	7.10668	348.1025	339.9980	35.1270	574.0560
339.9975	8.10811	361.0299	339.9982	40.1305	601.3008
339.9972	9.10894	373.1505	339.9979	45.1342	626.6953
339.9974	10.1097	384.5986	339.9980	50.1377	650.5457
		T = 360 K			
360.0035	3.60431	209.76342	360.0068	15.11430	385.6209
360.0038	4.10477	223.69018	360.0068	17.61611	409.3941
360.0041	5.10564	247.37102	360.0070	20.11812	431.1227
360.0043	6.10652	267.42612	360.0071	25.12183	470.0037
360.0041	7.10735	285.07002	360.0076	30.12523	504.3614
360.0063	8.10916	300.97840	360.0076	35.12856	535.4053
360.0063	9.10996	315.52936	360.0079	40.13200	563.8809
360.0063	10.1107	329.01183	360.0080	45.13534	590.2901
360.0066	12.6125	359.17157	360.0079	50.13883	615.0017
		T = 380 K			
379.9993	7.10726	224.9016	380.0009	17.6150	367.4996
379.9991	8.10808	244.6132	380.0010	20.1167	390.9009
380.0000	9.10888	262.0764	380.0007	22.6185	412.3590
380.0000	10.1096	277.8750	380.0013	25.1198	432.2510
380.0000	11.1103	292.3777	380.0012	30.1232	468.3905
380.0006	12.1110	305.8404	380.0015	35.1266	500.7893
380.0002	13.1118	318.4458	380.0017	40.1301	530.3400
380.0006	14.1125	330.3234	380.0019	45.1335	557.6372
380.0001	15.1132	341.5818	380.0021	50.1371	583.0904
		T = 400 K			
400.0023	10.1078	232.8047	400.0032	20.1156	355.4325
400.0022	11.1086	249.0350	400.0029	22.6176	378.0372
400.0027	12.1093	263.9298	400.0030	25.1193	398.8761

Continued on next page.

Continued from previous page.

T / K	p / MPa	w / $\mathrm{m\,s^{-1}}$	T / K	p / MPa	w / $\mathrm{m\,s^{-1}}$
400.0027	13.1101	277.7464	400.0031	27.6211	418.2842
400.0027	14.1108	290.6672	400.0031	30.1227	436.4942
400.0027	15.1115	302.8336	400.0029	35.1264	470.0197
400.0028	16.1122	314.3546	400.0032	40.1299	500.4618
400.0032	17.1130	325.3107	400.0038	45.1334	528.4832
400.0030	18.1139	335.7753	400.0037	50.1370	554.5489
400.0030	19.1148	345.7996			
		T = 420 K			
420.0040	13.1092	243.7532	420.0042	27.6203	389.8148
420.0039	14.1099	257.3130	420.0043	30.1221	408.5356
420.0042	15.1106	270.0594	420.0042	35.1253	442.8944
420.0039	16.1114	282.1070	420.0041	40.1289	474.0097
420.0040	17.1122	293.5449	420.0044	45.1326	502.5902
420.0040	18.1130	304.4480	420.0043	50.1361	529.1208
420.0041	19.1137	314.8765	420.0044	55.1397	553.9602
420.0038	12.1084	229.2328	420.0045	60.1432	577.3592
420.0039	20.1147	324.8813	420.0048	70.1504	620.6355
420.0042	22.6166	348.2966	420.0048	80.1575	660.1155
420.0039	25.1184	369.8223	420.0047	90.1653	696.5910

Table B.6. Measurement results for the speed of sound in liquid region of the refrigerant 365mfc.

T / K	p / MPa	w / m s^{-1}	T / K	p / MPa	w / m s^{-1}
		T = 250 K			
249.9964	1.10524	921.6555	249.9962	12.6112	976.6687
249.9964	2.10581	926.7284	249.9963	15.1128	987.7796
249.9963	3.10629	931.7415	249.9963	17.6145	998.6250
249.9961	4.10688	936.6956	249.9965	20.1162	1009.233
249.9961	5.10739	941.5925	249.9965	25.1197	1029.767
249.9960	6.10831	946.4364	249.9964	30.1232	1049.473
249.9957	7.10889	951.2249	249.9963	35.1267	1068.446
249.9958	8.10814	955.9554	249.9953	40.1298	1086.735
249.9961	9.10881	960.6443	249.9955	45.1332	1104.430
249.9962	10.1095	965.2801	249.9955	50.1367	1121.557
		T = 260 K			
259.9980	1.10431	881.5677	259.9958	20.1183	973.7958
259.9980	2.10481	886.9571	259.9963	25.1218	995.2141
259.9974	3.10532	892.2756	259.9969	30.1258	1015.717
259.9976	4.10593	897.5254	259.9971	35.1292	1035.405
259.9984	5.10633	902.7031	259.9972	40.1326	1054.353
259.9980	6.10790	907.8238	259.9971	45.1360	1072.647
259.9971	7.10917	912.8867	259.9974	50.1395	1090.325
259.9970	8.10995	917.8838	259.9966	60.1463	1124.064
259.9972	9.11074	922.8231	259.9963	70.1533	1155.908
259.9966	10.1116	927.7103	259.9975	80.1603	1186.110
259.9971	12.6133	939.6793	259.9974	90.1673	1214.882
259.9965	15.1148	951.3417	259.9967	100.174	1242.393
259.9964	17.6166	962.7033			
		T = 280 K			
279.9955	1.10439	803.3083	279.9960	20.1176	905.7148
279.9955	2.10489	809.4137	279.9959	25.1210	929.0056
279.9953	3.10541	815.4221	279.9958	30.1245	951.1694
279.9958	4.10602	821.3350	279.9963	35.1280	972.3370
279.9956	5.10656	827.1570	279.9967	40.1313	992.6241
279.9958	6.10780	832.8932	279.9973	45.1349	1012.137
279.9961	7.10852	838.5460	279.9970	50.1383	1030.929
279.9963	8.10928	844.1188	279.9973	60.1452	1066.642

Continued on next page.

Continued from previous page.

T / K	p / MPa	w / m s^{-1}	T / K	p / MPa	w / m s^{-1}
279.9954	9.11025	849.6194	279.9975	70.1522	1100.181
279.9958	10.1109	855.0439	279.9974	80.1592	1131.866
279.9956	12.6126	868.2947	279.9971	90.1662	1161.953
279.9959	15.1142	881.1350	279.9973	100.172	1190.626
279.9959	17.6159	893.5994			
		$T = 300$ K			
299.9969	1.10450	727.0963	299.9975	20.1174	841.1458
299.9971	2.10502	734.0609	299.9975	25.1210	866.4418
299.9970	3.10550	740.9013	299.9982	30.1251	890.3439
299.9968	4.10600	747.6075	299.9982	35.1286	913.0644
299.9970	5.10700	754.1873	299.9982	40.1320	934.7355
299.9970	6.10762	760.6470	299.9983	45.1355	955.4830
299.9979	7.10715	766.9609	299.9983	50.1390	975.3853
299.9981	8.10781	773.2044	299.9985	60.1459	1013.064
299.9981	9.10842	779.3399	299.9984	70.1529	1048.274
299.9974	10.1102	785.3677	299.9983	80.1598	1081.398
299.9976	12.6120	800.0633	299.9983	90.1668	1112.745
299.9973	15.1138	814.2243	299.9985	100.174	1142.546
299.9974	17.6157	827.9055			
		$T = 320$ K			
320.0053	1.10313	652.2757	320.0006	20.1190	779.9832
319.9934	2.10492	660.3661	320.0003	25.1226	807.4372
319.9931	3.10553	668.2375	320.0001	30.1261	833.1938
319.9924	4.10630	675.9168	320.0001	35.1297	857.5144
319.9903	5.10770	683.4099	319.9993	40.1336	880.5863
319.9904	6.10864	690.7398	319.9992	45.1372	902.5939
319.9905	7.10932	697.9113	319.9994	50.1406	923.6323
319.9904	8.11003	704.9310	319.9991	60.1476	963.2452
320.0004	9.11117	711.7661	319.9992	70.1547	1000.074
320.0005	10.1119	718.5217	319.9996	80.1617	1034.591
320.0006	12.6137	734.8611	319.9995	90.1688	1067.145
320.0005	15.1154	750.5041	319.9998	100.176	1098.003
320.0005	17.6172	765.5264			
		$T = 340$ K			
339.9992	1.10582	578.1534	339.9990	20.1160	722.0333
339.9990	2.10643	587.6467	339.9987	25.1192	751.7822
339.9989	3.10696	596.8302	339.9989	30.1225	779.4654

Continued on next page.

Continued from previous page.

T / K	p / MPa	w / $\mathrm{m\,s^{-1}}$	T / K	p / MPa	w / $\mathrm{m\,s^{-1}}$
339.9987	4.10749	605.7315	339.9985	35.1242	805.4163
339.9986	5.10805	614.3598	339.9985	40.1277	829.9307
339.9989	6.10906	622.7510	339.9982	45.1311	853.1856
339.9989	7.10973	630.9185	339.9982	50.1346	875.3405
339.9989	8.10887	638.8574	339.9982	60.1416	916.8579
339.9986	9.10942	646.6210	339.9973	70.1500	955.2657
339.9986	10.1099	654.2023	339.9973	80.1571	991.1170
339.9987	12.6114	672.4332	339.9975	90.1643	1024.811
339.9989	15.1129	689.7404	339.9974	100.171	1056.678
339.9989	17.6144	706.2416			
		T = 360 K			
360.0022	1.10209	503.7389	360.0004	20.1166	667.3068
360.0016	2.10272	515.1993	360.0006	25.1201	699.4996
360.0014	3.10333	526.1435	360.0007	30.1235	729.1854
360.0010	4.10397	536.6366	360.0010	35.1269	756.8297
360.0009	5.10479	546.7254	360.0004	40.1304	782.7753
360.0010	6.10619	556.4503	360.0003	45.1339	807.2747
360.0011	7.10694	565.8425	359.9996	50.1369	830.5223
360.0013	8.10767	574.9355	359.9994	60.1439	873.8904
360.0011	9.10839	583.7530	359.9997	70.1509	913.7996
360.0011	10.1091	592.3172	359.9997	80.1579	950.9084
360.0014	12.6109	612.7340	359.9997	90.1649	985.6855
360.0012	15.1127	631.9222	359.9995	100.172	1018.481
360.0006	17.6149	650.0681			
		T = 380 K			
379.9935	1.10078	427.2749	379.9938	20.1155	615.5578
379.9931	2.10166	441.6587	379.9934	25.1190	650.3331
379.9931	3.10207	455.1163	379.9935	30.1226	682.0782
379.9931	4.10271	467.8002	379.9936	35.1262	711.4161
379.9930	5.10345	479.8231	379.9930	40.1302	738.7893
379.9931	6.10471	491.2680	379.9929	45.1338	764.5134
379.9932	7.10549	502.2121	379.9933	50.1373	788.8314
379.9930	8.10627	512.7080	379.9931	60.1443	833.9678
379.9935	9.10751	522.8075	379.9930	70.1514	875.3113
379.9935	10.1083	532.5405	379.9930	80.1585	913.6044
379.9934	12.6101	555.5033	379.9930	90.1656	949.3881
379.9935	15.1119	576.8129	379.9931	100.173	983.0529

Continued on next page.

Continued from previous page.

T / K	p / MPa	w / $\mathrm{m\,s^{-1}}$	T / K	p / MPa	w / $\mathrm{m\,s^{-1}}$
379.9933	17.6137	596.7616			
		T = 400 K			
400.0017	1.60520	355.5224	400.0024	20.1180	566.8596
400.0013	2.10565	364.9449	400.0024	25.1215	604.3133
400.0011	3.10643	382.3765	400.0028	30.1249	638.1405
400.0015	4.10725	398.3077	400.0029	35.1283	669.1586
400.0009	5.10809	413.0523	400.0028	40.1318	697.9238
400.0030	6.10781	426.8037	400.0031	45.1353	724.8279
400.0031	7.10864	439.7661	400.0026	50.1380	750.1635
400.0033	8.10938	452.0331	400.0026	60.1452	796.9819
400.0029	9.11016	463.7031	400.0026	70.1523	839.6647
400.0029	10.1109	474.8478	400.0024	80.1593	879.0590
400.0026	12.6127	500.7808	400.0025	90.1664	915.7696
400.0025	15.1145	524.4761	400.0026	100.174	950.2304
400.0023	17.6162	546.3942			
		T = 420 K			
419.9940	2.10332	280.0197	419.9933	7.10563	378.1990
419.9938	3.10280	305.0827	419.9934	8.10635	392.7626
419.9936	4.10355	326.4912	419.9935	9.10710	406.4023
419.9935	5.10427	345.4077	419.9933	10.1078	419.2571
419.9934	6.10497	362.5067			

Bibliography

[1] **Abramowitz, M.; Stegun, I.**: *Handbook of Mathematical Functions* (Dover, New York, 1965).

[2] **Ahrendts, J.; Baehr, H.D.**: Die direkte Verwendung von Meßwerten beliebiger thermodynamischer Zustandsgrößen zur Bestimmung kanonischer Zustandsgleichungen, Forsch. Ing.-Wes., **45** (1) 1–36, 1979.

[3] **Ahrendts, J.; Baehr, H.D.**: Die Anwendung nichtlinearer Regressionsverfahren bei der Aufstellung thermodynamischer Zustandsgleichungen, Forsch. Ing.-Wes., **45** (2) 51–56, 1979.

[4] **Aleksandrov, A.A.; Larkin, D.K.**: An experimental determination of the velocity of sound in water within a wide range of temperature and pressure (in Russian), Teploenergetika, **23** (2) 75–78, 1976; engl. translation in Therm. Eng., **23** (2) 72, 1976.

[5] **Aleksandrov, A.A.; Kochetkov, A.I.**: Experimental determination of ultrasonic velocity in water at temperatures of 266–423 K and pressures up to 100 MPa (in Russian), Teploenergetika, **26** (9) 65–66, 1979; engl. translation in Therm. Eng., **26** (9) 558–559, 1979.

[6] **Aleksandrov, A.A.; Kochetkov, A.I.**: The Investigation of Sound Velocity in Water at High Pressures, in: *Water and Steam – Their Properties and Current Industrial Applications*, Proc. 9th Int. Conf. on the Properties of Water and Steam, edited by J. Straub and K. Scheffler, pp. 221–224, (Pergamon, Munich, 1980).

[7] **Angus, S.; Armstrong, B.; de Reuck, K.M.**: *International Tables of the Fluid State–7 Propylene (Propene)* (Pergamon, Oxford, 1980).

[8] **ANSI/IEEE**: *IEEE Standard on Piezoelectricity*, ANSI/IEEE Standard 176-1987 (Institute of Electrical and Electronics Engineers, New York, 1988).

[9] **Atkins, P.W.**: *Physikalische Chemie*, 3rd ed. (VCH, Weinheim, 2002).

[10] **Baehr, H.D.**: *Thermodynamik (in German)*, 11th ed. (Springer, Berlin, 2005).

[11] **Baehr, H.D.**: Thermodynamische Fundamentalgleichungen und charakteristische Funktionen (in German), Forsch. Ing.-wesen, **64** (1) 35–43, 1998.

[12] **Ball, S.J.; Trusler, J.P.M.**: The speed of sound of n-hexane and n-hexadecane at temperatures between 298 and 373 K and pressures up to 100 MPa, Int. J. Thermophys., **22** (2) 427–443, 2001.

[13] **Barlow, A.J.; Yazgan, E.**: Phase Change method for the measurement of ultrasonic wave velocity and a determination of the speed of sound in water, Br. J. Appl. Phys., **17** (6) 807–819, 1966.

[14] **Barlow, A.J.; Yazgan, E.**: Pressure dependence of the velocity of sound in water as a function of temperature, Br. J. Appl. Phys., **18** (5) 645–651, 1967.

[15] **Becker, E.; Bürger, W.**: *Kontinuumsmechanik (in German)* (Teubner, Stuttgart, 1975).

[16] **Beckermann, W.**: *Messung der Schallgeschwindigkeit an Arbeitsstoffen der Energietechnik (in German)* (VDI, Düsseldorf, 1993).

[17] **Beckermann, W.; Kohler, F.**: Acoustic determination of ideal gas heat capacity and second virial coefficients of some refrigerants between 250 and 420 K, Int. J. Thermophys., **16** (2) 455–464, 1995.

[18] **Benedetto, G.; Gavioso, R.M.; Spagnolo, R.; Grigiante, M.; Scalabrin, G.**: Vapor-phase Helmholtz equation for HFC-227ea from speed-of-sound measurements, Int. J. Thermphys., **22** (4) 1073–1088, 2001.

[19] **Benedetto, G.; Gavioso, R.M.; Albo, P.A.G.; Lago, S.; Madonna Ripa, D.; Spagnolo, R.**: A microwave-ultrasonic cell for sound speed measurements in liquids, Int. J. Thermophys., 26 (6) 1651–1665, 2005.

[20] **Benedetto, G.; Gavioso, R.M.; Albo, P.A.G.; Lago, S.; Madonna Ripa, D.; Spagnolo, R.**: Speed of sound of pure water at temperatures between 274 and 394 K and pressures up to 90 MPa, Int. J. Thermophys., 26 (6) 1667–1680, 2005.

[21] **Biswas, S.N.; Seldam, C.A. ten**: The equation of state and heat capacity of nitrogen at high pressures determined from speeds of sound, J. Chem. Thermodyn., **23** (8) 725-737, 1991.

[22] **Biswas, S.N.; Seldam, C.A. ten**: Determination of thermodynamic properties of methane from high pressure speed-of-sound data, Fluid Phase Equilibria, **74**, 219–233, 1992.

[23] **Blanke, W.**: Eine neue Temperaturskala. Die Internationale Temperaturskala von 1990 (ITS-90), PTB-Mitteilungen, **99** (6) 411–418, 1989.

[24] **Blanke, W.**: Änderungen durch die Einführung der neuen Internationalen Temperaturskala von 1990, Brennstoff-Wärme-Kraft, **43** (12) 571–574, 1991.

[25] **Boley, B.A.; Weiner, J.H.**: *Theory of Thermal Stresses*, (Wiley, New York, 1967).

[26] **Brice, J.C.**: Crystals for quartz resonators, Rev. Mod. Phys., **57** (1) 105–146, 1985.

[27] **Cady, W.G.**: *Piezoelectricity* Vol. 1 (Dover, New York, 1964).

[28] **Cady, W.G.**: *Piezoelectricity* Vol. 2 (Dover, New York, 1964).

[29] **Chávez, M.; Sosa, V.; Tsumura, R.**: Speed of sound in saturated pure water, J. Acoust. Soc. Am., **77** (2) 420–423, 1985.

[30] **Comité International des Poids et Mesures**: The International Temperature Scale of 1968, Metrologia, **5** (2) 35–44, 1969.

[31] **Cottrell, T.L.; McCoubrey, J.C.**: *Molecular energy transfer in gases* (Butterworths, London, 1961).

[32] **Costa Gomez, M.F.; Trusler, J.P.M.**: The speed of sound in nitrogen at temperatures between $T = 250$ K and $T = 350$ K and at pressures up to 30 MPa, J. Chem. Thermodyn., 30 (5) 527–534, 1998.

[33] **Dael, W. van**: *Thermodynamic Properties and the Velocity of Sound*, in: *Experimental Thermodynamics Volume II - Experimental Thermodynamics of Non-reacting Fluids*, ed. by B.L. Neindre and B. Vodar, pp. 527–577 (Butterworths, London, 1975).

[34] **Daridon, J.L.**: Mesure de la vitesse du son dans des fluides sous pression composés de constituants gazeux et liquides, Acustica, **80**, 416–419, 1994.

[35] **Daridon, J.L.; Lagourette, B.; Grollier, J.-P.E.**: Experimental measurements of the speed of sound in n-hexane from 293 K to 373 K and up to 150 MPa, Int. J. Thermophys., **19** (1) 145–160, 1998.

[36] **Davis, L.A.; Gordon, R.B.**: Compression of mercury at high pressure, J. Chem. Phys., **46** (7) 2650–2660, 1967.

[37] **Deghani, G.A.**: Experimentelle Bestimmung der lokalen Erdbeschleunigung "g" im Laborraum 18/H7 des Instituts für Thermodynamik der Universität der Bundeswehr Hamburg (in German), Report, Institute of Geophysics at the University Hamburg, 2003.

[38] **Ding, Z.S.; Alliez, J.; Boned, C.; Xans, P.**: Automation of an ultrasound velocity measurement system in high-pressure liquids, Meas. Sci. Techn., **8**, 154–161, 1997.

[39] **Douglas, T.B.**: Conversion of existing calorimetrically determined thermodynamic properties to the basis of the International Practical Temperature Scale of 1968, J. Res. Natl. Bur. Stand., **73A** (5) 451–470, 1969.

[40] **Ernst, S.; Marczak, W.; Manikowski, R.; Zorebski, E.; Zorebski, M.**: A sing-around apparatus for group velocity measurements in liquids. Testing by standard liquids and discussion of the errors, Acoust. Lett., **15** (7) 123–130, 1992.

[41] **Erokhin, N.F.; Kal'yanov, B.I.**: Experimental investigation of the velocity of ultrasound in the critical region of water (in Russian), Teplofizika Vysokikh Temperatur, **17** (2) 290–298, 1979; engl. translation in High Temp., **17** (2) 245–251, 1979.

[42] **Erokhin, N.F.; Kal'yanov, B.I.**: Extremal behaviour of ultrasonic velocity and of some other quantities in the supercritical region of water (in Russian), Teploenergetika, **27** (11) 50–52, 1980; engl. translation in Therm. Eng., **27** (11) 634–636, 1980.

[43] **Estrada-Alexanders, A.F.; Trusler, J.P.M.**: The speed of sound in gaseous argon at temperatures between 110 K and 450 K and at pressures up to 19 MPa, J. Chem. Thermodyn., **27** (10) 1075–1089, 1995.

[44] **Estrada-Alexanders, A.F.; Trusler, J.P.M.**: The speed of sound and derived thermodynamic properties of ethane at temperatures between 220 K and 450 K and pressures up to 10.5 MPa, J. Chem. Thermodyn., **29** (9) 991–1015, 1997.

[45] **Estrada-Alexanders, A.F.; Trusler, J.P.M.**: Speed of sound in carbon dioxide at temperatures between (220 and 450) K and pressures up to 14 MPa, J. Chem. Thermodyn., **30** (12) 1589–1601, 1998.

[46] **Estrada-Alexanders, A.F.; Trusler, J.P.M.; Zarari, M.P.**: Determination of thermodynamic properties from the speed of sound, Int. J. Thermophys., **16** (3) 663–673, 1995.

[47] **Estrada-Alexanders, A.F.; Justo, D.**: New method for deriving accurate thermodynamic properties from speed-of-sound, J. Chem. Thermodyn., **36** (5) 419–429, 2004.

[48] **Evstefeev, V.N.; Skripov, V.P.; Chukanov, V.N.**: Experimental determination of the speed of sound in superheated ordinary and heavy water (in Russian), Teplofizika Vysokikh Temperatur, **17** (2) 299-305, 1979; engl. translation in High Temp., **17** (2) 252–257, 1979.

[49] **Ewing, M.B.**: Interaction second acoustic virial coefficients of (N_2 + Ar) between 90 and 373 K, Physica A, **184**, 437–450, 1992.

[50] **Ewing, M.B.; Goodwin, A.R.H.**: Speeds of sound, perfect-gas heat capacity, and second virial coefficient for air at the temperature 255 K and pressures in the range 0.031 MPa to 6.9 MPa, J. Chem. Thermodyn., **25** (3) 423–427, 1993.

[51] **Ewing, M.B.; McGlashan, M.L.; Trusler, J.P.M.**: The temperature-jump effect and the theory of the thermal boundary layer for a spherical resonator. Speeds of sound in argon at 273.16 K, Metrologia, **22** (2) 93–102, 1986.

[52] **Ewing, M.B.; Trusler, J.P.M.**: Speeds of sound in CF_4 between 175 and 300 K measured with a spherical resonator, J. Chem. Phys., **90** (2) 1106–1115, 1989.

[53] **Ewing, M.B.; Trusler, J.P.M.**: Second acoustic virial coefficients of nitrogen between 80 and 373 K, Physica A, **184**, 415–436, 1992.

[54] **Ewing, M.B.; Trusler, J.P.M.**: Primary acoustic thermometry between $T = 90$ K and $T = 300$ K, J. Chem. Thermodyn., **32** (9) 1229–1255, 2000.

[55] **Fawcett, D.**: *Measurement and Prediction of Speed of Sound, with Application to Gas Flow Metering in Australian Natural Gases* (Ph.D.-Thesis, Department of Physics and Energy Studies, Murdoch University, Perth, Australia, 1995).

[56] **Fay, E.**: Differenzen zwischen den Temperaturwerten der IPTS-68 und denen der IPTS-48, PTB-Mitteilungen, **81** (6) 416–420, 1971.

[57] **Fröba, A.P.; Will, S.; Leipertz, A.**: Die dynamische Lichtstreuung als universelle Meßtechnik zur Bestimmung von Stoffdaten am Beispiel von Toluol, Chem.-Ing.-Tech., **71** (3) 257–261, 1999.

[58] **Fröba, A.P.**: *Simultane Bestimmung von Viskosität und Oberflächenspannung transparenter Fluide mittels Oberflächenlichtstreuung (in German)*, Berichte zur Energie- und Verfahrenstechnik, Schriftenreihe 2.1, Lehrstuhl für Technische Thermodynamik, Friedrich Alexander Universität Erlangen/Nürnberg, 2001.

[59] **Fröba, A.P.; Krzeminski, K.; Leipertz, A.**: Thermophysical Properties of 1,1,1,3,3-Pentafluorobutane (R365mfc), submitted to Int. J. Thermophys., 2003.

[60] **Fröba, A.P.; Botero, C.; Leipertz, A.**: Thermal diffusivity, sound speed, viscosity, and surface tension of R227ea (1,1,1,2,3,3,3-heptafluoropropane), submitted to Int. J. Thermophys., 2005.

[61] **Fujii, K.-I.**: Accurate measurements of the sound velocity in pure water under high pressure, National Research Laboratory of Metrology, Personal Communication, Tsukuba, Japan, 2000.

[62] **Fujii, K.-I.; Masui, R.**: Accurate measurements of the sound velocity in pure water by combining a coherent phase-detection technique and a variable path length interferometer, J. Acoust. Soc. Am., **93** (1) 276–282, 1993.

[63] **Gillis, K.A.**: Thermodynamic properties of two gaseous halogenated ethers from speed-of-sound measurements: difluoromethoxy-difluoromethane and 2-difluoromethoxy-1,1,1-trifluoroethane, Int. J. Thermophys., **15** (5) 821–847, 1994.

[64] **Gillis, K.A.; Moldover, M.R.**: Practical determination of gas densities from the speed of sound using square-well potentials, Int. J. Thermophys., **17** (6) 1305-1324, 1996.

[65] **Gitis, M.B.; Khimunin, A.S.**: Diffraction Effects in Ultrasonic Measurements (Review), Soviet Physics - Acoustics, **14** (4) 413–431, 1969.

[66] **Greenspan, M.; Tschiegg, C.E.**: Effect of dissolved air on the speed of sound in water, J. Acoust. Soc. Am., **28** (3) 501, 1956.

[67] **Greenspan, M.; Tschiegg, C.E.**: Sing-around ultrasonic velocimeter for liquids, Rev. Sci. Instrum., **28** (11) 897–901, 1957.

[68] **Greenspan, M.; Tschiegg, C.E.**: Speed of sound in water by a direct method, J. Res. Natl. Bur. Stand., **59** (4) 249–254, 1957.

[69] **Grosso, V.A. del; Mader, C.W.**: Speed of sound in pure water, J. Acoust. Soc. Am., **52** (5) 1442–1446, 1972.

[70] **Gruzdev, V.A.; Khairulin, R.A.; Komarov, S.G.; Stankus, S.V.**: Thermodynamic properties of HFC-227ea, Int. J. Thermophys., **23** (3) 809–824, 2002.

[71] **Guedes, H.J.R.; Zollweg, J.A.**: Speed of sound in liquid R134a, Int. J. Refrig., **15** (6) 381–385, 1992.

[72] **FEZEN**: Datenbank für Stähle und NE-Metalle, Blatt 1.4571.41.03.0, Physikalische Eigenschaften nach SEW 310, Tafel 43 (DVS, Düsseldorf, 2000).

[73] **Harris, G.R.**: Review of transient field theory for a baffled planar piston, J. Acoust. Soc. Am., **70** (1) 10–20, 1981.

[74] **Harris, G.R.**: Transient field of a baffled planar piston having an arbitrary vibration amplitude distribution, J. Acoust. Soc. Am., **70** (1) 186–204, 1981.

[75] **He, M.G.; Liu, Z.G.; Yin, J.M.**: Measurements of speed of sound with a spherical resonator: HCFC-22, HFC-152a, HFC-143a, and propane, Int. J. Thermophys., **23** (6) 1599–1615, 2002.

[76] **Herzfeld, K.F.; Litovitz, T.A.**: *Absorption and Dispersion of Ultrasonic Waves* (Academic, New York, 1959).

[77] **Hirschfelder, J.O.; Curtiss, C.F.; Bird, R.B.**: *Molecular theory of gases and liquids* (John Wiley, New York, 1954).

[78] **Holton, G.; Hagelberg, M.P.; Kao, S.; W.H. Johnson, J.**: Ultrasonic-velocity measurements in water at pressures up to 10000 kg/cm^2, J. Acoust. Soc. Am., **43** (1) 102–107, 1968.

[79] **Horváth-Szabó, G.; Høiland, H.; Høgseth, E.**: An automated apparatus for ultrasound velocity measurements improving the pulse-echo-overlap method to a precision better than 0.5 ppm in liquids, Rev. Sci. Instrum., **65** (5) 1644–1648, 1994.

[80] **Hozumi, T.; Sato, H.; Watanabe, K.**: Ideal-gas specific-heat and second virial coefficient of HFC-125 based on sound-velocity measurements, Int. J. Thermophys., **17** (3) 587–595, 1996.

[81] **Hozumi, T.; Ichikawa, T.; Sato, H.; Watanabe, K.**: Determination of second virial coefficients and virial equations of R-32 (difluoromethane) and R-125 (pentafluoroethane) based on speed-of-sound measurements, Int. J. Thermophys., **20** (6) 1677–1688, 1999.

[82] **Hurly, J.J.**: Thermophysical properties of gaseous CF_4 and C_2F_6 from speed-of-sound measurements, Int. J. Thermophys., **20** (2) 455–484, 1999.

[83] **Hurly, J.J.**: Thermophysical properties of gaseous tungsten hexaflouride from speed-of-sound measurements, Int. J. Thermophys., **21** (1) 185–206, 2000.

[84] **Hurly, J.J.**: Thermophysical properties of chlorine from speed-of-sound measurements, Int. J. Thermophys., **23** (2) 455–475, 2002.

[85] **Hurly, J.J.**: Thermophysical properties of nitrogen triflouride, ethylene oxide, and trimethyl gallium from speed-of-sound measurements, Int. J. Thermophys., **23** (3) 667–696, 2002.

[86] **Hurly, J.J.; Schmidt, J.W.; Gillis, K.A.**: Equation of state and ideal-gas heat capacity of a gaseous mixture of 1,1,1,2-tetrafluoroethane, pentafluoroethane, and difluoromethane, Int. J. Thermophys., **18** (3) 655–682, 1997.

[87] **Ikeda, T.**: *Fundamentals of piezoelectricity* (Oxford University, Oxford, 1990).

[88] **Kabelac, S.**: Die Schallgeschwindigkeit als thermodynamische Zustandsgröße (in German), Forsch. Ing.-Wesen, **64** (3) 47–54, 1998.

[89] **Kabelac, S.; Flohr, F.; Stadtländer, C.**: Entwicklung eines Arbeitsfluids für Hochtemperatur Wärmepumpen (in German), p. 71–82 in: DKV-Tagungsbericht 2005, Band II.1, Deutscher Kälte- und Klimatechnischer Verein, Stuttgart, 2005.

[90] **Khimunin, A.S.**: Numerical calculation of the diffraction corrections of the precise measurement of ultrasound absorption, Acustica, **27** (4) 173–181, 1972.

[91] **Khimunin, A.S.**: Numerical calculation of the diffraction corrections for the precise measurement of ultrasound phase velocity, Acustica, **32**, 192–200, 1975.

[92] **Kinsler, L.E.; Frey, A.R.; Coppens, A.B., Sanders, J.V.**: *Fundamentals of Acoustics*, 4th ed. (Wiley, New York, 2000).

[93] **Kortbeek, P.J.; Muringer, M.J.P.; Trappeniers, N.J.; Biswas, S.N.**: Apparatus for sound velocity measurements in gases up to 10 kbar: Experimental data for argon, Rev. Sci. Instrum., **56** (6) 1269–1273, 1985.

[94] **Kortbeek, P.J.; Ridder, J.J. van de; Biswas, S.N.; Schouten, J.A.**: Measurement of the compressibility and sound velocity of helium up to 1 GPa, Int. J. Thermophys., **9** (3) 425–438, 1988.

[95] **Kortbeek, P.J.; Trappeniers, N.J.; Biswas, S.N.**: Compressibility and sound velocity measurements on N_2 up to 1 GPa, Int. J. Thermophys., **9** (1) 103–116, 1988.

[96] **Kortbeek, P.J.; Schouten, J.A.**: Measurements of the compressibility and sound velocity in methane up to 1 GPa, revisited, Int. J. Thermophys., **11** (3) 455–466, 1990.

[97] **Kozhevnikov, V.F.; Arnold, D.I.; Briggs, M.E.; Naurzakov, S.P.; Viner, J.M.; Taylor, P.C.**: A pulsed phase-sensitive technique for acoustical measurements, J. Acoust. Soc. Am., **106** (6) 3424–3433, 1999.

[98] **Kraft, K.**: *Bestimmung von Schallgeschwindigkeit und Schalldämpfung transparenter Fluide mittels der Dynamischen Lichtstreuung (in German)*, Berichte

zur Energie- und Verfahrenstechnik, Schriftenreihe 95.4, Lehrstuhl für Technische Thermodynamik, Friedrich Alexander Universität Erlangen/Nürnberg, 1995.

[99] **Kroebel, W.; Mahrt, K.-H.**: Recent results of absolute sound velocity measurements in pure water and sea water at atmospheric pressure, Acustica, **35**, 154–164, 1976.

[100] **Kuttruff, H.**: Physik und Technik des Ultraschalls (Hirzel, Stuttgart, 1988).

[101] **Lacam, A.**: Variations de la vitesse des ultrasons dans le propane en fonction de la température et de la pression, J. Phys. Rad., **15** (12) 830–831, 1954.

[102] **Lacam, A.**: Étude expérimentale de la propagation des ultrasons dans les fluides en fonction de la pression (1200 atmosphéres) et de la température (200 °C), J. Rech. C.N.R.S., **34** (3) 25–56, 1956.

[103] **Laher, R.R.; Gilmore, F.R.**: Improved fits for the vibrational and rotational constants of many states of nitrogen and oxygen, J. Phys. Chem. Ref. Data, **20** (4) 685–712, 1991.

[104] **Lainez, A.; Miller, J.F.; Zollweg, J.A.; Street, W.B.**: Volumetric and speed-of-sound measurements for liquid tetrachloromethane under pressure, J. Chem. Thermodyn., **19** (12) 1251–1260, 1987.

[105] **Lainez, A.; Gopal, P.; Zollweg, J.A.; Street, W.B.**: Speed-of-sound measurements for liquid trichlorofluoromethane under pressure, J. Chem. Thermodyn., **21** (7) 773–777, 1989.

[106] **Lambert, J.D.**: *Vibrational and Rotational Relaxation in Gases* (Oxford University, Oxford, 1977).

[107] **Leipertz, A.**: Thermophysical properties of fluids by light scattering, Fluid Phase Equilibria, **125**, 219–233, 1996.

[108] **Lemmon, E.W.; McLinden, M.O.; Huber, M.L.**: Reference Fluid Thermodynamic and Transport Properties Database (RefProp), NIST Standard Reference Database 23, Version 7.0, National Institute of Standards and Technology, Gaithersburg, 2005.

[109] **Lemmon, E.W.; McLinden, M.O.; Wagner, W.**: A reference equation of state for the thermodynamic properties of propane for temperatures from the melting line to 650 K and pressures up to 1000 MPa, in preparation, 2005.

[110] **Lemmon, E.W.**, personal communication, National Institute of Standards and Technology, Boulder, 2006.

[111] **Lemmon, E.W.**, personal communication, National Institute of Standards and Technology, Boulder, 2006.

[112] **Lemmon, E.W.; Span, R.**: Short fundamental equations of state for 20 industrial fluids, J. Chem. Eng. Data, in press, 2006.

[113] **Lu, Z.; Daridon, J.L.; Lagourette, B.; Ye, S.**: Phase comparison technique for measuring liquid-liquid phase equilibrium, Rev. Sci. Instrum., **70** (4) 2065–2068, 1999.

[114] **Mamedov, A.M.**: On the ultrasonic velocity in water in the liquid temperature and pressure range (in Russian), Inzh. Fiz. Zh., **36** (1) 156–160, 1979.

[115] **Mangum, B.W.; Furukawa, G.T.; Kreider, K.G.; Meyer, C.W.; Ripple, D.C.; Strouse, G.F.; Tew, W.L.; Moldover, M.R.; Johnson, B.C.; Yoon, H.W.; Gibson, C.E.; Saunders, R.D.**: The Kelvin and Temperature Measurements, J. Res. Natl. Inst. Stand. Technol., **106** (1) 105–149, 2001.

[116] **Marczak, W.**: Water as a standard in the measurements of speed of sound in liquids, J. Acoust. Soc. Am., **102** (5) 2776–2779, 1997.

[117] **Mason, W.P.**: *Piezoelectric Crystals and Their Application to Ultrasonics* (Nostrand, Princeton, 1950).

[118] **Matheson, A.**: *Molecular Acoustics* (Wiley-Interscience, London, 1971).

[119] **McSkimin, H.J.**: Ultrasonic pulse technique for measuring acoustic losses and velocities of propagation in liquids as a function of temperature and hydrostatic pressure, J. Acoust. Soc. Am., **29** (11) 1185–1192, 1957.

[120] **McSkimin, H.J.**: Velocity of sound in distilled water for the temperature range 20 °C – 75 °C , J. Acoust. Soc. Am., **37** (2) 325–328, 1965.

[121] **Mehl, J.B.**: Acoustic resonance frequencies of deformed spherical resonators, J. Acoust. Soc. Am., **71** (5) 1109–1113, 1982.

[122] **Mehl, J.B.; Moldover, M.R.**: Spherical acoustic resonator: Effects of shell motion, J. Acoust. Soc. Am., **78** (2) 783–788, 1985.

[123] **Mehl, J.B.**: Measurement of the ratio of the speed of sound to the speed of light, Phys. Rev. A, **34** (4) 3341–3344, 1986.

[124] **Mehl, J.B; Moldover, M.R.**: Precision acoustic measurements with a spherical resonator: Ar and C_2H_4, J. Chem. Phys., **74** (7) 4062–4077, 1981.

[125] **Mehl, J.B.; Moldover, M.R.**: Precondensation phenomena in acoustic measurements, J. Chem. Phys., **77** (1) 455–465, 1982.

[126] **Mehl, J.B.; ; Moldover, M.R.; Laurent, P.**: Designing quasi-spherical resonators for acoustic thermometry, Metrologia, **41** (4) 295–304, 2004.

[127] **Miller, J.F.**: *An apparatus for the measurement of sound velocity in fluids at high pressures and application of the sound velocity in developing an equation of state for carbon tetrachloride* (Ph.D.-Thesis, Faculty of the Graduate School, Cornell University, Ithaca, 1986).

[128] **Miyamoto, H.; Watanabe, K.**: A thermodynamic property model for fluid-phase propane, Int. J. Thermophys., **21** (5) 1045–1072, 2000.

[129] **Mohr, P.J.; Taylor, B.N.**: CODATA recommended values of the fundamental physical constants: 2002, Rev. Mod. Phys., **77** (1) 1–108, 2005.

[130] **Moldover, M.R.; Mehl, J.B.; Greenspan, M.**: Gas-filled spherical resonators: Theory and experiment, J. Acoust. Soc. Am., **79** (2) 253–272, 1986.

[131] **Moldover, M.R.; Trusler, J.P.M.; Edwards, T.J.; Mehl, J.B.; Davis, R.S.**: Measurement of the universal gas constant R using a spherical acoustic resonator, Phys. Rev. Lett., **60** (4) 249–252, 1988.

[132] **Moldover, M.R.; Trusler, J.P.M.; Edwards, T.J.; Mehl, J.B.; Davis, R.S.**: Measurement of the universal gas constant R using a spherical acoustic resonator, J. Res. Natl. Bur. Stand., **93** (2) 85–144, 1988.

[133] **Moldover, M.R.; Boyes, S.J.; Meyer, C.W.; Goodwin, A.R.H.**: Thermodynamic Temperatures of the Triple Points of Mercury and Gallium and in the Interval 217 K to 303 K, J. Res. Natl. Inst. Stand. Technol., **104** (1) 11–46, 1999.

[134] **Morse, P.M.; Ingard, K.U.**: *Theoretical Acoustics* (McGraw-Hill, New York, 1968).

[135] **Muringer, M.J.P.; Trappeniers, N.J.; Biswas, S.N.**: The effect of pressure on the sound velocity and density of toluene and n-heptane up to 2600 bar, Phys. Chem. Liq., **14** (4) 273–296, 1985.

[136] **Niepmann, R.**: *Messung der Ultraschallgeschwindigkeit in Flüssigkeiten über einen größeren Temperatur- und Druckbereich (in German)* (Dissertation, Institut für Thermo- und Fluiddynamik, Ruhr-Universität Bochum, 1983).

[137] **Niepmann, R.**: Thermodynamic properties of propane and n-butane. 2. Speeds of sound in the liquid up to 60 MPa, J. Chem. Thermodyn., **16** (9) 851–860, 1984.

[138] **Noury, J.**: Vitesse des ultrasons de 585 kHz dans le propane au voisinage de l'état critique, J. Phys. Rad., **25** (12) 831–832, 1954.

[139] **Novikov, I.I.; Avdonin, V.I.**: Velocity of sound in saturated and superheated steam, Report at the 7th Int. Conf. on the Properties of Steam, Tokyo, 1968.

[140] **Oakley, B.A.; Barber, G.; Worden, T.; Hanna, D.**: Ultrasonic parameters as a function of absolute hydrostatic pressure. I. A review of the data for organic liquids, J. Phys. Chem. Ref. Data, **32** (4) 1501–1533, 2003.

[141] **Oakley, B.; Hanna, D.; Shillor, M.; Barber, G.**: Ultrasonic parameters as a function of absolute hydrostatic pressure. II. Mathematical models of the speed of sound in organic liquids, J. Phys. Chem. Ref. Data, **32** (4) 1535–1544, 2003.

[142] **Papadakis, E.P.**: Ultrasonic phase velocity by the pulse-echo-overlap method incorporating diffraction phase corrections, J. Acoust. Soc. Am., **42** (5) 1045–1051, 1967.

[143] **Petitet, J.P.; Tufeu, R.; Neindre, B.L.**: Determination of the thermodynamic properties of water from measurements of the speed of sound in the temperature range 251.15-293.15 K and the pressure range 0.1-350 MPa, Int. J. Thermophys., **4** (1) 35–50, 1983.

[144] **Petitet, J.P.; Denielou, L.; Tufeu, R.; Neindre, B.L.**: Velocity of sound in supercritical water up to 700 °C and 300 MPa, Int. J. Thermophys., **7** (5) 1065–1075, 1986.

[145] **Physikalisch-Technische Bundesanstalt**: Internationale Praktische Temperaturskala von 1968 (IPTS-68), PTB-Mitteilungen, **81** (1) 31–43, 1971.

[146] **Pires, P.F.; Guedes, H.J.R.**: The speed of sound and isentropic compressibility of liquid difluoromethane (HFC32) from T = (248 to 343) K and pressures up to 65 MPa, J. Chem. Thermodyn., **31** (3) 55–69, 1999.

[147] **Pires, P.F.; Guedes, H.J.R.**: The speed of sound, and derived thermodynamic properties of liquid trifluoromethane (HFC23) from T = (258 to 303) K at pressures up to 65 MPa, J. Chem. Thermodyn., **31** (1) 479–490, 1999.

[148] **Pires, P.F.; Esperanca, J.M.S.S.; Guedes, H.J.R.**: Ultrasonic speed of sound and derived thermodynamic properties of liquid 1,1,1,2,3,3,3-heptafluoropropane (HFC227ea) from 248 K to 333 K and pressures up to 65 MPa, J. Chem. Eng. Data, **45** (4) 496–501, 2000.

[149] **Prandtl, L.; Oswatitsch, K.; Wieghardt, K.**: *Führer durch die Strömungslehre (in German)*, 11th ed. (Vieweg, Braunschweig, 1990).

[150] **Preston-Thomas, H.**: The international temperature scale of 1990 (ITS-90), Metrologia, **27** (1) 3–10, 1990.

[151] **Press, W.H.; Teukolsky, S.A., Vetterling, W.T.; Flannery, B.P.**: *Numerical Recipes in Fortran 77 – The Art of Scientific Computing*, Vol. 1, 2nd Ed. (Cambridge University, Cambridge, 2001).

[152] **Rayleigh, J.W.S.**: *The Theory of Sound*, Vol. I (Dover, New York, 1945).

[153] **Rayleigh, J.W.S.**: *The Theory of Sound*, Vol. II (Dover, New York, 1945).

[154] **Ruschmeyer, K.**: *Piezokeramik (in German)* (Expert, Renningen-Malmsheim, 1995).

[155] **Schouten, J.A.; Trappeniers, N.J.; Goedegebuure, W.**: Electrical feedthrough for gas pressures up to 10000 bar and low temperatures, Rev. Sci. Instrum., **50** (12) 1652–1653, 1979.

[156] **Seldam, C.A. ten; Biswas, S.N.**: Determination of the equation of state and heat capacity of argon at high pressures from speed of sound data, J. Chem. Phys., **94** (3) 2130–2135, 1991.

[157] **Seldam, C.A. ten; Biswas, S.N.**: Thermodynamic properties of fluid helium at high pressures determined from speeds of sound, J. Chem. Phys., **96** (8) 6163–6166, 1992.

[158] **Soldatenko, Y.A.; Dregulyas, E.K.**: Speed of Sound and calculation of the caloric properties of ethylene and propylene in the supercritical region (in Russian), Proc. 3rd All-Union Scientific-Technical Thermodynamics Conference, 1968, 344–352, 1970.

[159] **Solvay Fluor & Derivate GmbH**: Solkane© 227ea Pharma and Solkane© 134a Pharma – HFA Propellants for Medical Use, Technical Manual, Solvay Fluor & Derivate GmbH, Hannover, 2003.

[160] **Span, R.**: *Multiparameter Equations of State* (Springer, Berlin, 2000).

[161] **Span, R.; Lemmon, E.W.; Jacobsen, R.T.; Wagner, W.; Yokozeki, A.**: A reference equation of state for the thermodynamic properties of nitrogen for temperatures from 63.151 K to 1000 K and pressures to 2200 MPa, J. Phys. Chem. Ref. Data, **29** (6) 1361–1433, 2000.

[162] **Span, R.; Wagner, W.**: Equations of state for technical applications. I. Simultaneously optimized functional forms for nonpolar and polar fluids, Int. J. Thermophys., **24** (1) 1–40, 2003.

[163] **Span, R.; Wagner, W.**: Equations of state for technical applications. II. Results for nonpolar fluids, Int. J. Thermophys., **24** (1) 41–110, 2003.

[164] **Span, R.; Wagner, W.**: Equations of state for technical applications. III. Results for polar fluids, Int. J. Thermophys., **24** (1) 111–162, 2003.

[165] **Spurk, J.H.; Aksel, N.**: *Strömungslehre (in German)*, 6th ed. (Springer, Berlin, 2006).

[166] **Stimson, H.F.**: The International Temperature Scale of 1948, J. Res. Natl. Bur. Stand., **42** (3) 209–217, 1949.

[167] **Stimson, H.F.**: International Practical Temperature Scale of 1948, J. Res. Natl. Bur. Stand., **65A** (3) 139–145, 1961.

[168] **Straty, G.C.**: A fluorine compatible low temperature electrical feedthrough, Rev. Sci. Instrum., **43** (1) 156–157, 1972.

[169] **Straty, G.C.**: Hypersonic velocities in saturated and compressed fluid methane, Cryogenics, **15** (12) 729–731, 1975.

[170] **Sun, T.F.; Kortbeek, P.J.; Biswas, S.N.; Trappeniers, N.J.; Schouten, J.A.**: An ultrasonic method for the accurate determination of the melting line: data for cyclohexane and benzene, Ber. Bunsenges. Phys. Chem., **91** (10) 1013–1017, 1987.

[171] **Szabó, I.**: *Höhere Technische Mechanik (in German)* (Springer, Berlin, 1960).

[172] **Tardajos, G.; Gaitano, G.G.; Espinosa, F.R.M. de**: Accurate, sensitive, and fully automatic method to measure sound velocity and attenuation, Rev. Sci. Instrum., **65** (9) 2933–2938, 1994.

[173] **Terres, E.; Jahn, W.; Reissmann, H.**: Zur Kenntnis der Bestimmung von adiabatischen Exponenten leicht siedender Kohlenwasserstoffe bei verschiedenen Drücken und Temperaturen durch Messung der Ultraschallgeschwindigkeit, Brennstoff-Chemie (in German), **38** (9/10) 129–160, 1957.

[174] **Thurston, R.N.; Pierce, A.D.** (Eds.): *Ultrasonic Measurement Methods*, Physical Acoustics Vol. XIX (Academic Press, Boston, 1990).

[175] **Tiersten, H.F.**: *Linear Piezoelectric Plate Vibrations* (Plenum, New York, 1969).

[176] **Tillner-Roth, R.**: *Fundamental Equations of State* (Shaker, Aachen, 1998).

[177] **Trusler, J.P.M.**: *Physical Acoustics and Metrology of Fluids* (Adam Hilger, Bristol, 1991).

[178] **Trusler, J.P.M.; Zarari, M.**: The speed of sound and derived thermodynamic properties of methane at temperatures between 275 K and 375 K and pressures up to 10 MPa, J. Chem. Thermodyn., **24** (9) 973–991, 1992.

[179] **Trusler, J.P.M.; Zarari, M.P.**: Second and third acoustic virial coefficents of methane at temperatures between 125 K and 375 K, J. Chem. Thermodyn., **27** (7) 771–778, 1995.

[180] **Trusler, J.P.M.; Zarari, M.P.**: The speed of sound in gaseous propane at temperatures between 225 K and 375 K and at pressures up to 0.8 MPa, J. Chem. Thermodyn., **28** (3) 329–335, 1996.

[181] **Trusler, J.P.M.; Wakeham, W.A.; Zarari, M.P.**: Second and third interaction virial coefficients of the (methane+propane) system determined from the speed of sound, Int. J. Thermophys., **17** (1) 35–42, 1996.

[182] **Trusler, J.P.M.; Wakeham, W.A.; Zarari, M.P.**: Model intermolecular potentials and virial coefficients determined from the speed of sound, Molec. Phys., **90** (5) 695–703, 1997.

[183] **Trusler, J.P.M.**: Equation of state for gaseous propane determined from the speed of sound, Int. J. Thermophys., **18** (3) 635–654, 1997.

[184] **Tsumura, R; Straty, G.C.**: Speed of sound in saturated and compressed fluid ethane, Cryogenics, **17** (4) 195–200, 1977.

[185] **Wagner, W.**: *Eine mathematisch-statistische Methode zum Austellen thermodynamischer Gleichungen – gezeigt am Beispiel der Dampfdruckkurve reiner Stoffe*, Fortschr.-Ber. VDI, Reihe 3, Nr. 39 (VDI, Düsseldorf, 1974).

[186] **Wagner, W., Saul, A.; Pruss, A.**: International equations for the pressure along the melting and the sublimation curve of ordinary water substance, J. Phys. Chem. Ref. Data, **23** (3) 515–527, 1994.

[187] **Wagner, W., Pruss, A.**: The IAPWS formulation 1995 for the thermodynamic properties of ordinary water substance for general and scientific use. J. Chem. Phys. Ref. Data, **31** (2) 387–535, 2002.

[188] **Will, S.; Fröba, A.P.; Leipertz, A.**: Thermal diffusivity and sound velocity of toluene over a wide temperature range, Int. J. Thermophys., **19** (2) 403–414, 1998.

[189] **Williams, A.O.**: The piston source at high frequencies, J. Acoust. Soc. Am., **23** (1) 1–6, 1951.

[190] **Wilson, W.D.**: Speed of sound in distilled water as a function of temperature and pressure, J. Acoust. Soc. Am., **31** (8) 1067–1072, 1959.

[191] **Wiryana, S.; Slutsky, L.J.; Brown, J.M.**: The equation of state of water to 200 °C and 3.5 MPa: potential models and the experimental pressure scale, Earth Planetary Sci. Lett., **163** (1) 123–130, 1998.

[192] **Ye, S.**: *Mesure et exploitation de la vitesse d'ultrasons dans des liquides en pression; application a des fluides complexes d'origine petroliere* (Thèse de Doctorat, Laboratoire de Physique des Matériaux Industriels, Université de Pau et des Pays de l'Adour, 1990).

[193] **Ye, S.; Alliez, J.; Lagourette, B.; Saint-Guirons, H.; Arman, J.; Xans, P.**: Réalisation d'un dispositif de mesure de la vitesse et de l'atténuation d'ondes ultrasonores dans des liquides sous pression, Rev. Phys. Appl., **25** (6) 555–565, 1990.

[194] **Younglove, B.A.**: Speed of sound in parahydrogen, J. Acoust. Soc. Am., **38** (3) 433–438, 1965.

[195] **Younglove, B.A.**: Velocity of sound in liquid propane, J. Res. Natl. Bur. Stand., **86** (2) 165–170, 1981.

[196] **Younglove, B.A.; Ely, J.F.**: Thermophysical properties of fluids. II. Methane, ethane, propane, isobutane, and normal butane, J. Phys. Chem. Ref. Data, **16** (4) 577–798, 1987.

[197] **Younglove, B.A.; Frederick, N.V.; McCarty, R.D.**: *Speed of sound data and related models for mixtures of natural gas constituents*, NIST Monograph 178, U.S. Government Printing Office, Washington, 1993.

[198] **Zachmanoglou, E.C.; D.W. Thoe**: *Introduction to Partial Differential Equations with Applications* (Dover, New York, 1986).

[199] **Zuckerwar, A.J.**: *Handbook of the Speed of Sound in Real Gases, Vol. 1: Theory* (Academic, San Diego, 2002).

[200] **Zuckerwar, A.J.**: *Handbook of the Speed of Sound in Real Gases, Vol. 2: Measurements* (Academic, San Diego, 2002).

[201] **Zuckerwar, A.J.**: *Handbook of the Speed of Sound in Real Gases, Vol. 3: Speed of Sound in Air* (Academic, San Diego, 2002).